

**INVESTIGATION OF SURFACE CRACK GROWTH BEHAVIOUR UNDER VARIABLE
PRESSURE FLUCTUATIONS IN NEAR-NEUTRAL PH ENVIRONMENTS**

By
Devin W. Engel

A thesis submitted in partial fulfillment of the requirements for the degree of

Master of Science
in
Materials Engineering

Department of Chemical and Materials Engineering

University of Alberta

ABSTRACT

The goal of this investigation was to study the corrosion fatigue behaviour and mechanisms of surface cracks, semi-elliptical in shape, when exposed to near-neutral pH environments conducive to the environments experienced in the field. To better simulate field conditions, while avoiding the financial and technical burdens of full-scale testing, a simple, yet effective test setup was implemented. A novel sample geometry possessing three surface cracks with their notches removed, dubbed the Surface Crack Tension (SCT) specimen, was used in combination with a simulated coating disbondment, with a gap size of 5 mm, inside of a sealed corrosion cell containing a ground water solution to study the effect of location inside of coating disbondments on crack growth behaviour. The corrosion cell used in the study was sealed from the atmospheric environment, and the bulk solution was purged with 5 % CO₂ + N₂ bal. away from the disbondment over the duration of the tests to maintain a *pH* of 6.29 and a deaerated environment.

Underload-type variable amplitude loading schemes were designed and implemented to better simulate the pressure fluctuations that are experienced on a routine basis by pipelines in operation at locations where the majority of stress corrosion failures occur. It was found that crack growth rates (da/dN) were enhanced by up to several orders of magnitude when subjected to underload-type loading waveforms in comparison to constant amplitude loading for loading frequencies from 10⁻³ Hz to 10⁻¹ Hz. Additionally, the crack growth rates for underload-type schemes comprising of either high *R*-ratio cycles (minor cycles) or static holds in between underload events were compared. The introduction of minor cycles into underload-type loading schemes demonstrated a greater enhancement in crack growth rates over constant amplitude loading, in comparison to the introduction of static holds between underload events. The enhancement in crack growth rates in the NNpH environments by segments of quasi-static or static loads between underloads were attributed to the time-dependent accumulation of hydrogen leading up to an underload. Minor cycles were determined to provide greater growth enhancements because of their cyclic nature.

The crack growth rates for all of the waveforms tested, as well as the growth enhancement by variable amplitude loading, decreased as the distance into the coating disbondment increased. This was related to a CO₂ gradient induced by the disbondment which resulted in a decreasing concentration of hydrogen towards the bottom of the coating disbondment. ICP analysis

determined that there was a non-uniform Fe concentration distribution throughout the system. The non-uniform distribution of iron was determined to be a result of the transport, by gravity and diffusion, of Fe away from the Open Mouth of the disbondment. This led to enhanced dissolution rates outside of the disbondment and increased hydrolysis rates towards the bottom of the disbondment. In spite of the semi-elliptical geometry, with ($a:c$) aspect ratios of 0.17 – 0.21, it was determined that the depth growth rates were similar to the surface, with the surface growth rates exceeding the depth growth rate for the cracks located above the disbondment's Open Mouth. This was rationalized to be an effect of crack closure effects and a steep hydrogen concentration gradient in the specimens' thickness. A simulated hydrostatic test was also performed on the cracks to determine whether the test would retard or accelerate growth rates, with the results indicating that the plastic damage caused by hydrostatic testing could lead to either situation depending on the subsequent applied loads.

DEDICATION

I want to express my deepest thanks to my parents, Stan and Joyce Engel, for everything that you have done for me, particularly over these past few years – I'd be truly lost without your support. I should say thanks to my *helpful* brothers Braden, Kenton, and Justin for their 'support' during my time in University as well. This is dedicated to you all, and to the *wee ones*, King and Link, who will hopefully one day feel proud of their uncle.

*“When I became a man I put away childish things,
including the fear of childishness and the desire to be very grown up.”*

– C.S. Lewis

ACKNOWLEDGEMENTS

My sincere and absolute gratitude to Dr. Weixing Chen for all of the opportunities and assistance he has generously provided me with over the past five years. Thank you.

A special thank you to Drs. Hao Zhang, Reg Eadie, and Jingli Luo for their help and assistance during my MSc and prior works. Also, special thanks must be given to both Dr. Mengshan Yu (mentor) and Jerome Ang (mentee) for their constant support during my degree, whether it was research related or not.

Thank you to all of my colleagues, past and present: Karina Chevill, Ziqiang Dong, Afolabi Egbewande, Alex Hosack, Keqiang Hu, Josh Knechtel, Lana Labrecque, Hamid Niazi, Zeynab Shirband, Olayinka Tehinse, Xiao Xing, Zhezhu Xu, Jiaxi Zhao, and the AdvEn family.

A big thanks to the CME and EAS departments' technical staff for all of the assistance over the years, including: Nathan Gerein, Diane Caird, Shiraz Merali, Marion Pritchard, Heather Green, Lily Laser, Jack Gibeau, Walter Boddez, Clark Bicknell, Les Dean, Herb Green, James Mckinnon, Dave Parlin, and Bob Smith.

Thank you to the sponsors for their financial support: TransCanada Pipelines Ltd, Enbridge Pipelines Inc, Natural Science and Engineering Research Council of Canada (NSERC), and the Pipeline Research Council International (PRCI).

TABLE OF CONTENTS

Abstract	ii
Dedication	iv
Acknowledgements	v
Table of Contents	vi
List of Figures	x
List of Tables	xix
List of Abbreviations	xxi
CHAPTER 1: Introduction.....	1
CHAPTER 2: Literature Review	3
2.1 Transmission Pipeline Integrity	3
2.1.1 SCC of Pipeline Steels	6
2.2 Characteristics of NNpHSCC	7
2.2.1 Environment and Corrosion.....	8
2.2.2 Microstructural Factors	13
2.2.3 Crack Initiation	14
2.2.4 Field Characteristics.....	15
2.3 Corrosion Fatigue Behaviour	16
2.3.1 Inert Fatigue	16

2.3.2 Corrosion Fatigue.....	18
2.4 NNpH Corrosion Fatigue	31
2.4.1 Monotonic Loading (SCC Debate)	31
2.4.2 Constant Amplitude (CA) Loading.....	33
2.4.3 NNpH Crack Models	38
2.5 Surface Cracks	43
2.6 Variable Amplitude (VA) Loading.....	44
2.6.1 Effect of Minor Cycles.....	47
2.6.2 Effect of Underload Frequency and Max Stress Intensity	50
2.6.3 Effect of Static Holds	51
2.7 Research Objectives	52
CHAPTER 3: Experimental Methods.....	54
3.1 Introduction.....	54
3.2 Material and Specimen.....	54
3.2.1 Material.....	54
3.2.2 Surface Crack Tension (SCT) Specimens.....	56
3.2 Corrosion Cell and Environment	58
3.2.1 Corrosion Cell	58
3.2.2 Test Solution	59
3.3 Mechanical Loading Conditions	59

3.3.1 Test I & II Waveforms	61
3.4 End of Test Procedure	63
3.5 Characterization	64
3.5.1 Pretest Crack Characterization.....	64
3.5.2 Post-Test Crack Characterization.....	66
3.5.3 Solution Analysis	70
CHAPTER 4: Results.....	72
4.1 Surface Characterization.....	72
4.1.1 Surface Crack Growth.....	72
4.1.2 Surface Morphology	77
4.2 Depth Morphology	84
4.3 Fracture Surface Characterization.....	88
4.3.1 Growth Band Measurements.....	88
4.3.2 Corrosion Characteristics	90
4.3.3 Microscopic Features	93
4.3.4 Hydrostatic Test Damage.....	97
4.4 Cell Solution Analysis	97
CHAPTER 5: Discussion.....	100
5.1 Waveform Effects on Surface Crack Growth Behaviour.....	100
5.1.1 Constant Amplitude (CA)	100

5.1.2 Variable Amplitude (VA)	109
5.2 Disbondment Effects on Surface Crack Growth Behaviour	115
5.2.1 Local Disbondment Environments	115
5.2.2 Local Crack Environments.....	121
5.2.3 Disbondment Effect on Crack Growth Behaviour	124
5.3 Hydrostatic Testing	129
CHAPTER 6: Conclusions and Recommendations	131
6.1 Comparison of Crack Geometries.....	131
6.1.1 Constant Amplitude Loading	131
6.1.2 Variable Amplitude Loading	132
6.2 Coating Disbondment Effects	133
6.2.1 Local Environment Effects	133
6.2.2 Effect of Local Environments on Crack Growth.....	134
6.3 Minor Study of Hydrostatic Testing	135
6.4 Recommendations for Future Work.....	136
Bibliography.....	138
APPENDIX A: Supplementary Data – DCPD System and Data	149
References	156
APPENDIX B: Supplementary Data – Additional Crack Images	157

LIST OF FIGURES

Figure 2.1	Distribution of the primary causes of reported ruptures on NEB-regulated pipelines (6).....	4
Figure 2.2	The number of NEB-regulated Pipeline ruptures from the years 1991 – 2009 (6). 6	
Figure 2.3	SCC crack colony on the external surface of a high-pressure gas transmission pipeline (11).	7
Figure 2.4	Example of high pH SCC intergranular cracking along ferrite and pearlite grains on a pipeline that failed while in service operation (4).....	8
Figure 2.5	Typical NNpHSCC crack found the field which initiated from a pit, and demonstrates increasing lateral corrosion along the crack walls as the crack mouth is approached (15).	9
Figure 2.6	Iron carbonate corrosion products formed on a pipeline steel surface after exposure to a near-neutral pH solution purged with CO ₂ (17).....	10
Figure 2.7	Calculated equilibrium constant values as a function of the ratio of species at equilibrium and <i>pH</i> (16).....	11
Figure 2.8	Corrosion rate at the open mouth (OM) at various gap sizes for 5% CO ₂	12
Figure 2.9	Cracks formed on a tensile specimen during long-term cyclic loading in a NNpH environment (35).....	14
Figure 2.10	SEM images of well developed-cracks from both densely (a) and sparsely (b) populated colonies (42).	16
Figure 2.11	Typical variation of fatigue crack growth behaviour of metals showing the three growth regions (48).	17

Figure 2.12	Illustrations representing the crack growth behaviour of (a) time-dependent, (b) cycle dependent (true), and (c) cycle-time-dependent (general) corrosion fatigue.	20
Figure 2.13	Effect of frequency on CF crack propagation within the plateau region of ΔK for A710 and API-2H steels in aerated 3% NaCl, -1000mV (SCE) (62).	24
Figure 2.14	Schematic showing the hydrogen sources of the two forms of hydrogen assisted cracking: hydrogen-environment-assisted cracking (HEAC) and internal-hydrogen-assisted cracking (IHAC) (75).	31
Figure 2.15	Crack length extension (μm) as a function of test time (h) for two different simulated soil environments and various loading conditions (29).	33
Figure 2.16	Pressure fluctuations recorded over time for a high-pressure gas transmission pipeline (80).	34
Figure 2.17	Crack growth rate (da/dN) as a function of ΔK for X-65 pipeline steel in (a) C2 and (b) NOVATW test solutions. $K_{\text{max}} = 35 - 55 \text{ MPa}\sqrt{\text{m}}$ and $\Delta K = 10 - 28 \text{ MPa}\sqrt{\text{m}}$ (28).	35
Figure 2.18	Dependence of crack growth (da/dN) on K_{max} with (a) da/dN vs. K_{max} (28) and (b) da/dN vs. ΔK (46).	36
Figure 2.19	The variation of da/dN with frequency in C2 solution and in-air, at constant K_{max} ($33 \text{ MPa}\sqrt{\text{m}}$) and ΔK ($16.5 \text{ MPa}\sqrt{\text{m}}$) (54). Their reference (6) corresponds to this literature's reference (28).	37
Figure 2.20	Comparison of net growth over time for two different NNpH solutions, C2 (pH = 6.29) and NOVATW (pH = 7.11). (a) $\Delta K = 16 \text{ MPa}\sqrt{\text{m}}$, $K_{\text{max}} = 47.1 \text{ MPa}\sqrt{\text{m}}$ and (b) $\Delta K = 12 \text{ MPa}\sqrt{\text{m}}$, $K_{\text{max}} = 35.3 \text{ MPa}\sqrt{\text{m}}$	39
Figure 2.21	Cyclic crack growth rates (da/dN) of varying test frequencies fitted with the superposition model (85).	40

Figure 2.22	Crack growth rate (mm/s) as a function of crack tip strain rate fitted with the strain rate model (81).....	41
Figure 2.23	da/dN data as a function of the combined factor for (a) C2 and (b) NOVATW solutions (28).....	43
Figure 2.24	Demonstrating the environmentally short crack effect in NNpH environments based on the Combined Factor threshold value of through-thickness cracks (86).	45
Figure 2.25	Typical crack growth behaviour under several combinations of underload and overload cycles (96).....	46
Figure 2.26	Identification of pressure fluctuations on (a) oil and (b) gas pipeline spectra (96).	48
Figure 2.27	Simulated underload-type spectra used in the experiments studying the effects of minor cycles (54).	48
Figure 2.28	Plots comparing the effects of the number of minor cycles in air and C2 solution. (a) Crack growth rate of individual minor cycles. (b) Crack growth rate of underloads. (c) Acceleration Factor (99).	49
Figure 2.29	Demonstrating the effects of varying (a) K_{max} and (b) f_{UL} in underload-type spectra in C2 solution and in-air (54).....	51
Figure 2.30	Graphical demonstration of the effect of static holds for $K_{max} = 33 \text{ MPa}\sqrt{\text{m}}$, $\Delta K_{UL} = 16.5 \text{ MPa}\sqrt{\text{m}}$, and $f_{UL} = 1 \times 10^{-3} \text{ Hz}$, with (a) varying hold times (100) and (b) in comparison to UL&MC and CA waveforms for $n = 697$ and $t_{hold} = 15.5\text{h}$ (80)...	52
Figure 3.1	The stress-strain curve for the X-60 pipeline steel used to machine test specimens.	55
Figure 3.2	Long tensile sample geometry, dimensions, and notch locations.....	56

Figure 3.3	(Left) drawing of the original corrosion cell design and (right) the corrosion cell used in testing.....	56
Figure 3.4	The two types of variable amplitude waveforms used during testing. LHS: Underload and Minor Cycles (UL&MC) and RHS: Underload and Hold (UL&H).	61
Figure 3.5	Simulated hydrostatic test load procedure used in Test II taken from literature (106).	63
Figure 3.6	Demonstrating the replica measurements taken to determine pretest crack length using stitched SEM images of pretest crack replicas.	66
Figure 3.7	Illustrating the locations on Test I's cracks' surfaces, where CUT indicates where the samples were sectioned for depth profile characterization. TOP refers to the OM.	68
Figure 3.8	XRD profile for Test I's Middle crack's fracture surface with peaks detected other than BCC-iron, but they could not be identified.	70
Figure 4.1	Net surface crack growth (μm) in C2 solution plotted as a function of time for all three cracks in Test I.	74
Figure 4.2	Crack growth rates (dc/dN) of CA and UL&MC waveforms for the OM, Middle, and Bottom cracks in Test I as a function of load frequency (Hz).	75
Figure 4.3	Histogram illustrating the growth rates of the OM, Middle, and Bottom crack locations of Test II for the two waveforms tested in C2 solution.	77
Figure 4.4	SEM SE images of Test II's pretest crack tips (replicas) for the Bottom crack. All cracks used in the study were similar to those above. The blues arrows indicate the crack tip locations.	78
Figure 4.5	Low (left) and high (right) magnification BSE post-test SEM images of Test I, where (a), (b), and (c) are the cracks at the Open Mouth, Middle, and Bottom	

	disbondment locations. The blue arrows indicate the crack tip locations, while the blue ovals encircle the thin crack crevice regions.	79
Figure 4.6	SE post-test images of the OM crack in Test I's, with red arrows indicating the locations where pretest scratches from abrasive grinding are still visible within areas surrounding thin crack crevice locations.	79
Figure 4.7	Images of the bulk surface corrosion at the (a) OM, (b) Middle, and (c) Bottom crack regions in Test I after seven days of exposure to C2 solution. The dark grey areas are locations of dissolution.	80
Figure 4.8	SEM BSE high magnification images of Test I's polished crack tips where (a,b), (c,d), and (e,f) are the OM, Middle, and Bottom cracks, respectively.	81
Figure 4.9	BSE image of Test I's OM crack tip after an intermediate (6 μm) polish showing a large amount of micro-cracks in the region ahead of the crack tip.	82
Figure 4.10	SE SEM images of the etched crack tips of Test I demonstrating the transgranular crack paths at the (a) OM, (b) Middle, and (c) Bottom crack locations.	82
Figure 4.11	Comparison of SEM images of Test II's post-test crack tips, where (a,b), (c,d), and (e,f) are the OM, Middle, and Bottom cracks. The BSE images on the left (a,c,e) are the real crack tips after hydrostatic testing and the SE images on the right (b,d,f) are replicas before hydrostatic testing with the blue circles indicating the crack tip regions.	83
Figure 4.12	SEM BSE high magnification images of Test II's polished crack tips where (a,b), (c,d), and (e,f) are the OM, Middle, and Bottom cracks, respectively.	84
Figure 4.13	Low magnification images of Test I (a-c) and Test II's (d-f) crack depth profiles, where (a&d), (b&e), and (c&f) are the cracks at the OM, Middle, and Bottom cracks, respectively. Arrows indicate the approximate pretest crack locations and red circles highlight the near surface dissolution regions.	85

Figure 4.14	EDS profile obtained using an area scan on the corrosion products wedged inside of Test I's Bottom crack along its depth profile.	86
Figure 4.15	High magnification images of Test I (a-c) and Test II's (d-f) crack depth profiles, where (a&d), (b&e), and (c&f) are the cracks at the OM, Middle, and Bottom cracks, respectively. Arrows indicate the approximate pretest crack locations....	88
Figure 4.16	Low magnification BSE images of Test I's (a) OM, (b) Middle, and (c) Bottom crack fracture surfaces. The green and blue lines indicate the start of testing in air and C2 solution, respectively.	89
Figure 4.17	SE FESEM images demonstrating growth band measurements in the depth on the fracture surfaces of the OM from (a) Test I and (b) Test II. The cracks had their corrosion products removed prior to imaging.	91
Figure 4.18	Striations from UL&MC waveforms on the fracture surfaces of Test I's (a) OM for $f = 10^{-3}$ Hz and (b) Bottom cracks for $f = 10^{-2}$ Hz. Blue arrows indicate the crack propagation direction.	94
Figure 4.19	Striations generated by the UL&MC (a-d) and UL&H (c-d) waveforms in Test II on the (a,b) OM, (c,d) Middle, and (e,f) Bottom crack fracture surfaces.	95
Figure 4.20	Low (left) and high (right) magnification in-lens FESEM fractography showing evidence of hydrogen-induced-cracking (HIC) within the cleavage plane of several cracks. The features on the right-hand side are located within the blue boxes on the left. Blue arrows indicate locations of key features: C (cavity), P (protrusion), MC (micro-crack), U (undulation), S (slip line), and MV (microvoid).	96
Figure 4.21	Damage on the fracture surfaces in Test II by hydrostatic testing for the (a) OM, (b) Middle, and (c) Bottom cracks. Hydrotest damage is definable by dimpled ridges and quasi-cleavage or smoothed features. The arrows indicate the cleavage (blue), hydrostatic damage (red), and the crack front (purple). The red ellipses indicate locations of ductile void formation between the quasi-cleave zone of the hydrostatic test damage and the cleavage plane from fracturing the sample open.	98

Figure 5.1	Log plot of CA crack growth rates as a function of frequency where: SCT-OM represents the OM crack constant amplitude data from Test I with $K_{\max} = 13.8$ MPa $\sqrt{\text{m}}$ and $\Delta K = 12.5$ MPa $\sqrt{\text{m}}$; CT-Yu (54) is the data for CT specimens where $K_{\max} = 33$ MPa $\sqrt{\text{m}}$ and $\Delta K = 16.5$ MPa $\sqrt{\text{m}}$	101
Figure 5.2	Log plot of CA crack growth rates as a function of the Combined Factor, where: SCT-OM represents the OM crack constant amplitude data from Test I with $K_{\max} = 13.8$ MPa $\sqrt{\text{m}}$ and $\Delta K = 12.5$ MPa $\sqrt{\text{m}}$; CT-Yu (54) is the data for CT specimens where $K_{\max} = 33$ MPa $\sqrt{\text{m}}$ and $\Delta K = 16.5$	107
Figure 5.3	Log plot of UL&MC crack growth rates as a function of frequency where: SCT represents the OM crack's UL&MC surface data from Test I with $K_{\max} = 13.8$ MPa $\sqrt{\text{m}}$, $\Delta K = 12.5$ MPa $\sqrt{\text{m}}$ and CT-Yu $K_{\max} = 33$ MPa $\sqrt{\text{m}}$, $\Delta K = 16.5$ MPa $\sqrt{\text{m}}$ (99). Minor cycles: SCT, $n = 100$, $f = 5 \times 10^{-3}$ Hz, $R = 0.9$; CT-Yu, $n = 697$, $f = 5 \times 10^{-3}$ Hz, $R = 0.9$	110
Figure 5.4	Log plot of crack growth rates for all three waveform types, where: SCT represents Test I and II OM crack's average surface data (where applicable) and CT-Yu is data taken from literature (54, 100). [Underloads/CA: $R_{UL,SCT} = 0.1$, $R_{UL,CT} = 0.1$, and $f_{UL/CA} = 10^{-3}$ Hz] [Minor Cycles: $n = 100$, $f_{MC} = 5 \times 10^{-3}$ Hz, $R_{MC} = 0.9$] [Static Hold: $K_I = K_{\max}$, $t_{\text{hold}} = 350$ min]	115
Figure 5.5	Iron distribution profile of the various key locations within the corrosion cell used in the current study.....	119
Figure A.1	Long tensile sample DCPD lead configuration for Test II.	149
Figure A.2	Potential change of X60 steel as a function of temperature for $L_p = 2$ mm.....	151
Figure A.3	Temperature-normalized DCPD potential drop plot (ΔV vs. Time) for the OM crack of Test I	152
Figure A.4	Temperature-normalized DCPD potential drop plot (ΔV vs. Time) for the Middle crack of Test I	152

Figure A.5	Temperature-normalized DCPD potential drop plot (ΔV vs. Time) for the Bottom crack of Test I	153
Figure A.6	Temperature-normalized DCPD potential drop plot (ΔV vs. Time) for the Middle crack of Test II	155
Figure A.7	Temperature-normalized DCPD potential drop plot (ΔV vs. Time) for the Bottom crack of Test II	155
Figure B.1	SE images of Test I's pretest replicas of the (a,b) OM, (c,d) Middle, and (e,f) Bottom crack tips.	158
Figure B.2	SE images of Test II's pretest replicas of the (a,b) OM, (c,d) Middle, and (e,f) Bottom crack tips.	159
Figure B.3	BSE full surface profile post-test images of Test I's (a) OM, (b) Middle, and (f) Bottom cracks.	160
Figure B.4	SE partial surface profile post-test images of Test I's (a) OM, (b) Middle, and (f) Bottom cracks.	161
Figure B.5	BSE full surface profile post-test images of Test II's (a) OM, (b) Middle, and (f) Bottom cracks.	161
Figure B.6	Low mag BSE images of Test I's (a) OM, (b) Middle, and (c) Bottom crack fracture surfaces.....	162
Figure B.7	Low mag BSE images of Test II's (a) OM, (b) Middle, and (c) Bottom crack fracture surfaces.	163
Figure B.8	SE FESEM images demonstrating growth bands in the depth on the fracture surfaces of the (a) OM, (b) Middle, and (c) Bottom cracks of Test I.	164
Figure B.9	SE FESEM images demonstrating growth bands in the depth on the fracture surfaces of the (a) OM, (b) Middle, and (c) Bottom cracks of Test II.	165

- Figure B.10** SE FESEM images demonstrating growth bands at the midway point on the fracture surfaces of the (a) OM, (b) Middle, and (c) Bottom cracks of Test I. 166
- Figure B.11** SE FESEM images demonstrating growth bands at the midway point on the fracture surfaces of the (a) OM, (b) Middle, and (c) Bottom cracks of Test II. 167

LIST OF TABLES

Table 2.1	Summary of variables affecting corrosion fatigue of steel in aqueous environments (52).....	21
Table 3.1	Composition of X60 pipeline steel	55
Table 3.2	In air fatigue precracking schedule using the stepped force shredding method ...	57
Table 3.3	Composition of the simulated NNpH solution (C2) used during testing. $pH = 6.29$	60
Table 3.4	Crack geometries and stress intensity values for CA cycles & underloads in Tests I and II.	60
Table 3.5	Summary of mechanical waveforms and testing parameters of Tests I and II.	62
Table 4.1	Summary of calculated surface crack growth data for Test I for all waveforms in C2 solution.	73
Table 4.2	Summary of calculated surface crack growth data for Test II for both waveforms in C2 solution. *The crack growth rates of the OM were determined using the Middle DCPD data.	76
Table 4.3	Summary of the elemental compositions (at. %), determined through EDS, of the corrosion products along the crack depth profiles of Test I.....	87
Table 4.4	Net growth (Δa) and crack growth rates (da/dN) of Tests I and II determined by fracture surface growth band measurements at the depth and midway point locations for each crack.....	92
Table 4.5	Summary of average crack growth rates (da/dN) determined by striation measurements.....	93
Table 4.6	pH measurements at various locations within the cell for Tests I and II.	99

Table 4.7	ICP chemical species analysis (ppm) from various locations within the cell of Test I.	99
Table A.1	Summary of DCPD data and calculations used to determine Test I's growth rates in C2 solution (dc/dN).	154
Table A.2	Summary of DCPD data and calculations used to determine Test II's growth rates in C2 solution (dc/dN).	156

LIST OF ABBREVIATIONS

AES	Auger Electron Spectroscopy
AIDE	Adsorption-Induced Dislocation Emission
API	American Pipeline Institute
BSE	Backscattered Electron
CA	Constant Amplitude
CEPA	Canadian Energy Pipeline Association
CF	Corrosion Fatigue
CP	Cathodic Protection
EAC	Environmentally-Assisted Cracking
EDM	Electrical Discharge Machining
EDS	Energy-Dispersive X-Ray Spectroscopy
EMAT	Electromagnetic Acoustic Transducer
FESEM	Field Emission Scanning Electron Microscopy
FPZ	Fracture Process Zone
HAC	Hydrogen-Assisted Cracking
HE	Hydrogen Embrittlement
HEAC	Hydrogen-Environment-Assisted Cracking
HEDE	Hydrogen-Enhanced Decohesion
HELP	Hydrogen-Enhanced Localized Plasticity
HIC	Hydrogen-Induced Cracking
HpH	High pH
HpHSCC	High pH Stress Corrosion Cracking
ICP-MS	Inductively Coupled Plasma Mass Spectroscopy
IHAC	Internal-Hydrogen-Assisted Cracking
ILI	In-line Inspection
MFL	Magnetic Flux Leakage
MOP	Maximum Operating Pressure
NEB	National Energy Board
NNpH	Near-Neutral pH

NNpHSCC	Near-Neutral pH Stress Corrosion Cracking
OCP	Open Circuit Potential
OM	Open Mouth
PPMA	Poly(methyl methacrylate)
RLE	Ripple Load Effect
RTC	Room Temperature Creep
SCC	Stress Corrosion Cracking
SE	Secondary Electron
SEM	Scanning Electron Microscope
SMYS	Specified Minimum Yield Strength
SSRT	Slow Strain Rate Testing
TMCP	Thermo-Mechanically Controlled Process
UL&MC	Underload and Minor Cycles
UL&H	Underload and Hold
VA	Variable Amplitude
XRD	X-Ray Dispersive

CHAPTER 1: INTRODUCTION

Since its discovery in 1985 (1, 2), near-neutral pH stress corrosion cracking (NNpHSCC) has been reported by pipeline operators in Europe, Asia, Australia, the US, and Canada (3), with the primary occurrence of NNpHSCC on Canadian pipelines (4). However, in spite of over 30 years of research, NNpHSCC still remains a problematic pipeline integrity issue as a full understanding of the initiation and propagation mechanisms elude researchers to this day. This proves to be a major concern as cracking by NNpHSCC can eventually lead to fast rupture or leaks in oil and gas pipelines (4), which has and will continue to cause economic losses and, more importantly, pose a significant danger to public health and safety and the environment.

It is well known that cracking on pipelines in NNpH environments occurs under pipeline coating failures, which allows for the ground water to contact the steel, and cyclic loading caused by the pressure fluctuations experienced by the pipe during operation. As discussed within the Literature Review (Chapter 2) of this work, in spite of experimental research studies on both coating disbondments and variable amplitude loading to simulate the environment and pressure fluctuations experienced by pipelines in the field, little work has been done to combine the two critical factors. Additionally, little to no experimental work has been performed using surface cracks which have their notches removed or are semi-elliptical in shape, which would best represent cracks in the field.

Therefore, the current investigation was performed to establish a fundamental understanding of shallow surface crack growth behaviour in NNpH environments under variable pressure fluctuations. More specifically, field conditions were simulated using polymer corrosion cells equipped with shieldings that imitated disbonded pipeline coatings, while variable amplitude fatigue waveforms were used to simulate the pressure fluctuations typically experienced by pipelines downstream from compressor stations. From the results presented in the study, the variable amplitude corrosion fatigue behaviour of surface cracks in NNpH environments at several locations under a coating disbondment and open circuit potential (OCP) conditions was established. It was found that surface cracks grow at mechanical thresholds considerably lower than those of traditional fracture mechanics specimens. Additionally, based on the experimental findings using simulated coating disbondments, it was suggested that decreasing hydrogen

reduction reaction rates were responsible for decreasing crack growth rates as cracks were located deeper into coating disbondment. The structure of the thesis is described in the following paragraph.

First, an introductory review of the current understandings on NNpH crack environments, initiation, and field crack behaviours and an in-depth review of general corrosion fatigue and NNpH corrosion fatigue are provided within Chapter 2. Second, the experimental techniques used to simulate pipeline cracking in NNpH environments under coating disbondments and the characterization methods to obtain the results are described in Chapter 3. Next, Chapter 4 and Chapter 5 present and discuss the results obtained through two longer term tests, respectively. Chapter 5 provides in-depth comparisons of the corrosion fatigue behaviour of surface cracks to traditional fracture mechanics specimens, the local environments under coating disbondments, and crack growth behaviours under coating disbondments. Finally, the main findings and conclusions resulting from this dissertation are reviewed and presented alongside recommendations for future research in Chapter 6.

CHAPTER 2: LITERATURE REVIEW

The following chapter of this work will develop and provide a concise, yet comprehensive review on the general characteristics and cracking mechanisms of near-neutral pH stress corrosion cracking (NNpHSCC). First, a brief overview of Canadian pipelines and the two types of SCC they experience will be provided. Then, the general characteristics and necessary conditions for the occurrence of NNpHSCC, such as environmental conditions, will be detailed. Afterwards, the focus will shift to the areas of research on crack growth behaviours relating to the propagation of cracks through corrosion fatigue. Finally, the research objectives of the current work will be highlighted based on identified areas of interest from the Literature Review.

2.1 TRANSMISSION PIPELINE INTEGRITY

In a recent report by Alberta Energy Regulator, it was tallied up that over 415 000 km of pipeline, primarily steel (86 %), crisscrossed the province of Alberta by the end of the year 2012 (5). Of Alberta's total pipelines, 60.3 % carry natural gas and 4.9 % carry crude oil, transporting the large majority of the 3.7 trillion ft³ and 203 million barrels of natural gas and crude oil produced in the province in 2012, respectively. Thus, any incident, be it a leak, rupture, or otherwise in Alberta's pipelines can readily lead to a large economic loss for both companies and the province.

The National Energy Board (NEB) of Canada defines pipeline rupture as a "loss of containment event that immediately impairs the operation of a pipeline." The primary causes of NEB-regulated ruptures from 1991 – 2009 were by cracking (38 %) and metal loss (27 %) (**Figure 2.1**). The former was primarily caused by hydrogen-induced and mechanical delayed cracking, stress corrosion, and corrosion fatigue, while the latter corresponds to either external or internal corrosion (6). SCC accounted for 13 % of the total NEB pipeline ruptures from 1994 – 2003, or approximately 1/3 of the crack related ruptures (7).

NEB-Regulated Pipeline Rupture Causes

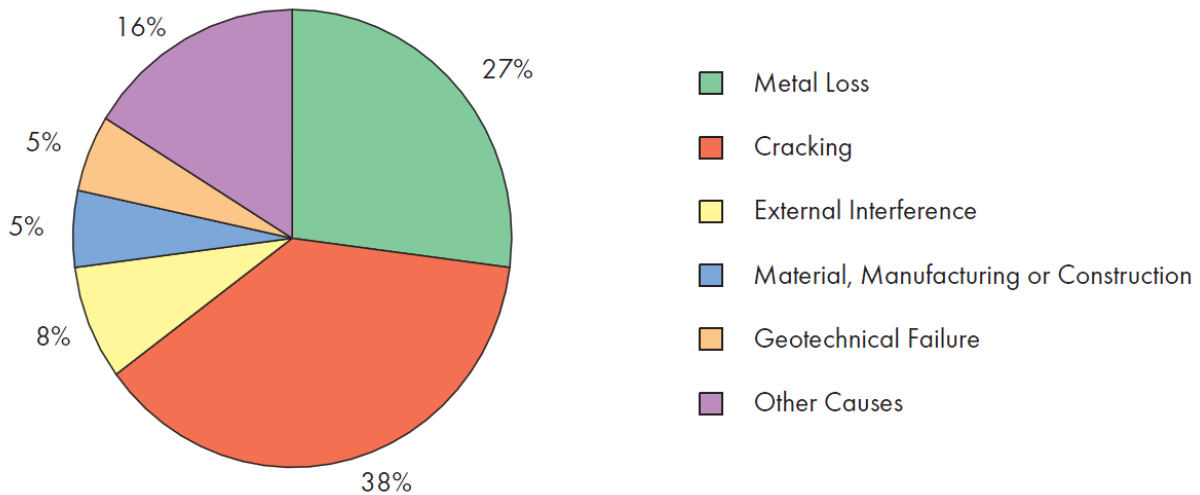


Figure 2.1 Distribution of the primary causes of reported ruptures on NEB-regulated pipelines (6).

Figure 2.2 shows the frequency of ruptures on NEB-regulated pipelines per year from 1991 – 2009. As illustrated, since 1999 the average rate of ruptures per year have steadily declined. This can be correlated to the implementation of mandates which require the development of pipeline integrity and mitigation programs for all NEB-regulated companies under OPR-99, amongst other programs and regulations introduced thereafter (6). For example, specifically for the case of SCC management, several recommended practices have been proposed by the Canadian Energy Pipeline Association (CEPA) including (3):

1) *SCC Condition Assessment.*

A type of engineering assessment, which involves a documented evaluation, within the scope of the SCC management plan, on the effects of relevant variables upon the suitability of the pipe body, applying engineering principles. This involves the required assessment of (I) the severity of individual SCC features and (II) any need for immediate or future pipe segment mitigation following the detection of SCC. Type (I) assessments evaluate the imposed risk of detected SCC based on non-subjective data, e.g. crack depth, length, and stress levels. Type (II) assessments require more subjective variables, such as the quantification of SCC growth rates.

2) *In-line Inspection (ILI).*

Operators have the option of using in-line inspection tools to inspect operating pipelines for the presence of stress corrosion cracks. However, it is currently unavailable for all pipeline sizes and has not been proven quite to the extent as other tools, such as magnetic flux leakage (MFL) and ultrasonic metal-loss tools. The two primary detection technologies being employed for SCC detection are ultrasonic and Electromagnetic Acoustic Transducer (EMAT).

The primary advantage of in-line inspections over hydrostatic testing and condition assessments is time and cost efficiency. In-line inspections can be ran on oil lines while the pipeline is still operating, unlike hydrotesting, and it can sample a large length of pipe for flaws, unlike excavations. From in-line inspections the quantity, density and location of SCC features are known, as well as the maximum feature lengths and depths are known within the range “bins” output of the tool.

3) *Hydrostatic Testing.*

During a hydrostatic test, a pipe segment is temporarily removed from service, purged of natural gas, and filled with water until the desired pressure is achieved. Hydrostatic testing has been shown, through years of use and research to be an effective means of safely removing near-critical axial defects in pipelines, providing a margin of safety against in-service failure of the section tested. Based on the results, field engineers can determine how to carry out repairs and reinforcements, re-evaluate the maximum operating pressure (MOP), or if the pipe section needs replacement.

There are two components to a hydrostatic test; (I) the “high” pressure test to rupture all near-critical axial defects and (II) the “low” pressure test to detect any defects which did not rupture but have caused leaks. High pressure tests typically test at pressures from 125 % MOP to 110 % SMYS, for 1 – 2h, while low pressure tests test at pressures from 90 % to 100 % SMYS or 110 % MOP to 125 % MOP, all depending on which standard is followed by the operator for the procedures. Other than cost and time, the major drawback to hydrostatic testing is if no failures occur during testing any information on the quantity, density and locations of SCC that may exist remain unknown.

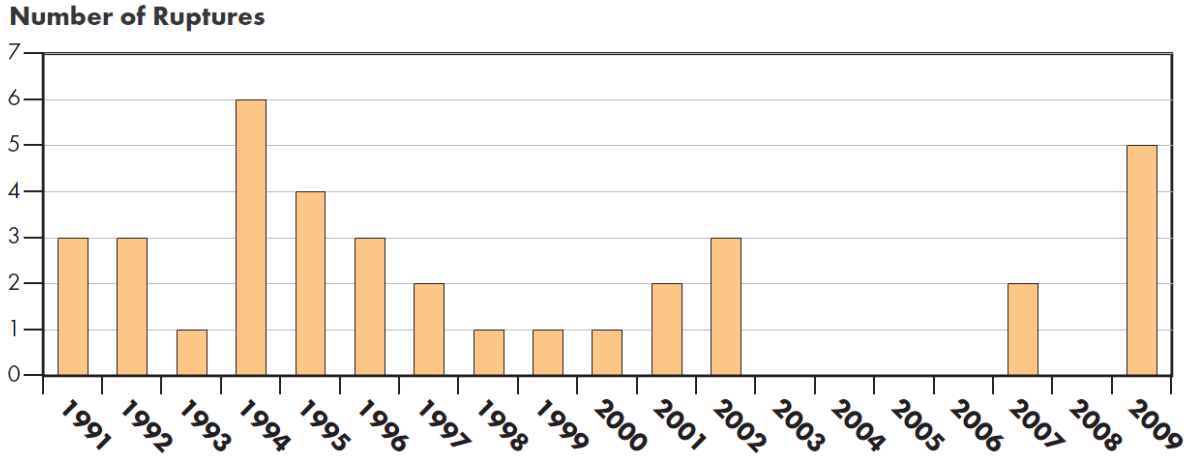


Figure 2.2 The number of NEB-regulated Pipeline ruptures from the years 1991 – 2009 (6).

2.1.1 SCC OF PIPELINE STEELS

SCC, a form of environmentally-assisted cracking (EAC), occurs when three general conditions are simultaneously met: the material must be susceptible to SCC, tensile stresses exist above some threshold value, and a crack-promoting environment is present. Typically most, if not all, of pipeline steels are susceptible to SCC. Tensile stresses are provided by the internal pressure of the transported medium, while the corrosive environment is established through the contact of the bare steel surface with ground water that has penetrated under a failed section of the pipe's external coating (4, 8, 9). The severity of SCC depends on the extent of the coating disbondment (4).

There are two forms of SCC which can occur for pipeline steels depending on whether or not cathodic protection can reach the steel surface under the coating disbondment. Extensive reviews comparing the two forms can be found in literature (4, 8, 9), and the main features of the first will only be briefly mentioned in the next paragraph. Regardless of the form, the most identifying characteristic of pipeline SCC is the formation of patches or colonies (e.g., **Figure 2.3**) of parallel cracks on the external surface of the pipe, typically oriented in the longitudinal direction (10). These cracks are closely spaced, vary in length in depth, and may coalesce to form single, long cracks that may eventually lead to rupture. Typically, both forms' fracture surfaces are covered with black magnetite or iron carbonate corrosion products and films (8). In the absence of CO₂, neither form of SCC will occur (9).

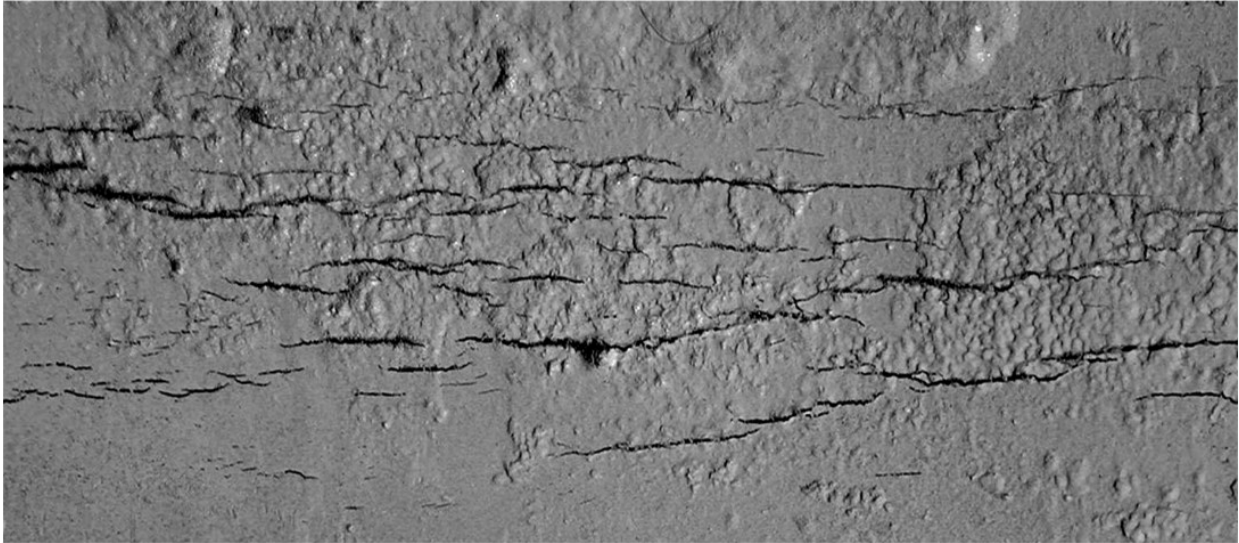


Figure 2.3 SCC crack colony on the external surface of a high-pressure gas transmission pipeline (11).

This first form of SCC, known as classical, traditional, intergranular, or high pH (HpH) SCC occurs when cathodic protection is able to reach the pipeline surface under the coating disbondment. HpHSCC most prominently occurs in environments containing concentrated carbonate-bicarbonates ($\text{CO}_3\text{-HCO}_3$), with *pH* levels ranging from 8.5 – 10. Cracks of this form are usually sharp, propagate intergranularly, and show minimal evidence of corrosion attack along the crack walls as exemplified in **Figure 2.4**. The mechanism of crack propagation is well attributed to grain boundary dissolution in combination with repeated passive film formation and rupture; the rate of crack propagation follows a temperature dependence in accordance with the Arrhenius Law, increasing as temperature increases. The other form of SCC will be discussed in great detail in the next section.

2.2 CHARACTERISTICS OF NNpHSCC

The second form of SCC, known as transgranular or near-neutral pH SCC occurs when little or no CP can reach the steel surface under the coating disbondment. NNpHSCC cracks (e.g., **Figure 2.5**) are characterised by significant lateral corrosion of the crack sides, transgranular crack paths, and propensity to occur in dilute ground water solutions (4, 8, 9). As the central focus of the current work is NNpHSCC the environment, corrosion mechanism, metallurgical susceptibility, and field crack characteristics will be explored in greater detail than the traditional, high pH form of SCC previously discussed.

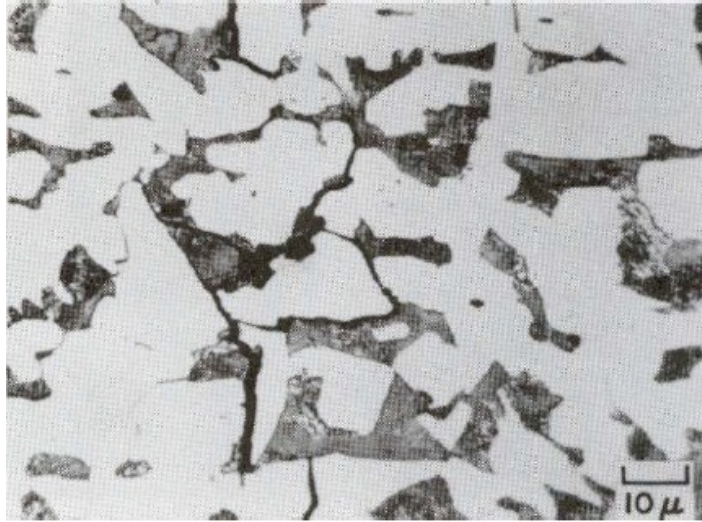


Figure 2.4 Example of high pH SCC intergranular cracking along ferrite and pearlite grains on a pipeline that failed while in service operation (4).

2.2.1 ENVIRONMENT AND CORROSION

Near-neutral ground water solutions typically vary in pH from 5.5 to 8.5, where the CO₂ derives from the decay of organic matter in the soil surrounding the coating disbondment (2, 12). The solution can then maintain a *pH* level from 5.5 – 8.5, dependent on the CO₂ partial pressure, through an equilibrium between dissolved CO₂ and bicarbonate ions (4); a reduction of *pH* can be associated with increasing bicarbonate solutions. Although bicarbonates are the primary species in the system, solutions often contain additional chemical species in low concentrations such as chlorides, sulphates and nitrates (13, 14). However, if a steady supply of CO₂ is not maintained the rate of hydroxyl ion formation will exceed the formation of bicarbonate and the *pH* levels will rise (12).

NNpH environments exist under pipeline coating disbondments when the supply of CO₂ to the ground water solution is maintained with little to no CP, i.e. at open circuit potential (OCP). CP plays a critical role in NNpH environments, as low *pH* solutions will persist so long as inadequate cathodic current flows along the pipe surface. Such conditions are mostly achieved when the pipe's coating is a poor conductor, i.e. tape coatings, with the exception of asphalt coatings if the surrounding soil has a very high electrical resistivity (4). Furthermore, the severity of crack formation at sites of coating failure sites has been found to depend on the extent and shape of the disbondment (2).

Therefore, in order to adequately describe the environmental corrosion aspect of NNpHSCC two major factors must be discussed: CO₂ corrosion attack and coating disbondment geometry and soil location. The former relates to the mechanism of corrosion damage on the exposed steel surface, while the latter determines the conditions and extent to which the corrosion damage may occur.

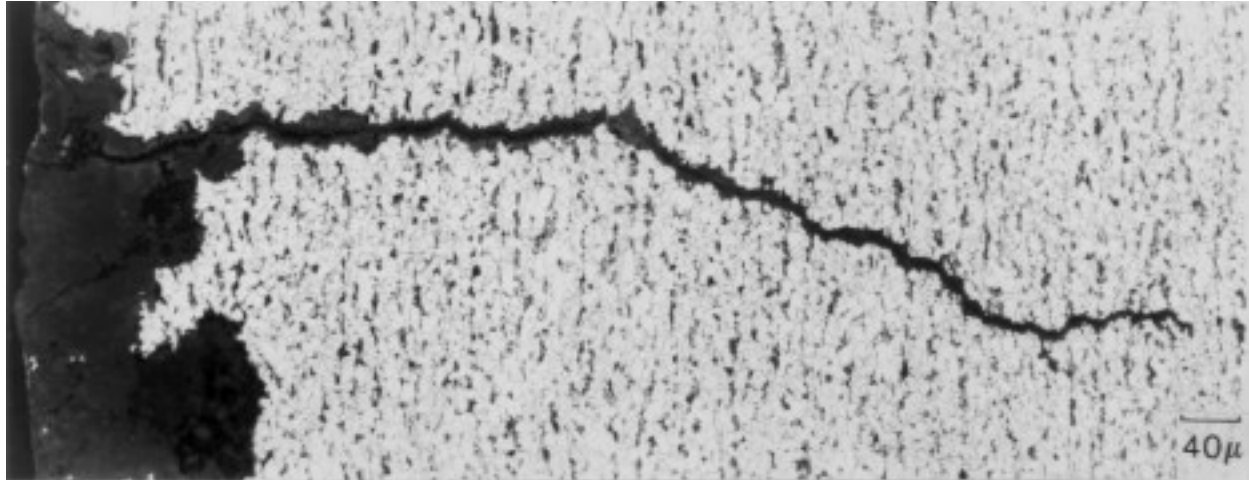


Figure 2.5 Typical NNpHSCC crack found the field which initiated from a pit, and demonstrates increasing lateral corrosion along the crack walls as the crack mouth is approached (15).

2.2.1.1 CO₂ Corrosion Mechanism (Dissolution)

In anaerobic conditions, the corrosion of steel in the presence of CO₂ in the NNpH range results the following sequence of reactions (12, 16-19):

Hydration of carbon dioxide



Dissociation of carbonic acid



Oxidation of iron (anodic)



Precipitation of iron-carbonate



Reduction of ionic hydrogen (cathodic)



Overall reaction



It is important to note that the formation of FeCO_3 within the NNpH system is kinetically slow, and forms porous, non-passivating deposits (**Figure 2.6**), i.e. it does not form a protective film as it does in the high pH system (16-18).

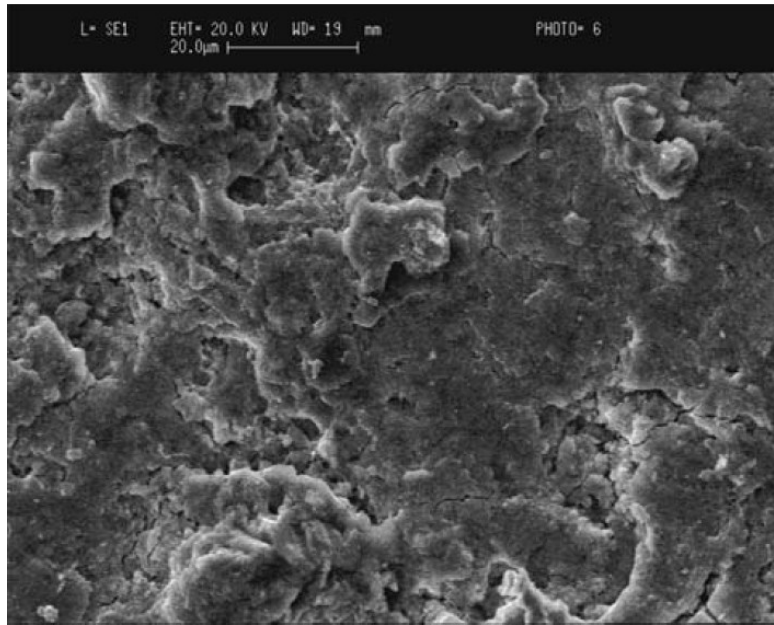


Figure 2.6 Iron carbonate corrosion products formed on a pipeline steel surface after exposure to a near-neutral pH solution purged with CO_2 (17).

In addition to the reduction of hydrogen ions, another cathodic reaction can occur for $\text{H}_2\text{O}-\text{CO}_2$ system when $pH > 5$:

Reduction of water (cathodic)



However, the direct reduction of water is a kinetically controlled and slow process and hydrogen generation is predominated by the weak carbonic acid route. It is because of the multiple cathodic reactions that an enhanced corrosion rate of steel is found in the CO_2 NNpH system, as a result in an increased driving force for the dissolution of iron via **Eq. 2.3**. Furthermore, based on the above

reactions, an increase in P_{CO_2} would cause an increase in the hydrogen generated which explains the greater extent of corrosion attack and embrittlement of pipeline steels in many experimental studies with increasing P_{CO_2} (16, 17, 20).

Figure 2.7 demonstrates the ratio of carbonate based species within the typical NNpH range of 5.5 – 8.5 and bicarbonate dominated region (16). When the pH value is around 6.38, an equilibria between the CO_2^- species in **Eq. 2.2** establishes and their concentrations are approximately equal (**Eq. 2.6**) (12, 16). This buffering capability of the bicarbonate system was considered within the Colwell-Leis mechanism, which accounted for the generation of hydrogen and formation of $FeCO_3$ in the absence of changes in pH (16).

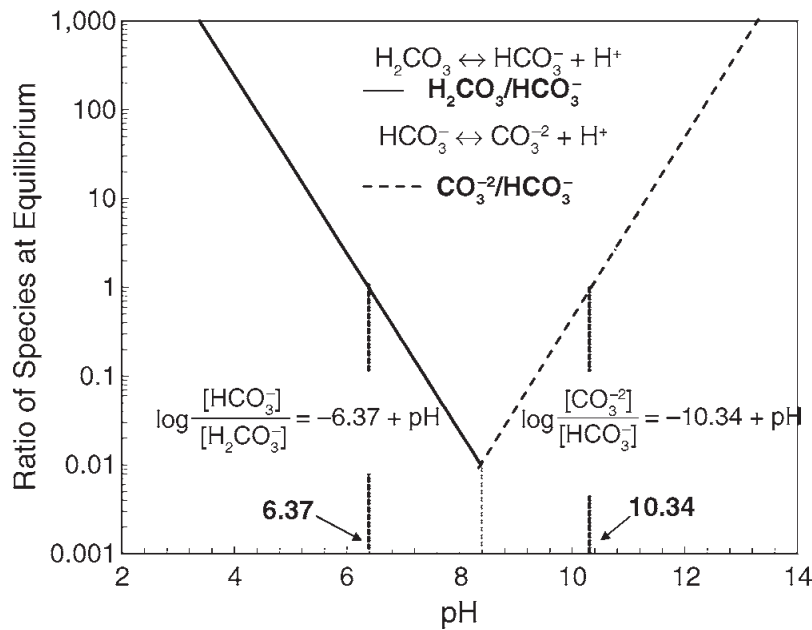


Figure 2.7 Calculated equilibrium constant values as a function of the ratio of species at equilibrium and pH (16).

$$\log(HCO_3^-/H_2CO_3) = -6.38 + pH \quad (2.8)$$

2.2.1.2 Coating Disbondment Geometry and Location

The general corrosion rate of C2, a commonly used simulated ground water solution (21), saturated with 5 % CO_2 is about 0.05 mm/year (22). Field studies have indicated that the extent of disbondment, a.k.a. the geometric gap size between the steel surface and coating, and holiday size have an effect on general corrosion and the occurrence of SCC (2). The occurrence of SCC

colonies correlated well with sites of minor disbondments such as wrinkles resulting from poor coating application or soil stresses. The OCP corrosion rates of X-65 steel coupons submerged in C2 solution, saturated with varying amounts of CO₂ (2 % – 20 %), within various simulated disbondment gap sizes (2 mm – 10mm) has been studied in depth by Chevil, *et al.* (22, 23). The corrosion rates (mil/year) for 5% CO₂ at various positions into the disbondments are shown in **Figure 2.8**. For a 10 mm gap size, corrosion rates decreased linearly further into the disbondment, while the corrosion rates of the 2 mm and 5 mm gap sizes rapidly approached zero ~ 2.5 cm into the disbondment. It can be said that both the 2 mm and 5 mm gap sizes better represent field findings where CP has difficulty reaching the exposed steel surface at the site of minor disbondment, while the 10 mm gap size is representative of a major disbondment where general corrosion attack will occur.

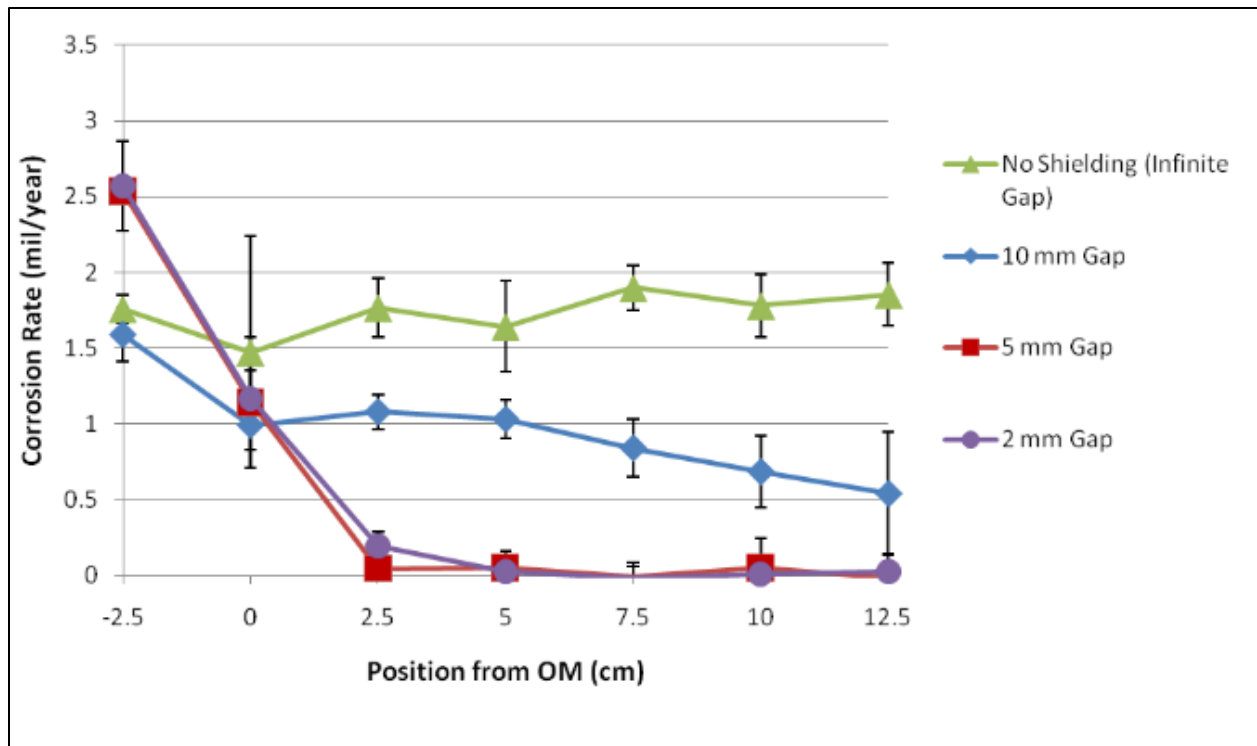


Figure 2.8 Corrosion rate at the open mouth (OM) at various gap sizes for 5% CO₂

In the case of polyethylene tape coatings, the above disbondment situation with little to no CP can be readily achieved because of the poor electrical conductivity of the material. However, a coating disbondment is not the only requirement for the environmental conditions of NNpHSCC to be

established and there exists factors pertaining to the location of the soil surrounding the pipe which must also be present.

1) *CO₂ levels.*

It is known that concentrations of CO₂ exist within the soil surrounding pipelines via the decomposition of organic matter, with seasonal variations from 4 % during the winter up to 23% during spring (2). While it has been found that corrosion rates generally increase with increasing CO₂ levels from 2 % – 20% (24), the opposite trend has been demonstrated for crack growth rates within a coating disbondment (25). Decreasing crack growth rates with increasing CO₂ levels were attributed to an enhancement in the blunting effect by corrosion, in spite of increased levels of hydrogen.

2) *Soil type.*

The tendency for SCC to occur under polyethylene tape coatings is significantly higher, by a factor of ~7.5, in regions containing soils composed of clays and silts (lacustrine soils) over those composed of sands and gravels (glaciofluvial materials). This is because clays and silts tend to have poor drainage properties and a higher amount of retained ground water can be found in these regions. However, the opposite is true for the coatings with higher electrical conductivities such as asphalt coatings. In fact, it has been reported that over 80% of SCC colonies detected under asphalt coatings were located in regions of dry terrain consisting of sandy soils or sand and bedrock (2). Such dry terrains possess very high electrical resistivity, minimizing the amount of CP which can reach under the asphalt conditions (4).

2.2.2 MICROSTRUCTURAL FACTORS

Pipes of all grades of micro-alloyed American Petroleum Institute (API) steels are considered susceptible to NNpHSCC (26), confirmed by studies of crack initiation and propagation using X52 (11), X60 (11), X65 (15, 16, 27-31), X70 (26), X80 (26, 32, 33), and X100 (34). In spite of extensive studies on crack initiation and propagation, little to no evidence exists that any one of these materials are more susceptible than the other to cracking in NNpH environments. An extensive study performed by Beavers, *et al.* on the susceptibility of various grades of pipeline which experienced in-service failure also found that there exists no significant microstructural

variations between locations where SCC colonies are found and locations remote to the colonies (26). Thus, material susceptibility is best related to crack initiation and defects.

2.2.3 CRACK INITIATION

The propensity for crack initiation from small corrosion pits on the pipe surfaces has been found to be inversely related to the rate of corrosion, which attacks locations of local stress concentrations via general dissolution (30). Crack initiation is a competitive process where many different types of initiation sites can exist simultaneously along a pipes surface, with pit nucleation and subsequent crack initiation from pits occurring at the most favourite sites first.

A dominant site for micro-pit formation, and likely the most important site, occurs at near-surface locations of residual tensile stresses around 216 ± 104 MPa (26, 35, 36). Residual stresses on pipe surfaces are often introduced by pipe fabrication, coating surface preparation, installation, and mechanical damage (26). Such cracks can be seen in **Figure 2.9**, where mechanically short cracks initiated from the bottom of pits which formed at sites of residual tensile stresses while under cyclic stress in C2 solution.

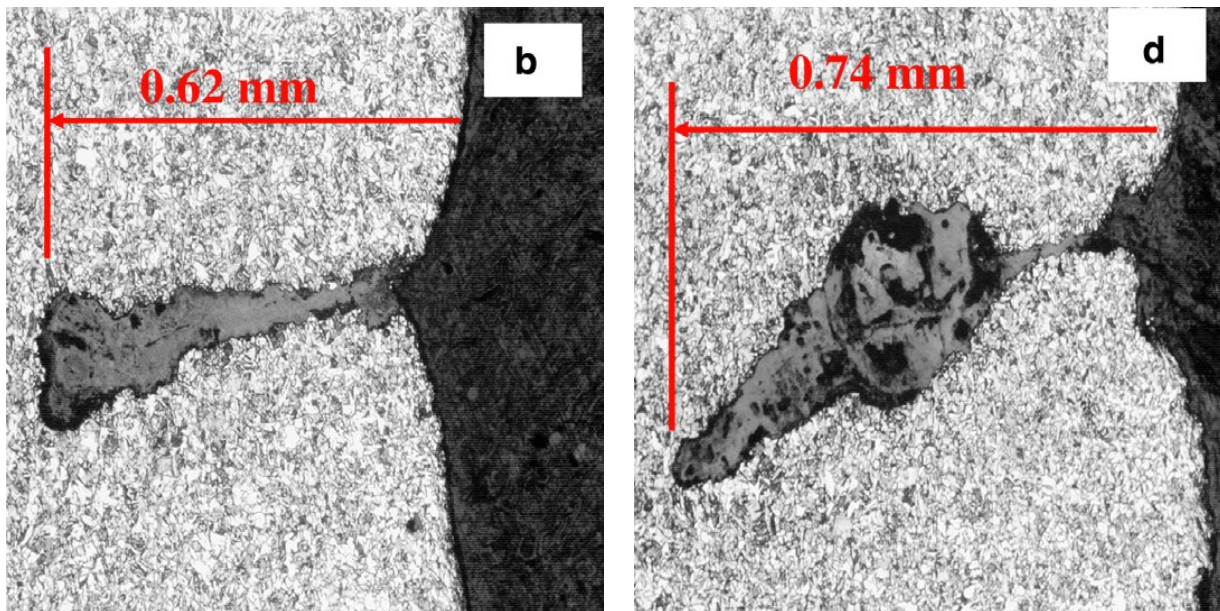


Figure 2.9 Cracks formed on a tensile specimen during long-term cyclic loading in a NNpH environment (35).

Inclusions, such as MnS, introduced by the Thermo-mechanically Controlled Process (TMCP) and pipe fabrication are another more prevalent site for pit formation because of the enhanced

dissolution at these sites by galvanic effects (27, 30, 37). Other crack initiation sites include persistent slip bands (20, 30), aligned defects (30), gouges and scratches (2, 13, 30), long-seam and toe welds (2, 32, 37, 38), surface oxides and mill-scale (15, 30), pearlite-ferrite banded microstructure interfaces (39), and the boundary of coating disbondments (27, 30).

Crack initiation in NNpH environments has been shown to be enhanced by cyclic stresses in the as-received form (15, 39-41). However, cyclic loading could potentially reduce the propensity of crack initiation by the relief of residual stresses through cyclic straining (39). The introduction of CP during cyclic loading further reduces crack initiation by reducing the frequency of pitting and the acidification of those pits, i.e. CP reduces the hydrogen at the bottom of pits (40). However, if CP is applied, regions of incomplete CP under a coating disbondment will see enhanced crack initiation because of the enhanced hydrogen production on the steel surface and little to no effect on the acidification on pits in these regions (41). Most likely, cyclic loading helps to initiate pitting on the surface, but is irrelevant in the early stages of crack growth which should occur through largely by dissolution.

2.2.4 FIELD CHARACTERISTICS

Typically, cracks within colonies found in the field possess depth to length aspect ratios as low as 0.1 (42). Statistically, ~ 95 % of the crack population will fall into dormancy as pit-like or wide, blunted cracks upon reaching a depth of ~ 1.0 mm, such as those in **Figure 2.10**, according to field observations from oil and gas pipelines (30). The reasons for crack dormancy at a depth of 1 mm is not particularly well understood, but has been related to a rapid reduction in the rate of dissolution as the crack depth approaches 1 mm and a rapid reduction in the mechanical driving force by dissolution induced blunting (43).

The mechanisms behind crack propagation following dormancy are not as well understood but it is known that the 5 % remaining population can grow either by continuous or discontinuous growth mechanisms (25, 29). As continuous crack propagation in NNpH environments has never been observed under static loading conditions (29, 44), which are conducive to traditional SCC, the mechanisms for crack propagation past 1mm have been modelled around cyclic loading or corrosion fatigue for that 5 % of the population which continue to grow (25, 28, 29, 45, 46). As such, corrosion fatigue and its mechanisms will be the main focus of the following section.

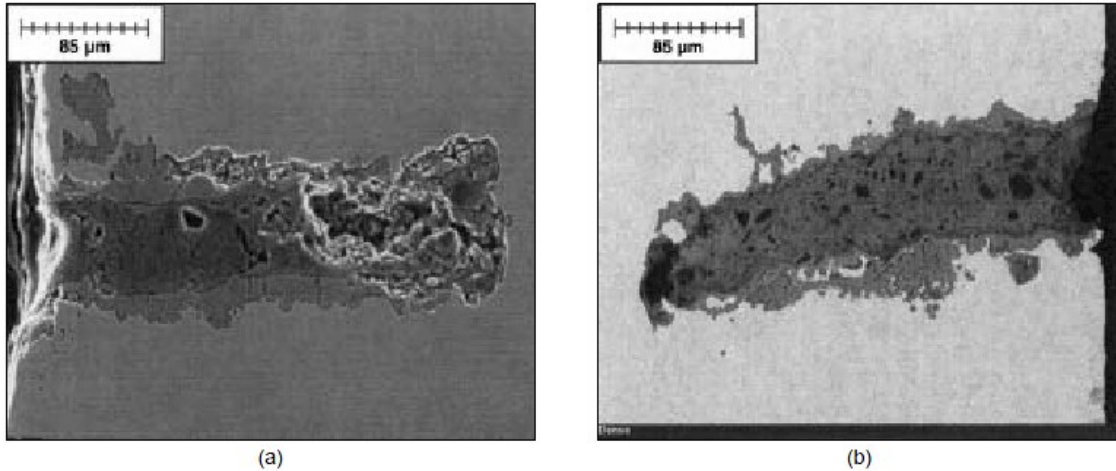


Figure 2.10 SEM images of well developed-cracks from both densely (a) and sparsely (b) populated colonies (42).

2.3 CORROSION FATIGUE BEHAVIOUR

The following section of this review will largely focus on the mechanisms and properties of general and NNpH corrosion fatigue, popularly known as NNpHSCC, in terms of macro-crack propagation. For brevity's sake, inert fatigue and its mechanisms will be briefly introduced. Next, a strong fundamental review of the types of corrosion fatigue, hydrogen-assisted cracking and its mechanisms, and the critical variables of corrosion fatigue will be given. Finally, the state-of-art in both constant amplitude (CA) and variable amplitude (VA) NNpH corrosion fatigue of pipeline steels will be discussed in detail.

2.3.1 INERT FATIGUE

Fatigue involves the accumulative mechanical damage and failure of materials caused by cyclically applied loads, accounting for over 80 % of all service failures (47). Crack propagation occurs through the competition of intrinsic damage mechanisms, which cause crack extension, and extrinsic shielding mechanisms, acting behind the crack-tip to impede growth. Intrinsic mechanisms acting within the plastic zone, involving the generation of micro-cracks or voids through processes such as dislocation pile-ups, lead to repetitive blunting and resharpening of the crack-tip under cyclic loading. Conversely, extrinsic mechanisms retard growth through either the generation of inelastic zones surrounding the crack wake (zone shielding) or the premature contact of crack surfaces by wedging, bridging, and/or sliding (contact shielding) (47).

In fatigue, subcritical crack growth can occur at stress intensity (K) levels well below the fracture toughness (K_{IC}) through accumulative damage by plastic deformation in the plastic zone. As such, the general fatigue crack growth behaviour in metals can be described in terms of its primary variable, i.e. the nominal stress-intensity range ($\Delta K = K_{\max} - K_{\min}$), as shown in **Figure 2.11**.

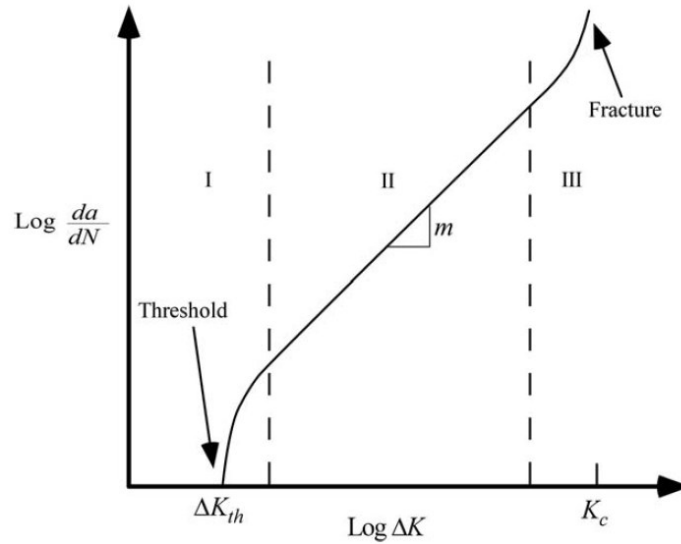


Figure 2.11 Typical variation of fatigue crack growth behaviour of metals showing the three growth regions (48).

As shown in **Figure 2.11**, there exists three distinct regions of fatigue crack growth in metals. In Region I, the crack growth rate per fatigue cycle (da/dN) approaches zero as ΔK approaches the fatigue threshold value (ΔK_{th}), below which the crack will not grow. The growth behaviour within this region is sensitive to microstructure and flow properties, such as the material's grain size (48).

Region II demonstrates a linear behaviour on the log-log plot, described by what is widely known as the *Paris Law* (47, 48):

$$da/dN = C(\Delta K)^m \quad (2.9)$$

where C and m ($2 \sim 4$) are experimentally determined material constants. From **Eq. 2.9**, the fatigue crack growth behaviour within Region II is only dependent on ΔK , and is insensitive to the stress intensity ratio ($R = K_{\min}/K_{\max}$). Here, the crack growth rate is insensitive to microstructural and flow properties for a given material, but two different materials (e.g., steel and Ti alloys) will demonstrate significantly different fatigue behaviours. Propagating cracks within Region II will

generate small ridges perpendicular to the direction of crack growth, known as striations, by a repeated blunting and sharpening process caused by irreversible shear on two-slip systems $\sim 45^\circ$ to the crack plane (47). Not every fatigue cycle will generate striations, but their average interspacing can provide good approximations of the value of da/dN (48).

Within Region III, da/dN will rapidly accelerate as K_{\max} approaches the value of K_c , and the onset of large-scale deformation occurs. Cracks typically spend a very small fraction of their life in Region III, however, and it provides little in terms of engineering application.

It is of particular importance to briefly introduce *The Unified Approach* for latter discussions, which is an alternative to the traditional ΔK modelling of fatigue behaviour. The Unified Approach was proposed by Sadananda and Vasudevan, both prominent authors in the field of fatigue research and modelling, and it can be mathematically described as (49, 50):

$$da/dN = C' \cdot \Delta K^m \cdot K_{\max}^n \quad (2.10)$$

where C' , m , and n are material constants. In The Unified Approach, both K_{\max} and ΔK are considered simultaneously, for metals and alloys, as crack driving forces with their own intrinsic thresholds that must be met concurrently for crack propagation to occur. Here, K_{\max} is considered as the fundamental force for crack propagation – dictating the extent of the fracture – and ΔK dictates the extent of cyclic plastic damage processes at the crack tip. Alternatively, K_{\max} and ΔK can be thought of the governing parameters of the monotonic and plastic zones, respectively. It is therefore rational that one parameter will dominate for a given range of R , with K_{\max} being the limiting factor at low R (fatigue-dominated) and ΔK at high values of R (fracture-dominated).

2.3.2 CORROSION FATIGUE

In a large, comprehensive report reviewing the subject (51), Gangloff has defined corrosion fatigue as damage resulting from the “synergistic interaction of cyclic plastic deformation and local chemical or electrochemical reactions.” Gangloff went on to further define three distinct forms of corrosion fatigue based on differences in the effect of the environment and frequency (f) on crack growth per cycle (da/dN):

1) *Time-dependent*

The contribution to da/dN by the environment is inversely proportional to frequency when the contribution to crack growth rate by SCC is constant with stress intensity (K), above some stress intensity threshold K_{ISCC} . From **Figure 2.12a**, time-dependent corrosion fatigue crack growth rates can be accurately described as a super-position of SCC crack growth rates (da/dt) over the unloading and loading portions of fatigue cycles. The crack growth rates by fatigue (da/dN) are proportional to $(1/\alpha f)$, where α is the proportion of the load-cycle time that corrosion fatigue damage occurs.

2) *True corrosion fatigue*

There exists two forms of true corrosion fatigue, the first form, known as cycle-dependent corrosion fatigue, typically occurs at low values of ΔK and da/dN is accelerated independently of loading frequency. Cycle-dependent corrosion fatigue displays enhanced growth rates, but similar behaviour to that of inert fatigue. The second form of true corrosion fatigue, cycle-time-dependent is characterized by an acceleration in da/dN with decreasing frequency, reflecting a synergy between mechanical and corrosion contributions to fatigue damage. In this form, cyclic deformation lowers the susceptibility to environmental damage and/or cracking and is particularly prevalent for materials possessing high SCC thresholds or immunity to SCC. Both forms of true corrosion fatigue demonstrate similar da/dN responses to ΔK , as shown in **Figure 2.12b**. For cycle-time-dependent corrosion fatigue, da/dN is proportional to $(1/\alpha f)^\beta$, where β is on the order of 0.5.

3) *General corrosion fatigue*

This is the most general form of corrosion fatigue, and has been referred to as “cyclic SCC.” It is the combination of both time- and cycle-time-dependent corrosion fatigue behaviour. Below K_{ISCC} , accelerations in da/dN will occur following cycle-time dependent behaviour, as shown in **Figure 2.12c**. However, once K_{ISCC} has been surpassed the material will exhibit ΔK independency and exhibit time-dependent corrosion fatigue behaviour.

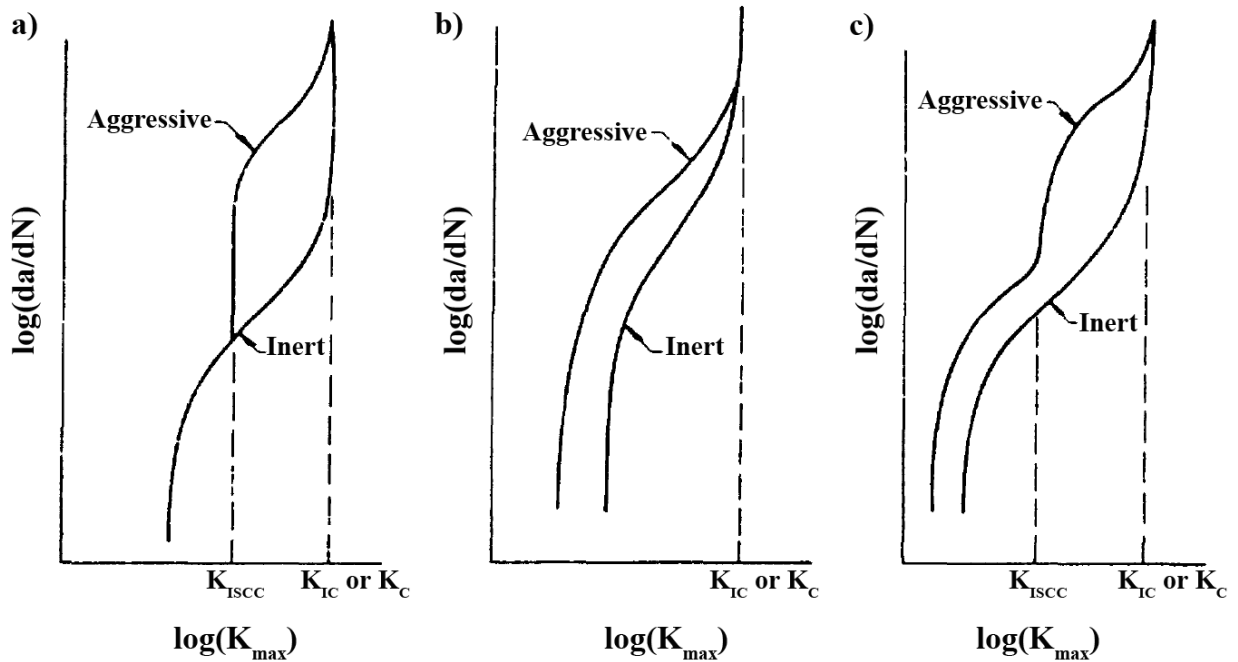


Figure 2.12 Illustrations representing the crack growth behaviour of (a) time-dependent, (b) cycle dependent (true), and (c) cycle-time-dependent (general) corrosion fatigue.

The mechanism(s) through which the above three forms of CF cause damage are often specific to mechanical loading, material, and environmental variables. It's important to note that K_{ISCC} in **Figure 2.12a&c** does not necessarily correlate to the static loading threshold, yet instead it should be viewed as a threshold value where environment-assisted-cracking under fatigue occurs. Additionally, the damage modes vary with said variables, but may include one or more of the following models: hydrogen embrittlement, film rupture and anodic dissolution, surface films, adsorbed atoms, and anodic dissolution and plasticity (51). As hydrogen assisted cracking through hydrogen embrittlement is the most relevant and accepted of these models for the NNpH system (4, 8, 15, 28, 29, 37) it will be the only model discussed in a later section.

2.3.2.1 Critical Variables in Corrosion Fatigue

The development of life prediction models for corrosion fatigue is incredibly tedious owing to the amount of interacting variables involved which have an impact on crack growth behaviour. This is further complicated by the cycle-time-dependent nature of corrosion fatigue in steels in aqueous environments (52). To demonstrate, a list of the mechanical, environmental, and metallurgical variables which effect the crack growth rates of steels in both passivating and non-passivating

dilute NaCl environments is provided in **Table 2.1**. Given the significant amount of variables, this section will only focus on several of the more critical variables applicable to steels in aqueous environments with propagating cracks of dimensions $> 100 \mu\text{m}$.

Table 2.1 Summary of variables affecting corrosion fatigue of steel in aqueous environments (52).

Type	Variables
Mechanical	ΔK , mean stress, residual stress, frequency, waveform, crack size and geometry
Environmental	Temperature, pH, potential, conductivity, ion content (Cl^- , H^+ , O_2 , Mg^{2+} , Ca^{2+}), solution flow, exposure time
Metallurgical	Yield strength, sample thickness, composition, microstructure

2.3.2.1.1 Stress Intensity Range (ΔK)

The effect of ΔK on da/dN is considerably more complicated in aqueous environments than that of inert because of the additional chemical processes involved. The dependency of cycle-time-dependent corrosion fatigue on ΔK can be explained with three *growth regions*, following **Figure 2.12c**:

- 1) *Region I*, near-threshold growth where the crack growth behaviour mimics that of inert environments, but at enhanced growth rates owing to a reduction in ΔK_{th} by the environment. In other words, crack growth is cycle-dependent.
- 2) *Region II*, above ΔK_{th} where cyclic deformation simulated “stress corrosion cracking” occurs (52), and a rapid increase in da/dN occurs relative to inert environments. The crack growth rate is mechanically limited as chemical and electrochemical reactions can proceed rapidly and still exhibits similar behaviour to inert fatigue.
- 3) *Region III*, at greater ΔK values, a plateau behaviour of nearly K -independent da/dN is observed. The plateau behaviour can be understood as chemical transport limited environmental cracking. Further increases in ΔK breaks this behaviour, but such a region

is of little engineering importance as both da/dN and ΔK are unrealistically high for typical structural applications.

2.3.2.1.2 Max Stress Intensity (K_{max})

In general, increasing the max stress intensity leads to increases in crack growth rates as it is the dominating mechanical driving force for fracture. This is particularly true at low growth rates, whether an inert or aggressive environment is present (52). For systems involving hydrogen embrittlement, this effect is better understood in terms of the effect of K_{max} on hydrogen. This demonstrated by considering the equilibrium concentration of hydrogen in the stressed lattice ahead of a crack tip following:

$$c_{eq} = c_0 \exp\left(\frac{\sigma_{hyd}\Omega}{k_B T}\right) \quad (2.11)$$

where c_{eq} and c_0 are the equilibrium and zero-stress concentrations of hydrogen, respectively, σ_{hyd} is the hydrostatic stress ahead of the crack tip, Ω is the partial molar volume of hydrogen, k_B is Boltzmann's constant, and T is temperature (53, 54).

As shown in **Eq. 2.11** the concentration of hydrogen is exponentially proportional to the hydrostatic stress which is proportional to the plastic zone size, both of which are proportional to K_{max} (55). Additionally, the diffusion or time-dependent accumulation of hydrogen has been modelled in terms of crack-tip opening displacement, which is directly proportional to K_{max} (56). Alternatively, the driving force for hydrogen diffusion has been modelled in terms of chemical potential and the hydrostatic stresses ahead of the crack tip (54, 57, 58), following **Eq. 2.12** below:

$$\mu = \mu_0 + k_B T \ln\left(\frac{c}{1-c}\right) + \sigma_{hyd}\Omega \quad (2.12)$$

where, k_B is Boltzmann's constant, T is temperature, Ω is the partial molar volume of one H atom, μ_0 is constant, and c is the concentration of hydrogen some far distance away from the crack tip that is assumed to be a constant value, c_0 (54).

Thus, it is rational that K_{max} plays a dominating role in corrosion fatigue damage, aside from its contribution to inert mechanical damage, by increasing the 'space' for hydrogen to accumulate

and the rate at which it fills this ‘space.’ This is a synergistic interaction as K_{\max} enhances hydrogen damage and accumulation while hydrogen simultaneously lowers the threshold for fracture.

2.3.2.1.3 Stress Intensity Ratio (R)

Although R is a descriptive parameter for the mechanical parameters and not a mechanical driving force, it is of particular use in corrosion fatigue systems where R is usually considered alongside crack closure – i.e., the premature contact of crack faces. It has been found that closure effects are aggravated by both low stress ratio loading and environments which produced corrosion debris within the crack (59), the latter of which can depend on R as well. The effect of the closure leads to reduces ΔK to an approximate effective value ($\Delta K_{\text{eff}} = K_{\max} - K_{\text{cl}}$), or alternatively an effective increase in stress ratio to K_{cl}/K_{\max} . Consequently, an increase in R by closure would lead to a transient reduction in crack growth rates determined experimentally. This results in authors employing test methods which avoid crack closure using constant K_{\max} and high R values (59), but this may not necessarily reflect the conditions that the material encounters in-service.

Although little has been done to advance models of closure for corrosion fatigue, it has been demonstrated that it can be reduced through increasing loading frequency (f) and, generally, the R value, particularly for short cracks (60). The reduced effect closure by increasing f may be because of enhanced mixing within the crack (see Section 2.3.2.1.7). Enhanced fluid flow could prevent the formation of corrosion product scales along the crack walls by reducing the concentration of metal ions below their respective solubility limits required to form corrosion products. Increasing the R value, however, reduces mixing within the crack but helps to avoid premature crack surface contact. Therefore, a complex dependence of crack growth on R and its related effects on closure can be expected.

2.3.2.1.4 Frequency (f)

The dependency of corrosion fatigue on time is arguably its most critical aspect and, in general, da/dN tends to increase with decreasing frequency (52). However, this is not always the case and it’s important to discuss various phenomena which can occur with changes in frequency. For example, each of the three ΔK regions in cycle-time dependent corrosion fatigue can have their own unique frequency responses.

Within Region I growth, i.e. near-threshold growth, there are two da/dN responses to frequency; either da/dN will remain constant or increase with increasing loading frequency. The frequency independent da/dN response has been well-established for steels and nickel based alloys in aqueous environments, while the latter case was specific to a Ti based alloy and the film rupture mechanism (52, 61).

Active and passivating steels in aqueous environments can potentially exhibit three regimes of da/dN behaviour in response to frequency near the end of Region II, where the ΔK dependency begins to plateau (52, 62), as illustrated in **Figure 2.13**. As frequency decreases, there is an initial mild increase in da/dN , followed by a rapid increase in da/dN for intermediate frequencies, and finally a third regime is observed for very low frequencies where da/dN has saturated or begins to plateau. Although the first two frequency regimes are typical, the final low frequency regime response varies and it's possible that growth rates would not plateau or possibly even decrease. The three regimes of frequency response have also been reported for aluminum and titanium based alloys, with the frequency ranges varying based on the alloy and environment (52).

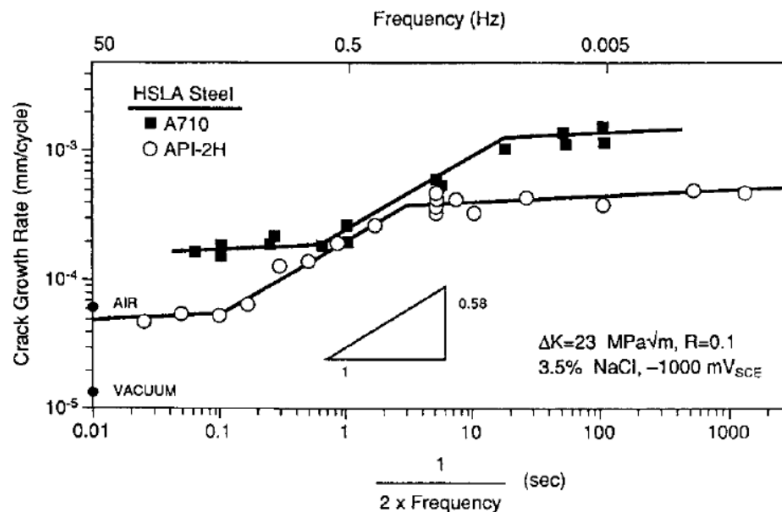


Figure 2.13 Effect of frequency on CF crack propagation within the plateau region of ΔK for A710 and API-2H steels in aerated 3 % NaCl, -1000mV (SCE) (62).

The three regimes of frequency response displayed in **Figure 2.13** can be understood in terms related to hydrogen transport and reactions. At high frequencies, the loading rate is sufficiently high that hydrogen diffusion or production is too slow to participate in crack propagation. As frequency is lowered there is greater exposure time per cycle, resulting in increased current passed

for electrochemical reactions to proceed (see Section 2.3.2.1.8) or hydrogen uptake at the crack tip per cycle which causes in an acceleration in da/dN . However, at sufficiently low frequencies the reaction per cycle can reach completion or the hydrogen concentration within the hydrostatic zone can reach saturation leading to a plateau in da/dN .

2.3.2.1.5 *Waveform*

The effect of different cyclic loading waveforms in aqueous environments has only been studied by a handful of authors, with very little work done on variable amplitude loading excluding the NNpH corrosion fatigue field (Section 2.3.4). Studies have suggested that there is little difference in growth rates between sinusoidal, triangular, and positive sawtooth constant amplitude waveforms for steels in simulated saltwater at OCP (63) and with applied CP (56). The same studies found that a decrease in crack growth occurs for negative sawtooth and square waveforms, which is to be expected because the loading portion of a cycle is the controlling factor in corrosion fatigue and the unloading portion contributes very little (64).

The decrease in crack growth rates in square waveforms, with or without a minimum load hold time, can be attributed to the hydrogen within the plastic zone. In the absence of cyclic damage during the holds at peak stress, dislocations will rapidly move away from the hydrostatic zone and decrease the total hydrogen in the plastic zone as a result – in spite of an increased diffusion driving force for hydrogen because of the high stress intensity holds. Of the studies which used square waveforms the longest peak stress hold time was ~ 100 s (64), a relatively short amount of time, and may not adequately describe the corrosion fatigue behaviour for structural applications which undergo square waveform cyclic damage.

Square waveforms have been found to enhance corrosion fatigue crack growth rates of aluminum alloys (65, 66) and steels (67) when high R cycles, a.k.a. ripple loads or minor cycles, are superimposed on the max stress intensity hold. Each study concluded that the ripple load effect (RLE) only had a strong influence on materials that demonstrate high SCC resistance (high K_{ISCC}), with reductions up to 72 % for ripple loads of $R = 0.95$ (67), resulting in reductions of the time-to-failure and thresholds for crack growth. The RLE was minimal for SCC-susceptible materials as the ripple loads were well above the SCC thresholds, which allowed for a stress-intensity based condition for the RLE to be developed (67):

$$[\Delta K_{th}/(1 - R)] \leq K_{max}^{RL} \leq K_{ISCC} \quad (2.13)$$

where K_{max}^{RL} is the max stress intensity of the ripple loads. Therefore, based on **Eq. 2.11**, the RLE is only present when the stress intensity of the ripple loads exceeds the threshold for fatigue growth (ΔK_{th}), but is below the threshold for static crack growth (K_{ISCC}).

2.3.2.1.6 Crack Size and Geometry: Short Crack Growth

It is well known that mechanically short cracks, of depths less than 1mm but greater than 100 μm , display significantly different fatigue behaviour than long cracks in inert (48) or aqueous environments (68). In inert environments, short cracks tend to grow at greater rates than longer cracks at the same applied ΔK and at ΔK levels well below the long crack fatigue threshold, ΔK_{th} , because of the crack closure effects present for longer cracks. The short crack effect can be more pronounced in hydrogen producing environments, depending on the material and environment. For example, Gangloff found that small surface and edge cracks, 0.1 – 2 mm in depth, grow up to 500 times faster than long through-thickness cracks, 15 – 40 mm in length, at constant ΔK in aerated seawater (68). The size-scale over which the aforementioned environmentally short-crack behaviour can be observed is variable, but is typically under ~ 2 mm (60). Therefore, to avoid confusion, short cracks for the remainder of the discussion will refer to cracks which are environmentally short, while small cracks will only refer to surface cracks under 100 μm .

For OCP conditions, it was hypothesized that small cracks grow at unpredictably rapid rates because of an enhancement in cathodic hydrogen generation within the occluded crack, owing to an increase in hydrolytic acidification and decreased oxygen inhibition (68). As crack chemistry is influenced by the occluded crack surface area to solution volume ratio, the effect increases with decreasing crack size or, equivalently, the crack mouth opening displacement. Alternatively, if the source of hydrogen is from bulk charging or dissolution, a short surface crack can be considered closer to the source of hydrogen at all locations along the crack. As a result, the transport time required to reach steady state will be much smaller than a large through-thickness crack, allowing a short crack to more readily access hydrogen (69). The impact of crack size and geometry on crack chemistry will be explained in terms of fluid flow and potential within the following subsections.

2.3.2.1.7 Crack Fluid Flow

The environmental variables listed in **Table 2.1** all strongly affect corrosion fatigue crack growth rates, which is further complicated by their synergistic relationship with mechanical damage, and differences between bulk and occluded crack chemistries. Of these, the mass transport mechanism(s) of solution and reactive species are the most impacted by mechanical variables. Mass transport within a crack can occur by diffusion, ion migration, or fluid flow simultaneously (70).

Crack size and geometry also influence the forced flow of solution in the crack, which is induced by cyclic displacement of the crack walls (70). Typical fracture mechanics specimens with deep cracks, e.g. compact-tension (CT) specimens, are not as affected by solution advection owing to the ease of fluid flow through their through-thickness cracks. However, surface cracks have greater constraints owing to their geometry and shallow depths, and the laminar flow of solution is proportional to loading frequency, crack opening, and crack depth (70). For short cracks, fluid flow becomes less important relative to diffusion, the latter of which becomes the dominant mass transport mechanism at some critical depth:

$$I_{crit} \leq (D_N / f)^{1/2} (1 - R^\alpha)^{-1} \quad (2.14)$$

where D_N is the species' diffusion coefficient, f is frequency, R is the stress ratio, and α is a geometry dependent constant (~ 0.5 for a trapezoidal crack and unity for a parallel-sided crack) (71). From **Eq. 2.14**, it is evident that high R cycles and low frequencies produce very limited mixing, promoting mass transport by diffusion over advection at larger depths. Species which can diffuse or react quickly would likely be unaffected by fluid flow, however those which react slowly (e.g., metal cations) can build up in concentration past solubility limits at low flow rates.

2.3.2.1.8 Crack Potential and pH

Embrittling hydrogen can be contributed by crack tip processes (dissolution or film rupture), bulk sample surface reactions, or chemical and electrochemical reactions in the bulk environment. The reactions, e.g. total atomic hydrogen production, which occur along the bulk surface and crack surfaces can be described in terms of pH and potential alongside mechanical variables (70, 72). Often the electrochemical conditions within occluded cracks are rendered unique compared to the

bulk solution composition, electrode potential, and pH. The occluded crack reactions are thereby dictated by local pH and electrode potential.

The effects of bulk pH and potential on crack chemistry has been modelled in depth for steels in deaerated seawater containing CO_2 by Turnbull and Thomas (73). The authors found that crack tip pH and potential are only slightly dependent on bulk pH, particularly for $3 \leq pH \leq 8.5$, but demonstrate a strong dependence on external potential. Generally, under OCP and anodic potential conditions a net anodic current, or potential drop, emerges from the crack to balance the net cathodic current along the external surface. As a result, the crack chemistry can become dominated by crack tip dissolution and hydrolysis leading to acidification and greater H^+ reduction in near neutral electrolytes. If this plays a dominating role in crack growth, then da/dN is proportional to the amount of hydrogen cathodically adsorbed near the crack tip which depends Faradaically on the anodic current flow (charge passed) over a load cycle by dissolution (72). Metal dissolution, however, is restricted to maintain $[Fe^{2+}] \leq [Fe^{2+}]_{eq}$, while there is no such limit imposed on hydrogen evolution (73), and the limiting roles of charge transfer or crack tip dissolution per cycle can become minuscule when hydrogen is primarily contributed by bulk surface diffusion.

On the other hand, if cathodic potential is applied an over-all increase of hydrogen production occurs, as water hydrolysis becomes dominant (72, 73). Contrary to the anodic case, as the potential is made more negative, the pH of the crack becomes independent of potential and tends to increase towards alkaline conditions ($pH \approx 10$). This has been attributed to a transition from a potential dominated pH to one determined predominantly by water reduction, occurring at ≤ -800 mV (SCE) for BS4360 steel in 3.5 % NaCl with an OCP of -760 mV (SCE) (73).

These effects can become significant in low-conductivity solutions with smaller crack sizes because the total current emerging from a crack is proportional to its size (70). As previously stated, the crack chemistry is heavily influenced by the crack surface area to solution volume ratio, which can be simply expressed in terms of crack length (l) and width (w) as l^2/w (73). For example, it has been demonstrated that pH will remain approximately constant for a constant value of l^2/w , despite variations in the values of l and w . Additionally, for all external potentials, as l^2/w increases the crack tip pH increases as a result of an increase in the potential drop across the crack. This echoes the previous statement for short cracks where if the crack size (l^2/w) were to decrease a pH

drop would occur, ergo enhanced dissolution and hydrolysis leading to an increase in hydrogen production and uptake.

2.3.2.2 Hydrogen Assisted Cracking (HAC)

Hydrogen degradation of crack propagation resistance, often referred to as hydrogen assisted cracking (HAC), is a mechanism often invoked to explain crack propagation of steels in aqueous and gaseous hydrogen environments (51, 74, 75). Growth rates are often limited by slow kinetic steps in the local crack environment, i.e. mass transport and surface reactions, and by the diffusion of hydrogen to the plastic zone ahead of the crack tip. As such, Gangloff has categorized HAC into the following two forms based on the source of hydrogen to the fracture process zone (FPZ) ahead of the crack tip (74):

1) *Internal-hydrogen-assisted Cracking (IHAC).*

IHAC occurs when atomic hydrogen is introduced into the bulk of the material either by manufacturing operations or upon environmental exposure. The application of stress will cause the redistribution of hydrogen from the bulk “charged” material to the FPZ. IHAC can occur during loading in the absence of a hydrogen producing environment and does not require the application of stress during the hydrogen charging event.

2) *Hydrogen-environment-assisted Cracking (HEAC).*

Unlike IHAC, HEAC requires simultaneous mechanical loading and environmental exposure for the uptake of hydrogen to the crack tip process zone to occur. The majority of atomic hydrogen is reduced on locations near the crack tip surfaces, dissolved into the lattice, and then diffuses towards the FPZ, as illustrated by **Figure 2.14**. The mass transport mechanism of atomic hydrogen to the crack tip will differ depending on the environment, however, e.g. atomic hydrogen is produced by electrochemical cathodic reactions near and at the crack tip in electrolytes.

The fundamental mechanism for HAC, which is typically referred to as hydrogen embrittlement (HE) to avoid confusion with IHAC and HEAC, is controversial in terms of the atomic mechanism(s) through which hydrogen causes damage. Currently, there exists three main

candidates for the atomistic mechanism(s), all of which are heavily debated because of their lack of supporting experimental evidence (55):

1) *Hydrogen-enhanced Decohesion (HEDE)*

This model, developed in large part by Richard Oriani (53, 58), attributes HE to the dilation of the local lattice ahead of the crack-tip, caused by hydrostatic stresses, which allow for large concentrations of hydrogen to accumulate and segregate within the FPZ. Essentially, crack-tip stresses are able to overcome local maximum atomic cohesion strength of the lattice which have been weakened by the presence of hydrogen. Hydrogen damage then occurs at sites some distance ahead of the crack tip, where tensile stresses are at their maximum and the local fracture toughness (K_{IC}) has been lowered.

2) *Hydrogen-enhanced Localized Plasticity (HELP)*

HELP involves the enhancement in the mobility of dislocations in the presence of dissolved hydrogen which results in severe, localized plastic deformation that enables for subcritical crack growth which is brittle in nature. Through hydrogen accumulation around dislocation cores, the elastic energies of interactions between mobile dislocations and obstacles are reduced hydrogen accumulation around dislocation cores resulting in the enhancement of dislocation mobility and plasticity.

3) *Adsorption-induced Dislocation Emission (AIDE)*

AIDE attributes hydrogen-enhanced crack advance to enhanced dislocation emission from the crack-tip surface as a result of hydrogen-induced weakening of the host metal's local atomic bond strength. This results in dislocation emission from the crack front and along intersecting planes which favour crack-tip sharpening and propagation over blunting. Additionally, microvoid formation within the plastic zone, caused by plastic deformation during loading, assists in crack sharpening and propagation through the linkup of voids and their interaction with slip bands resulting from crack-tip dislocation emission.

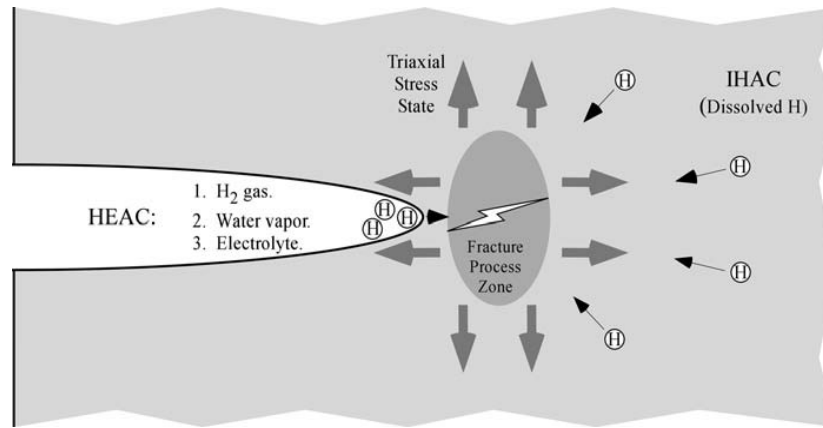


Figure 2.14 Schematic showing the hydrogen sources of the two forms of hydrogen assisted cracking: hydrogen-environment-assisted cracking (HEAC) and internal-hydrogen-assisted cracking (IHAC) (75).

2.4 NNpH CORROSION FATIGUE

The following section will demonstrate the corrosion fatigue behaviour of pipeline steels in NNpH environments. Demonstration of NNpH corrosion fatigue nature will be facilitated by drawing upon the previous discussion of general corrosion fatigue to reinforce the conclusions and trends drawn upon by major studies of failure mechanisms in NNpH environments.

2.4.1 MONOTONIC LOADING (SCC DEBATE)

The majority of early tests involving NNpH environments and pipeline steels were performed using monotonic loading, primarily through the use of slow strain rate testing (SSRT), assuming the mechanism was similar to NNpHSCC's high *pH* counterpart (4, 8, 15). In general, SSRT involves both high stresses and strains, at extremely slow strain rates, which are not conducive to typical pipeline operations. Arguably, the two most important discoveries from SSRT are that (i) significant reductions in ductility occur under SSRT in NNpH environments with or without microcrack formation, demonstrating hydrogen embrittlement (11, 15); and (ii) samples 'precharged' with hydrogen demonstrated similar ductility to those in air, indicating that the presence of the environment was necessary for hydrogen damage processes to occur (37).

There is currently debate by a specific group of authors using SSRT claiming that both crack initiation and propagation can occur under monotonic loading conditions, based on constant load or slow strain rate tests of American Pipeline Institute (API) steels in NNpH environments (20, 76, 77). This is a controversial claim, as over the decades since cracking was first observed on

pipelines in NNpH environments authors have not been able to observe crack propagation under monotonic loading alone, regardless if it's constant stress, displacement, or strain rate (8, 15, 29, 44). Settling such a debate is critical, because if crack propagation can indeed occur under monotonic loading, with the same mechanical operating conditions seen in the field (i.e., stress or stress-intensity), then the mechanism can be truly classified as SCC, over corrosion fatigue, based on the defining threshold for growth under static loading (K_{ISCC}) (78).

Simply put, the evidence provided by the authors arguing for SCC and crack propagation under monotonic loading is weak and echoes previous misconceptions brought on by the use of SSRT. To elaborate, this is because the stresses that the authors observed cracking under were either slightly below to well above the steels' SMYS, misrepresenting the conditions through which crack-based failures in the field occur where the MOP does not exceed 80 % SMYS. As such, the narrative changes entirely as not only are the field conditions misrepresented, but it's clear that the authors do not understand that both SCC and corrosion fatigue can occur for the same material and environment but are demarcated by the mechanical conditions experienced (78).

As previously discussed in Section 2.3.2, either cycle or cycle-time dependent corrosion fatigue can occur well below K_{ISCC} or for SCC immune materials, with the latter being the more common corrosion fatigue behaviour. Regardless of the form, corrosion fatigue has been exemplified in the work performed by Chen, *et al.* (29), where the authors demonstrated that under same stress intensity levels a crack that had been continuously propagating under constant amplitude (CA) cyclic conditions, typical of field operations, will fully arrest upon the application of a static hold (**Figure 2.15**). In C2 solution, crack arrest was observed on two occasions of differing K_{max} and ΔK conditions following a static hold with growth reinitiated immediately following the reapplication of CA loading. For NOVATW, crack dormancy after resuming CA at $\Delta K = 12.0$ MPa \sqrt{m} was likely because of the lower bulk environmental hydrogen contribution of the NOVATW solution which could not overcome the increased threshold for growth following the blunting of the crack tips induced by the static hold or dissolution.

Following the above discussion, it is understandable that referring to cracking in NNpH environments as NNpHSCC in further discussions is unwarranted. As such, the failure mode will be only referred to as near-neutral pH corrosion fatigue for the remainder of the literature review.

This will be reinforced in the following sub-section by demonstrating the relationships between crack growth in near-neutral pH environments and the mechanical properties previously discussed for corrosion fatigue in Section 2.3.2.

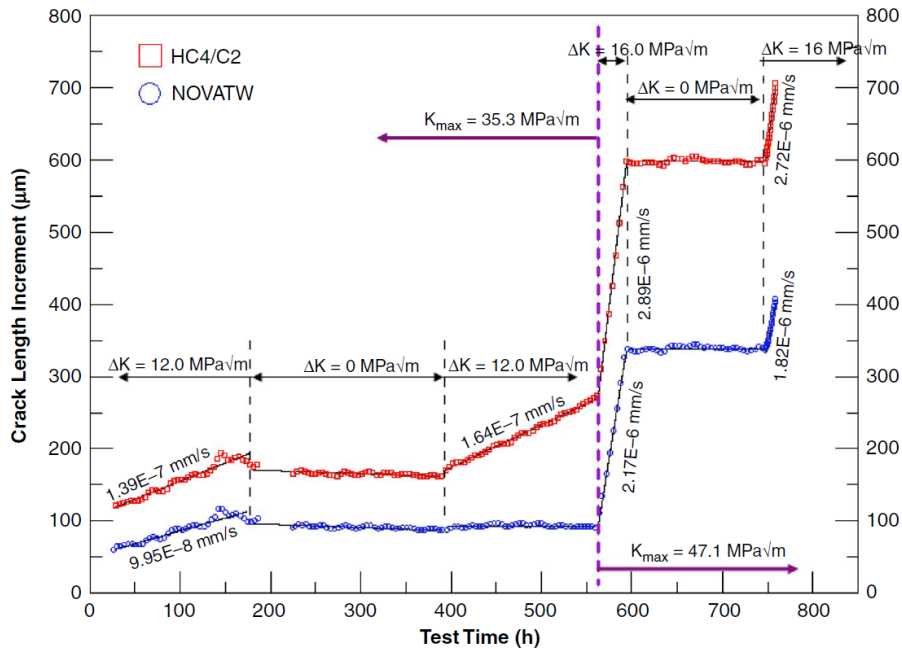


Figure 2.15 Crack length extension (μm) as a function of test time (h) for two different simulated soil environments and various loading conditions (29).

2.4.2 CONSTANT AMPLITUDE (CA) LOADING

Cyclic loading provides a much more realistic simulation of the mechanical forces experienced by pipelines in service, as illustrated by the pressure spectra in **Figure 2.16**. Such pressure fluctuations are typical within 30 km downstream from compressor stations where it has been reported that, over-all, TransCanada Pipelines experience approximately 80 % of their SCC failures, with the remainder within 55 km downstream (2). Early analysis of pipeline fluctuations revealed that large cyclic stresses, such the one in **Figure 2.16**, can occur many times over a year (30, 79). The large pressure fluctuations of $R \leq 0.9$ with frequencies varying from 10^{-5} Hz to 10^{-3} Hz, accounted for 10 % and 7 % of the total oil (79) and gas (30) transmission line pressure fluctuations, respectively, and can be attributed to events such as planned start/stops, flow rate changes, and planned outages. Understandably, researchers focused only on the corrosion fatigue behaviour of the large pressure fluctuations, in the form of constant amplitude loading.

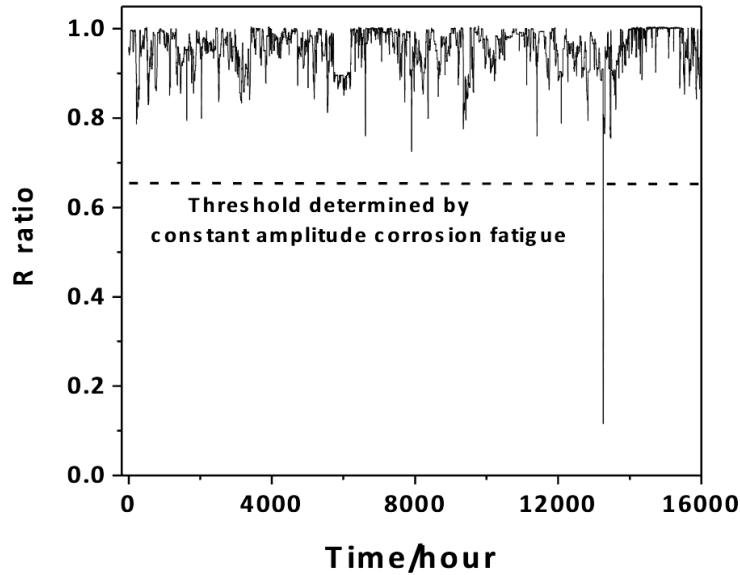


Figure 2.16 Pressure fluctuations recorded over time for a high-pressure gas transmission pipeline (80).

Laboratory testing of ‘near threshold’ or Region I corrosion fatigue (Section 2.3.2.1.1), is of little importance here because the early stage (Stage I) of crack growth in NNpH environments is almost entirely dominated by the dissolution process which continues until the crack has reached a depth of ~ 1.0 mm, after which 95 % of the crack population enter dormancy. To determine the crack growth mechanics of the 5 % of the population which continue to grow past dormancy (Stage II) many laboratory studies have been performed on the corrosion fatigue behaviour of pipeline steel within its respective ΔK Regions II and III (15, 25, 28, 29, 44-46, 54, 81-87).

2.4.2.1 Mechanical Considerations

Despite previous detailed explanations of critical variables to corrosion fatigue, it is important to demonstrate them here for the near-neutral pH environment, namely the effects of ΔK , K_{max} , and frequency. First, the dependency of da/dN on ΔK can be seen in **Figure 2.17** where it can be clearly seen that, in general, crack growth rates increase with increasing values of ΔK . Additionally, growth rates in C2 were much higher than in NOVATW, owing to the greater dissolution rates and thereby hydrogen production rates in the former solution (28). This reflects the synergistic effects of mechanical driving forces and the environment, or hydrogen, in NNpH corrosion fatigue (28, 29, 44, 46, 82), which are seemingly most influential within the low ΔK regime yet negligible in the higher ΔK regimes. Although this response to ΔK is a defining characteristic of fatigue,

regardless of the environment, a prevalent issue of corrosion fatigue also occurs here where growth rates cannot be solely described in terms of ΔK as they also vary with differing values of K_{\max} and frequency.

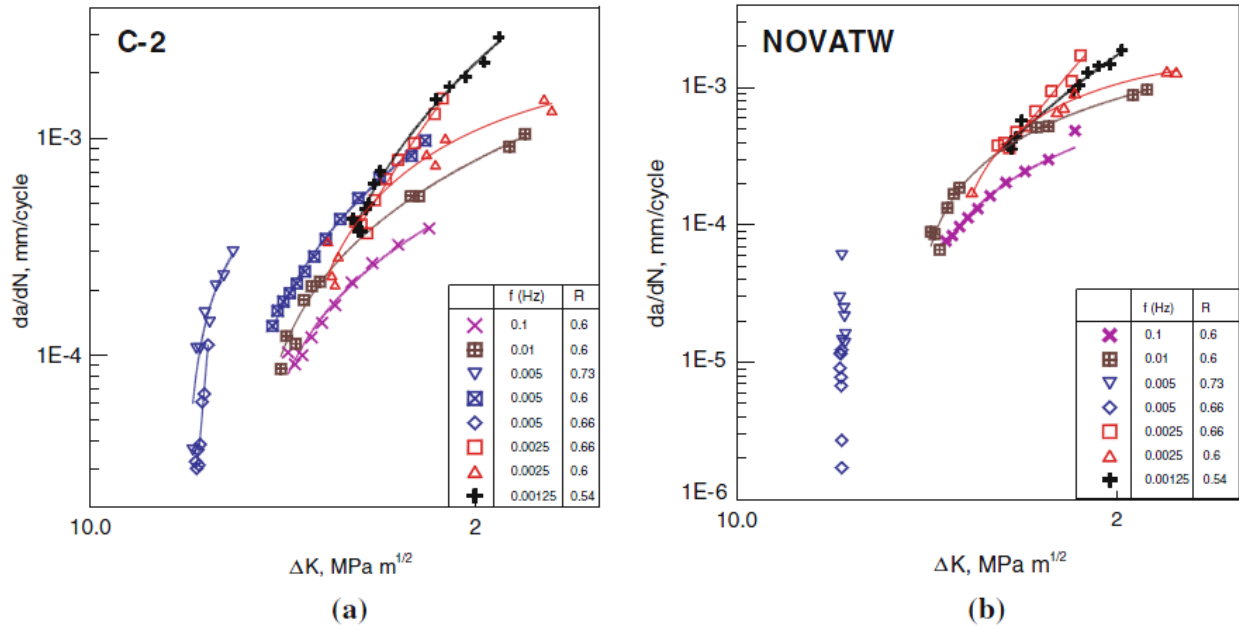


Figure 2.17 Crack growth rate (da/dN) as a function of ΔK for X-65 pipeline steel in (a) C2 and (b) NOVATW test solutions. $K_{\max} = 35 - 55 \text{ MPa}\sqrt{\text{m}}$ and $\Delta K = 10 - 28 \text{ MPa}\sqrt{\text{m}}$ (28).

A more in-depth examination of the effect of K_{\max} on crack growth behaviour is illustrated in **Figure 2.18** below for two different NNpH solutions of compositions detailed in literature (21, 46). It is important to note that **Figure 2.18a** shows the effect of K_{\max} on da/dN during near-constant ΔK testing and **Figure 2.18b** shows the effect of varying ΔK at differing values of K_{\max} . In spite of different NNpH solutions and mechanical testing methods, it is evident that da/dN increases with increasing K_{\max} for the same value of ΔK , and vice-versa, which is to be expected based on The Unified Approach (Section 2.3.1) and the dominance of K_{\max} on controlling hydrogen accumulation within the plastic zone (Section 2.3.2.1.2).

Finally, although an increase of da/dN with decreasing frequency in NNpH environments has been demonstrated by many authors (28, 44, 46, 54, 84-87), the frequency response in the NNpH corrosion fatigue system is best illustrated by the work of Yu, *et al.* (54) (**Figure 2.19**). The work demonstrated in **Figure 2.19** is unique from the work of others in that it specifically isolated frequency, i.e. both K_{\max} and ΔK were constant for each test, and frequencies more typical of

pressure fluctuations exhibited in the field ($< 10^{-3}$ Hz) were tested. The latter case was also performed in other literature (46), but the data suffered from significant scatter and is inaccurate in comparison to the data in **Figure 2.19**.

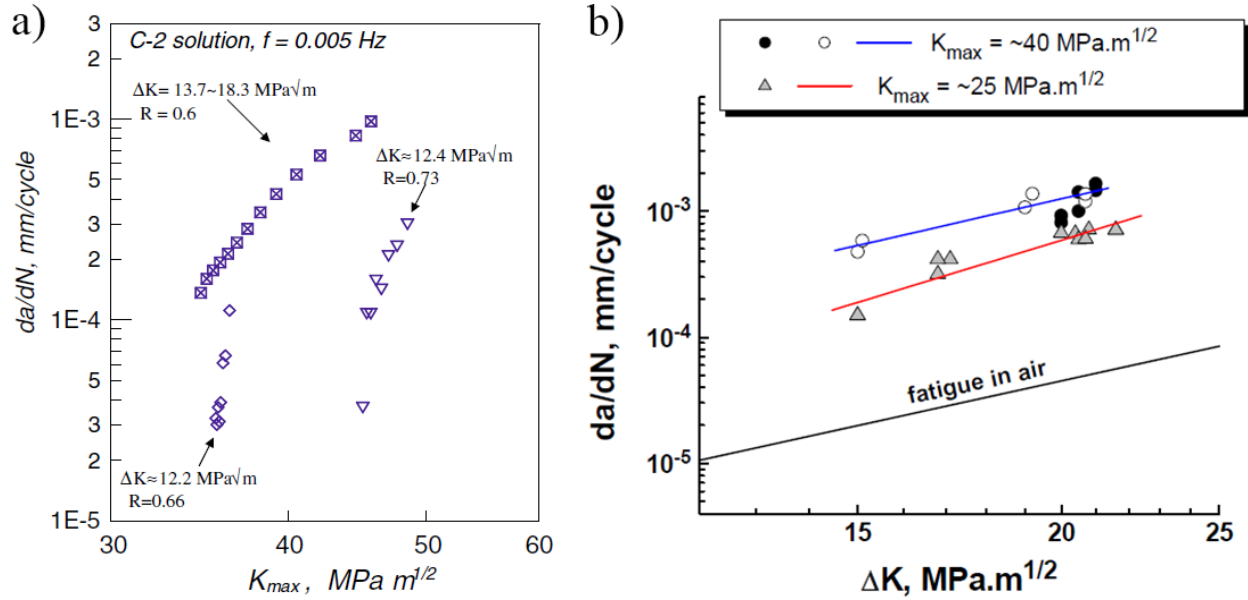


Figure 2.18 Dependence of crack growth (da/dN) on K_{max} with (a) da/dN vs. K_{max} (28) and (b) da/dN vs. ΔK (46).

In **Figure 2.19**, it can be seen that da/dN increases with decreasing frequency until a critical frequency of 10^{-3} Hz is reached, after this value da/dN begins to decrease at a decreasing rate with decreasing frequency. Based on modelling of cyclic loading assisted hydrogen accumulation within the hydrostatic zone, the authors concluded that at 10^{-3} Hz the equilibrium concentration or saturation of hydrogen within the hydrostatic zone available to participate in hydrogen embrittlement had been reached. After this point, a decrease in da/dN occurred which according to the authors was because of crack tip blunting effects caused by time-dependent room temperature creep (RTC), detailed elsewhere (88-90), and crack tip dissolution. The latter is most likely the case, as the low bulk surface dissolution rate of C2 (1.6×10^{-9} mm/s) could be significantly enhanced by crack tip straining and the lower pH (acidification) of the crack tip solution (83). The different cycle-time dependent “near plateau” low frequency regime response in **Figure 2.19** from that previously stated in Section 2.3.2.1.4 is not particularly troubling, as the frequency response within the low frequency regime can vary between materials and systems and will not always plateau.

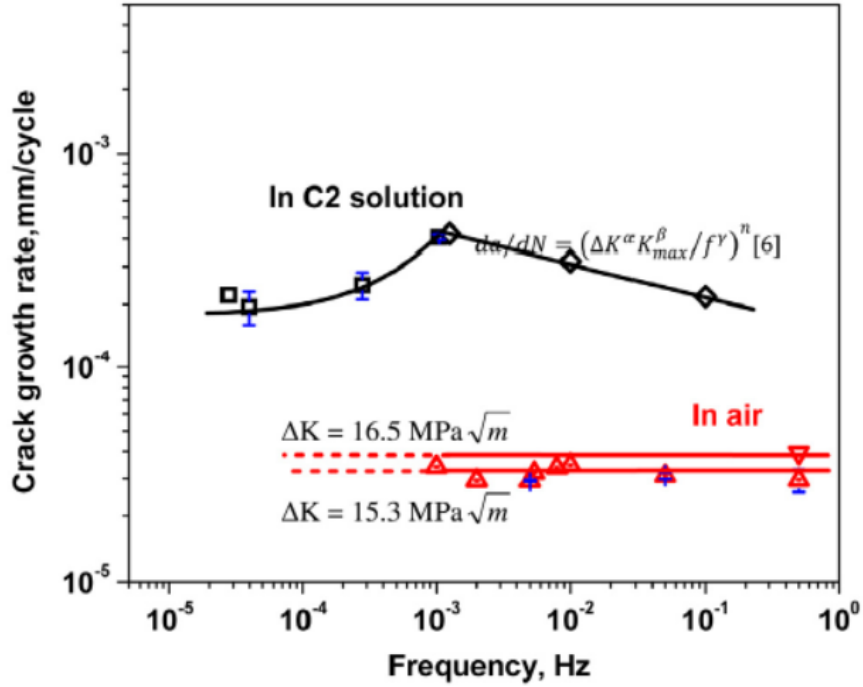


Figure 2.19 The variation of da/dN with frequency in C2 solution and in-air, at constant K_{max} (33 MPa \sqrt{m}) and ΔK (16.5 MPa \sqrt{m}) (54). Their reference (6) corresponds to this literature's reference (28).

2.4.2.2 Environmental Considerations

The synergistic interaction of the environment through the bulk production of atomic hydrogen on the steel surface (Section 2.2.1) and the mechanical variables listed in the previous section for NNpH corrosion fatigue has been studied in great detail by Chen, *et al.* in several studies (28, 29, 44). Mainly, a critical aspect of this system is the competition between dissolution and mechanical related crack tip blunting and sharpening processes (29), which are dominated by the dissolution of crack tips, crack walls, and the bulk surface.

Intrinsically, crack tip sharpening can occur by mechanical cyclic loading (ΔK), however the emission of mobile dislocations ahead of the crack tip induced by the cyclic strain act as mobile hydrogen traps, assisting in the segregation of hydrogen within the crack tip plastic zone. On the other hand, hydrogen enhances the mobility of these dislocations through slip localization (29). Furthermore, the diffusion and accumulation of hydrogen within the plastic zone is dominated by K_{max} , which facilitates hydrogen embrittlement. Consequently, hydrogen embrittlement lowers the resistance to fracture which has already been established as a K_{max} controlled process.

Additionally, decreasing the loading frequency enhances these synergies by increasing the time available for the time-dependent processes of hydrogen diffusion and transport to the crack tip plastic zone to occur.

The above sharpening processes are limited in their capabilities, i.e. if one or more conditions are not aggressive enough crack tip blunting will prevail. For example, in the absence of sufficiently aggressive mechanical driving forces, or under monotonic loading, crack tip blunting can prevail through the combination of RTC and crack tip dissolution (29). The former will increase with increasing levels of K_{max} , while the latter will increase with decreasing solution pH.

In the presence of sufficient mechanical driving forces crack growth rates tend to increase with decreasing pH (28), an understandable consequence in NNpH environments where the reduction of hydrogen is a consequence of the oxidation of iron, i.e. dissolution. In spite of greater crack tip dissolution rates, lowered pH levels have also been shown to lower the threshold for the reactivation of dormant crack (29), e.g. the case for C-2 solution (pH = 6.29) and NOVATW (pH = 7.11) previously demonstrated in **Figure 2.15**. These environmental effects (pH) are only important under benign loading conditions and are not as significant when loading conditions are aggressive, as demonstrated in **Figure 2.17** and **Figure 2.20** for two different NNpH solutions.

2.4.3 NNpH CRACK MODELS

Since the discovery of cracks in NNpH environments in the 1980's researchers have been attempted to generate models to describe the crack growth mechanics. More focus has been drawn towards the application of fatigue or corrosion fatigue models to predict growth, given that crack propagation has not been observed under monotonic loading. As such, the following section will focus on the most popular models in NNpH crack propagation.

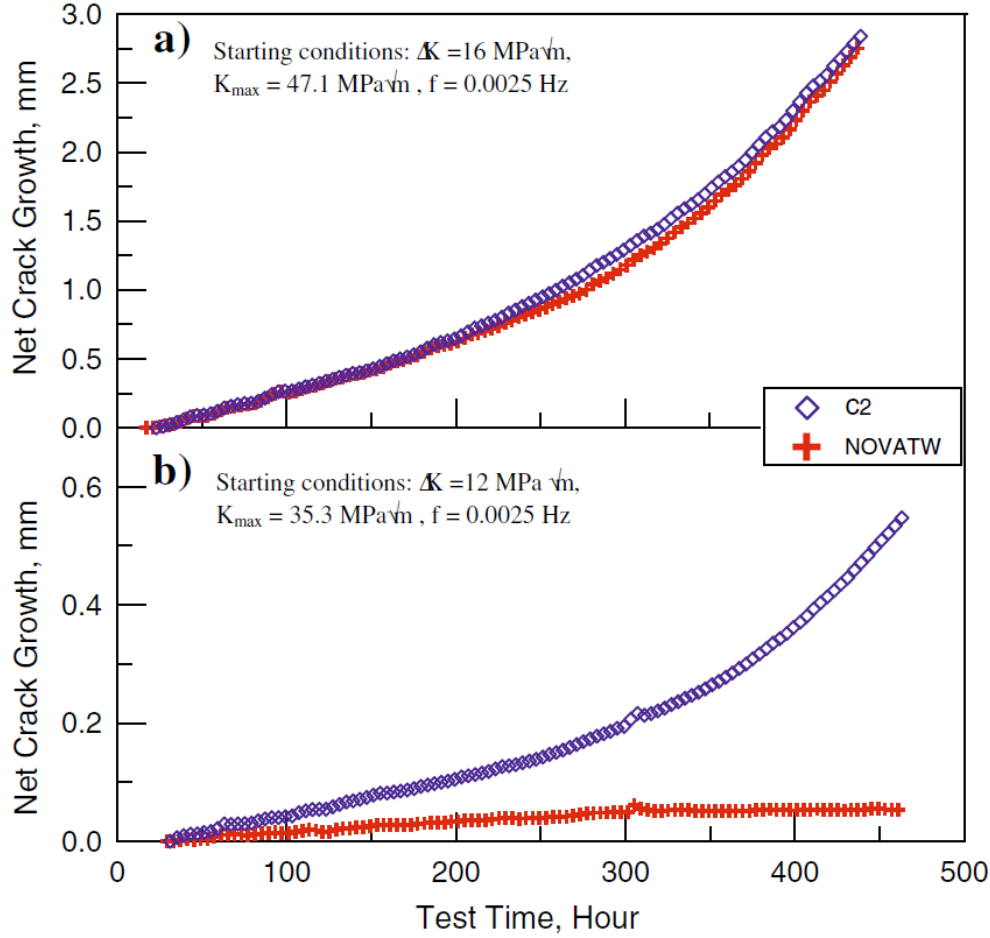


Figure 2.20 Comparison of net growth over time for two different NNpH solutions, C2 ($pH = 6.29$) and NOVATW ($pH = 7.11$). (a) $\Delta K = 16 \text{ MPa}\sqrt{\text{m}}$, $K_{\text{max}} = 47.1 \text{ MPa}\sqrt{\text{m}}$ and (b) $\Delta K = 12 \text{ MPa}\sqrt{\text{m}}$, $K_{\text{max}} = 35.3 \text{ MPa}\sqrt{\text{m}}$

2.4.3.1 The Superposition Model

The superposition model has been used in several studies in to fit crack growth data obtained by laboratory tests in NNpH environments (82, 84, 85) and field data (91). The model was originally proposed in 1969 by Wei and Landes (92), and is mathematically expressed as:

$$\left. \frac{da}{dN} \right|_{\text{total}} = \left. \frac{da}{dN} \right|_{\text{fatigue}} + \frac{1}{f} \cdot \left. \frac{da}{dN} \right|_{\text{SCC}} = C \cdot \Delta K^m + \frac{1}{f} \cdot \left. \frac{da}{dN} \right|_{\text{SCC}} \quad (2.15)$$

Eq. 2.15 is often invoked to describe time-dependent corrosion fatigue and is the combination of inert fatigue growth rates and time-dependent SCC (51). In the past, it is logical that researchers would use the superposition model given that cracking in NNpH environments was first

misdiagnosed as SCC and cracking was only observable under cyclic loading. The SCC component is taken as a constant, and the model is fitted to $da/dN-\Delta K$ plots such as in **Figure 2.21**.

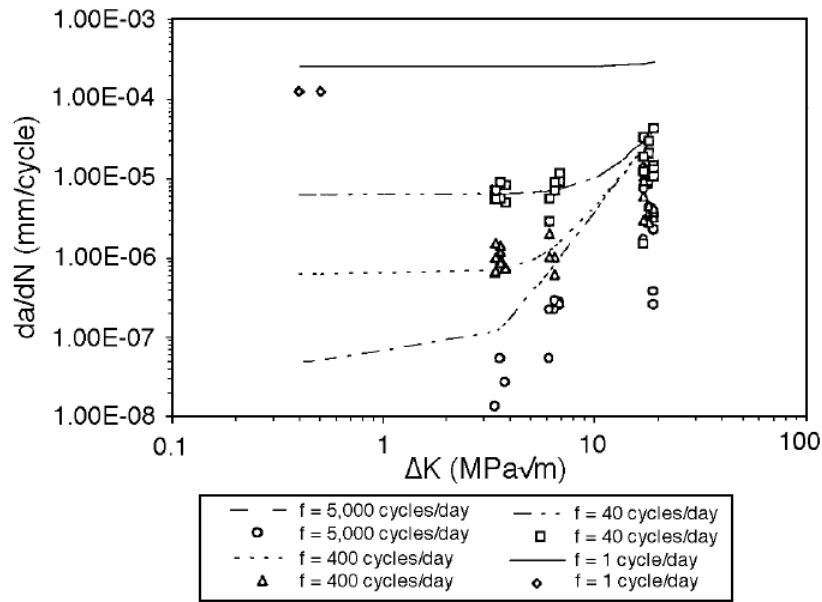


Figure 2.21 Cyclic crack growth rates (da/dN) of varying test frequencies fitted with the superposition model (85).

There are several major issues with using the superposition model. First, it assumes an SCC component to growth that is determined under constant load which has already been demonstrated to be uncharacteristic of cracking in NNpH environments. Second, the model consistently provides a poor fit to crack data determined in laboratory testing, except at very low frequencies and ΔK . Lastly, the fatigue component of the superposition model fails to include either frequency or K_{max} , which were demonstrated to have a significant influence on crack behaviour in Section 2.4.2.1.

2.4.3.2 Strain and Displacement Rate Models

Crack tip strain rate models have also been applied to describe growth rates in NNpH environments (81), with the general form below:

$$\dot{\varepsilon} = C_1 \cdot f \cdot (1 - R) \tag{2.16}$$

where ε is strain rate and C_1 is a constant. The use of a strain rate model has seen success fitting HpHSCC data because of its film formation, film rupture mechanism which is dictated by crack tip strain rate. Although dissolution and hydrogen uptake are enhanced by strains at the crack tip

(28, 82), the model suffers from significant scatter (**Figure 2.22**) and does not take into account ΔK . Attempts to model crack growth data with crack tip displacement rates, which includes ΔK , suffered from nearly as poor of a fit as strain rate models and still neglected the impact of K_{max} .

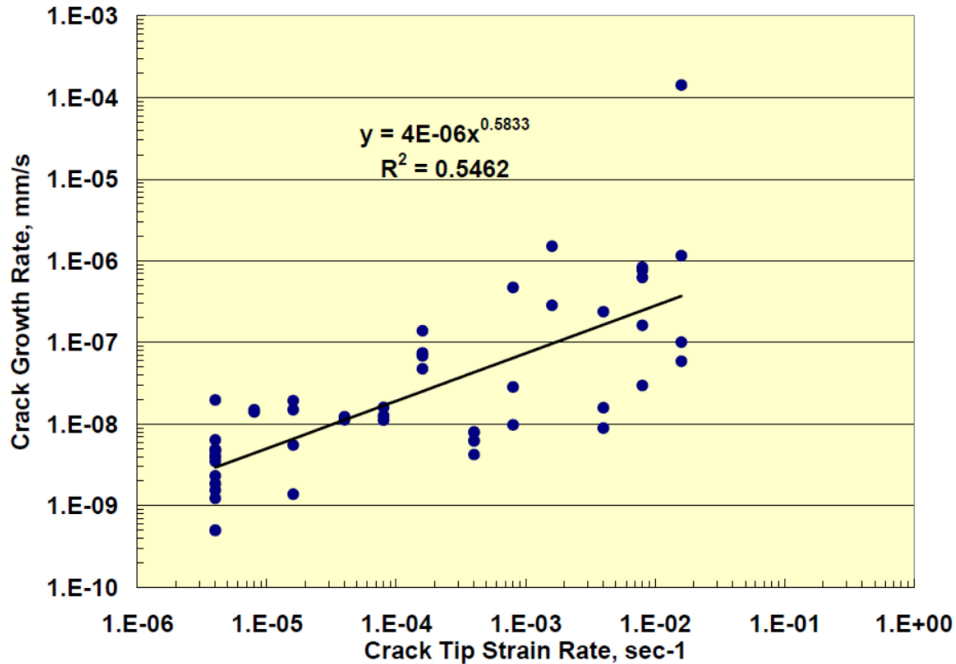


Figure 2.22 Crack growth rate (mm/s) as a function of crack tip strain rate fitted with the strain rate model (81).

2.4.3.3 The Combined Factor Model

Chen and Sutherby introduced a new model for crack propagation in NNpH environments in lieu of the problematic models introduced previously, known as the combined factor (28). The authors' model critically addressed both the corrosion fatigue behaviour and mechanical variables, where previous models had failed, with the updated form expressed as (43):

$$\frac{da}{dN} = A \left(\frac{\Delta K^\alpha K_{max}^\beta}{f^\gamma} \right)^n + h \quad (2.17)$$

$$A = \left[\frac{4\sqrt{2.476}(1 + \nu)\Omega}{3\pi k_B \sqrt{2\pi} \ln\left(\frac{1}{c_0}\right)} \right]^{2N} \quad (2.18)$$

where A , n ($=2$), α ($=0.67$), β ($=0.33$), γ ($=0.033$), and N ($=0.6n$) are constants, $\alpha + \beta = 1$, h is the dissolution in the depth direction, k_B is Boltzmann's constant, T is temperature, ν is Poisson's ratio, c_0 is the atomic ratio of H away from the plastic zone, and Ω is the partial molar volume of hydrogen. The value of γ varies depending on the environment and represents the environment's contribution to crack growth. The constant A describes the steady state contribution of hydrogen damage within the plastic zone.

The term $(\Delta K^\alpha K_{\max}^\beta / f^\gamma)$ is referred to as the combined factor, which includes the stress intensity terms following The Unified Approach, and the inverse dependence on frequency of cycle-time-dependent corrosion fatigue. The effectiveness of this model is demonstrated in **Figure 2.23** by plotting the crack growth data presented in **Figure 2.17** as a function of the combined factor. Unlike the previous models, the scatter is minimal and da/dN from varying mechanical conditions can be accurately fitted along the same trend line. The significance of the latter is this allows for a single threshold value to be defined for a wide range of ΔK , K_{\max} , and f values for a single environment. From **Figure 2.23**, the threshold values for C2 and NOVATW solutions are 8500 9250 $(\text{MPa}\sqrt{\text{m}})^3 \text{Hz}^{0.1}$, respectively, which can be expected based on the more aggressive environmental conditions of C2 solution.

Recalling **Figure 2.16**, the threshold for growth defined above was plotted as a dashed line on the pressure spectra which excluded all but one pressure fluctuation over a period of ~ 2 years. Based on CA loading and the combined factor, it would a considerable amount of time for the crack to grow sufficiently large for rupture to occur which significantly under-exaggerates growth rates which have been reported to be ~ 0.3 mm/yr in the field (83). Therefore, extensive investigations into the role of the previously neglected minor pressure fluctuations and their impact on crack growth behaviour were performed, as discussed within the next section.

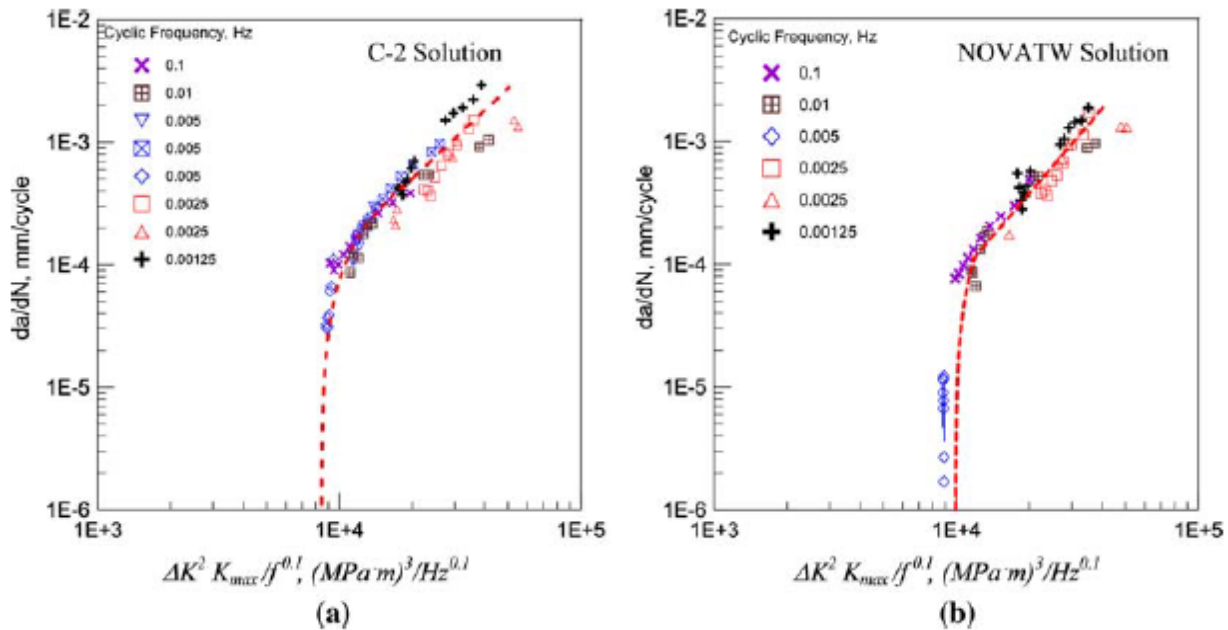


Figure 2.23 da/dN data as a function of the combined factor for (a) C2 and (b) NOVATW solutions (28).

2.5 SURFACE CRACKS

Little work has been performed over the years involving small, short, or surface cracks in NNpH environments. The most recent tests have primarily involved full-scale testing in soil boxes involving 0.3 mm wide semi-elliptical notches of lengths up to 100 mm and depths of 2.5 mm (93, 94) or simulated full-scale testing using relatively shorter 0.2 mm wide notched semi-circular cracks of lengths ~ 7.3 mm (25, 45, 95). Based on the dimensions of the cracks used, the former investigators used what can potentially be regarded as environmentally short cracks but not the latter and no size-scale effects are to be expected – i.e., the surface cracks are expected to behave similar to long through-thickness cracks. While nothing of particular significance came from the former work, given the unrealistic loading conditions at which growth was detected (95 % SMYS) and high R (0.9), there is merit in the latter works.

Investigators of surface cracks of lengths ~ 7.3 mm in length were able to determine two key factors in NNpH crack propagation behaviour:

- 1) Crack growth rates decreased further into coating disbondments at OCP conditions (45). This is related to a negative diffusion gradient in CO_2 concentration from the open mouth (OM) of the disbondment to the bottom of the disbondment. The decreasing levels of CO_2

results in decreasing hydrogen reduction, because of the decrease in dissolution rates, which reduces the effect of hydrogen embrittlement (see **Eq. 2.1 – Eq. 2.6**).

- 2) Establishment that there exists two thresholds for continuous crack propagation (25). The lower threshold occurs for sharp cracks and the upper threshold occurs for blunted cracks. In between these two threshold values for continuous growth a discontinuous growth mechanism occurs through repeated dormant-active cycles. Growth is reinitiated by the formation of microcracks at weakest links in the FPZ ahead of a blunt crack tip by a combination of cyclic loading, stress concentration, and hydrogen accumulation.

As previously stated, such cracks are not considered to be environmentally short and were even reported to grow at lower rates than through-thickness cracks under equivalent conditions (45). However, using data from NNpH full-scale tests involving surface cracks of lengths up to 35 mm and depths ranging from 1.58 – 3.22 mm it has been demonstrated that there is an environmentally-short crack effect in the NNpH corrosion fatigue system (86). This is illustrated in **Figure 2.24**, where the surface cracks in NS4 solution (labelled GRI-05/8668) grew at combined factor levels significantly below the threshold values of through-thickness cracks in NOVATW.

2.6 VARIABLE AMPLITUDE (VA) LOADING

Traditionally, the variable pressure fluctuations of pipelines are converted to cycle counts that are tabulated into bins of stress ranges using the simplified rainflow counting method outlined in ASTM Standard E1049-85 (81, 91). Afterwards, an inert fatigue, superposition, or strain rate model is applied to each stress range and linear summation of crack growth for each range is performed to determine the total crack growth rate. The major issue with this method is that similitude is assumed – i.e., the effects of prior loading history is neglected.

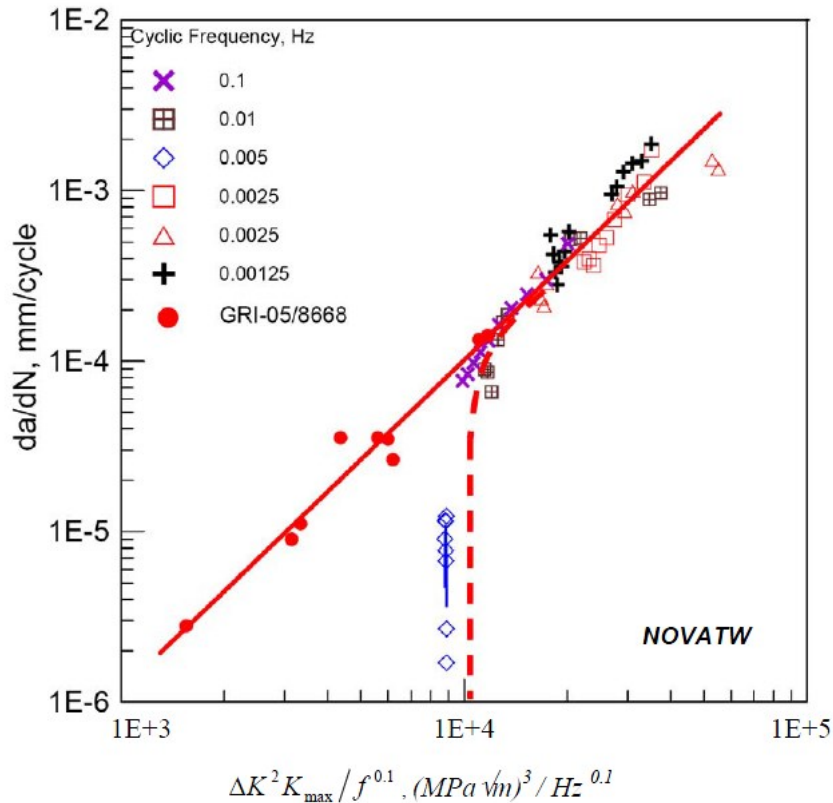


Figure 2.24 Demonstrating the environmentally short crack effect in NNpH environments based on the Combined Factor threshold value of through-thickness cracks (86).

In variable amplitude (VA) loading there are two primary types of spectra that are of concern; overload and underload type loading. **Figure 2.25** schematically the expected growth of CA (Type-I), underload (Type-II), overload (Type-V), and combinations of the latter two spectra (Type-III and IV) as a function of load cycles. As illustrated, an acceleration of crack growth occurs under underload type loading while any combination of overload type loading results in a retardation of crack growth. The reasoning behind these effects of variable amplitude are known as load-history interaction, where an overload or underload will modify crack tip conditions which affects subsequent growth from smaller cyclic loads (48).

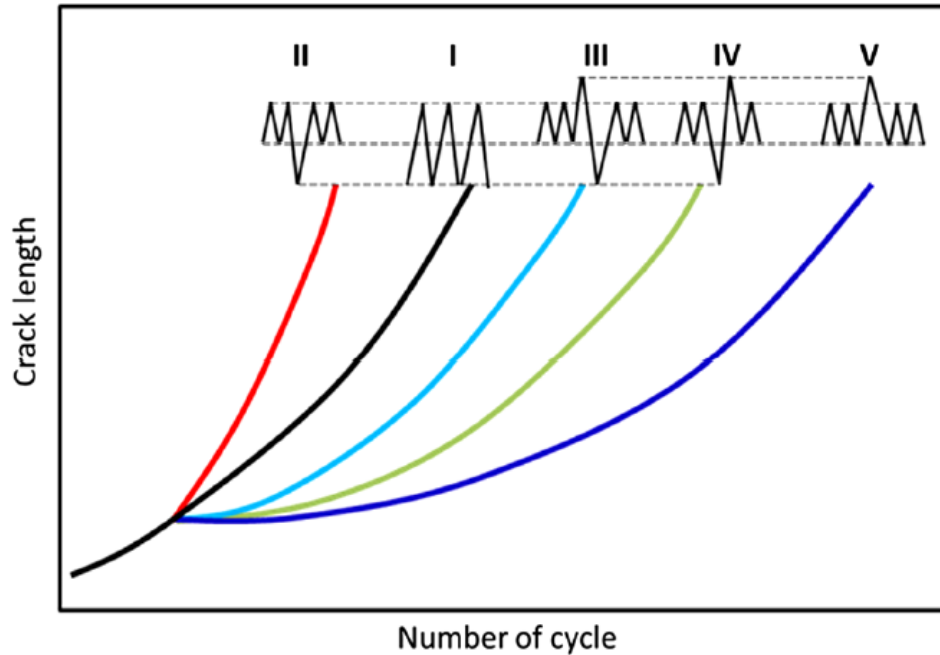


Figure 2.25 Typical crack growth behaviour under several combinations of underload and overload cycles (96)

Several possible mechanisms have been proposed to explain the effect(s) of overloads (48):

1. Crack tip blunting delays growth while the crack tip resharpens.
2. Compressive residual stresses induced by the overload retard further crack growth.
3. Residual stresses behind the crack tip result in plasticity-induced closure as the crack proceeds into the overload plastic zone.

The effects of an underload, although not studied in as much depth as overloads, can be understood as either a combatant against retardation effects or as an accelerator either by causing crack advancement on its own or acceleration of the growth of the cycles that follow it (48, 97, 98). In order to quantify the effect of underloads, an acceleration factor, γ , has been used in past works (97, 98):

$$\gamma = \frac{\text{Crack growth rate measured in test } \left(\frac{da}{dN}\right) \text{ at } \Delta K}{\text{Crack growth rate calculated by linear summation of CA CGR response at } \Delta K} \quad (2.19)$$

The value of γ has been found to vary with the number of high R-ratio minor cycles (n) between underloads and their value of R (98). The same authors also found for Al-alloys that small accelerations ($\gamma = 1.3$) in crack growth occurred by changes to plasticity-induced closure, while

one alloy saw significant enhancements ($\gamma = 12$) owing to a reduction in microstructural induced closure. It is unclear if the previously discussed RLE in Section 2.3.2.1.5 is related to the acceleration effect discussed here because the authors of the studies on RLE only focused on the reduction of K_{ISCC} with limited variations in waveforms (65-67).

Inspired by previous work done in variable amplitude studies, Yu *et al.* performed significant work to study the acceleration effect of underload-type spectra of pipeline steels in NNpH environments (54, 80, 99, 100). The work on underload-type spectra will be the focus for the remainder of this section, however it is important to note that the significance of Yu's work has already been adopted in pipeline pressure analysis to address its application to integrity management (96, 101). This is a key factor for the future of life predictions, as significant statistical analysis of SCADA data has identified that underload, mean load, and overload type spectra all occur on both gas and oil pipelines (**Figure 2.26**). These pressure fluctuations occur close to or downstream from suction and discharge sites, respectively. Identification of the effects of VA effects on pipeline crack growth and recent statistical analysis based on VA spectra have clearly demonstrated that even further work is required to improve pipeline operators' ability to assess whether lines are fit for service.

2.6.1 EFFECT OF MINOR CYCLES

The effect of varying minor cycles on crack growth behaviour of X-60 pipeline steel CT samples in NNpH environments was detailed in-depth by Yu, *et al.* (99). The waveform used for testing, dubbed Underload and Minor Cycles (UL&MC) spectra is illustrated in **Figure 2.27**. The authors performed experiments in air and C2 solution using constant values of $K_{max} = 33 \text{ MPa}\sqrt{\text{m}}$, R for the underloads ($R_{UL} = 0.5$) and minor cycles ($R_{MC} = 0.9$), and frequency for the underloads ($f_{UL} = 10^{-3} \text{ Hz}$) and minor cycles ($f_{MC} = 5 \times 10^{-3} \text{ Hz}$). Plots demonstrating the major trends obtained in the study can be seen in **Figure 2.28**.

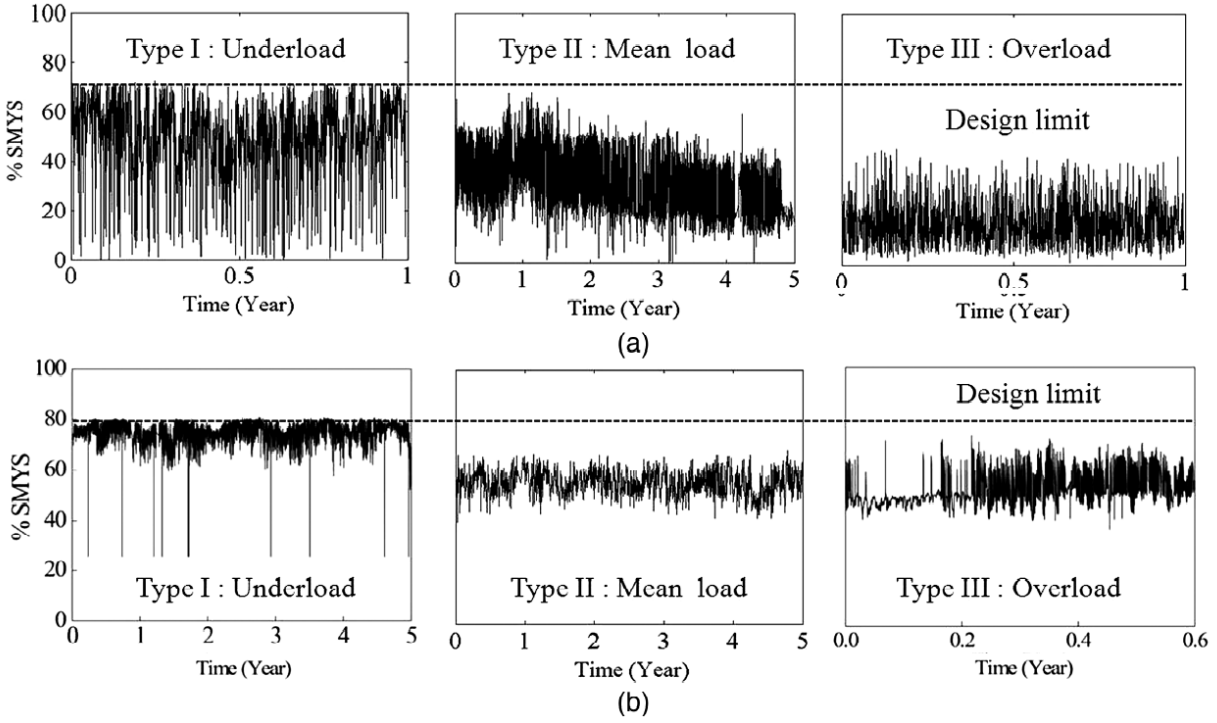


Figure 2.26 Identification of pressure fluctuations on (a) oil and (b) gas pipeline spectra (96).

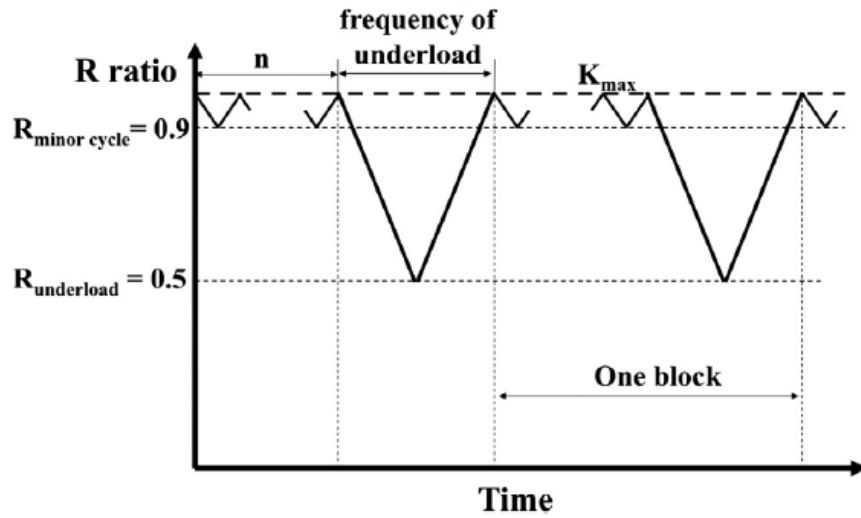


Figure 2.27 Simulated underload-type spectra used in the experiments studying the effects of minor cycles (54).

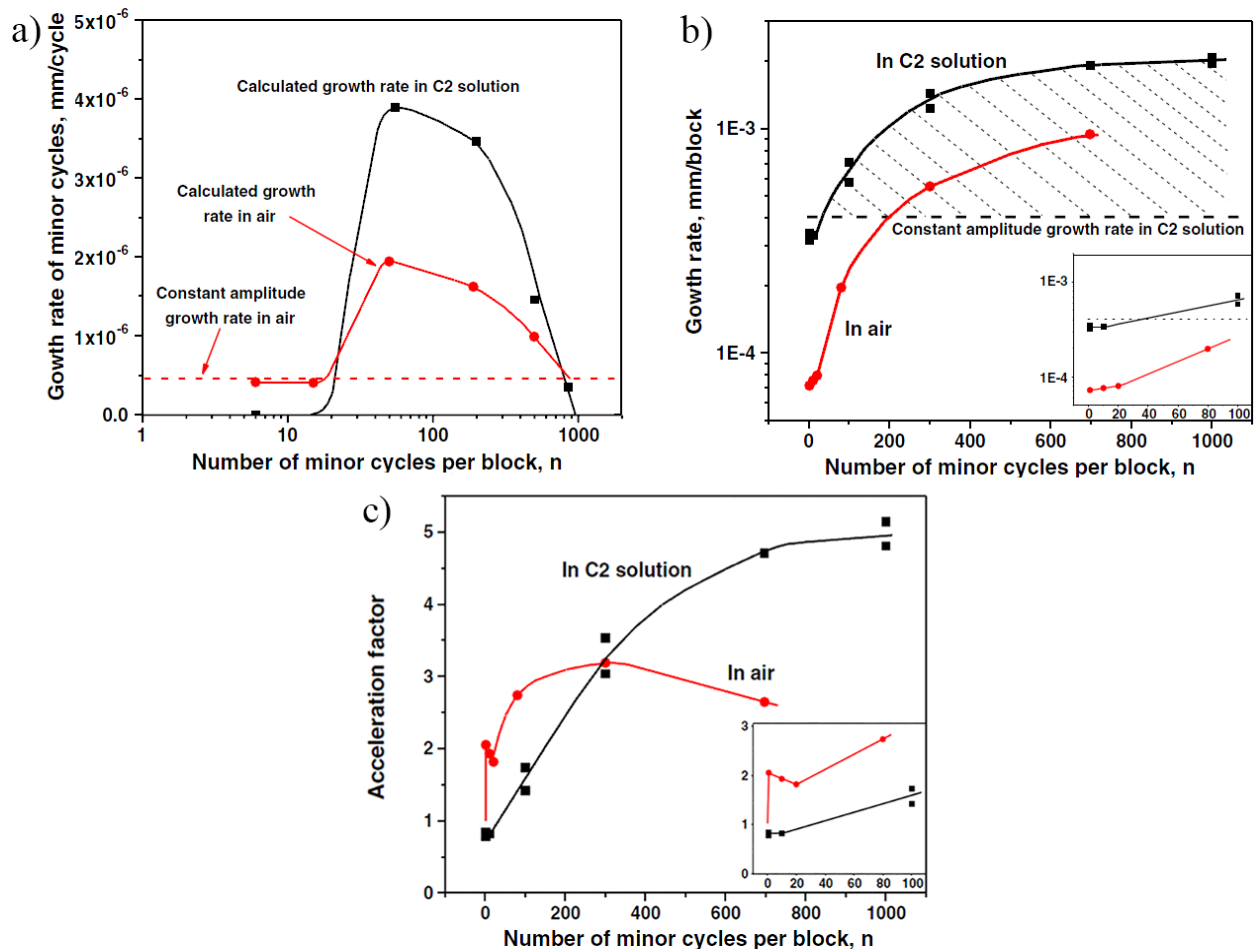


Figure 2.28 Plots comparing the effects of the number of minor cycles in air and C2 solution. (a) Crack growth rate of individual minor cycles. (b) Crack growth rate of underloads. (c) Acceleration Factor (99).

The major findings on the effect of minor cycles following the data in **Figure 2.28** as the number of minor cycles (n) varies from 1 – 697, in air, and 1 – 1000, in C2 solution, are as follows:

- 1) An enhancement of growth occurs in C2 solution in comparison to in-air for both minor cycles and underloads. This can be attributed to the embrittling effect of hydrogen contributed by the NNpH environment, as it is for CA loading.
- 2) Minor cycles contribute to crack growth directly through fatigue in both environments (**Figure 2.28a**). Both air and C2 minor cycles experience an incubation period up to about 15 cycles where no enhancement of growth occurs and a peak growth rate at 55 cycles. After 55 cycles, the enhancement of growth in C2 rapidly diminishes and minor cycle

growth rates rapidly approach in air. It was also found that minor cycles can contribute to crack growth at R values as high as 0.98.

- 3) The growth rate of underloads continue to increase as the number of minor cycles increase in both environments, in spite of the contribution by fatigue of minor cycles decreasing after $n = 55$ (**Figure 2.28b**). However, the enhancement in air increases more rapidly with increasing minor cycles, in spite of the embrittling effect of hydrogen in C2 solution.
- 4) The enhancement in growth of underloads (**Figure 2.28b**) and the acceleration factor (**Figure 2.28c**) both increase at a decreasing rate when $n > 300$ in C2 solution, while the latter decreases after $n > 300$ in air. The diminishing increase in C2 was attributed to either hydrogen embrittlement effects requiring less minor cycles to achieve similar growth rates or corrosion-induced blunting reducing the mechanical driving force with increasing minor cycles.

2.6.2 EFFECT OF UNDERLOAD FREQUENCY AND MAX STRESS INTENSITY

Yu, *et al.* also studied the effects of two varying underload conditions with $n = 300$ with $K_{\max} = 27 - 43 \text{ MPa}\sqrt{\text{m}}$ at $f_{\text{UL}} = 1 \times 10^{-3} \text{ Hz}$, and $n = 697$ with $f_{\text{UL}} = 1 \times 10^{-5} \text{ Hz}$ to $5 \times 10^{-1} \text{ Hz}$ at $K_{\max} = 33 \text{ MPa}\sqrt{\text{m}}$, with all other conditions as they are in Section 2.5.1 (54). Plots demonstrating the results of the study on varying K_{\max} and frequencies of underload-type waveforms are illustrated in **Figure 2.29**.

The major findings of this study on the effect of varying the frequency and K_{\max} of underloads are as follows:

- 1) Crack growth rate is affected by variations in frequency and K_{\max} in NNpH environments, but not in-air. This is related to the effects of hydrogen embrittlement within the NNpH environments, and is typical of corrosion fatigue systems as previously discussed.
- 2) Crack growth increases with increasing K_{\max} , as it would for constant amplitude loading, because of increased driving forces for hydrogen accumulation and diffusion in the plastic zone. The diminishing increases in crack growth were attributed to either RTC or a transition from linear elastic to elastic-plastic behaviour at the crack tip.

- 3) Crack growth rate increases with decreasing f , until a critical value of 10^{-3} Hz is reached, and growth plateaus. Although the critical frequency is the same as the CA case (**Figure 2.18**), no decrease in da/dN occurs after 10^{-3} Hz. The critical frequency was confirmed with atomic modelling of hydrogen within the plastic zone, demonstrating that a steady state level of hydrogen is obtained. However, no clear explanation for why a da/dN plateau rather than decrease in da/dN was observed for the underload and minor cycles case, but was most likely because of the enhanced hydrogen uptake by the minor cycles.

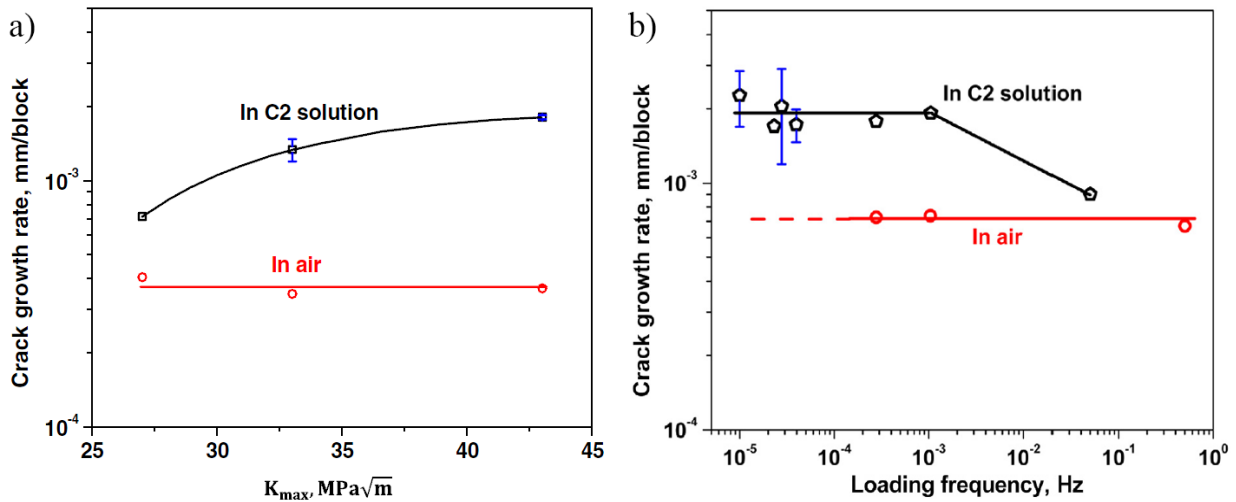


Figure 2.29 Demonstrating the effects of varying (a) K_{max} and (b) f_{UL} in underload-type spectra in C2 solution and in-air (54).

Additional work is currently being performed by the same group on the effects of underloads followed by immediate overloads (Type-IV in **Figure 2.25**) (102). Although the research is still in its infancy, the authors have found that when underloads are followed by overloads the crack growth rates are enhanced, not decreased as previously thought. These results only reinforce that significant work must be conducted under variable amplitude loading in NNpH environments to truly understand crack behaviour under field conditions.

2.6.3 EFFECT OF STATIC HOLDS

Yu, *et al.* also studied the effect of underloads followed by static holds, dubbed Underload and Hold (UL&H) spectra, at K_{max} instead of minor cycles (100). **Figure 2.30a** demonstrates that as the hold time increases, a general decrease in da/dN occurs, with an eventual increase in da/dN as hold time increases past 60 mins. The authors primarily related this growth behaviour to a gradual

exhaustion of mobile dislocations with increasing hold times which increases fracture resistance by fatigue and an eventual increase in da/dN by hydrogen embrittlement effects. The enhanced resistance to fatigue damage is reinforced by **Figure 2.30b**, where UL&H growth rates were $\sim 1/2$ of CA loading. Decreases in da/dN of corrosion fatigue damage with small hold times following cyclic loads was found in other systems as well, as previously discussed in Section 2.3.2.1.5.

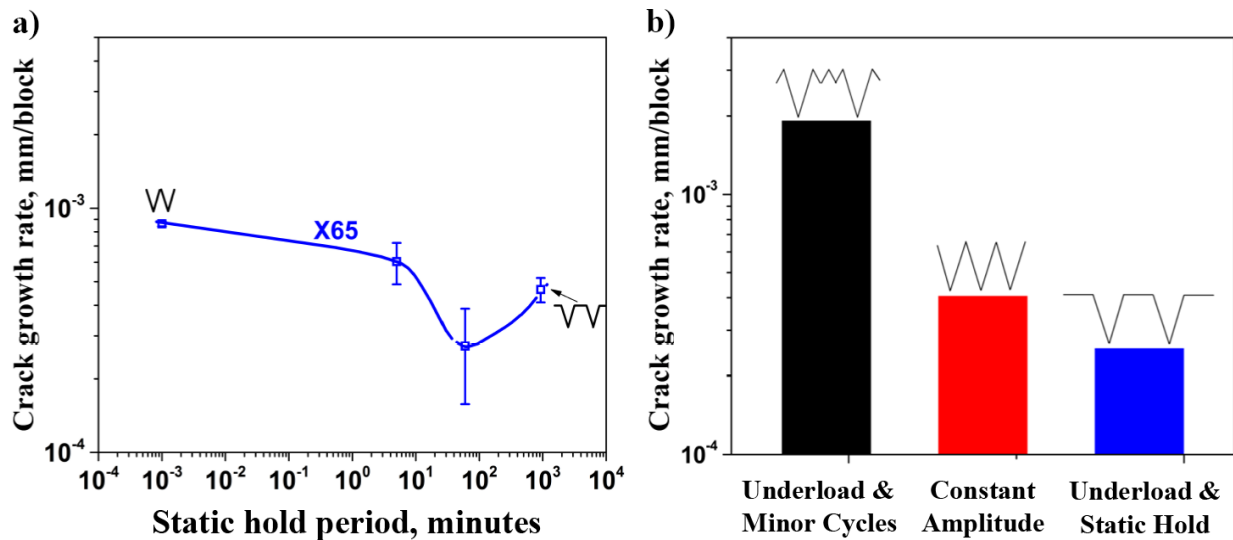


Figure 2.30 Graphical demonstration of the effect of static holds for $K_{max} = 33 \text{ MPa}\sqrt{\text{m}}$, $\Delta K_{UL} = 16.5 \text{ MPa}\sqrt{\text{m}}$, and $f_{UL} = 1 \times 10^{-3} \text{ Hz}$, with (a) varying hold times (100) and (b) in comparison to UL&MC and CA waveforms for $n = 697$ and $t_{hold} = 15.5 \text{ h}$ (80).

2.7 RESEARCH OBJECTIVES

Failures classified as ‘NNpHSCC’ occur in dilute CO_2 ground water environments under minor coating disbondments where CP cannot reach the pipe’s surface. Cracks often occupy the pipe surface in colonies consisting of many shallow cracks with aspect ratios up to 10 (length:depth). Only $\sim 5\%$ of cracks in the field propagate further past a depth of $\sim 1 \text{ mm}$, challenging researchers to determine the mechanisms through which propagation occurs. Traditionally, crack propagation was studied under constant amplitude load conditions until recently when crack behaviour was investigated under variable amplitude underload-type loading.

In spite of significant work on crack behaviour in NNpH environments, little to no work has been done to understand the following:

- 1) Short surface crack behaviour under constant or variable amplitude loading in NNpH environments.
- 2) Differences between through-thickness cracks and surface cracks in NNpH environments.
- 3) The effect of minor coating disbondments on surface crack growth and morphology.

Therefore, this investigation was initiated with the following goals in mind:

- 1) The effect of various loading conditions on shallow surface crack behaviour:
 - a. The effect of constant amplitude frequency.
 - b. The effect of underload frequency when minor cycles are introduced.
 - c. Compare underload growth behaviours between minor cycles and static hold waveforms.
 - d. Compare crack growth behaviours at the surface and depth of shallow surface cracks.
 - e. Comparison of surface and through-thickness crack behaviours under constant and variable amplitude loading conditions.
- 2) The effect of minor coating disbondments:
 - a. The effect on surface crack morphology at the surface and depth.
 - b. Study growth behaviour when a coating disbondment is introduced.

CHAPTER 3: EXPERIMENTAL METHODS

3.1 INTRODUCTION

The following chapter provides an outlined description of the experimental methods used to obtain the results presented in Chapter 4. Two long-term multi-waveform tests were performed using nearly identical experimental procedures to determine the effects of Type I variable pressure fluctuations in near-neutral pH environments on shallow, surface cracks under coating disbondments. In the interest of simulating a pipeline with short surface cracks under variable pressure fluctuations, a novel tensile sample was sealed, and isolated within a corrosion cell containing simulated near-neutral pH ground water solution. Additionally, the corrosion cell included an inner tube, called the shielding, to simulate the trapped ground water between a coating disbondment and pipe surface. The original sample (45) and test cell design (41) were developed elsewhere, while the experimental procedures described herein were developed for this investigation.

3.2 MATERIAL AND SPECIMEN

3.2.1 MATERIAL

The samples used in this study were machined from a section of X60 pipeline, an Fe-Mn steel with a ferrite-pearlite microstructure, that was removed from field operations after experiencing an in-service failure. No cracks or significant corrosion damage was present on the pipeline chunk. Specimens were machined with their gauge length orientated along the pipes longitudinal axis, and the composition of the steel is presented in **Table 3.1** (24). The mechanical properties of the steel were tested in accordance with ASTM Standard E8/E8M-09 using a 7.9 mm thick rectangular sheet-type sample and a crosshead speed of 0.014 mm/mm/s (Control Method C). The yield strength at 0.5 % strain was determined to be 447 MPa using the stress-strain curve shown in **Figure 3.1**. The average grain size of the material was determined to be $9.7 \mu\text{m} \pm 4.3 \mu\text{m}$ using the average grain intercept method, following ASTM Standard E112-13.

Table 3.1 Composition of X60 pipeline steel

Element	Composition, wt %
C	0.18
Mn	1.4
P	0.0175
S	0.0131
Si	0.0364
Cu	0.0326
Ni	0.0182
Cr	0.0284
Mo	0
V	0.0061
Al	0.0493
Sn	0.0031

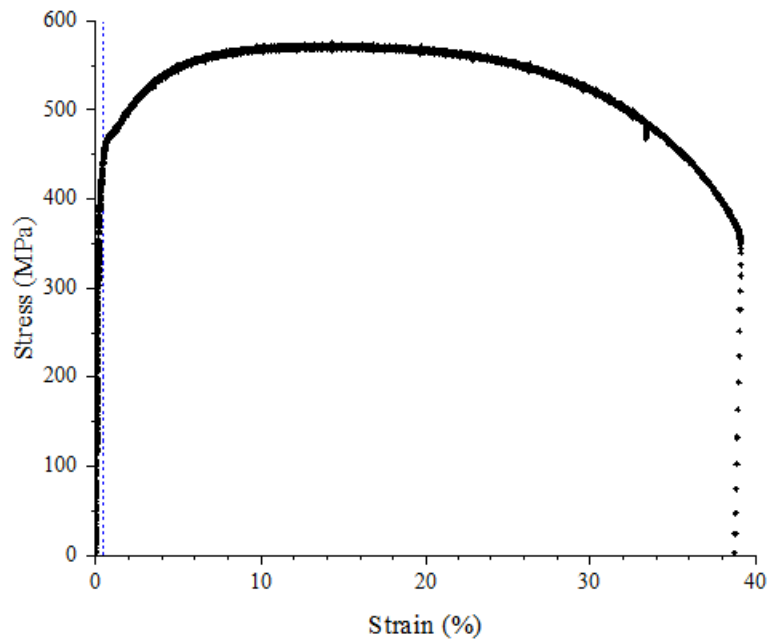


Figure 3.1 The stress-strain curve for the X-60 pipeline steel used to machine test specimens.

3.2.2 SURFACE CRACK TENSION (SCT) SPECIMENS

The long tensile X60 samples in this study – when required referred to as *surface crack tension (SCT)* specimens – possessed three reduced gauge sections measuring in dimensions at 30 mm × 23 mm × 7.9 mm ($l \times w \times t$), as seen in **Figure 3.2**. The SCT specimens were designed with three sections such that three cracks could simultaneously be exposed to localized environments under a coating disbondment, with the topmost crack located above the Open Mouth (OM) and the subsequent cracks, labelled Middle (M) and Bottom (B) located deeper into the disbondment (**Figure 3.3**) (45). To facilitate fatigue precracking, semi-circular electrical discharge machining (EDM) notches, 5 mm in length and 2.5 mm in depth, were machined at the center of each reduced gauge section. The notches were machined into the front surface of the samples – the same side as the external face of the original pipe section – and were orientated perpendicular to the loading axis.

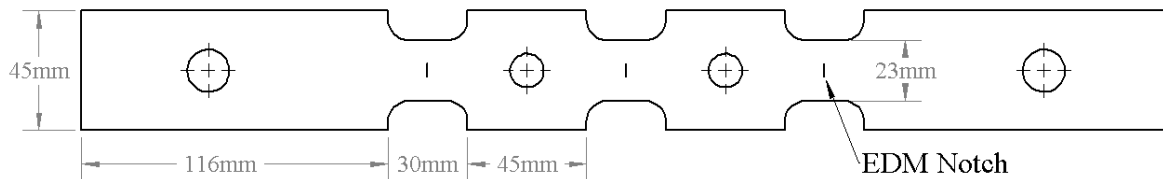


Figure 3.2 Long tensile sample geometry, dimensions, and notch locations

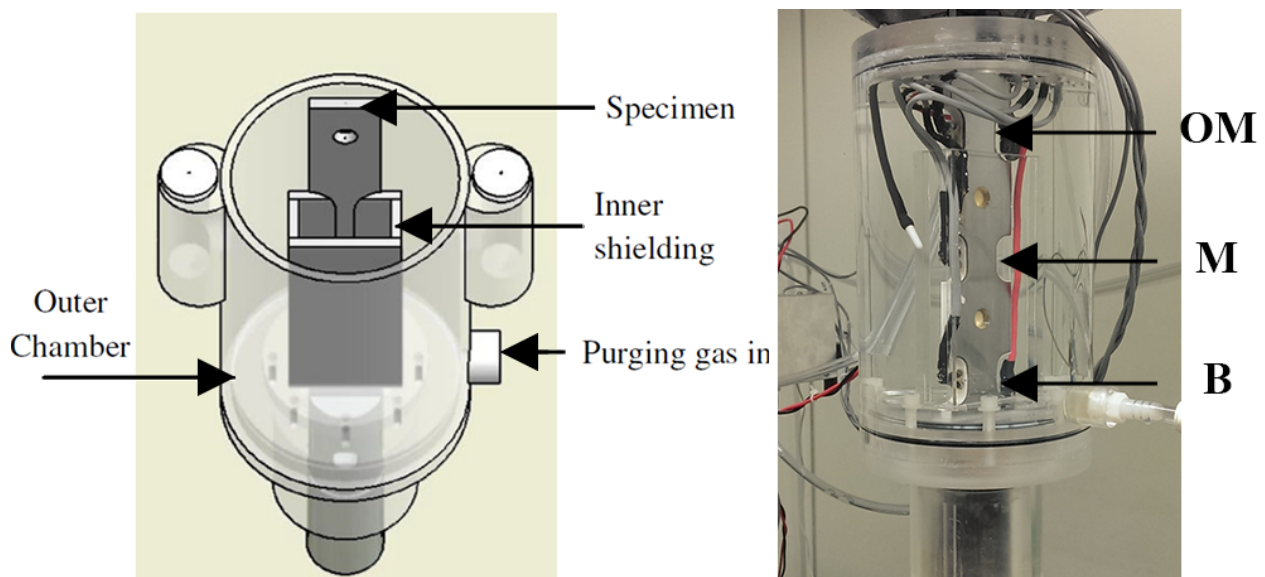


Figure 3.3 (Left) drawing of the original corrosion cell design and (right) the corrosion cell used in testing.

3.2.2.1 Fatigue Precracking

After EDM, the front surface was hand ground to a uniform 600 grit finish, cleaned in an acetone ultrasonic bath, and dried with cool air. The sample was then precracked in air with a triangular waveform to produce a sharp crack tip in accordance with ASTM Standard E647-13a, using the stepped force shredding method for growth rates $< 10^{-8}$ m/cycle (103). Precracking was performed on a MTS 612.13 servohydraulic load frame controlled by Instron's Wavemaker computer software. A summary of the parameters used for the load steps in the precracking schedule are presented in **Table 3.2**. On average, Steps 1 – 3 took an average of 10 000, 45 000, and 45 000 cycles, respectively.

Precracking was periodically interrupted to measure the crack lengths using a Vickers hardness tester equipped with a 40X objective lens and xy micrometer stage accurate to $\pm 5 \mu\text{m}$. The total crack growth from each end of the notch was controlled to 1.15 mm – 1.35 mm, with less than a 0.1 mm difference between the three total crack lengths of a specimen. If necessary, individual cracks were isolated from precracking by pinning specific locations along the sample into cylindrical adapters to lock cracks out.

Table 3.2 In air fatigue precracking schedule using the stepped force shredding method

<i>Step #</i>	<i>% SMYS</i>	<i>Frequency (Hz)</i>	<i>R</i>	Δc
1	70.4	5	0.1	$<0.15\text{mm}$
2	63.4	5	0.1	$\geq 0.50\text{mm}$
3	57.0	5	0.1	$\geq 0.50\text{mm}$

3.2.2.2 Pretest Crack Preparation

After precracking, the front face of the samples which contained the cracks were milled until each notch was removed leaving only sharp shallow cracks on the surface with an average gauge thickness of 5.21 μm . Notch removal is commonly used in short surface crack testing after fatigue precracking, particularly with single edge notch samples (69). The aspect ratio of the cracks after milling out the notches were typically around 0.17 – 0.2, with surface lengths between

5.2 – 6.6 mm. These cracks represented a much closer match to those found in the field possessing aspect ratios of 0.1 as compared to notched specimens.

After milling, the samples were degreased in an acetone ultrasonic bath. To remove grease and debris from inside of the $> 1 \mu\text{m}$ wide cracks, the samples were first loaded onto a servohydraulic frame at a static load of 50 % SMYS to open the cracks without causing damage to the tips. Next, a process of applying and removing 22 μm thick replica tape and spraying into the crack opening with acetone and compressed air was repeated several times. Finally, the sample was placed back into the ultrasonic bath with acetone for 24 h to ensure all contaminants were removed.

Rough measurements of the cracks were taken optically using a Buehler Vickers hardness tester equipped with a xy micrometer stage. During measurements the samples were left with a pattern of indents to provide markings used in pretest and post-test image characterization techniques, described in a later section. Additionally, since multiple waveforms were performed during testing the samples were setup for *in-situ* crack monitoring through a custom direct-current potential drop (DCPD) system, described in Appendix A.

Finally, the samples were placed into the bottom lid of the test cells (**Figure 3.3**) and the side and back surfaces of the sample coated with a multi-layered composite coating. The coating was comprised of an initial layer of cellulose acetate tape directly applied to the sample, with its edges covered in waterproof electrical coating. The tape and electrical coating were then bonded to a 3D printed PLA shell using two-part epoxy and the external PLA surfaces were coated with two-part epoxy. This was performed to protect the back and sides from the corrosive media to better simulate field conditions where only the external surfaces of the pipe are exposed to groundwater.

3.2 CORROSION CELL AND ENVIRONMENT

3.2.1 CORROSION CELL

A side-by-side comparison of the schematic and real image of the corrosion cell used for testing may be seen **Figure 3.3**. The corrosion cell, entirely fabricated from PMMA, was designed with two chambers in mind to effectively simulate the environment a buried line would experience under a coating disbondment. The inner chamber, dubbed the shielding, was placed around the

middle and bottom gauge sections and served to simulate a coating disbondment and thereby causing the solution inside to simulate ground water entrapped under a coating (45). There were 5 mm and 2 mm gaps between the crack surfaces and backside of the sample to the inner walls of the shielding, respectively. The distance of the OM, Middle, and Bottom cracks from the opening of the simulated disbondment (Open Mouth) were -10 mm (above), 65 mm, and 140 mm, respectively.

The outer chamber housed the bulk test solution for simulating the soil surrounding pipelines and to seal the test from the ambient environment and contaminants. Although o-rings served to prevent gas leakage into the cell, silicone rubber was applied to seal any openings and mating components to ensure that no oxygen could enter the cell during testing. Additionally, any openings that the sample passed through were sealed with multiple layers of silicone, with 24 h between each application of sealant. The bulk solution inside the cell was purged with 5 % CO₂ + 95 % N₂ gas mixture over the entire duration of the test through inlet and outlet lines installed into the lid of the cell. The inlet line was placed in such a fashion that CO₂ could only enter into the shielding via diffusion through the open mouth.

3.2.2 TEST SOLUTION

A dilute groundwater solution, known as C2 (**Table 3.3**), was used to simulate NNpH environments during testing (21). The solution was prepared using 4 L of ultra-pure Milli-Q water and lab grade reagents. Prior to testing, the solution was purged with 5 % CO₂ + 95 % N₂ gas during mixing for a minimum of 48 h until a measured *pH* of ~ 6.29 was achieved. Purging with CO₂ was necessary to ensure that no dissolved oxygen remained in solution and complete mixing occurred.

3.3 MECHANICAL LOADING CONDITIONS

The pretest crack parameters for Tests I and II may be found in **Table 3.4**. Variables $2c$ and a refer to the cracks total surface and depth lengths. The crack depths (a) reported in **Table 3.4** were determined by post-test fracture surface measurements. The column labelled as ‘precrack’ indicates values determined for the fatigue precrack length, prior to notch removal. Large

differences in the pretest lengths were unavoidable and likely occurred because of variations in the individual notch geometries and local microstructures.

Table 3.3 Composition of the simulated NNpH solution (C2) used during testing. $pH = 6.29$.

Species	Concentration (g/L)
MgSO ₄ · 7H ₂ O	0.0274
CaCl ₂	0.0255
KCl	0.0035
NaHCO ₃	0.0195
CaCO ₃	0.0606

Table 3.4 Crack geometries and stress intensity values for CA cycles & underloads in Tests I and II.

Crack Location	Precrack [2c]	Pretest [2c]	Pretest [a]	K_{max} [2c]	K_{max} [a]	ΔK [2c]	ΔK [a]	
		(mm)		(MPa√m)				
Test I	T	7.33	6.48	1.18	13.84	20.53	12.45	18.48
	M	7.28	5.65	1.03	12.80	19.06	11.52	17.15
	B	7.23	5.30	0.96	12.30	18.35	11.07	16.51
Test II	T	7.24	6.02	1.09	13.32	19.81	11.99	17.83
	M	7.26	5.79	1.05	13.00	19.34	11.70	17.41
	B	7.31	5.80	1.05	13.02	19.37	11.71	17.43

For all cyclic waveforms the maximum load applied was 80 % SMYS – except waveform #1 of Test II which was 57 % SMYS – which is the designed maximum allowable stress CSA Z662-03 Class 1 locations and lines granted special permits in the US (104). Based on crack geometry and stress, the max stress intensity (K_{max}) values were calculated using the Newman and Raju stress intensity solution for a semielliptical surface flaw in a flat plate for $a \leq c$ (105). The ΔK values were determined using a stress ratio (R) value of 0.1.

3.3.1 TEST I & II WAVEFORMS

Three types of cyclic waveforms were used during mechanical testing: Constant Amplitude (CA), Underload and Minor Cycles (UL&MC), and Underload and Hold (UL&H) spectra. The UL&MC and UL&H waveforms are shown in **Figure 3.4**, while CA loading can be considered as constant underloads. Additionally, the multiple waveforms used in Tests I and II are presented in **Table 3.5**.

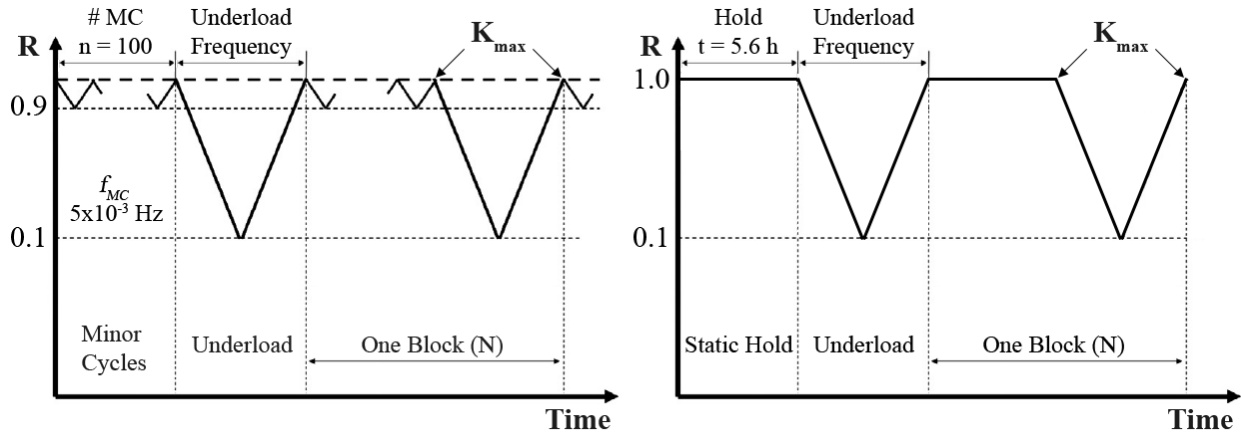


Figure 3.4 The two types of variable amplitude waveforms used during testing. LHS: Underload and Minor Cycles (UL&MC) and RHS: Underload and Hold (UL&H).

The goal of Test I was to study the effect of frequency under CA loading, the effect of underload frequency, and the enhancement in crack growth rate (da/dN), if any, by introducing minor cycles. As such, the loading frequency of CA cycles and underloads in Test I was varied from 10^{-3} Hz to 10^{-2} Hz at $R = 0.1$. Test II focused strictly on comparing the crack growth behaviour of underloads followed either by minor cycles or static holds at K_{max} . In both tests, the following mechanical variables were kept constant: $R_{UL} = 0.1$, $R_{MC} = 0.9$, $f_{MC} = 5 \times 10^{-3}$ Hz, and $n = 100$.

The calculated values of the Combined Factor of the depth and surface of the Tests' top cracks are recorded for their respective waveforms in **Table 3.5**. The top crack is represented because its local environment is the closest match to the bulk C2 solution for which the Combined Factor threshold value of long cracks (CT samples) was determined to be $8500 (\text{MPa}\sqrt{\text{m}})^3 \text{Hz}^{0.1}$ (28). Based on the Combined Factor values, the surface of the cracks cannot grow because they were well under the threshold, while the opposite is true in the case for the crack depths.

Table 3.5 Summary of mechanical waveforms and testing parameters of Tests I and II.

Waveform No.	Type	CA / UL	MC / H	Comb. Fact. (MPa√m) ³ Hz ^{-0.1}	Time (h)	Blocks (N)	
Test I	1	CA [Air]	$R = 0.1$ $f = 0.01$ Hz	-	N/A	198	7081
	2	CA	$R = 0.1$ $f = 0.001$ Hz	-	2c: 3823 a: 13952	531	1902
	3	CA	$R = 0.1$ $f = 0.01$ Hz	-	2c: 3037 a: 11082	425	15284
	4	CA	$R = 0.1$ $f = 0.1$ Hz	-	2c: 2412 a: 8803	195	70242
	5	UL&MC	$R = 0.1$ $f = 0.1$ Hz	$R = 0.9$ $f = 0.005$ Hz n = 100	2c: 2412 a: 8803	473	85
	6	UL&MC	$R = 0.1$ $f = 0.001$ Hz	$R = 0.9$ $f = 0.005$ Hz n = 100	2c: 3823 a: 13952	440	75
	7	UL&MC	$R = 0.1$ $f = 0.01$ Hz	$R = 0.9$ $f = 0.005$ Hz n = 100	2c: 3037 a: 11082	184	33
Test II	1	CA [Air]	$R = 0.1$ $f = 5$ Hz	-	-	2	36000
	2	CA [Air]	$R = 0.1$ $f = 0.1$ Hz	-	-	47	16922
	3	UL&MC	$R = 0.1$ $f = 0.001$ Hz	$R = 0.9$ $f = 0.005$ Hz n = 100	2c: 3823 a: 13952	1107	180
	4	UL&H	$R = 0.1$ $f = 0.001$ Hz	threshold = 5.56h	2c: 3823 a: 13952	1128	184
	5	HYDRO	-	-	-	10	-

3.3.1.1 Hydrostatic Test

In Test II, a simulated hydrostatic test was performed after the variable amplitude loading test was completed and its cracks replicated for characterization. The same corrosion cell and a fresh mixture of C2 solution was used during testing. The hydrostatic test was performed to determine

if there was any significant crack tip blunting or propagation with the surface cracks because it is commonly performed by pipeline operators for integrity management. The hydrostatic testing schedule for Test II's waveform #5 is equivalent to the 1-step hydrostatic test previously used by Kang, et al. (106) and is presented in **Figure 3.5**. Prior to testing, the surfaces of the cracks were coating using a multilayered composite coating composed of cellulose acetate tape, hydrophilic electrical coating, and two-part epoxy then hydrogen charged in C2 solution at OCP conditions for 10 days.

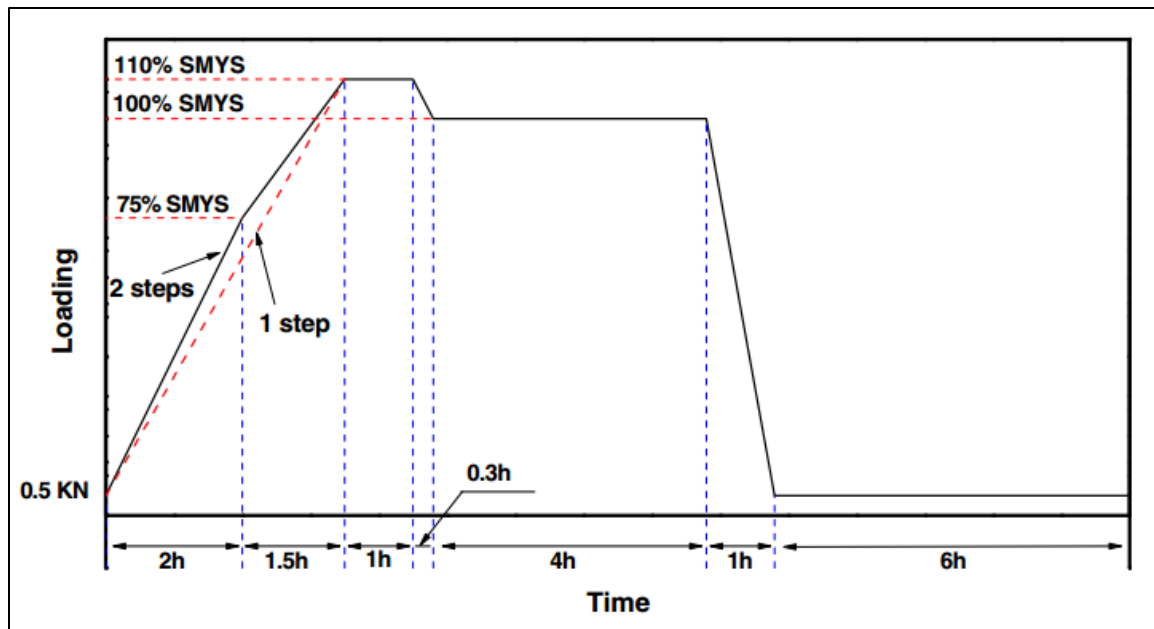


Figure 3.5 Simulated hydrostatic test load procedure used in Test II taken from literature (106).

3.4 END OF TEST PROCEDURE

All tests were controlled to ensure that an operator was present upon their completion. The load was controlled to maintain a small tensile stress equivalent to 5 % SMYS upon test completion to prevent the load frame from entering position control and applying a compressive load. A constant supply of CO₂ purged the cell and solution during the entire take-down procedure. The flow rate of CO₂ was adjusted if necessary to keep the supply steady enough to bubble out of a sealed container of water.

In the first step of the process two 10 mL samples of test solution were extracted from each of the various positions inside of the cell for chemical analysis. To remove solution from the cell,

graduated syringes attached to 1 mm OD plastic tubings were inserted into the cell through a small opening made in the top lid's seal on test completion. A bulk solution sample was taken from near the center of the cell outside of the shielding and another sample from the immediate vicinity of the top crack. Then, the bulk solution level was drained slowly until it was just below the OM of the shielding and solutions were extracted from within the shielding. The extraction tube was kept level with the meniscus of groundwater solution to avoid mixing within the shielding. To prevent cross-contamination, a clean extraction tubing was used at each location.

Once the sample solutions from the bottom of the shielding were extracted, the cracks were rinsed inside of the cell with ethanol as the remaining bulk solution drained. While the cracks were rinsed with ethanol, CO₂ flow was increased to prevent oxygen from entering the cell and the sample was loaded to half the testing stress to clean out any groundwater remaining on the crack walls. When the ethanol level reached the top crack, an extraction tube was placed in front of the cracks and ethanol was pumped into the cracks to help facilitate water removal through advection. After several minutes of cleaning the cracks inside of the cell the ethanol was allowed to drain from the cell. The specimens were allowed to dry inside the cell's CO₂ environment while the load was decreased to zero, and then removed from the loading frame and cell and immediately placed into an acetone ultrasonic bath for 24 h.

3.5 CHARACTERIZATION

The following section is a description of the methods and equipment used to characterize samples before and after testing.

3.5.1 PRETEST CRACK CHARACTERIZATION

Previously it was stated that the samples were indented to provide markings for further characterization and reference. This was in part due to the fact that the SCT specimens were too large to fit within any available SEM and obtaining accurate pretest measurements was difficult. Use of optical imaging was not possible because of the small pretest crack crevice width and small test growth in combination with optical microscopy's poor resolution and difficulty in imaging rough surfaces. Therefore, a procedural method was developed to determine pretest crack lengths and crack tip locations utilizing replica imaging techniques.

First, approximate crack lengths and tip locations were determined using an optical Vickers hardness tester, equipped with an xy micrometer stage, and a pattern of indents was left near the crack tips, as seen in **Figure 3.6**. Indents were placed at a distance of at least 2.5 times the side length of an indent's diamond perpendicular to the crack tips to avoid stress field interactions, following ASTM E384.

Cracks were then replicated several times for SEM imaging using 122 μm thick cellulose acetate, reported to be capable of replicating features as small as 10 nm (107), softened by acetone on the sample surface. Cellulose acetate replica tape was opted for over acrylic or rubber based replicas because of its superior resolution and ease of use (108). After drying, NEM tape – a conductive, double-sided carbon-based tape – was firmly placed on back of the negative replicas, mounted to a small Al sample stage, trimmed back to the edges of the stage, and sputtered with a thin layer of carbon. Colloidal graphite was dabbed on any over-hanging edges of the replica to facilitate carbon sputtering and prevent charging of the replica surface during imaging.

The replicas were then imaged using a Zeiss EVO LS15 EP-SEM at a low accelerating voltage (5 kV) at a working distance between 8 mm – 9 mm to prevent melting, distortion, or charging of the replicas' surfaces. Low and high magnification images were taken to determine the total crack lengths and crack tip locations, respectively. To determine the total crack length, first a total of 15 – 22 low magnification images were taken across the entire crack surface, then stitched together and subsequently measured using the Image J-2 software.

Finally, after the test had been completed, the real cracks were also imaged entirely along their length at low magnifications. Then, the images were stitched together and the crack length was measured as well as the crack tips' indent to indent lengths, as demonstrated in **Figure 3.6**. To account for shrinkage or stretching of the replicas, the indent to indent lengths were used alongside the measured crack lengths to apply a correction factor to the measured pretest length.

Eq. 3.1 was used to apply the correction factor to determine the pretest crack length ($a_{i, \text{adj}}$) may be seen below, where $a_{i, \text{meas}}$ is the replica's measured crack length, and d_{1-1} and d_{2-2} denote the indent-to-indent lengths between the two crack tips for the pretest and post-test measurements, as indicated by their respective subscripts.

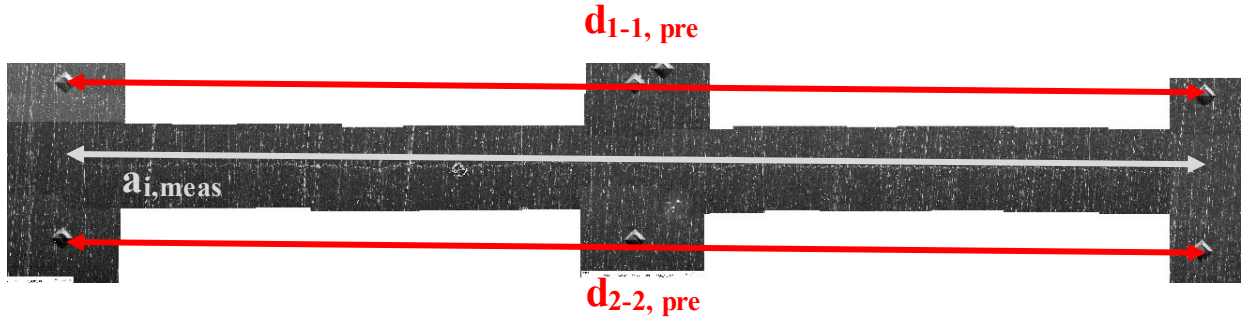


Figure 3.6 Demonstrating the replica measurements taken to determine pretest crack length using stitched SEM images of pretest crack replicas.

$$a_{i, \text{adj}} = a_{i, \text{meas}} \cdot (0.5) \cdot \left(\left[\frac{d_{1-1, \text{pre}}}{d_{1-1, \text{post}}} \right] + \left[\frac{d_{2-2, \text{pre}}}{d_{2-2, \text{post}}} \right] \right) \quad (3.1)$$

3.5.2 POST-TEST CRACK CHARACTERIZATION

After the tests were completed, the solution was removed from the cell, while the sample remained in a CO₂ gas environment to prevent oxidation until it could be removed. Then, the sample was removed from the corrosion cell and immediately placed into an acetone ultrasonic bath for 24 h. Next, several characterization steps were taken to obtain as much information about the samples and cracks as possible. Additionally, the post-test cracks were stored in sealed scintillation vials containing acetone in between characterization steps and transported within small re-sealable plastic containers containing Drierite desiccant to protect the cracks from the external environment and damage.

3.5.2.1 Post-test Surface

The OM, Middle, and Bottom gauge sections were cut into small, individual pieces containing the cracks and the majority of the gauge section. The cuts were then repeatedly strip cleaned to remove loose corrosion products with 122 μm replica tape until no visible corrosion product was stripped

off. Next, in order to remove any of the replica tape that remained on the surface of the samples, or on the inside of the cracks, the samples were then placed into and cleaned in an ultrasonic acetone bath.

The samples were then given a final clean in an ultrasonic ethanol bath for at least 6 h. In the ethanol bath, the samples were propped up at a diagonal with the cracks facing downwards to ensure that no acetone or debris remained along or inside of the top surface of the cracks. Then, the samples were dried in cool air and periodically sprayed at the cracks with small amounts of ethanol to wash away any evaporated films formed along the crack.

The cracks were then imaged across their entire length using a Zeiss EVO LS15 EP-SEM at low magnifications in both secondary electron (SE) and backscattered electron (BSE) modes and stitched together using ImageJ-2. High magnification images at the crack tips to observe their corrosion and crack tip morphologies.

3.5.2.2 Polished Surface

The samples were briefly ground to a 600 grit finish to remove most of the heavy corrosion. Next, in a criss-cross pattern, the sample surfaces were polished to a mirror finish using 6 μm , 3 μm , and 1 μm diamond oil slurry. In between polishes the samples were cleaned in an acetone ultrasonic bath to remove any oil, and a final cleaning was performed in the same manner as Section 3.5.2.1 prior to imaging.

SEM images were taken using across the entire crack, at low magnification, and stitched together in ImageJ-2 to determine crack growth and widths. High magnification SEM images were taken to analyze crack tip morphologies. The images of the polished surface were used to determine the total surface crack growth ($\Delta 2c$).

3.5.2.3 Cross-Section Characterization

To characterize the depth profile of the cracks the samples were sectioned perpendicular to the crack length using a precision saw mounted with a diamond coated wafer blade capable of cutting width of 0.3 mm. In Test I the cuts were made near the first transition of the wide and thin surface morphology as shown in **Figure 3.7**. For Test II, the cuts were made 1/3 along the crack lengths.

In either case, care was taken to preserve a fair portion of the mid-length of the crack for fracture surface analysis.

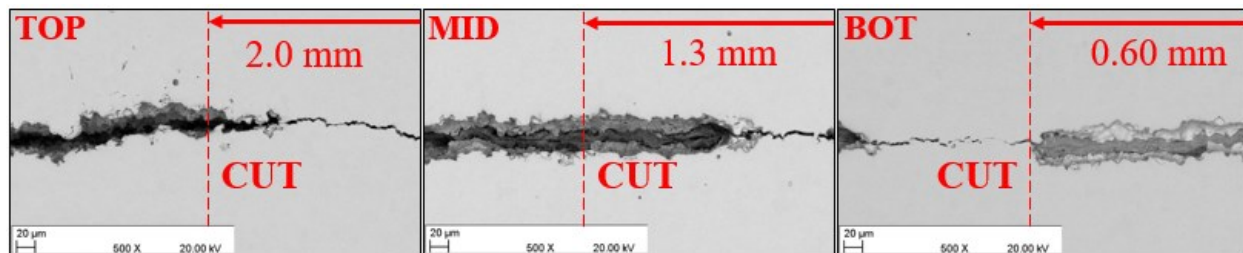


Figure 3.7 Illustrating the locations on Test I's cracks' surfaces, where CUT indicates where the samples were sectioned for depth profile characterization. TOP refers to the OM.

The cross-sections were ground, polished, cleaned, and imaged in the same manner as the polished surface profile. Test I's cross-sections were not mounted in two-part epoxy to avoid contaminating the corrosion products wedged inside the crack for energy dispersive X-ray spectroscopy (EDS) chemical analysis. It was necessary to perform EDS along the cross-sections because EDS would penetrate past the corrosion products on the fracture surface, but sample significantly more corrosion product through the sides of the crack without hitting the base metal. EDS analysis was performed using a Zeiss Sigma 300-VP FESEM equipped with a Bruker EDS system with dual-silicon drift detectors, each with a 60 mm² area and a resolution of 123 eV. EDS scans were performed using area scans at an accelerating voltage of 20.0 kV, typically achieving counts between 4 kcps to 11 kcps, and background noise was removed using the built-in Bruker software's Bremsstrahlung filter setting.

3.5.2.4 Etched Surfaces

An additional set of SEM images of the surface and depth profiles were taken after etching in order to analyze the surfaces microstructure and confirm transgranular growth. However, only the sections of the surface from the smaller cross-section pieces were etched to avoid damaging the fracture surface with etchant. Samples were etched with 2 % Nital by allowing the etchant to flow across the surfaces for 5 s – 10 s, at a drop of 2 % Nital per second. Immediately after etching, a final cleaning was performed in the same manner as Section 3.5.2.1 prior to imaging the exact same locations as in Section 3.5.2.3.

3.5.2.5 Fracture Surface

The larger portion of the cracks that was not used for the characterization of the depth profile were fractured open to analyze the fracture surfaces. First, to facilitate fracture the width and thickness of the samples' were reduced to 8 mm and 2 mm, respectively, and the sides and back of the samples were notched using a diamond tipped scribe to ensure a flat fracture. Then, the samples were placed into liquid nitrogen for up to four hours, removed, and fractured open by striking the backside notch using a cold chisel. The two halves were immediately placed into an acetone ultrasonic bath to prevent oxidation of the fresh surfaces and remove any loose corrosion products or oil remaining from surface polishing.

The two fracture surfaces were imaged using a Zeiss Sigma 300-VP FESEM, with three main goals while characterizing the surfaces. The first was to image the entire crack to observe its morphology and determine its aspect ratio. The second was to locate, image, and measure striations and their location from the cleavage plane in an attempt to determine the growth behaviour of the crack away from the surface. Third, the fracture surfaces were imaged at medium and low magnifications to identify and measure individual waveform growth regions along the fracture surface to supplement other methods.

If either an insufficient number of striations or no clear discernable growth regions were located the corrosion products were removed by dipping the fracture surface into a mixture of 6N HCl + 3.5 g/L hexamethylene tetramine, a solution recommended for steel corrosion product removal in ASTM Standard G1-03 (109). Through trial and error, it was determined that only 2 s – 4 s was required to remove corrosion products without causing significant damage to microscopic crack features. Immediately after the cracks were placed in the corrosion removal solution, they were sonicated in a methanol bath, and dried with cool air.

Attempts were also made to characterize the corrosion products on the fracture surfaces using the X-ray Diffraction technique with a Rigaku XRD Ultimate IV machine, equipped with both 2 mm and 5 mm slits and a Cu-source. However, no detectable or identifiable peaks other than BCC-iron were detected on either thin-film or bulk mode, as seen in **Figure 3.8** below.

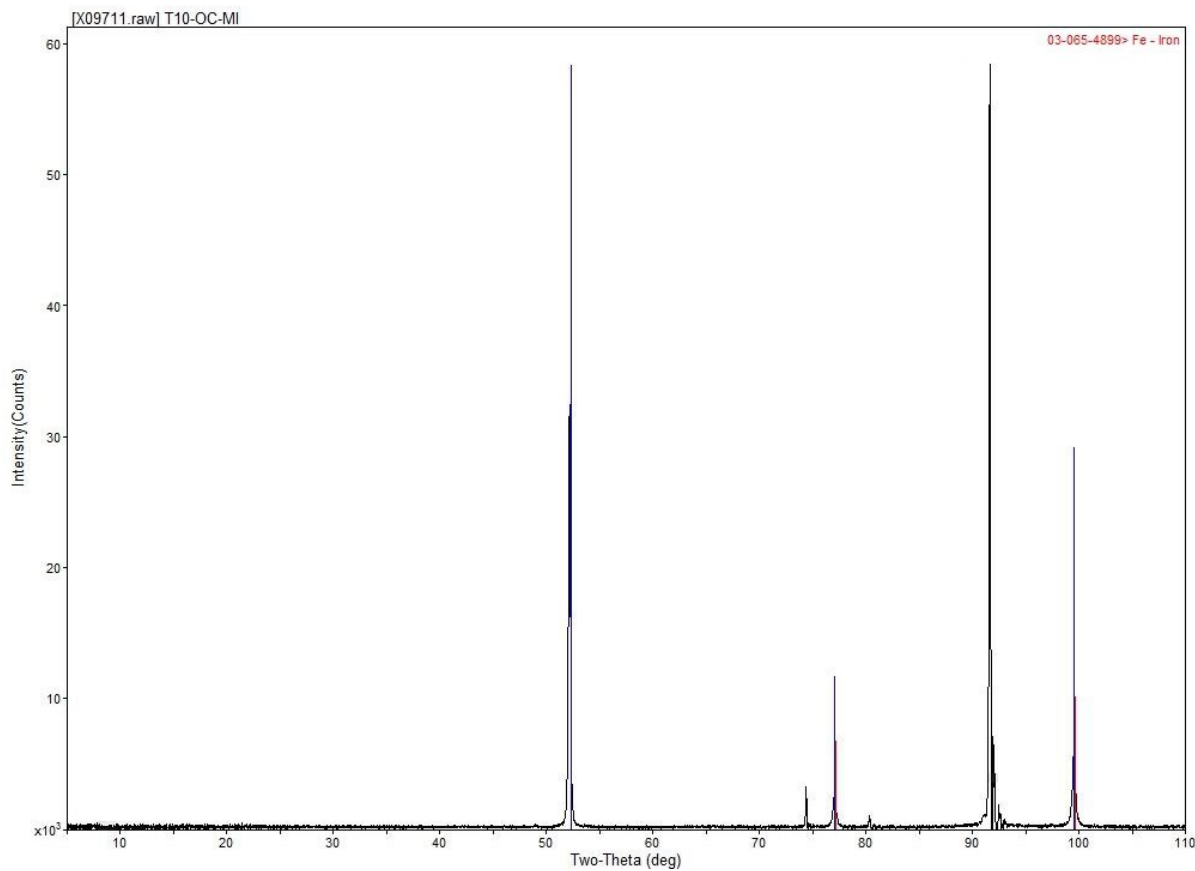


Figure 3.8 XRD profile for Test I's Middle crack's fracture surface with peaks detected other than BCC-iron, but they could not be identified.

3.5.3 SOLUTION ANALYSIS

The *pH* measurements were performed using a Fisher Scientific Ag/AgCl *pH* electrode (model No. 13-620-530A) and XL60 *pH* meter that were calibrated prior to taking each set of *pH* measurements using 4, 7, and 10 *pH* buffer solutions. Measurements were taken prior to adding solution to the testing cell and at the end of each test to determine the *pH* at various locations of the corrosion cell. The *pH* measurements were taken immediately upon the removal of 10 mL sample solutions from each location in the corrosion cell. The *pH* electrode was rinsed with electrode cleaning solution and Milli-Q water then dried off prior to each measurement to avoid cross-contamination.

The other set of 10 mL solutions removed from the cells were used to determine the elemental species concentrations at the multiple locations within the cell. Characterization of the solutions was performed using inductively coupled plasma mass spectrometry (ICP-MS). Two 1 mL

samples of each solution were taken per analysis, and provided as an average. No dilution of the samples was required. The ICP-MS characterization was performed by the technical staff of the University's local Earth and Atmospheric Sciences (EAS) faculty, and exact details on the procedure were not provided.

CHAPTER 4: RESULTS

4.1 SURFACE CHARACTERIZATION

The following section presents the characterization, trends, and observations of the surface of the cracks of Tests I and II. First, the crack growth rates of the various loading spectra will be presented separately. Next, the general crack morphologies and bulk surface corrosion features of the two tests will be discussed in greater detail using Test I for general trends and differences or discrepancies using Test II.

4.1.1 SURFACE CRACK GROWTH

4.1.1.1 Test I

The net surface growth ($\Delta 2c$) and crack growth rates (dc/dN) of the six waveforms tested in C2 solution are summarized in **Table 4.1**. Additionally, a visual comparison of the growth behaviour between the three cracks over the duration of the test is provided in **Figure 4.1**. The crack growth rates were determined separately for each crack using their individual sets of direct current potential drop (DCPD) system test data and their measured net growth after testing; additional information pertaining to the DCPD system, including potential data and conversions to crack growth is located in Appendix A. No surface crack growth data is provided for the first waveform tested, i.e. in-air CA loading, because there was no resolvable crack growth detected on the surfaces after the waveform was tested.

From the data presented in **Table 4.1** and **Figure 4.1**, several trends are readily observable:

- The net crack growth decreased from the Open Mouth (OM) to the Bottom crack locations for each waveform used during testing.
- As loading frequency decreased from 10^{-1} Hz to 10^{-3} Hz the crack growth rate per block increased at all locations for both CA and UL&MC loading.
- The growth per block of the UL&MC waveforms were markedly greater in comparison to their CA counterparts, regardless of location.

Table 4.1 Summary of calculated surface crack growth data for Test I for all waveforms in C2 solution.

Waveform		<i>Constant Amplitude</i>			<i>Underload and Minor Cycles</i>		
Frequency (Hz)	-	10^{-3}	10^{-2}	10^{-1}	10^{-3}	10^{-2}	10^{-1}
$\Delta 2c$ (μm)	OM	54.4	56.3	50.8	21.3	5.6	12.6
	M	46.2	7.2	6.1	12.5	4.5	5.5
	B	17.8	1.7	1.2	8.9	3.1	3.9
dc / dt (mm/s)	OM	2.9×10^{-8}	3.7×10^{-8}	7.2×10^{-8}	1.4×10^{-8}	8.4×10^{-9}	7.4×10^{-9}
	M	2.4×10^{-8}	4.7×10^{-9}	8.7×10^{-9}	7.9×10^{-9}	6.9×10^{-9}	3.3×10^{-9}
	B	9.3×10^{-9}	1.1×10^{-9}	1.7×10^{-9}	5.7×10^{-9}	4.7×10^{-9}	2.3×10^{-9}
dc / dN (mm/blk)	OM	1.4×10^{-5}	1.8×10^{-6}	3.6×10^{-7}	1.5×10^{-4}	8.4×10^{-5}	7.4×10^{-5}
	M	1.2×10^{-5}	2.4×10^{-7}	4.3×10^{-8}	8.7×10^{-5}	6.9×10^{-5}	3.3×10^{-5}
	B	4.7×10^{-6}	5.5×10^{-8}	8.3×10^{-9}	6.2×10^{-5}	4.7×10^{-5}	2.3×10^{-5}
Acceleration Factor	OM	-	-	-	10	46	205
	M	-	-	-	7	291	751
	B	-	-	-	13	845	2768

Note that in **Table 4.1** the Acceleration Factor refers to the ratio of growth of the CA to the UL&MC crack growth rates (da/dN). It was assumed that the minor cycles did not contribute to growth in the calculated value.

The CA growth behaviour demonstrated at the OM was initially expected for all crack locations, as it is typical of true corrosion for crack growth in terms of dc/dN or dc/dt to increase or decrease, respectively, with a decrease in loading frequency (**Figure 4.2**). Unlike the OM, however, a significant decrease in both dc/dN and dc/dt occurred for the Middle and Bottom cracks when the CA loading frequency was increased from 10^{-3} Hz to 10^{-2} Hz. The frequency response demonstrated by the Middle crack was more peculiar because its growth rate at 10^{-3} Hz (1.2×10^{-8} mm/blk) was similar to the rate of the OM (1.4×10^{-5} mm/blk), yet at 10^{-2} Hz the Middle crack entered a near-dormant state of growth similar to the Bottom crack.

The crack behaviour responses to loading frequency under UL&MC loading were less pronounced than under CA loading (**Figure 4.2**). Only slight differences in crack growth behaviour were observable between the OM, Middle, and Bottom locations. The primary difference between the cracks was that the OM experienced a greater decrease in growth rate when the load frequency was changed from 10^{-3} Hz to 10^{-2} Hz, while the other two cracks experienced a greater decrease in da/dN when the load frequency was changed from 10^{-2} Hz to 10^{-1} Hz.

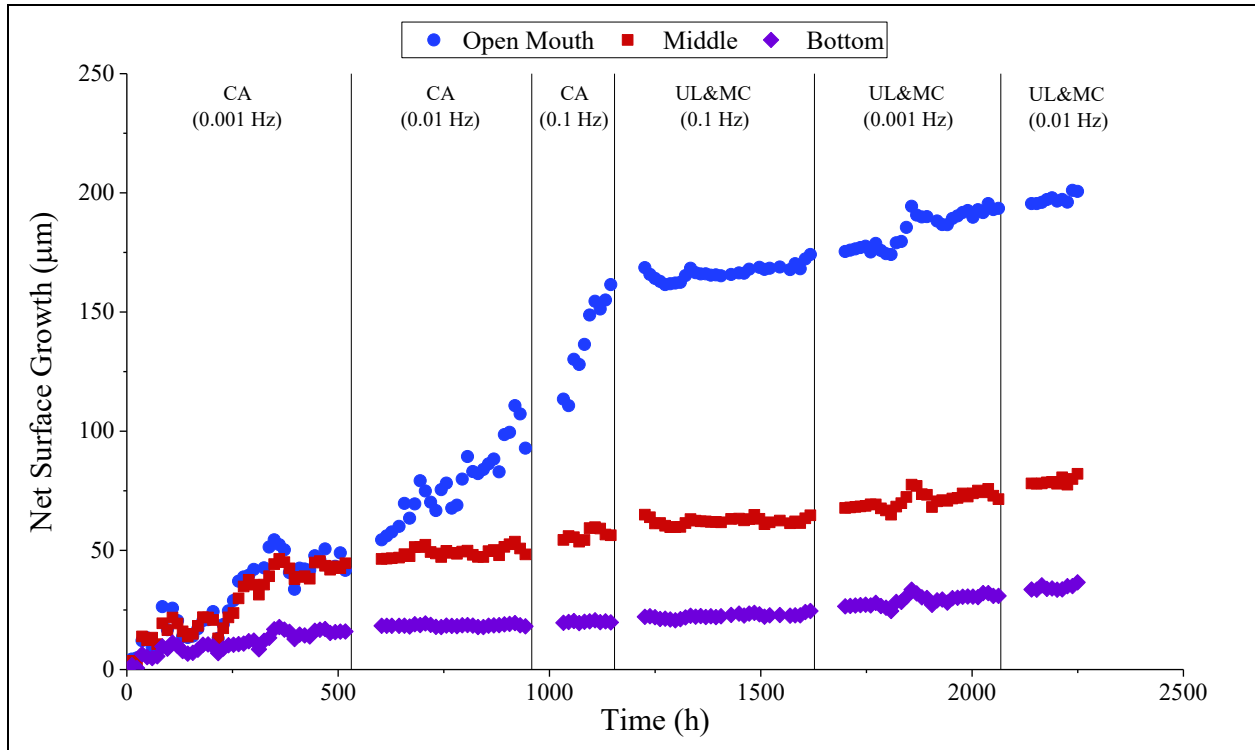


Figure 4.1 Net surface crack growth (μm) in C2 solution plotted as a function of time for all three cracks in Test I.

However, unlike frequency, the large differences in growth rate between the two types waveforms are clear and better represented by the Acceleration Factor values presented in **Table 4.1**. The acceleration factor was calculated by dividing the crack growth rates (dc/dN) of the UL&MC waveforms by the CA crack growth rates, assuming that the minor cycles did not directly contribute to crack growth. In general, the value of the Acceleration Factor increased as the underload frequency increased and increased from the OM to the Bottom crack locations, for a given underload frequency. The high values of the Acceleration Factor for the Middle and Bottom

cracks at loading frequencies of 10^{-2} Hz and 10^{-3} Hz appear to be a result of their low growth rates under CA loading frequencies of 10^{-2} Hz and 10^{-3} Hz.

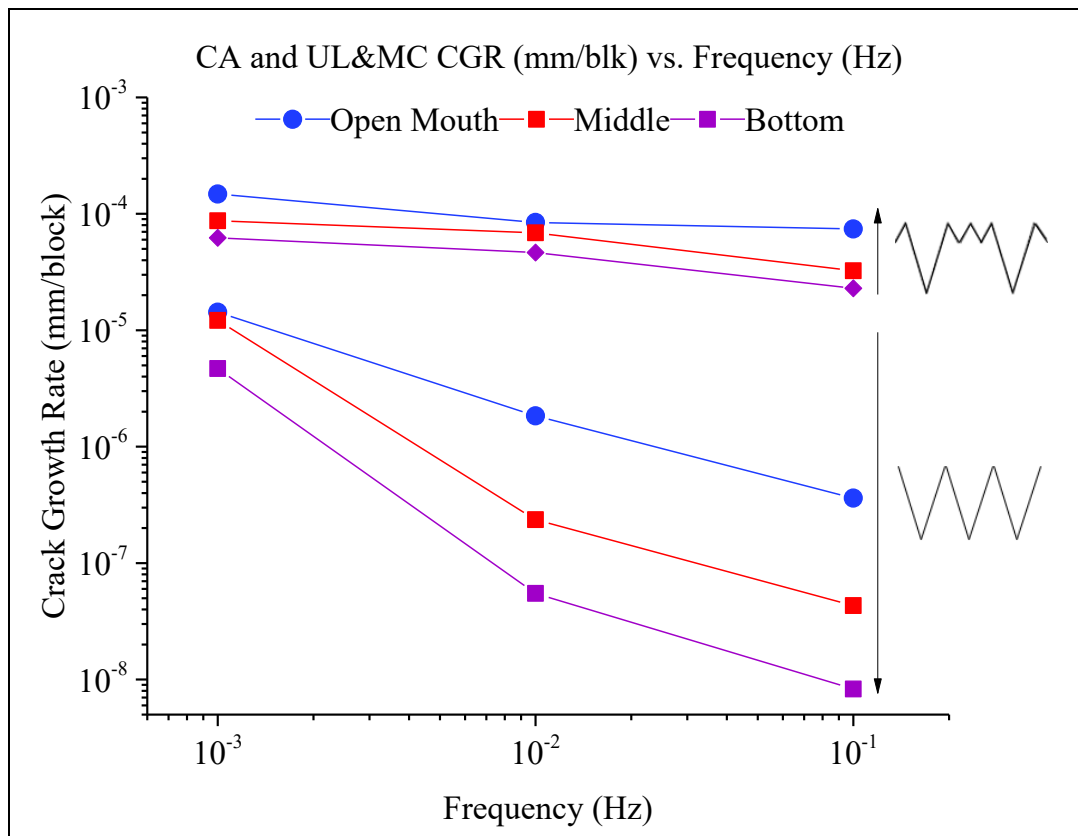


Figure 4.2 Crack growth rates (dc/dN) of CA and UL&MC waveforms for the OM, Middle, and Bottom cracks in Test I as a function of load frequency (Hz).

4.1.1.2 Test II

The net surface growth ($\Delta 2c$) and crack growth rates of the two waveforms tested in C2 solution in Test II are summarized in **Table 4.2**. Unfortunately, owing to a poor potential lead connection, the DCPD data at the OM was not used in order to avoid an erroneous representation of its growth. Further yet, portions of data from the Middle and Bottom cracks were omitted because of the issues at the OM, which eventually lead to an error in the potential drop system which required several days to test and repair just after the UL&H waveform began. Therefore, the growth rate data presented in **Table 4.2** for the OM was determined using the DCPD data of the Middle crack with the measured net growth at the OM, $136.1\mu\text{m}$, to provide approximate OM's growth rates. Similar

to Test I, the growth in-air is not shown for the surface because no measurable growth was detected on the surface after testing in air.

Table 4.2 Summary of calculated surface crack growth data for Test II for both waveforms in C2 solution. *The crack growth rates of the OM were determined using the Middle DCPD data.

Waveform		<i>Underload and Minor Cycles</i>	<i>Underload and Hold</i>
Frequency (Hz)	-	10^{-3}	10^{-3}
$\Delta 2c$ (μm)	OM	84.0	52.2
	M	35.1	21.8
	B	23.9	17.7
dc / dt (mm/s)	OM*	1.1×10^{-8}	7.1×10^{-8}
	M	4.4×10^{-9}	3.0×10^{-9}
	B	3.0×10^{-9}	2.4×10^{-9}
dc / dN (mm/blk)	OM*	2.3×10^{-4}	1.4×10^{-4}
	M	9.7×10^{-5}	5.9×10^{-5}
	B	6.6×10^{-6}	4.8×10^{-5}

Based on the measured net growth data, it is clear that the OM grew significantly more than the other two locations, more than doubling the growth at the Middle, while the Middle grew at a rate only slightly higher than the Bottom crack (**Figure 4.3**). The total net surface growth trends across the disbondment demonstrated by Test II are in agreement with those of Test I; crack growth decreased from the OM to the Bottom location, in spite of approximately equal stress intensity factor values at all locations and the same initial environment. Furthermore, the ratio of growth between the two waveforms (UL&MC to UL&H) decreased from 1.6 at the Middle crack to 1.4 at the Bottom.

It should be noted that no growth was expected at the surface in C2 solution for either test. First, an error in calculating the pretest stress intensity factors at the crack tips resulted in a significantly smaller K_{max} ($\sim 2/3$) during testing than the final value used during fatigue pre-cracking. This has

an effect of retarding crack growth, and will be discussed in great detail in Section 5.1.1. Second of all, a total lack of growth during CA loading in air lead to the belief that the former reason would prevent growth in C2 as well. Finally, based on the values presented in Section 3.3.1, the Combined Factor values of the tested mechanical conditions were less than half of the threshold value for continuous growth of long CT cracks in C2 solution; the threshold value indicates the value at which da/dN rapidly approaches zero.

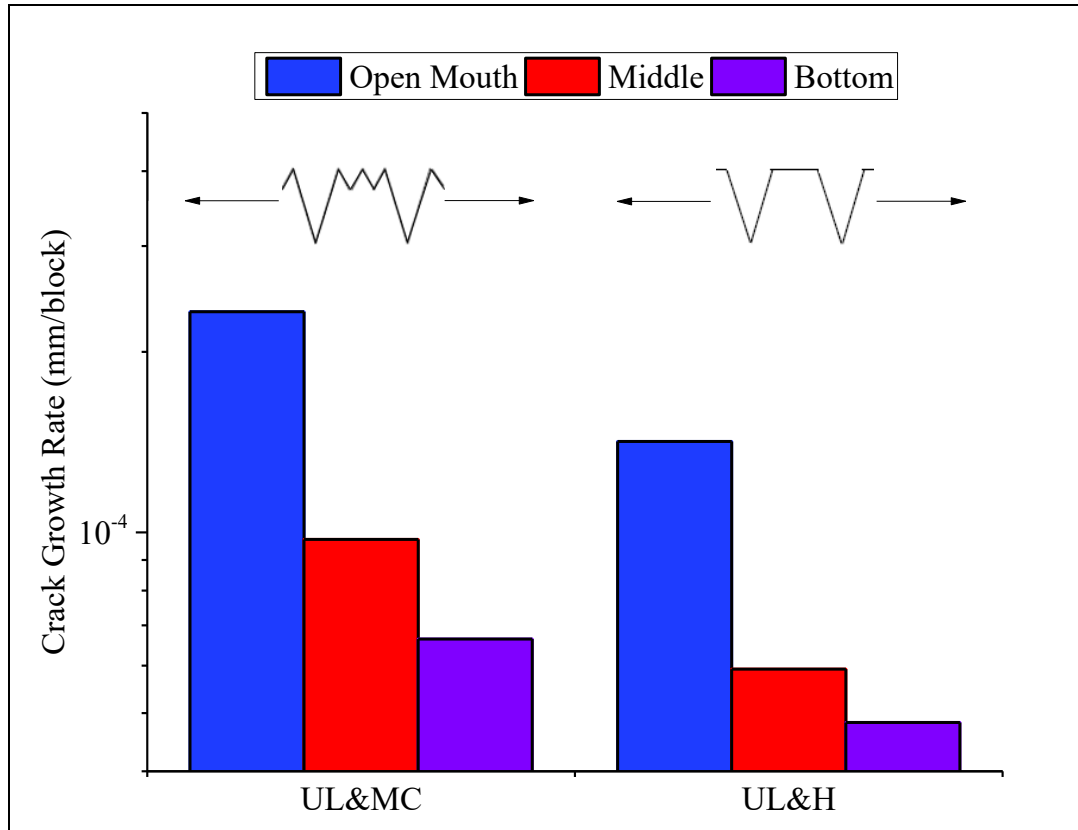


Figure 4.3 Histogram illustrating the growth rates of the OM, Middle, and Bottom crack locations of Test II for the two waveforms tested in C2 solution.

4.1.2 SURFACE MORPHOLOGY

High magnification images of replicas of the Bottom crack pretest crack tips of Test II are presented in **Figure 4.4**. As shown in **Figure 4.4**, prior to corrosion exposure the pretest crack tips were extremely narrow and sharp; this morphology occurred for all cracks used in testing. The remainder of the pretest crack images possessed the same morphology and are presented in Appendix B instead, along with more additional crack images.

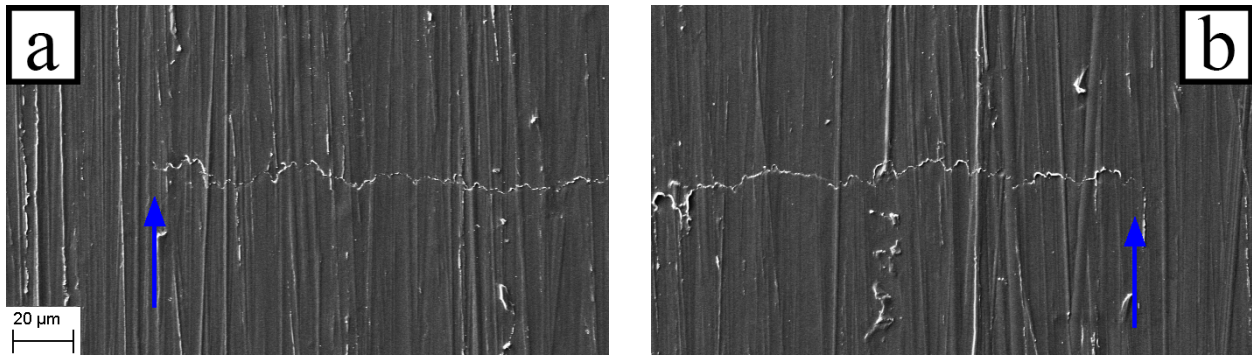


Figure 4.4 SEM SE images of Test II's pretest crack tips (replicas) for the Bottom crack. All cracks used in the study were similar to those above. The blues arrows indicate the crack tip locations.

4.1.2.1 Test I

The images in **Figure 4.5** demonstrate the significant near-surface dissolution that occurred on the cracks of Test I during exposure to C2 solution, which resulted in the formation of wide and shallow, or 'trough-like', crevices on the cracks' surfaces. The bulk material surrounding the wide crevice regions seemingly underwent more aggressive corrosion attack or selective dissolution than the surfaces away from the crack. Additionally, there were regions along the crack length that alternated with the trough-like crack crevices along the crack length, where the crack crevices were significantly thinner in comparison to the trough-like crevices. At the thin crevice locations, the corrosion attack of the material was comparatively benign and the abrasive scratches from pretest grinding were still distinguishable, such as the locations indicated by the red arrows in **Figure 4.6**. While corrosion products were visible inside of the cracks in the wide crevice regions, no corrosion products were found along the thin crevice regions or the bulk sample surface. Attempts at characterizing the compositions of the two regions using EDS produced no conclusive results that would indicate differences in composition between the two alternating crevice regions.

Further analysis of the post-test images presented in **Figure 4.5** revealed that the average crevice widths of the trough-like and thin regions increases from the OM (30 μm and 2.4 μm) to the Bottom (38.4 μm and 3.2 μm) crack locations. Also, the apparent depth of the trough decreases from the OM to Bottom locations. Similarly, the width of the cracks and in the regions of weak corrosion increase from the OM to bottom cracks. However, on the macroscopic level the general surface dissolution away from the cracks decreased from the OM to the Bottom crack locations (**Figure 4.7**).

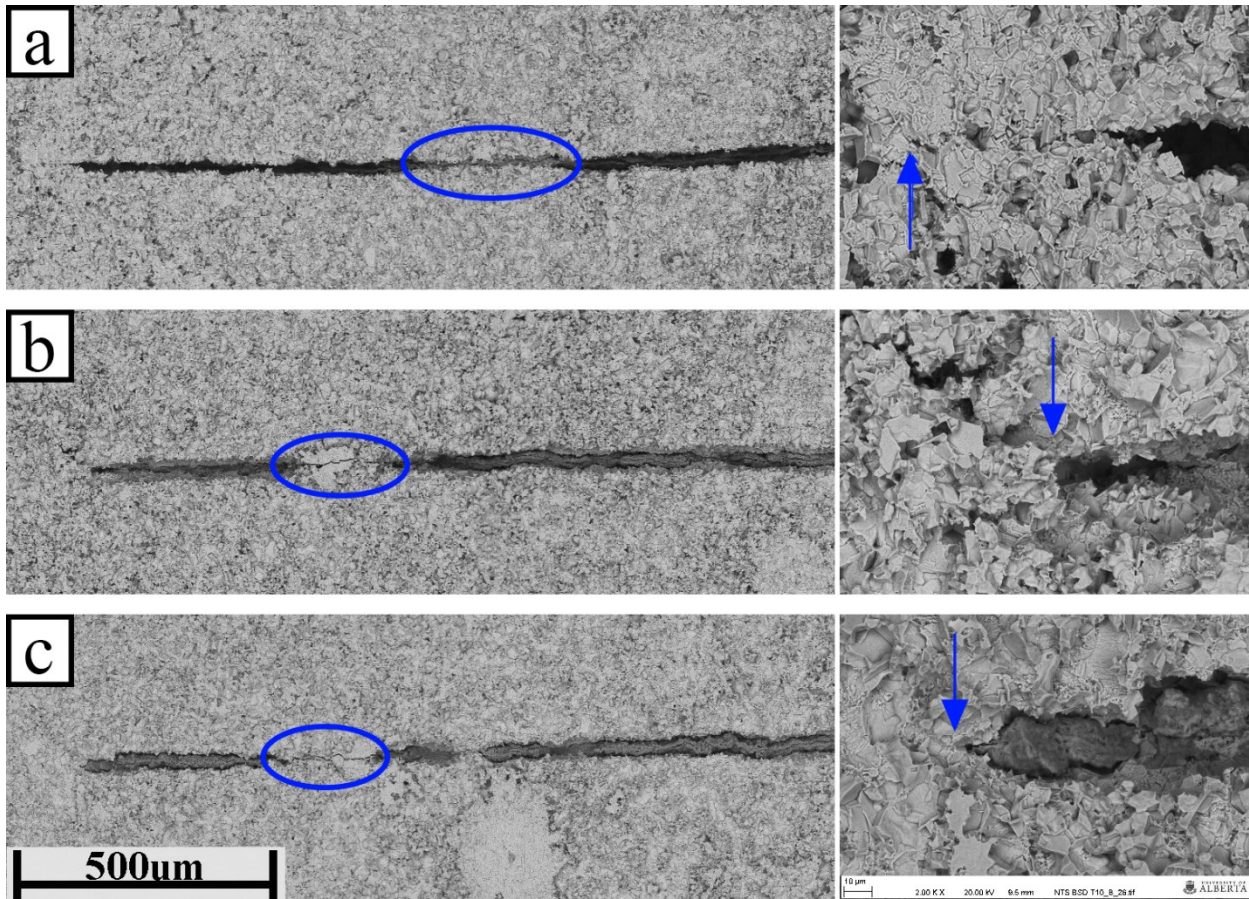


Figure 4.5 Low (left) and high (right) magnification BSE post-test SEM images of Test I, where (a), (b), and (c) are the cracks at the Open Mouth, Middle, and Bottom disbondment locations. The blue arrows indicate the crack tip locations, while the blue ovals encircle the thin crack crevice regions.

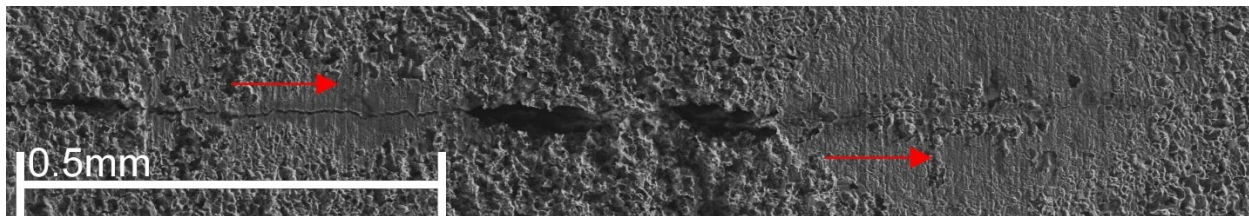


Figure 4.6 SE post-test images of the OM crack in Test I's, with red arrows indicating the locations where pretest scratches from abrasive grinding are still visible within areas surrounding thin crack crevice locations.

The crack tips (**Figure 4.5a**) on the OM surface were sharp and narrow in morphology and strikingly different from the blunted morphologies of the Middle and Bottom cracks. This can be attributed to the higher crack growth rate experienced at the OM (**Table 4.1**) exceeding the local dissolution rate. This morphology at the OM was no longer present after mechanical removal of the corroded surface and subsequent polishing on the surface, as demonstrated in **Figure 4.8a-b**,

and therefore the morphology must have been limited to a small fraction of the sample thickness. However, an SEM image of the surface after an intermediate polishing step revealed that micro-cracks formed on the surface in the region in front of the crack tips (**Figure 4.9**). These micro-cracks were only found within the plastic zone of the OM crack, and disappeared alongside the sharp crack tip morphology with further mechanical polishing.

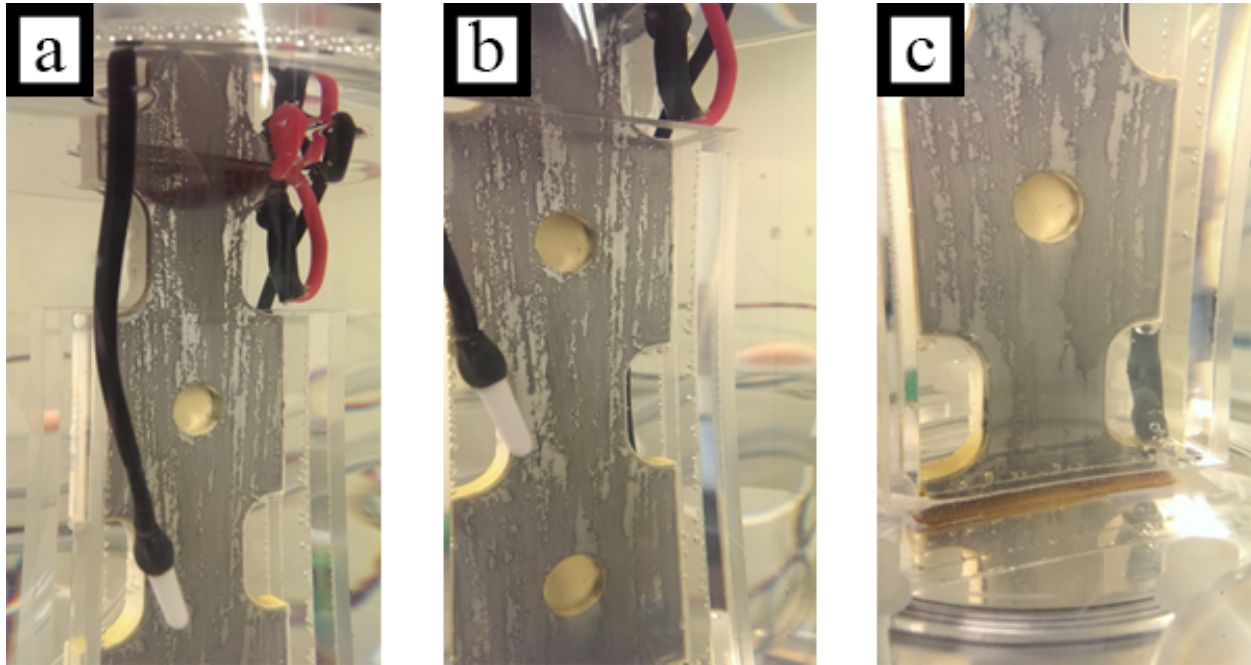


Figure 4.7 Images of the bulk surface corrosion at the (a) OM, (b) Middle, and (c) Bottom crack regions in Test I after seven days of exposure to C2 solution. The dark grey areas are locations of dissolution.

Figure 4.8c-f show the crack tip morphologies of the Middle and Bottom cracks. Both cracks demonstrated blunted balloon- or spearhead-like crack tip morphologies. At the bottom of the trough-like morphology, thin crevices just prior to the balloon-like cracks could be seen and were determined to be the approximate pretest crack tip locations. In fact, unless sharp, thin cracks have been occluded by the dissolved material and corrosion products at these locations both the middle and bottom cracks cannot technically be considered to be cracks, according to fundamental fracture mechanics principles. The blunted morphology is a visual indicator that the rates of crack propagation at the Middle and Bottom locations did not sufficiently exceed their local dissolution rates to prevent dissolution at the crack tips. In spite of the odd morphologies, all cracks appeared to have propagated transgranularly upon inspection of the etched surfaces (**Figure 4.10**).

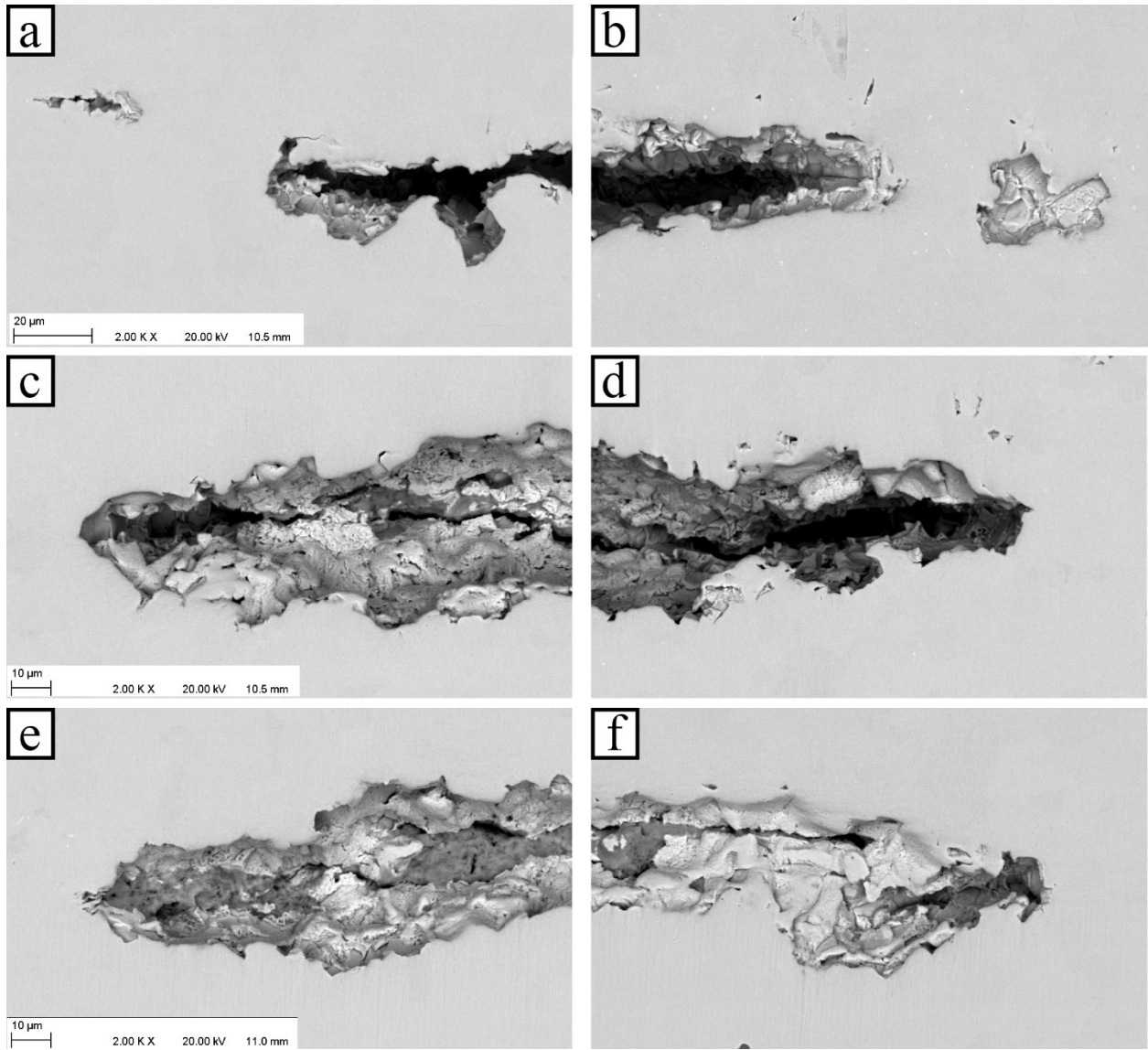


Figure 4.8 SEM BSE high magnification images of Test I's polished crack tips where (a,b), (c,d), and (e,f) are the OM, Middle, and Bottom cracks, respectively.

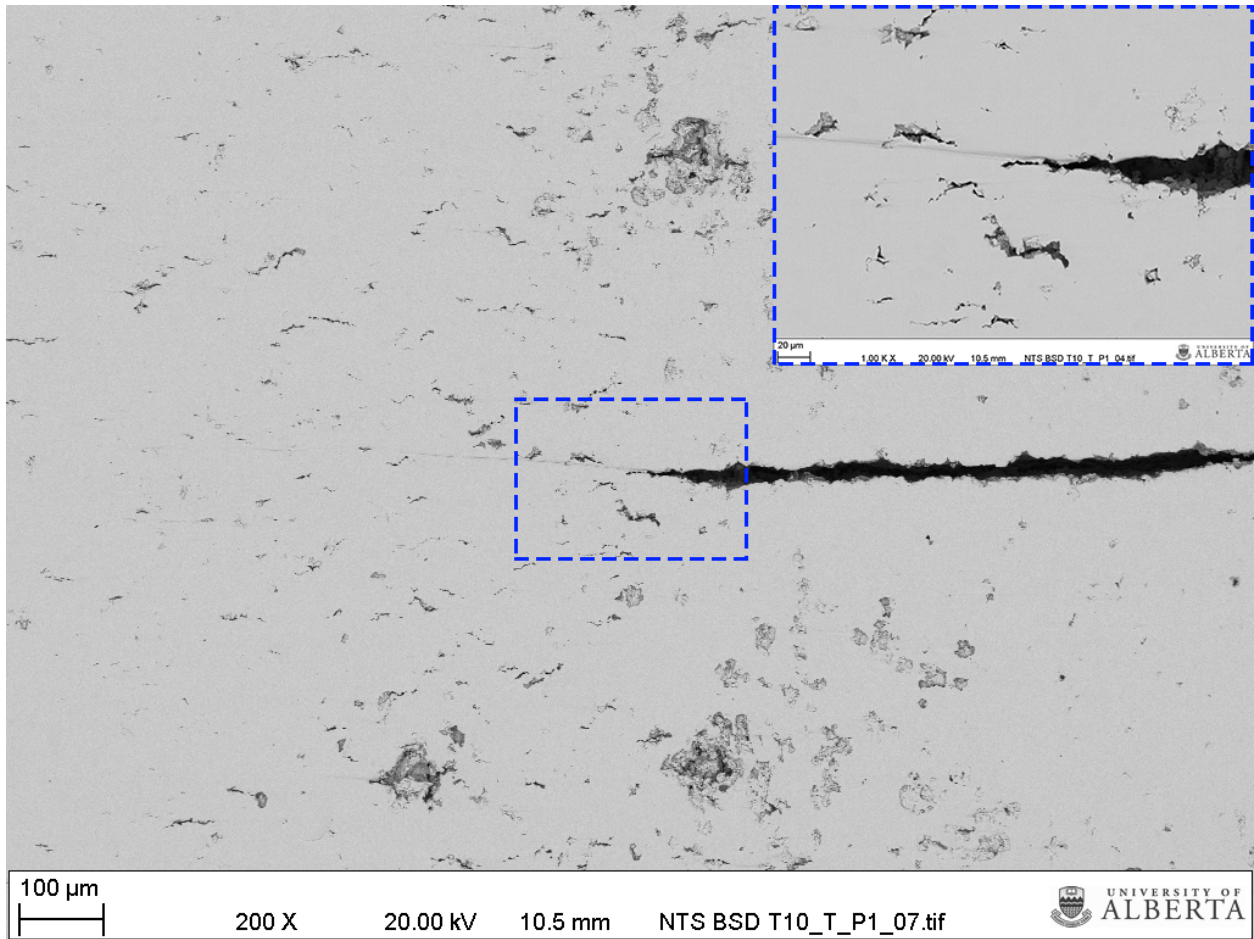


Figure 4.9 BSE image of Test I's OM crack tip after an intermediate (6 μm) polish showing a large amount of micro-cracks in the region ahead of the crack tip.

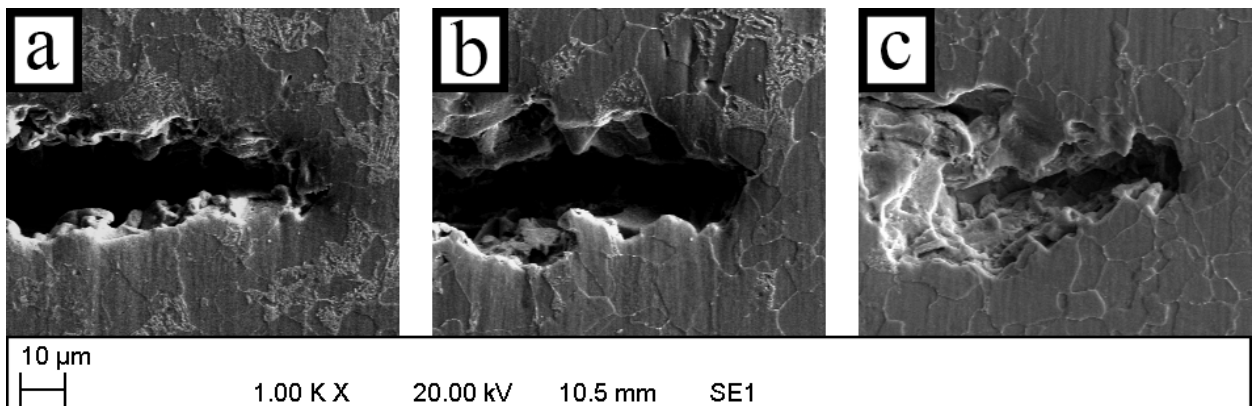


Figure 4.10 SE SEM images of the etched crack tips of Test I demonstrating the transgranular crack paths at the (a) OM, (b) Middle, and (c) Bottom crack locations.

4.1.2.2 Test II

Similar to Test I, the pretest cracks were narrow and sharp prior to being exposed to the corrosive environment and suffered from corrosion attack across the steel and crack surfaces indicated by the surface topography and widened crack crevices, as shown on the left hand side of **Figure 4.11**. Unlike Test I, there were no thin crevice features at the bottom of the trough-like, near surface dissolution locations for all three cracks. Instead, the crack walls are lined with thin corrosion product and relatively wide crack openings can be seen up to a small distance from the crack tips, e.g. **Figure 4.12c-d**. Additionally, regions near the crack of minimal corrosion attack were present but no thin crack crevices along the cracks in those regions were visible. Otherwise, the crack tips of Test II were quite similar to those of Test I, with the exception of one of the OM's crack tips.

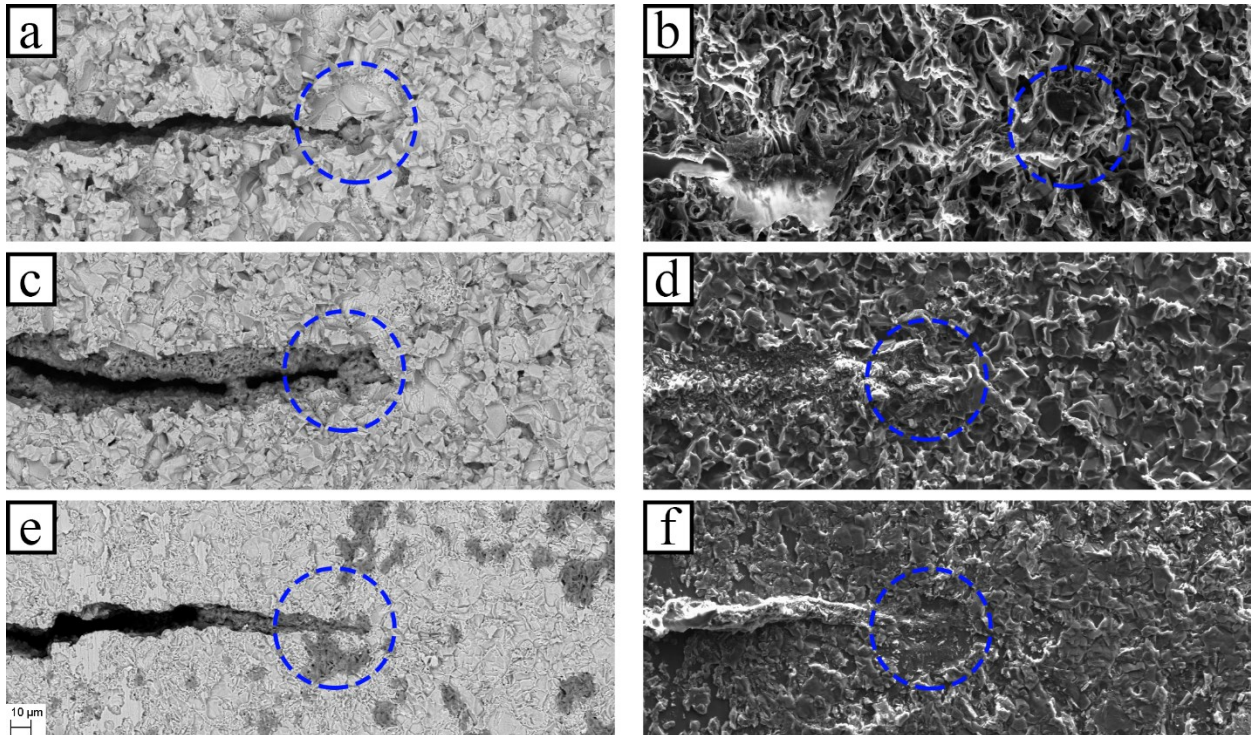


Figure 4.11 Comparison of SEM images of Test II's post-test crack tips, where (a,b), (c,d), and (e,f) are the OM, Middle, and Bottom cracks. The BSE images on the left (a,c,e) are the real crack tips after hydrostatic testing and the SE images on the right (b,d,f) are replicas before hydrostatic testing with the blue circles indicating the crack tip regions.

The crack widening can be attributed to the execution of hydrostatic testing on the sample after the cyclic waveforms had been performed, resulting in greater plastic deformation ahead of the crack tips and the opening of the cracks. Based on a comparison of replicas of the cracks before

and real cracks after hydrostatic testing there was no obvious growth or changes in crack tip morphology (**Figure 4.11**). Additionally, it was observed that in some locations along the replicas of the cracks, where the cellulose acetate could penetrate deep enough, that the same thin crack features as Test I were present prior to the hydrostatic test. Therefore, the cause of the widening occurred from a location other than the surface of the cracks.

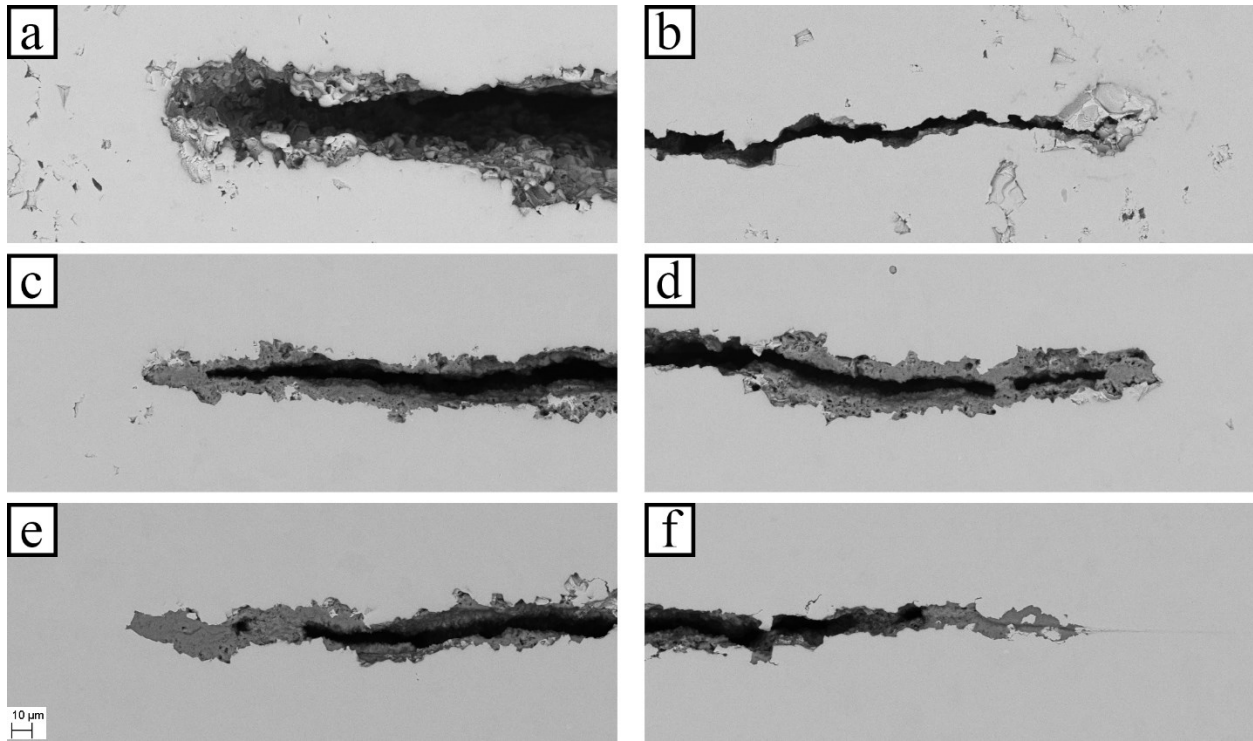


Figure 4.12 SEM BSE high magnification images of Test II's polished crack tips where (a,b), (c,d), and (e,f) are the OM, Middle, and Bottom cracks, respectively.

4.2 DEPTH MORPHOLOGY

Low magnification images of the cross-sectioned cracks' depth profiles for both tests are presented in **Figure 4.13**. As stated in Section 3.5.2.3, Test I's cracks were cross-sectioned at the first transition from the thin- to wide-crevice regions hence the significant differences in the length of the depth profiles seen in **Figure 4.13a-c**. The differences between the two tests were visually evident, where the depth profiles of Test I possessed thin crack morphologies filled with corrosion product and the profiles of Test II were wide and relatively free of corrosion product, except along the crack walls. It can be speculated that, based on EDS analysis, that the corrosion products inside of the cracks of Test I were either FeCO_3 or Fe_2O_3 based on atomic compositions (**Table 4.3**) and

stoichiometry with an example profile provided in Fig. Although EDS is generally poor for carbon detection, the bulk material was excluded in the EDS scans and a low-contamination, brand-new FESEM with an air-lock loading chamber was used to perform the scans. Other attempts at characterizing the corrosion products either in the depth profile or on the fracture surfaces of the cracks failed to provide any useful information.

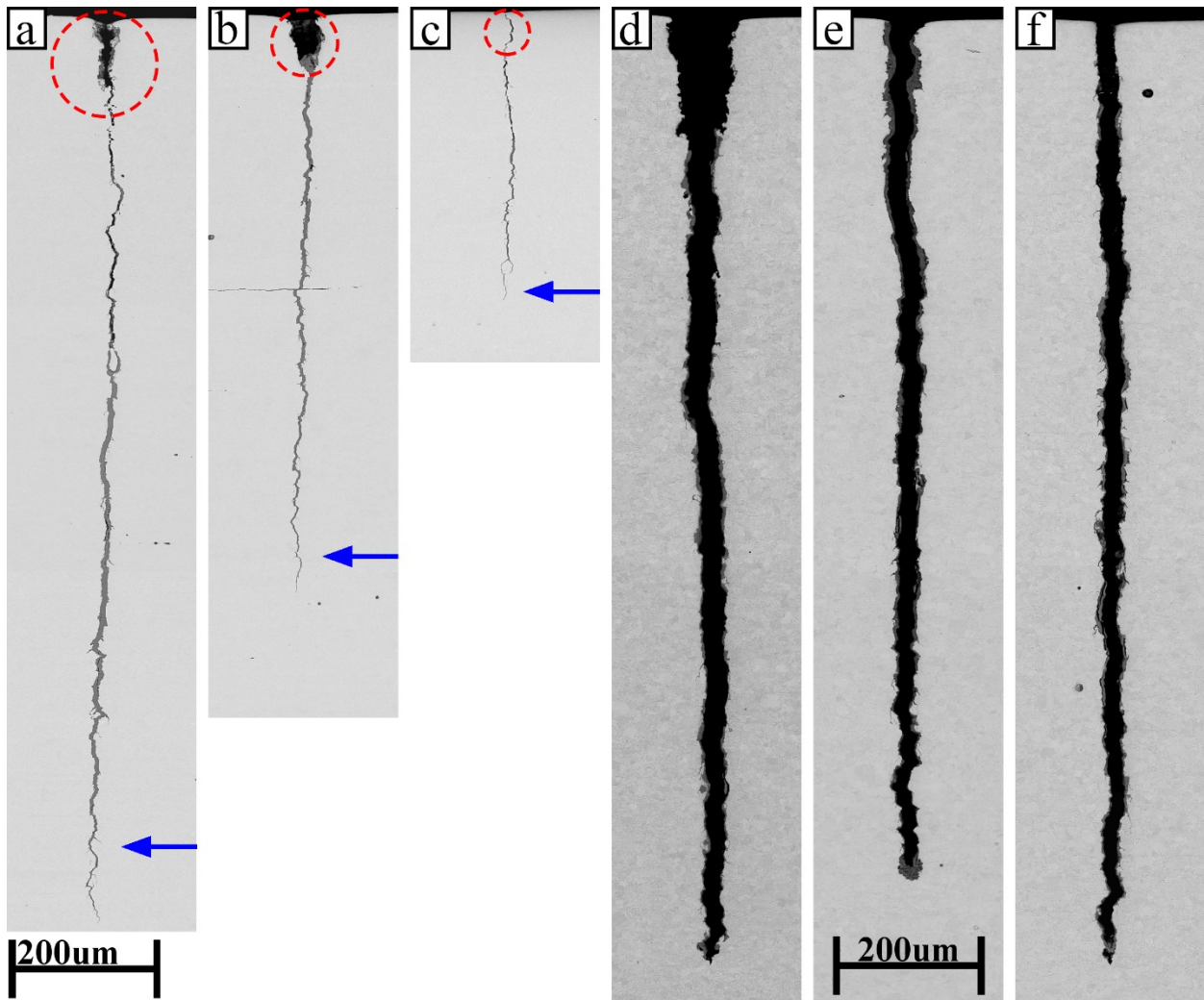


Figure 4.13 Low magnification images of Test I (a-c) and Test II's (d-f) crack depth profiles, where (a&d), (b&e), and (c&f) are the cracks at the OM, Middle, and Bottom cracks, respectively. Arrows indicate the approximate pretest crack locations and red circles highlight the near surface dissolution regions.

The arrows in **Figure 4.13a-c** show the approximate pretest crack tip locations, estimated based on the surface growth and crack morphology. Visual inspection of **Figure 4.13** and **Figure 4.15** revealed that the cracks of Test I remained sharp in the depth direction and propagated transgranularly. In **Figure 4.15a-c**, the crack widening 100 μm behind the crack tips decreased

from the OM to the Bottom cracks. Magnified images of the crack tips regions in **Figure 4.15a-c** show that the secondary cracks branching off from main cracks in the depth profiles propagated transgranularly, not intergranularly, which indicates that the secondary cracks did not grow by dissolution of the microstructure or grain boundaries.

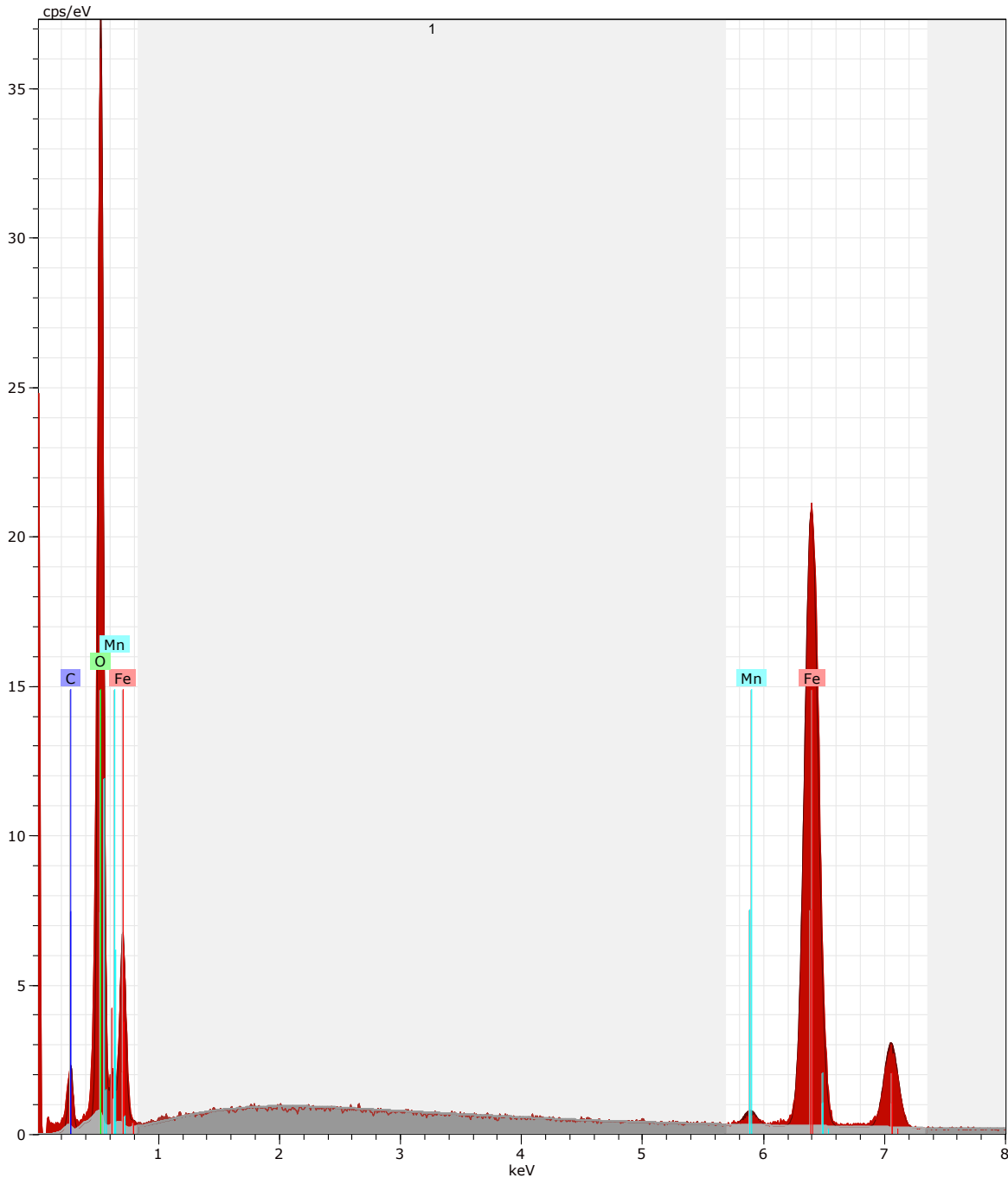


Figure 4.14 EDS profile obtained using an area scan on the corrosion products wedged inside of Test I's Bottom crack along its depth profile.

Table 4.3 Summary of the elemental compositions (at. %), determined through EDS, of the corrosion products along the crack depth profiles of Test I.

Crack Location	Distance from the Coating OM (mm)	Element (at. %)			
		Fe	O	C	Mn
Open Mouth	-10	35.6	52.0	11.7	0.7
Middle	65	29.2	56.9	13.3	0.6
Bottom	140	31.6	54.8	12.9	0.7

The differences between the near surface morphologies, i.e. the first 1/10 of the depth lengths, in **Figure 4.13a-c** are partially because of the locations of the profile cuts along the surfaces of the cracks. The profile cuts were located at a wide- to thin-crevice transition, a wide-crevice region, and a thin crevice region on the surfaces of Test I's OM, Middle, and Bottom cracks, respectively. Furthermore, the last 2/3 of crack depths of Test I, with the exception of the Middle crack, were compacted with corrosion products and little evidence of crack wall dissolution was present. With the exception of the first 1/10 of the OM where enhanced dissolution occurred, the regions which are compacted with corrosion products along the depth profiles of the OM and Bottom cracks in **Figure 4.13a** and **Figure 4.13c** have wider crevices than the regions which lack corrosion product.

The depth profiles of Test II were similar to the surface profiles where it appeared that significant widening occurred as a result of damage from the hydrostatic test. Surprisingly, in spite of tensile loads exceeding 100 % SMYS during the hydrostatic test the OM (**Figure 4.15a**) and Bottom (**Figure 4.15c**) crack tips were not overly blunt and were instead wedge shaped in morphology, while a small sharp crack tip can be seen coming out from the blunted morphology of the Middle crack in **Figure 4.15b**. Furthermore, the thickness of the corrosion products that lined the side walls of Test II's depth profiles were generally greater in width to the crack widths of Test I, except for at the crack tips of Test II.

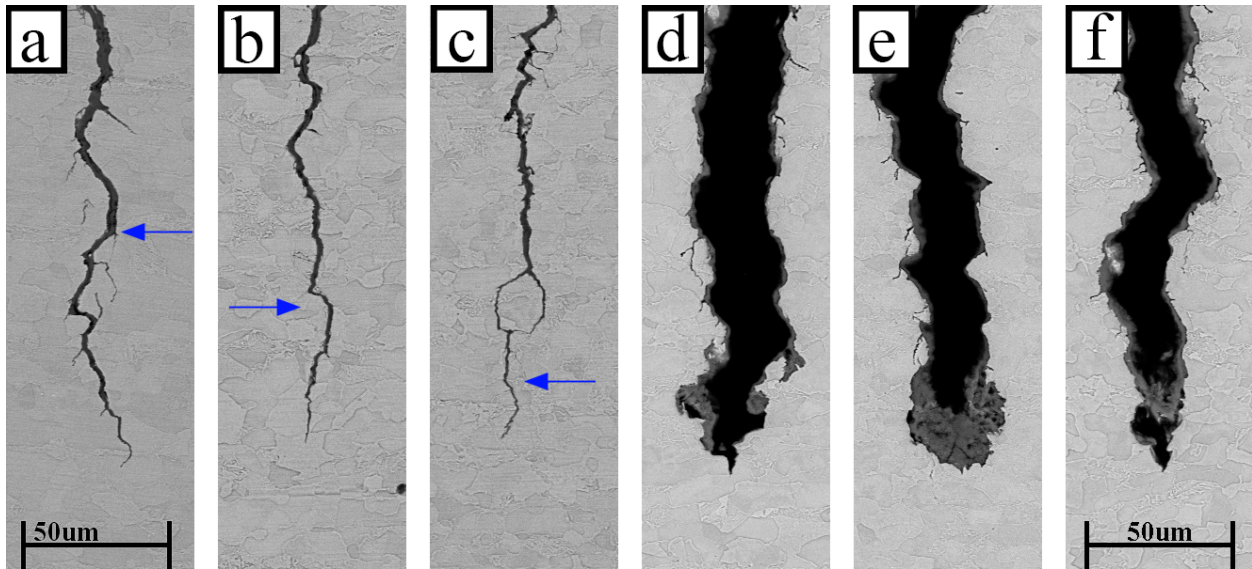


Figure 4.15 High magnification images of Test I (a-c) and Test II's (d-f) crack depth profiles, where (a&d), (b&e), and (c&f) are the cracks at the OM, Middle, and Bottom cracks, respectively. Arrows indicate the approximate pretest crack locations.

4.3 FRACTURE SURFACE CHARACTERIZATION

4.3.1 GROWTH BAND MEASUREMENTS

The low magnification BSE SEM images of Test I's cracks fracture surfaces are presented in **Figure 4.16**. The low magnification features of Test II were similar to those presented for Test I. The final aspect ratios of the OM, Middle, and Bottom were 0.21, 0.21, and 0.17 for Test I and 0.23, 0.21, and 0.19 for Test II, respectively. Additional fracture surface images from both Tests may be found in Appendix B.

The start of the test regions, or growth bands, in-air and C2 are marked by green and blue lines in the low magnification BSE images presented in **Figure 4.16**. The width of the bands was determined by measuring visibly different regions of morphology along the fracture surfaces near the cleavage walls. Measurements were performed using high magnification SE FESEM images, with examples shown in **Figure 4.17**. Two common locations on the fracture surface were used for the measurements; the first was at the bottom-most portion (depth) of the crack and the second at the 'midpoint' along the cleavage wall between the surface and depth crack tips. In **Figure 4.17**, the spacing between the inserted lines represent the averaged measurements of the depth growth

bands of both tests. The averaged midpoint and depth band widths for all of the cracks in Tests I and II are summarized in **Table 4.4**.

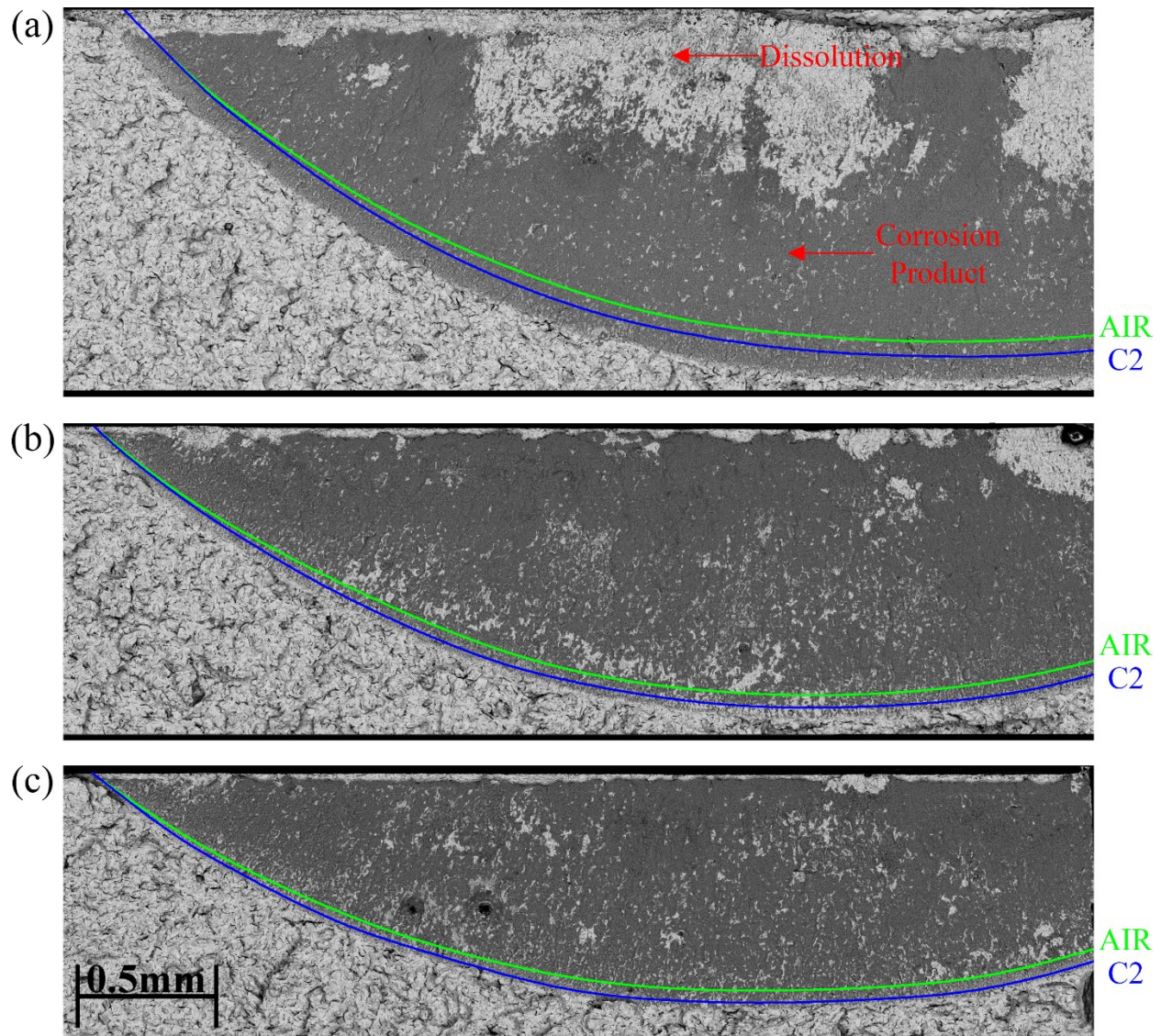


Figure 4.16 Low magnification BSE images of Test I's (a) OM, (b) Middle, and (c) Bottom crack fracture surfaces. The green and blue lines indicate the start of testing in air and C2 solution, respectively.

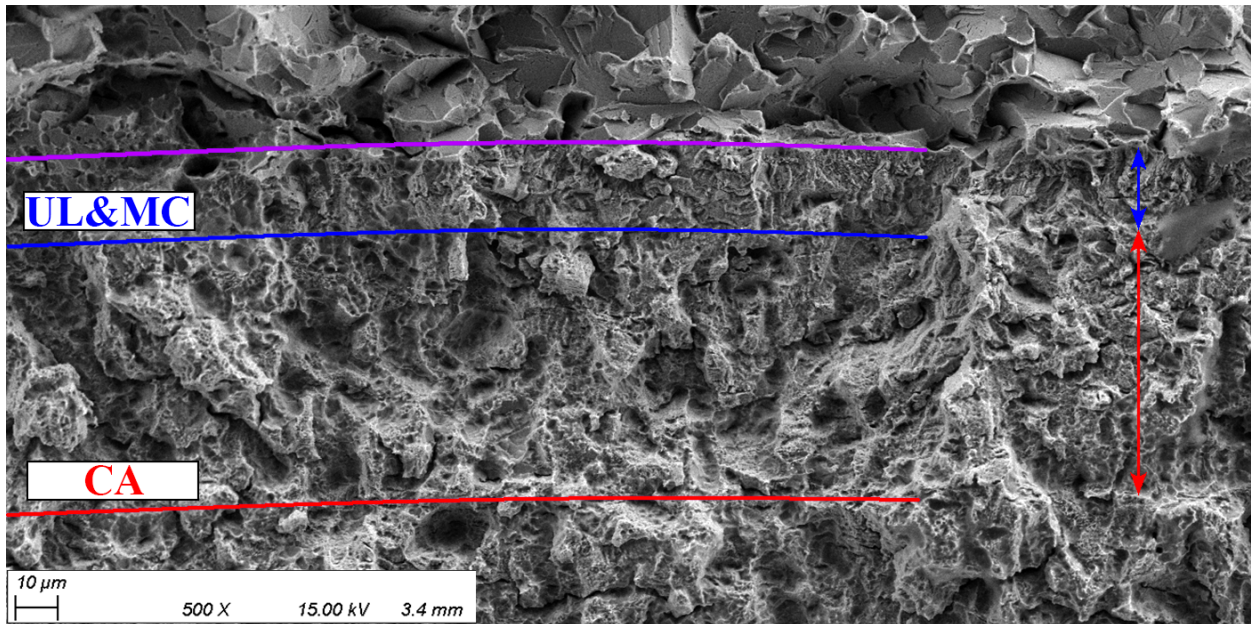
An issue, however, with the measurement technique is that similar waveforms, e.g. waveforms #2 – 4 and #5 – 7 of Test I, are difficult to differentiate – i.e., without clear morphologically different regions the measurements are largely dependent on user interpretation and subject to significant error and bias. Hence, the growth band measurements for Test I were tabulated as single, or summed, value per waveform type which included the total growth

contribution from all three frequencies for the two waveform types. Regardless, a comparison between half of the surface growth values (Δc) from **Table 4.1** and **Table 4.2** with the depth growth (Δa) in **Table 4.4** indicates that the crack depth grew less than the surface at the OM, equal to the surface at the Middle, and more than the surface at the Bottom crack locations in both tests.

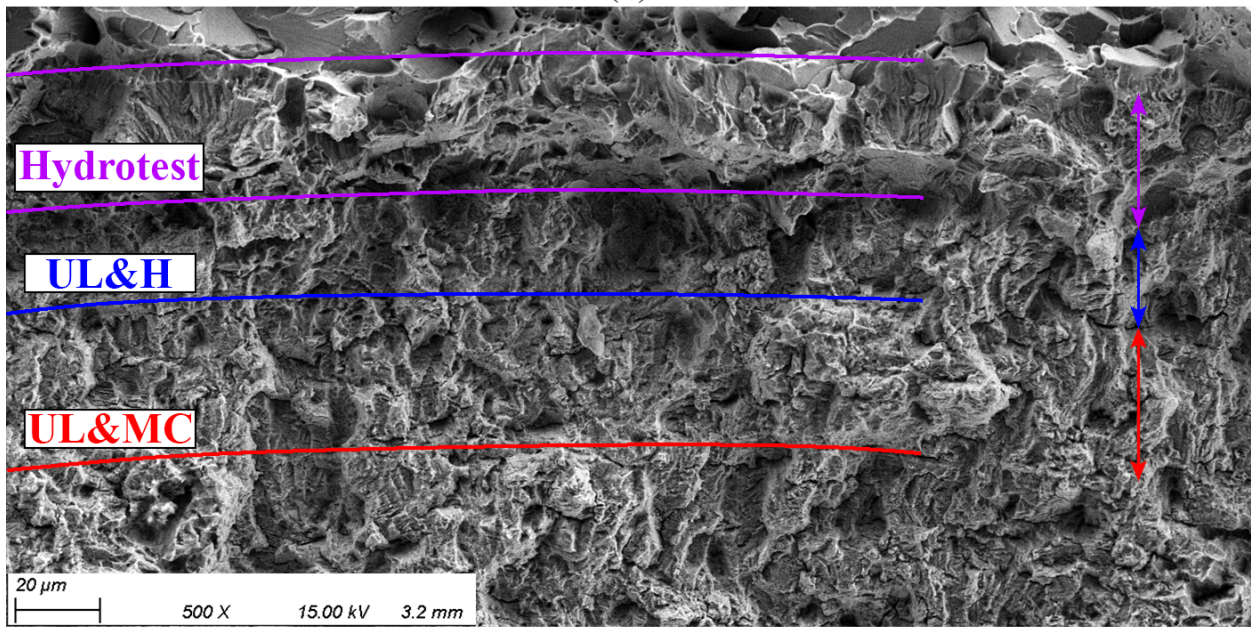
As stated previously in Section 4.1.1, no measurable growth was detected on the crack surfaces while under CA loading in air, but clear regions indicating crack growth on the fracture surfaces were present in the depth direction of the cracks. Unlike CA loading in C2 solution, only minor differences between the growth rates in air were determined for the two frequencies tested at 80 % SMYS (WF#1 Test I and WF#2 Test II). The minor variations in growth were most likely a result of different crack dimensions, stress intensity factors, and variations in local microstructures.

4.3.2 CORROSION CHARACTERISTICS

A dominating feature of the crack fracture surfaces was the corrosion along the fracture surface (**Figure 4.16**). A form of corrosion deposit, previously identified as potential mixture of FeCO_3 , FeOH , and Fe_2O_3 in Section 4.2, was visible across the majority of the surface. Bare metal surfaces, a result of crack wall dissolution, occurred along the top of the fracture surfaces with regions where dissolution of the fracture surface walls proceeded noticeably further into the depth of the cracks. The locations where a greater area of dissolution occurred on the fracture surface were determined to be the locations of weaker corrosion attack and thin crack-crevices along the surface profiles (**Figure 4.5**) – i.e., the trough-like regions seen along the surface profiles are the locations where dissolution into the crack depth occurred to a lesser extent along the fracture surfaces. Furthermore, the general penetration of dissolution attack into the depth direction decreased from the OM to the Bottom crack. The same trends occurred on the fracture surfaces of Test II as those discussed above for Test I.



(a)



(b)

Figure 4.17 SE FESEM images demonstrating growth band measurements in the depth on the fracture surfaces of the OM from (a) Test I and (b) Test II. The cracks had their corrosion products removed prior to imaging.

Table 4.4 Net growth (Δa) and crack growth rates (da/dN) of Tests I and II determined by fracture surface growth band measurements at the depth and midway point locations for each crack.

Test No.	Waveform Type	Crack Location	Δa (μm)		da / dN (mm/blk)	
			Mid	Depth	Mid	Depth
Test I	WF #1 CA (air)	OM	46.9	58.5	6.6×10^{-6}	8.3×10^{-6}
		M	39.8	52.1	5.6×10^{-6}	7.4×10^{-6}
		B	42.0	51.5	5.9×10^{-6}	7.3×10^{-6}
	WF #2 - 4 CA (C2)	OM	68.5	69.2	-	-
		M	29.4	30.1	-	-
		B	12.3	12.8	-	-
	WF #5 - 7 UL&MC	OM	18.3	18.4	-	-
		M	11.9	11.7	-	-
		B	8.8	10.1	-	-
	Test II	WF #1 CA (air)	OM	62.9	94.4	1.7×10^{-6}
M			63.0	113.2	1.8×10^{-6}	3.1×10^{-6}
B			70.0	107.8	1.9×10^{-6}	3.0×10^{-6}
WF #2 CA (air)		OM	74.4	107.2	4.4×10^{-6}	6.3×10^{-6}
		M	82.4	115.7	4.9×10^{-6}	6.8×10^{-6}
		B	79.0	114.2	4.7×10^{-6}	6.7×10^{-6}
WF #3 UL&H		OM	24.8	23.4	1.3×10^{-4}	1.3×10^{-4}
		M	11.3	11.0	6.1×10^{-5}	6.0×10^{-5}
		B	8.4	9.2	4.6×10^{-5}	5.0×10^{-5}
WF #4 UL&MC		OM	37.9	41.4	2.1×10^{-4}	2.3×10^{-4}
		M	17.6	17.9	1.0×10^{-4}	1.0×10^{-4}
		B	13.1	14.4	7.3×10^{-5}	8.0×10^{-5}
Hydrostatic Testing		OM	30.7	35	-	-
		M	12.6	23.2	-	-
		B	12.6	17.5	-	-

4.3.3 MICROSCOPIC FEATURES

4.3.3.1 Striations

The average crack growth rates determined by measuring striations along the fracture surfaces of Tests I and II are summarized in **Table 4.5**. Growth rates were determined by measuring the striations' interspatial distances using a line intercept method and dividing total distance by the number of visible striations. The perpendicular distance from the cleavage wall to the striations' locations were noted to assist in the identification of which waveforms striations belonged to, if it was not clear. No striations were located for the CA waveforms of Test I, likely because they were generally obscured by corrosion products and their small widths and interspacing. Further yet, striations of the UL&MC waveforms were only differentiable based on their interspacing and crack wall distances, and no clear mini-striations were observed (**Figure 4.18**). The latter could have been the result of corrosion – either the features were dissolved or obscured by corrosion products – or it was possible that the minor cycles did not directly contribute to crack growth through fatigue damage.

Table 4.5 Summary of average crack growth rates (da/dN) determined by striation measurements.

Frequency (Hz)	Crack Location	<i>Underload and Minor Cycles</i> da / dN (mm/blk)			<i>Underload and Hold</i> da / dN (mm/blk)
		10^{-3}	10^{-2}	10^{-1}	10^{-3}
Test I	OM	2.9×10^{-4}	2.3×10^{-4}	1.9×10^{-4}	-
	M	1.1×10^{-4}	7.8×10^{-5}	4.8×10^{-5}	-
	B	5.8×10^{-5}	4.2×10^{-5}	3.3×10^{-5}	-
Test II	OM	2.8×10^{-4}	-	-	1.4×10^{-4}
	M	1.6×10^{-4}	-	-	6.8×10^{-5}
	B	9.4×10^{-5}	-	-	6.6×10^{-5}

Similar to Test I, no CA striations were observed in Test II, however striations from the VA waveforms were easily located. Care was taken to only measure striations where the test growth

region under VA loading was clearly differentiable from the damage of the hydrostatic test. Additionally, attempts were made to either locate multiple sets of striations within close proximity to clearly define UL&MC and UL&H damage, or directly within a line such as those in **Figure 4.19c-d**. There were no markings that could be definitively identified as mini-striations observed for the UL&MC waveform of Test II, and the striations generated by the two waveforms were similar in appearance. In general, for both tests, the growth rates determined by striations were greater than those by other physical features, however this was to be expected because not every fatigue cycle generates a striation.

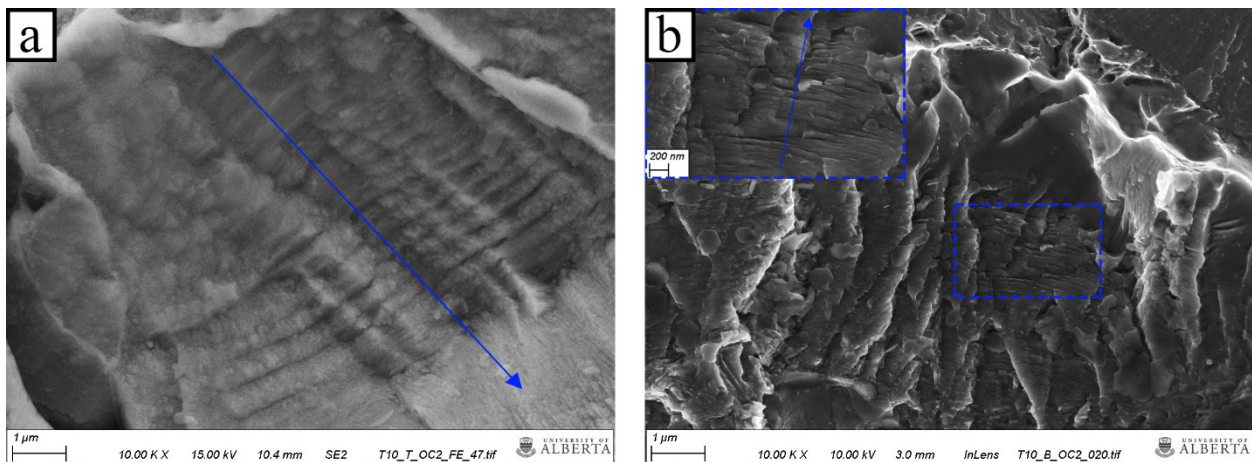


Figure 4.18 Striations from UL&MC waveforms on the fracture surfaces of Test I's (a) OM for $f = 10^{-3}$ Hz and (b) Bottom cracks for $f = 10^{-2}$ Hz. Blue arrows indicate the crack propagation direction.

4.3.3.2 Hydrogen Damage

For all cracks in the study, sub-micron cavities and protrusions decorated the post-test cleavage, typically within several grains from the crack front (**Figure 4.20a-b**). The sub-micron markings often accompanied micro-cracks (**Figure 4.20c-d**) and plastic deformation along grain boundaries (**Figure 4.20e-f**). These features were located on the fracture surfaces of both tests, and therefore cannot be attributed to a specific waveform or loading condition. Additionally, features which appeared to be slip lines were found on cleavage facets leading to grain boundaries where plastic deformation could be found (**Figure 4.20f**). Based on the location and characteristics of the features in **Figure 4.20** they can be attributed to hydrogen segregation and damage within the plastic zone(s) ahead of the crack fronts.

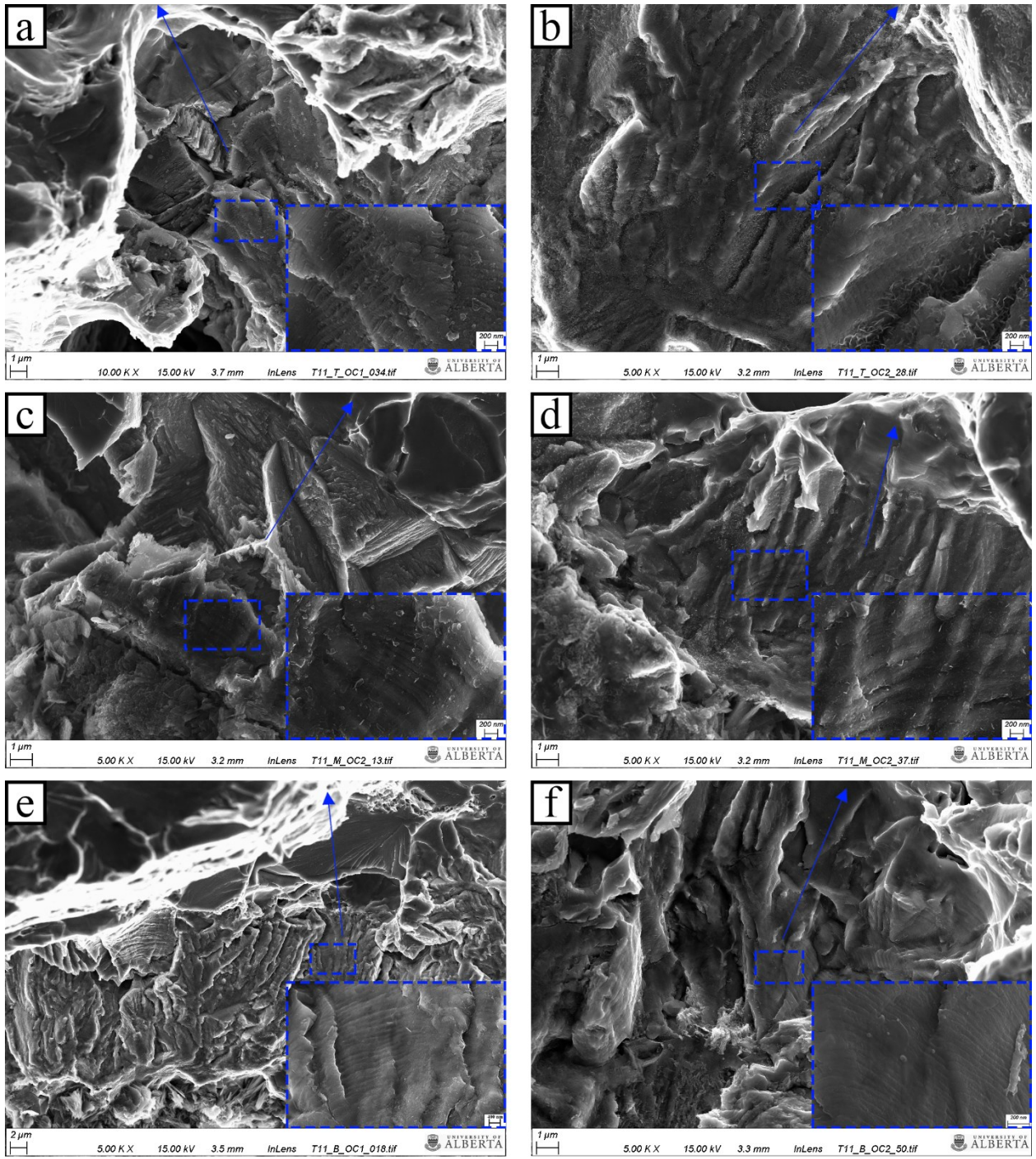


Figure 4.19 Striations generated by the UL&MC (a-d) and UL&H (c-d) waveforms in Test II on the (a,b) OM, (c,d) Middle, and (e,f) Bottom crack fracture surfaces.

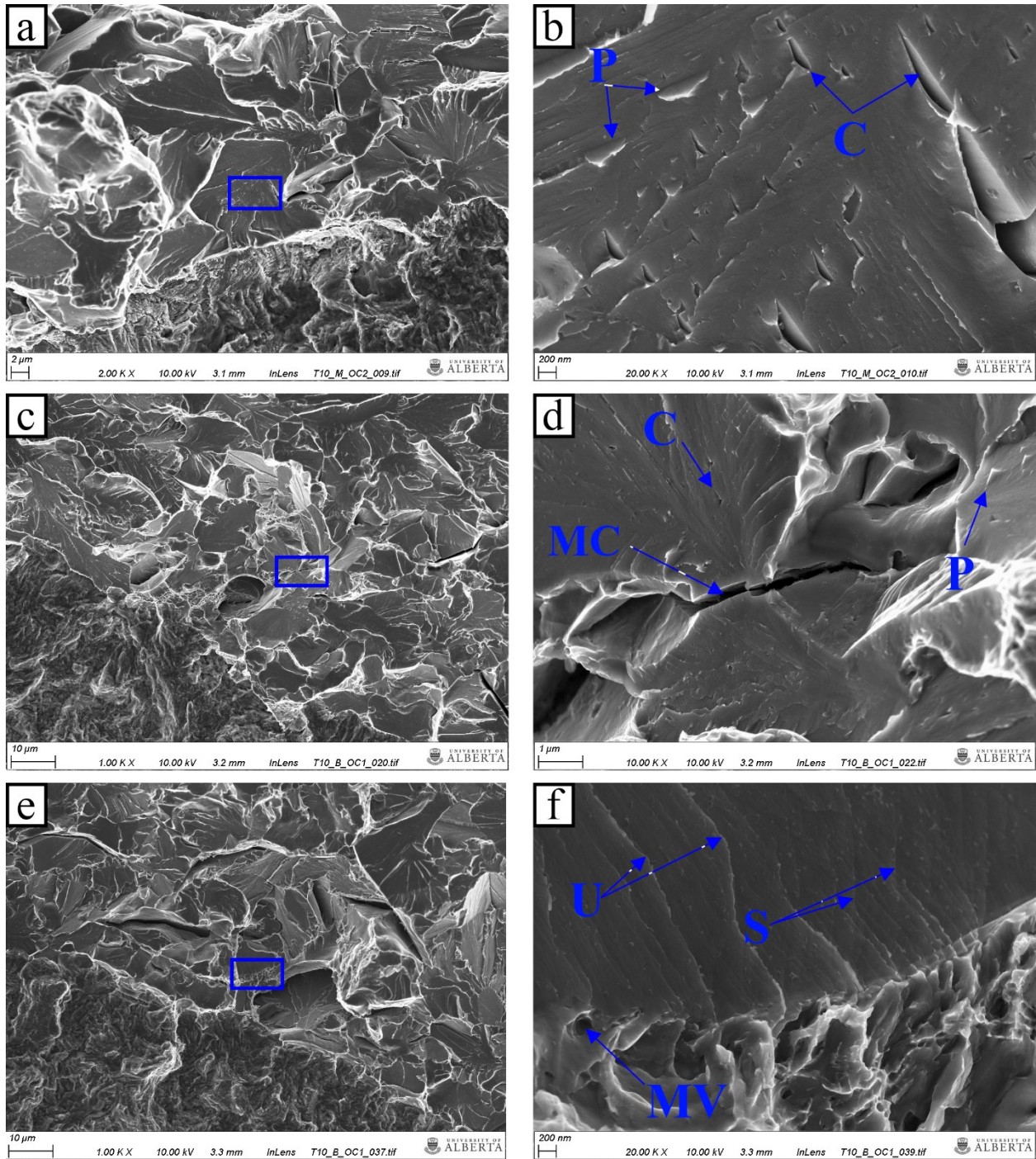


Figure 4.20 Low (left) and high (right) magnification in-lens FESEM fractography showing evidence of hydrogen-induced-cracking (HIC) within the cleavage plane of several cracks. The features on the right-hand side are located within the blue boxes on the left. Blue arrows indicate locations of key features: C (cavity), P (protrusion), MC (micro-crack), U (undulation), S (slip line), and MV (microvoid).

4.3.4 HYDROSTATIC TEST DAMAGE

The fracture surfaces of Test II had an additional region of damage in-between the cleavage wall and the crack front (**Figure 4.21**), with average widths presented previously in **Table 4.4**. Shear ridges or ductile tearing demarcated the regions hydrostatic and corrosion fatigue damage, with corrosion products formed on the fracture surface of the latter, as seen in **Figure 4.21**. The regions of hydrostatic damage had a quasi-cleavage morphology and were absent of corrosion damage, owing to the coatings used during hydrogen-charging and testing. Crack advance under hydrostatic testing was evident by dense regions of ductile dimple formation, which is indicated by the red ellipses in **Figure 4.21**.

4.4 CELL SOLUTION ANALYSIS

The post-test *pH* measurements of the test solution of the bulk solution and OM, Middle, and Bottom disbondment locations are presented **Table 4.6**. On average, the bulk solution in the cell maintained a *pH* value that was close to the initial solution *pH* of 6.29. At the OM the *pH* rose to 6.39 with a small, non-linearly decreasing gradient towards the bottom crack location with a *pH* of 6.25.

The post-test ICP mass spectroscopy measurements of the solutions extracted from Test I are summarized in **Table 4.7**. Unfortunately, the vials from Test II were damaged and could not be characterized. Of the elements presented in **Table 4.7**, the two that stand out are K and Fe. At the disbondment locations, K decreases from the OM to the Bottom, but Fe is the highest at the Middle position and lowest at the OM. It was expected that the Bottom position would have the highest concentrations of the elements, owing to gravitational effects, but this was clearly not the case for Fe. As there were no corrosion products found on the surfaces of the sample the loss of species could have only occurred through either precipitation of products on the cell surfaces or diffusion into the bulk solution.

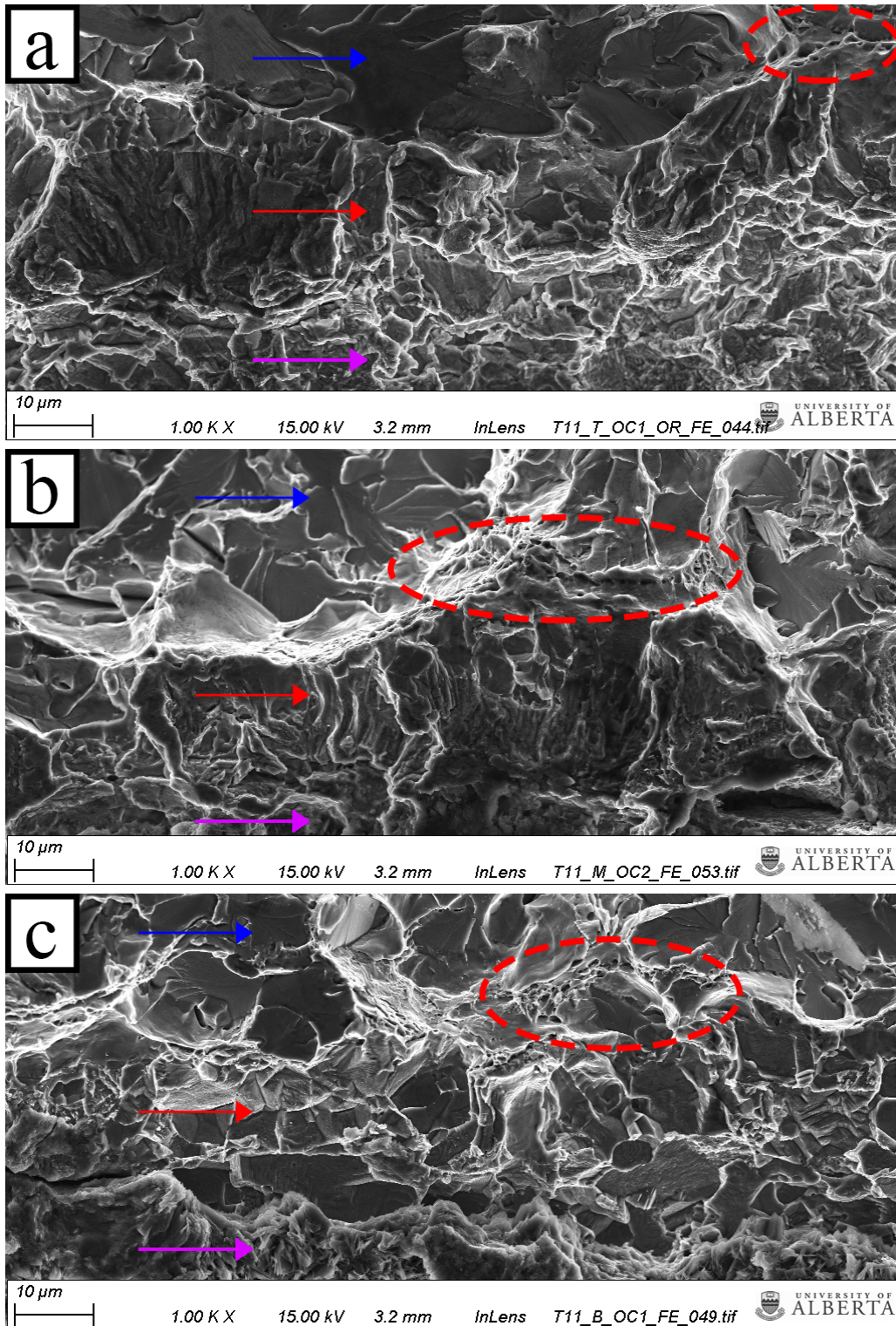


Figure 4.21 Damage on the fracture surfaces in Test II by hydrostatic testing for the (a) OM, (b) Middle, and (c) Bottom cracks. Hydrotest damage is definable by dimpled ridges and quasi-cleavage or smoothed features. The arrows indicate the cleavage (blue), hydrostatic damage (red), and the crack front (purple). The red ellipses indicate locations of ductile void formation between the quasi-cleavage zone of the hydrostatic test damage and the cleavage plane from fracturing the sample open.

Table 4.6 *pH* measurements at various locations within the cell for Tests I and II.

Location Inside Cell	Distance from the Coating OM (mm)	Test I	Test II (pH)	Average
Bulk	-	6.30	6.29	6.30
Open Mouth	-10	6.38	6.37	6.38
Middle	65	6.30	6.31	6.31
Bottom	140	6.25	6.24	6.25

Table 4.7 ICP chemical species analysis (ppm) from various locations within the cell of Test I.

Location Inside Cell	Distance from the Coating OM (mm)	Test 10 Species Concentrations (ppm)				
		Na	Mg	K	Ca	Fe
Bulk	-	11.7	3.09	3.09	34.2	9.4
Open Mouth	-10	11.9	3.03	10.70	33.7	21.5
Middle	65	12.3	3.02	6.41	33.0	39.0
Bottom	140	12.0	3.07	4.43	33.9	27.3

CHAPTER 5: DISCUSSION

The focus of this chapter will be on the effects of variable waveform conditions, namely their frequency, minor cycles, and holds on the crack growth behavior of the X60 SCT cracks in NNpH conditions. Most of the first section's discussion will involve direct comparisons with CT crack data obtained by other authors in order to establish a strong foundation and understanding of the SCT cracks' corrosion fatigue behaviour. The second major section will focus on the differences in growth of the SCT cracks under the coating disbondment, growth in the depth direction, and the impact of hydrostatic testing.

5.1 WAVEFORM EFFECTS ON SURFACE CRACK GROWTH BEHAVIOUR

For an effective analysis of the novel surface crack tension (SCT) samples' growth behaviour the crack growth data from similar works that were performed using traditional compact tension (CT) specimens will be used for comparison purposes (28, 29, 54, 80, 99, 100). To clearly show the similarities and differences, the crack growth trends for constant amplitude (CA) and underload and minor cycles (UL&MC) waveforms with frequencies ranging from 10^{-3} Hz to 10^{-1} Hz will be discussed first. Then, the acceleration effect of minor cycles and the effect of their substitution with static holds in underload and hold (UL&H) waveforms will be addressed. Additionally, for a fair and accurate comparison, only the surface growth data (dc/dN) from the simulated disbondments' Open Mouth (OM) cracks in Tests I and II will be used in the discussions involving both the SCT and CT data. The surface growth data is used in order to compare the same stress state conditions (plane stress), while the OM crack data is used because the local environments at the OM most closely match those of the CT data, for reasons discussed later within Section 5.2.1.

5.1.1 CONSTANT AMPLITUDE (CA)

To facilitate discussion, the variation of CA crack growth rates with frequency for Test I's OM crack, labelled SCT-OM, is plotted alongside data found in literature for CT samples in C2 solution environments and presented in **Figure 5.1**. The data labelled as CT-Yu was directly pulled from literature (54) for X60 CT specimens with the following loading parameters: $K_{\max} = 33 \text{ MPa}\sqrt{\text{m}}$, $R = 0.5$, $\Delta K = 16.5 \text{ MPa}\sqrt{\text{m}}$, with frequency varying from 1.0×10^{-3} Hz to 2.8×10^{-5} Hz. The CT data from 10^{-3} Hz to 10^{-1} Hz, however, was extrapolated based on the Combined Factor Model for

predicting growth rates of X65 CT specimens in C2 solution as a function of K_{\max} , ΔK , and frequency, for $f \geq 10^{-3}$ Hz (Section 2.4.3.3). The initial loading conditions and crack growth rates per waveform for the SCT-OM data can be found in **Table 3.4** and **Table 4.1**, respectively.

5.1.1.1 Mechanical Response in NNpH Environments

Although the results for the Middle and Bottom cracks of Test I are not presented in **Figure 5.1**, all three cracks of Test I demonstrated the same general trend, i.e. CA crack growth rates increase with a decrease in frequency in the frequency range of 10^{-3} Hz to 10^{-1} Hz. These results agree well with the CA data for CT specimens presented in **Figure 5.1** and with results found for other NNpH corrosion fatigue (CF) systems (28, 44, 54, 82, 84-87), in spite of differences in crack and sample geometry.

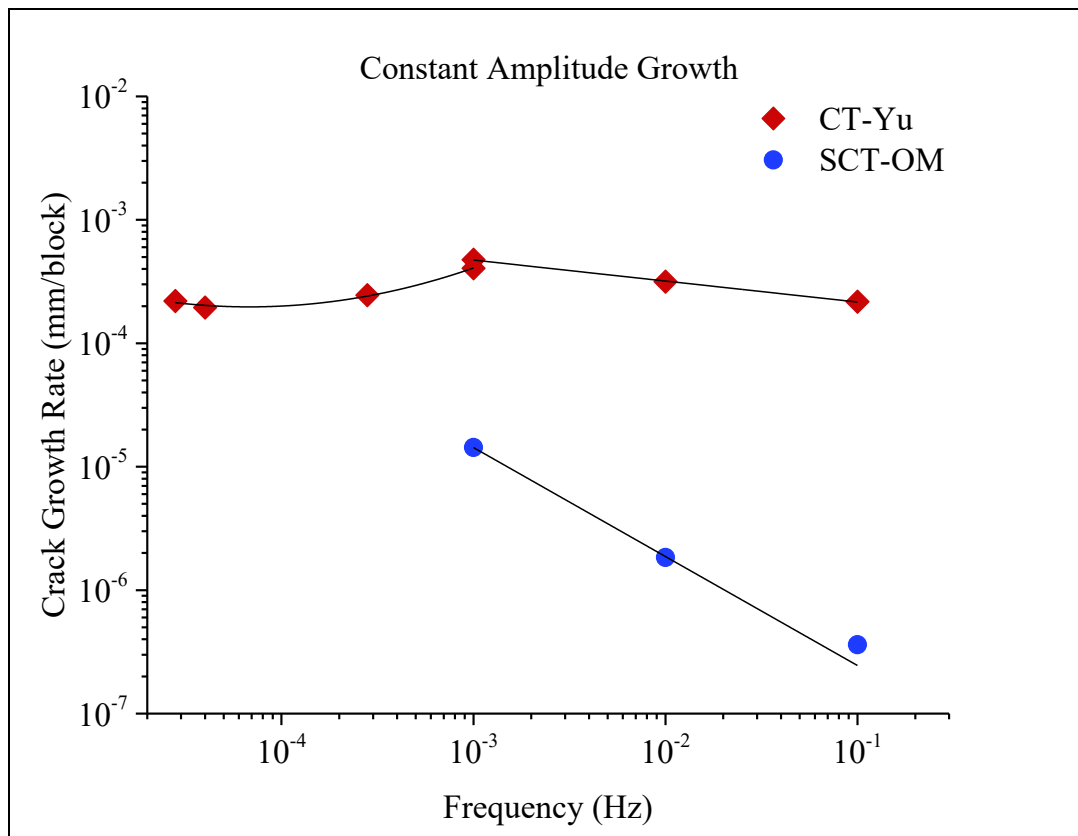


Figure 5.1 Log plot of CA crack growth rates as a function of frequency where: SCT-OM represents the OM crack constant amplitude data from Test I with $K_{\max} = 13.8 \text{ MPa}\sqrt{\text{m}}$ and $\Delta K = 12.5 \text{ MPa}\sqrt{\text{m}}$; CT-Yu (54) is the data for CT specimens where $K_{\max} = 33 \text{ MPa}\sqrt{\text{m}}$ and $\Delta K = 16.5 \text{ MPa}\sqrt{\text{m}}$.

The results from the two systems do not agree entirely, however, and there are two notable differences between the data and trends for the OM crack of Test I and that of the CT specimens:

- 1) The crack growth rates (dc/dN) of SCT-OM were at least one order of magnitude less than the growth rates of the CT samples, for a given frequency.
- 2) The sensitivity to loading frequency, i.e. the change in crack growth rate (dc/dN), is greater for the SCT-OM crack than the CT sample data, which is visually evident by the slopes of the two data sets in **Figure 5.1**.

The underlying causes for the above discrepancies between the two crack geometries is, for the greater part, because of the differences in the applied values of K_{\max} and ΔK during testing. Additional effects on the SCT-OM crack's surface were present because of the higher values of K_{\max} and ΔK used during fatigue pre-cracking and residual compressive stresses generated by milling the surface to remove the notches. Not only do these factors cause an intrinsic difference in growth behaviour through inert mechanisms of damage, but they also effect the environmental contributions to growth. For the sake of brevity, the concepts behind the substantial effect of K_{\max} and ΔK will only be briefly explained, as needed, because they were already discussed in great detail throughout Chapter 2.

Recall the intrinsic roles of K_{\max} and ΔK according to The Unified Approach (Section 2.3.1), where K_{\max} and ΔK are both considered fundamental driving forces of fatigue crack propagation responsible for the rupture of atomic bonds and cyclic plastic damage ahead of the crack, respectively (49, 50). This is critical in order to understand the differences in the growth behaviour of the two crack types because there was a large difference in the applied K_{\max} between the two sets of data; where K_{\max} values of $33 \text{ MPa}\sqrt{\text{m}}$ and $13.8 \text{ MPa}\sqrt{\text{m}}$ were applied at the surface crack tips of the CT and SCT cracks, respectively. In comparison to K_{\max} , the values of ΔK for the two data sets were close, differing by $4.0 \text{ MPa}\sqrt{\text{m}}$, but the cyclic plastic damage at the CT crack tips would have occurred to a greater extent. Therefore, based on the mechanical conditions, the SCT-OM growth rates are understandably lower than the CT growth rates in C2 solution. However, when testing was performed in-air there was no growth at the surface of the SCT-OM crack surface and environmental contributions to growth must be considered to properly understand the CA frequency response of surface cracks in the NNpH test environment.

In the NNpH system hydrogen is present on the bare steel surface owing to the (anodic) dissolution of iron and (cathodic) reduction of hydrogen from solution, following **Eq. 2.1 – 2.7** (12, 16, 17, 19, 83). Any hydrogen which does not recombine into $H_{2(g)}$ can diffuse towards crack tip, dissolve into the metal's lattice, and accumulate within the plastic zone of the crack leading to hydrogen embrittlement (HE) (53, 55, 56, 58, 110, 111) . The HE mechanism has been well embraced as major contributor to crack growth in NNpH environments (7, 11, 15, 25, 28, 29, 37, 44-46, 54, 81-87, 99), and the key relationships between the mechanical and environmental factors are discussed next in terms of the two crack growth data sets of **Figure 5.1**.

Of the two mechanical driving forces it is difficult to say which has a greater influence on the kinetics of hydrogen near the SCT crack tips. This is, for the large part, because only the load frequency was varied and not the applied stress. However, the chemical or environmental effects, as they relate to K_{max} and ΔK , can still be used to explain the pronounced sensitivity of SCT-OM and are briefly reviewed below:

- 1) It is known that the equilibrium concentration of dissolved hydrogen in the iron's lattice located some distance ahead of the crack tip is exponentially proportional to the hydrostatic stress in the plastic zone, following **Eq. 2.11** (28, 53-55, 58). Additionally, the hydrostatic stress about the crack tip reduces the chemical potential of hydrogen, generating a gradient towards the unstressed surroundings or increases the driving force for hydrogen diffusion to the FPZ (**Eq. 2.12**) (54, 57, 58, 112). As the hydrostatic stress and plastic zone size are related to K_{max} it can be seen as the governing driving force for hydrogen accumulation ahead of the crack tip.
- 2) The cyclic loading component, ΔK , will cause mobile dislocations to emit from the crack tip that can drag hydrogen towards the hydrostatic zone at accelerated rates and greater distances in comparison to interstitial diffusion driven by concentration gradients alone (29, 58). These dislocations can annihilate upon reaching the hydrostatic zone, depositing hydrogen, and elevating the levels of hydrogen concentration present within the plastic zone.

Based on the above environmental factors higher concentrations of hydrogen are achievable within the larger plastic zone size of the CT crack (1 mm) in comparison to that of the SCT-OM crack

(0.15 mm), based on K_{\max} . Also, the smaller stresses that exist at the SCT-OM crack tip provide a lower driving force for hydrogen diffusion to the plastic zone and would rely more on the enhanced transport of hydrogen through mobile dislocations. The greater reliance on plasticity, or dislocations, over more brittle growth of SCT-OM was evidenced by **Figure 4.9**, where significant micro-cracking was observed in the plastic zone ahead of the sharp crack tip. The presence of micro-cracks is indicative of alternating blunt and sharp crack behaviour, where more dislocations are emitted during the blunted stage leading to greater hydrostatic stresses ahead of the crack, increasing hydrogen's ability to sample microstructural defects in the plastic zone (110). Once sufficient hydrogen has accumulated, micro-cracks can initiate within the plastic zone, and those immediately ahead of the crack tip can propagate back to the main crack to cause crack advance and sharpening. The micro-cracks themselves can enhance hydrogen uptake within the plastic zone through their crack tip stresses and their greater hydrogen trapping capability in comparison to dislocations and other steel microstructural features (113).

The synergistic effect of K_{\max} with environmental factors is evident, as the CT data reached its peak growth rate at 10^{-3} Hz and began to plateau with further decreases in frequency. This would indicate that the growth was chemically limited and that the hydrostatic zone was saturated with hydrogen (110), which was confirmed by the authors of the CT study by modelling the hydrogen distribution in the plastic zone using K_{\max} and ΔK relationships (54). On the other hand, a strong frequency response is demonstrated by SCT-OM because its growth was mechanically limited, based on the fact that no growth detected at the surface during in-air loading. As such, the cycle-time accumulation of hydrogen played a more critical role in crack extension and each decade of decrease in frequency yielded markedly greater crack growth rates.

The SCT-OM's lack of crack growth in air under CA loading can be largely attributed to the higher final fatigue pre-crack K_{\max} and ΔK , which are estimated to be $19.1 \text{ MPa}\sqrt{\text{m}}$ and $17.2 \text{ MPa}\sqrt{\text{m}}$, respectively, and the compressive residual stress on the surface induced by the notch removal process. Assuming pure plane strain behaviour and using the Irwin approximation, which underestimates the plastic zone size, a plastic zone size of 0.097 mm exists because of pre-cracking at the surface and it is unlikely that either of the crack tips grew out their pre-crack plastic zones during testing in solution. The fact that crack growth occurred in the NNpH environment is significant on its own, and a testament to the effectiveness of hydrogen damage in this corrosion

fatigue system. Albeit that one of the above reasons was an experimental error, the two events can still be considered important in terms of pipeline operations and their impact on crack growth as explained in the following paragraphs.

The greater pre-crack crack tip stress states can be considered representative of an overload event during pipeline operations (96, 101). The larger pre-crack stresses essentially introduced a *steady state* overload of 38 %. The effect of a typical overload introduces a plastic zone greater in size and the resulting compressive residual, or internal, stresses from the yielding of the material than the nominal fatigue cycles, or those of the average ΔK value in the system (48). As a result, crack growth following an overload is retarded by the greater compressive stresses and plasticity-induced closure by residual stresses behind the crack tip as the crack grows into the overload zone. It is important to understand the differentiation here between underloads in the field and here, where *steady state* growth occurred during pre-cracking, meaning the crack tip during testing did not grow into the overload zone, but was instead already within it. Additionally, pre-crack growth would have occurred under plane strain conditions resulting in a smaller plastic zone at the surface than if the overload occurred during testing, where the surface crack tip is under plane stress conditions.

The compressive residual stresses introduced by the milling process would retard crack growth, similar to the stresses introduced by an overload. Both tensile and compressive residual stresses are known to occur throughout the steel's thickness, because of the pipe forming process, which can either enhance or suppress crack growth, respectively. The effect of residual stresses on pipe bodies in NNpH crack initiation and growth were studied in depth by Van Boven and Chen, *et al.* (35, 36), where the authors determined that initiation, growth, and dissolution are all enhanced by locations of high residual tensile stress and vice-versa for residual compressive stresses. It was determined that cyclic loading prior to testing can relieve residual stresses along the surface of steel, and likely the compressive stresses on the SCT specimens were reduced through CA loading in air prior to adding C2 solution (35, 36). Strain softening could also have occurred under loading in C2 solution, owing to the presence of hydrogen, but the effect is debatable with bulk hardening and softening effects reported to occur for same alloy; the point is moot because bulk material deformation is not representative of the high triaxial stresses, strain gradients, and hydrogen content that exist ahead of a crack tip (55).

The enhanced dissolution under the thin crevice region behind crack tip of the SCT-OM crack (see **Figure 4.5a** and **Figure 4.8a-b**) can also be partially attributed to the compressive residual stresses caused by the milling process. Since the compressive stresses would be highly localized to the top surface an equivalent tensile stress would result in the microstructure below and a galvanic stress cell can form, consequently leading to the anodic attack of the microstructure of tensile residual stress (35, 36). Also, the subsurface of the specimen would experience strain hardening and grain refinement as a result of deformation and heat, leading to an increase in dislocation density and grain refinement and therefore enhanced hydrogen trapping along the subsurface (58, 113).

5.1.1.2 The Combined Factor

As the SCT cracks demonstrated a clear frequency response under CA loading, the corrosion fatigue behaviour can either be categorized as time-dependent or cycle-time-dependent, the latter within the “near-plateau” ΔK region and frequency regime where a frequency dependency occurs (52). However, the range of test frequencies was not sufficiently large to determine if there was a high or low frequency plateau region at the OM, a characteristic of cycle-time-dependent CF, because only a select number of frequencies could be tested due to limited test time. Despite this, the corrosion fatigue behaviour can be identified as cycle-time-dependent because it has been well-established as the form of corrosion fatigue experienced by through thickness cracks in NNpH environments and short or shallow crack behaviour should not change this fact (28, 54).

Based on the assumption of cycle-time dependent corrosion fatigue behaviour, the same data from **Figure 5.1** for $f \geq 10^{-3}$ Hz can also be plotted as a function of the cracks' Combined Factor values, as seen in **Figure 5.2**. From **Figure 5.2**, the OM of Test I grew under CA loading with Combined Factors ($\Delta K^2 K_{\max}/f^{0.1}$) ranging from 2412 – 3823 $(\text{MPa}\sqrt{\text{m}})^3 \text{Hz}^{0.1}$ **Table 3.4** in spite of Combined Factor being well below the threshold for continuous growth of CT specimens in C2 solution (8500 $(\text{MPa}\sqrt{\text{m}})^3 \text{Hz}^{0.1}$ for $f \geq 10^{-3}$ Hz) (28). Owing to the fact that the SCT cracks are environmentally short by nature, which are known to propagate at mechanical conditions well below long crack thresholds (60, 68, 69), crack growth below a Combined Factor value of 8500 $(\text{MPa}\sqrt{\text{m}})^3 \text{Hz}^{0.1}$ is reasonable.

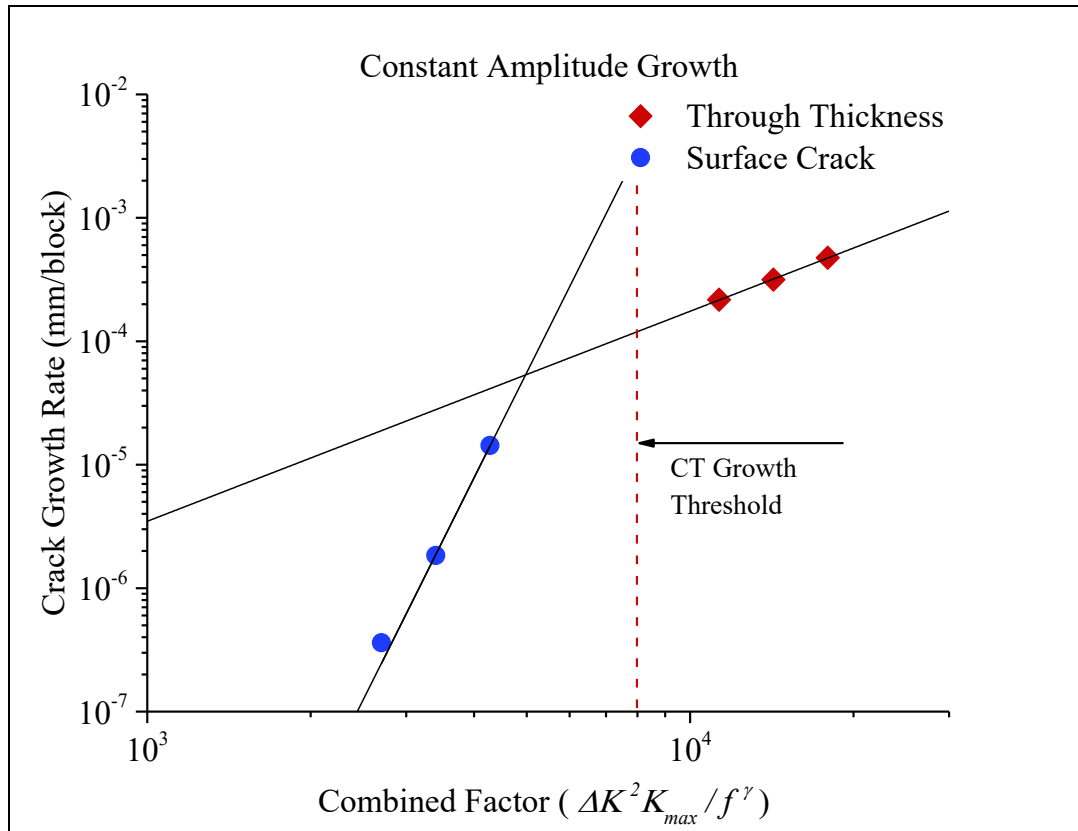


Figure 5.2 Log plot of CA crack growth rates as a function of the Combined Factor, where: SCT-OM represents the OM crack constant amplitude data from Test I with $K_{max} = 13.8 \text{ MPa}\sqrt{\text{m}}$ and $\Delta K = 12.5 \text{ MPa}\sqrt{\text{m}}$; CT-Yu (54) is the data for CT specimens where $K_{max} = 33 \text{ MPa}\sqrt{\text{m}}$ and $\Delta K = 16.5$

In his review on environmentally short crack effects Turnbull identified the primary crack size sensitivity effects which may arise, depending on the material and environment (69):

- Depletion of reactive species into the crack, and discharge of products generated by reactions within the crack to the bulk environment.
- Differences in the corrosion potential drop between long and short cracks and the conjoined local crack chemistry.
- Effect of bulk solution flow over the crack.
- Crack accessibility to hydrogen supply, when bulk charging controls cracking.

Transport of species in and out of the crack will indeed effect crack growth, but it causes a reduction in the SCT cracks' growth rates through corrosion debris wedging which is discussed further in Section 5.2.3. Otherwise, fluid flow is not of particular importance under CA loading

because there are no reactions involving passivation or hydrogenation which can hinder or enhance damage and only the cathodic reduction of hydrogen has a direct impact on crack growth. The effect of bulk solution flow is unimportant as well, because there was no forced fluid flow over the cracks.

Of the four crack size effects listed both the effects on local crack chemistry and accessibility to hydrogen supply can be considered influential in the NNpH system. Local crack chemistry effects were discussed in detail in Sections 2.3.2.1.6 – 2.3.2.1.8, where it was discussed that the shorter the crack, the greater the potential drop across the crack. As a result, the SCT-OM crack experiences enhanced dissolution and hydrolysis leading to acidification of the crack tip chemistry, thereby a greater local hydrogen concentration (70, 72, 73). The significant dissolution that occurred at the subsurface of the crack found after mechanical polishing (**Figure 4.8a**) is evidence of crack tip acidification. Local crack tip hydrogen production as a potential source has been considered negligible in the past when compared to bulk surface charging (29), which is reasonable at more aggressive loading conditions like those used to determine the Combined Factor threshold (28). However, as discussed in the previous section, the lower loading conditions of the SCT crack leads to a greater sensitivity to hydrogen's contribution to growth and crack tip hydrogen production could be critical at these conditions.

The accessibility to the hydrogen source of the crack, i.e. the bulk hydrogen on produce on the sample surface, is important for the same reasons listed in the previous paragraph. This effect arises because of hydrogen diffusion through the specimen thickness, leading to hydrogen gradients throughout its thickness. Consequently, hydrogen can reach steady state quicker for cracks that are shorter in depth or thinner samples. However, this effect is potentially superficial and growth rates would have to be compared after through-thickness transport of hydrogen has reached steady state in both sample types (73) under equivalent surface conditions to avoid the effects explained in the previous section.

In terms of the Combined Factor the SCT-OM crack is likely misrepresented in **Figure 5.2** because the corrosion cells of the two test systems are different, where the CT data was obtained through tests in bulk C2 solution and SCT data was obtained through tests involving coating disbondments. The different environment would affect the value of γ , which represents the environmental

contribution to crack propagation (28). The OM location in Tests I and II experience enhanced dissolution (22) and, consequently, greater hydrogen reduction rates in comparison to samples in bulk solution, owing to disbondment effects further discussed in Section 5.2. As a result, the value of γ should be greater for SCT-OM than the contrasted CT data to reflect the enhanced hydrogen production at the OM location.

5.1.2 VARIABLE AMPLITUDE (VA)

In the following subsections the effects of the underload frequency, minor cycles, and holds on the behaviour of the SCT crack geometry will be discussed. To do so, similar to section 5.1.1, direct comparisons between SCT-OM and CT crack data will be utilized.

5.1.2.1 Effect of Underload Frequency

A comparison of the variation of UL&MC crack growth rates with frequency for Test I's OM crack, labelled SCT-OM, and data found in literature for X65 CT samples in C2 solution environments (54), labelled CT-Yu, are presented in **Figure 5.3**. The underload parameters for the data presented in **Figure 5.3** are the same as the CA tests of the previous section. The minor cycles parameters for the data labelled as CT-Yu for X65 CT specimens are $n = 697$ (number of cycles), $R_{MC} = 0.9$, and $f = 5 \times 10^{-3}$ Hz, only differing from the SCT data in the number in minor cycles between underloads ($n = 100$) and K_{max} . The data SCT-OM-ADJ was determined by simply adjusting the growth at 10^{-3} Hz to the predicted growth rate at $K_{max} = 33 \text{ MPa}\sqrt{\text{m}}$, following the logarithmic relationship determined using $da/dN - K_{max}$ data from literature (54), and then back-calculating the growth rates at 10^{-2} Hz and 10^{-1} Hz using the fitted power law for the original SCT-OM data.

It is observable from **Figure 5.3** that the UL&MC data for two cracks follow a similar trend, where a decrease in loading frequency causes an increase in crack growth rates but at lower rates for SCT-OM. The lower crack growth rates can be rationalized by the differences in K_{max} between the two sets of data, for the same reasons explained in the previous section for CA loading. However, it can be seen that when the SCT-OM growth rates are adjusted for a K_{max} value of $33 \text{ MPa}\sqrt{\text{m}}$ that the predicted growth rates exceed those of the CT crack. The data for SCT-OM-ADJ was determined using a relationship for CT data and only provides some insight on what the growth

would be at K_{\max} 33 MPa \sqrt{m} , with possible rates exceeding those of the CT cracks due to short crack effects.

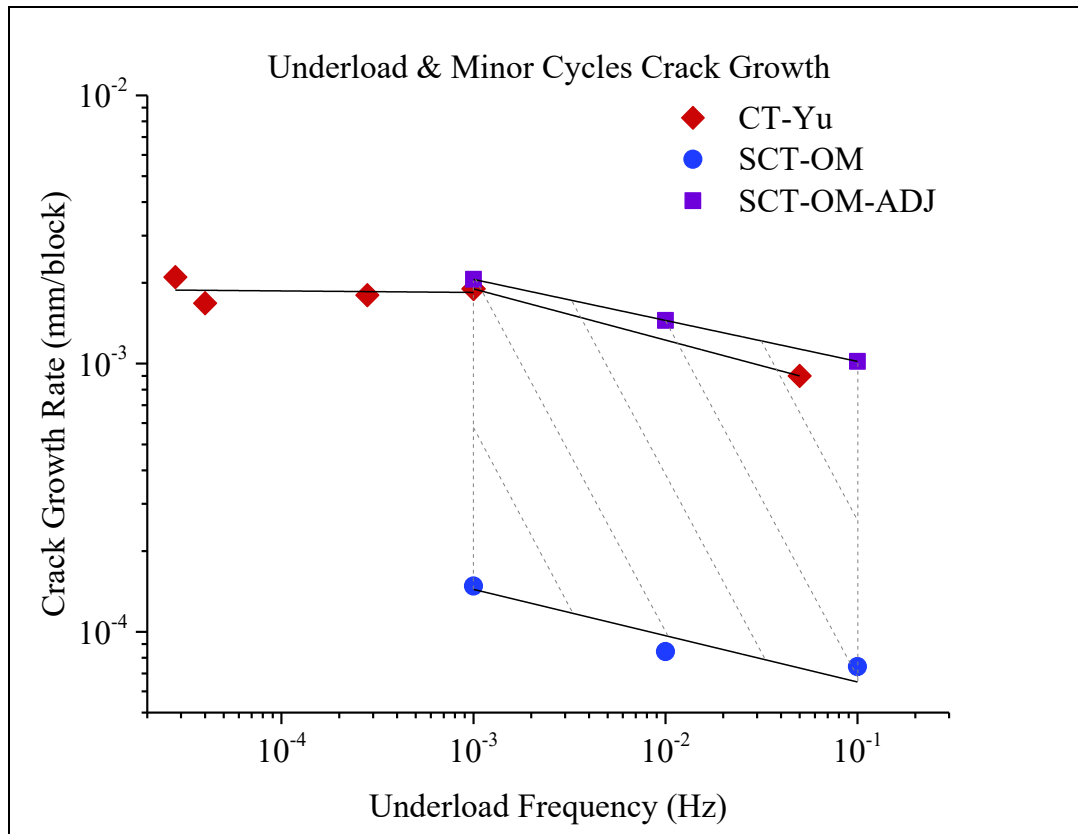


Figure 5.3 Log plot of UL&MC crack growth rates as a function of frequency where: SCT represents the OM crack’s UL&MC surface data from Test I with $K_{\max} = 13.8$ MPa \sqrt{m} , $\Delta K = 12.5$ MPa \sqrt{m} and CT-Yu $K_{\max} = 33$ MPa \sqrt{m} , $\Delta K = 16.5$ MPa \sqrt{m} (99). Minor cycles: SCT, $n = 100$, $f = 5 \times 10^{-3}$ Hz, $R = 0.9$; CT-Yu, $n = 697$, $f = 5 \times 10^{-3}$ Hz, $R = 0.9$.

Contrary to the CA waveforms, the SCT crack growth rates demonstrate a decreased sensitivity to frequency when compared to the CT specimens in the 10^{-3} Hz to 10^{-1} Hz range. The increase in crack growth rates from 10^{-3} Hz to 10^{-1} Hz, for both data sets, and decrease in the frequency sensitivity of the SCT data within this range cannot be entirely attributed to the effect of hydrogen accumulation in the same manner as the CA data. For CA, the increase in growth rates with decreasing frequency was explained through a cycle-time-dependent accumulation of hydrogen by bulk diffusion to the fracture process zone over a load cycle, which was proportional to K_{\max} . Although this same effect of hydrogen uptake during the underload cycles will occur, it may be altered by the presence of minor cycles and other effects must be considered when considering the impact of underload frequency.

It is known that hydrogen accumulation within the hydrostatic zone can occur during the quasi-static, high R cyclic loading of the minor cycles in a manner similar to that of CA cycles (54, 80, 99). Certainly the greater growth rates (mm/blk) measured under UL&MC loading in comparison to the CA is convincing enough of this effect. It is unlikely that a transient sensitivity effect occurred in the DCPD data used to determine the SCT-OM growth rates by blunting effects at the crack tip, through either room temperature creep (88-90) or dissolution, as evidenced by the thin, sharp post-test crack tip shown in **Figure 4.5a** – the dissolution below the thin-crevice subsurface in the region just behind the crack, as discussed in Section 5.1.1.1, would not have a significant impact because it does not affect K_{max} . Further yet, it was determined that at $n = 697$ the crack growth rates of the CT cracks reach a saturation state with little enhancement in growth with further increases in n , yet still demonstrate a sensitivity to the underload frequency for hydrogen uptake and damage when subjected to UL&MC spectra (99).

The lowered sensitivity of the SCT crack to underload frequency can then be understood through a greater, or perhaps near equilibrium concentration of hydrogen accumulated during the minor cycles within the crack tips plastic zone. This would not reduce the magnitude of the cycle-time dependent accumulation of hydrogen during an underload, but reduce its effect relative contribution to the over-all damage during a loading block. As such, the argument of CA is reversed and the greater mechanical factors of the CT cracks cause a greater sensitivity to frequency for hydrogen accumulation based damage under UL&MC loading. Further yet, based on the discussion of the previous section, hydrogen production by dissolution at or near the crack tip during the underload portion of the UL&MC waveforms can be seen to have an enhanced role in crack propagation for the SCT crack. It is possible that during the minor cycles regime of the waveform the hydrogen production near the crack tip becomes limited by local solution chemistry. This is because of the poor solution replenishment of anodic (HCO_3^-) species as a result of the high R ratio. During the underload portion the lower R ratio cycle allows for a greater replenishment of fresh solution which would enhance anodic dissolution at the crack tip and therefore hydrogen production.

To elaborate, because of the lower R value of the underloads of the SCT cracks they would experience lower exposure times at greater crack openings for a given frequency which could limit fluid access to the freshly generated surface but increase mixing between the crack tip and bulk

environment (71). Also, the lower stress intensity, high geometrical constraints – attributable to the sharp, shallow semi-elliptical shape and compacted corrosion products (e.g., **Figure 4.13a-c**) – and lower volume of the SCT cracks would lead to a lower volumetric fluid flow rate reducing the “refreshment” effect on hydrogen generation for the SCT cracks (70, 73). Consequently, overall the SCT cracks would have lower mixing effectively reducing their sensitivity to underload frequency.

5.1.2.2 The Acceleration Effect of Minor Cycles

As there was major constraints on both time and project scope, the crack growth behavior with varying amounts of minor cycles could not be determined for the current system. Additionally, because of the damage caused by the corrosion products formed during testing any possible minor cycle striations could not be located, and the crack growth per minor cycle could not be determined – that is if the minor cycles directly contributed to growth at all. However, the crack growth behavior of CT specimens with both varying R and n between underloads in air and C2 solution has been studied in great detail by Yu, et al. (99) and whatever comparisons in crack behavior between the two systems will be made. This will be done by comparing the growth rates of the two systems under the same conditions as those in the previous section, but with additional extrapolated CT crack growth data.

The crack growth rates for the SCT-OM and CT cracks, with $n = 100$ at an underload frequency of 10^{-3} Hz, were 1.9×10^{-4} mm/blk (average of Test I and II) and 6.4×10^{-4} mm/blk, respectively. When comparing the growth rates it is interesting that the ratio of the growth rates, 0.297, are similar to the ratio of their mechanical contribution to growth, 0.239, as defined by the Combined Factor ($\Delta K^2 K_{\max}$). The value of the ratio of Test I’s UL&MC OM growth rate at 10^{-3} Hz, 1.5×10^{-4} mm/blk, to the CT specimen, 0.234, is even closer to the $\Delta K^2 K_{\max}$ ratio. This reflects the synergy between loading conditions and the accumulation of hydrogen, where the ratio of crack growth rates between the two cracks begin to approach a direct relationship to K_{\max} and ΔK under more aggressive loading conditions – at least at this specific underload frequency and number of minor cycles.

Even if the minor cycles did not directly contribute to the fatigue growth of the SCT-OM crack, it is evident that they can still enhance hydrogen damage through their quasi-static loading condition,

by dislocation emission (ΔK) and hydrostatic stresses (K_{\max}) in the plastic zone. Another possible contribution to damage enhancement during minor cycles could be the generation of dislocations at the surface through hydrogen gradients (58, 114) and corrosion (58). Although the hydrogen generated in NNpH conditions is not necessarily high, the high strains in the plastic zone could enhance dissolution (115) and ergo hydrogen production within the region. Additionally, a combination of time and the hydrostatic stresses within the region would lead to an opportunity for greater quantities of hydrogen away from the crack to diffuse towards the plastic zone. If dissolution can indeed generate dislocations, then it is possible that hydrogen could become entrapped by a dislocation generated away from the plastic zone, enhancing the rate and distance of diffusion than interstitial diffusion of hydrogen alone, and be deposited within the plastic zone – granted that the dislocation’s motion is not entirely impeded in the process. It is also possible that relief of the compressive stresses within the plastic zone and on the surface from the pre-crack and notch removal procedures, respectively, occurred, similar to CA loading, reducing the retarding effect on growth by the compressive residual stresses.

The difference in Acceleration Factors, or the ratio UL&MC to CA crack growth rates (da/dN), are striking, however, where the Acceleration Factor is 10 for the SCT crack but only ~ 1.6 for the CT specimen (54). This builds upon previous discussions (see Section 5.1.1.1) on the weak driving force for hydrogen diffusion for the SCT cracks in comparison to the CT specimens during CA loading, owing to the high hydrogen damage dependency of the former and the deleterious cycle and time-dependent hydrogen accumulation during the minor cycles block (Section 5.5.2.1).

Unfortunately, CT data is not available to quantitatively compare the acceleration factor with increasing underload frequency at $n = 100$, nor SCT data to compare the acceleration factor with a varying amount of minor cycles. It can be inferred, however, that the impact of minor cycles on growth is significantly greater for SCT cracks and increases as frequency increases, based on the data available. Furthermore, it was reported that a peak Acceleration Factor of five occurs at $n = 1000$ for the CT specimens, at an underload frequency of 10^{-3} Hz, which is still much less than the value determined here of 10 for $n = 100$.

5.1.2.3 The Effect of Static Holds

The UL&H crack growth rates (3.4×10^{-4} mm/blk) for an equivalent hold time of 100 minor cycles (350 min) for the CT data, with the same conditions as the previous waveforms, was extrapolated from literature (100) and plotted alongside the UL&MC and CA data for both crack types in **Figure 5.4**. For a proper comparison, the growth data of Test II was used for the VA waveforms where both were tested on the same crack and better represent the difference in growth between the two waveforms. It is quite clear from the plot that differences in growth between the UL&H and UL&MC spectra exist for both crack types, yet to a lesser extent for the SCT-OM crack; the ratio of UL&H to UL&MC growth for the SCT and CT cracks were 1.6 and 1.9, respectively. Similarly, the ratio of growth between the two cracks for the UL&H waveform, 0.41, is only slightly higher than that of the UL&MC, 0.36. The lower ratio of growths for the UL&MC waveform could be a result of the use of Test II's Middle DCPD data to determine the OM's growth rates, or the lower mechanical contribution of minor cycles to crack growth for the SCT cracks.

Contrary to the CT specimens, the SCT UL&H waveform demonstrated enhanced crack growth per block in comparison to CA loading. This is in large part attributable to the significantly lower growth rates experienced by the SCT crack during CA loading and an increase in hydrogen segregation to the crack tip, proportional to K_{max} , during the static hold periods. The static hold is less effective than minor cycles in terms of enhancing crack growth because it lacks the additional traffic of reversible hydrogen trap sites to the hydrostatic zone in the form of mobile dislocations, which are generated by the dynamic straining of the latter. This reduces the synergistic interaction of hydrogen embrittlement and mechanical damage ahead of the crack tip during an underload (100). It can also be seen by **Figure 4.12a** that blunting occurred at one of the crack tips of Test II, which based on the comparison to Test I's crack tips is a result of the UL&H waveform. Blunting of the crack tip would have reduced K and therefore the driving force for crack propagation. As a result the crack growth rate of UL&MC spectra is only 1/3 of the UL&MC spectrum.

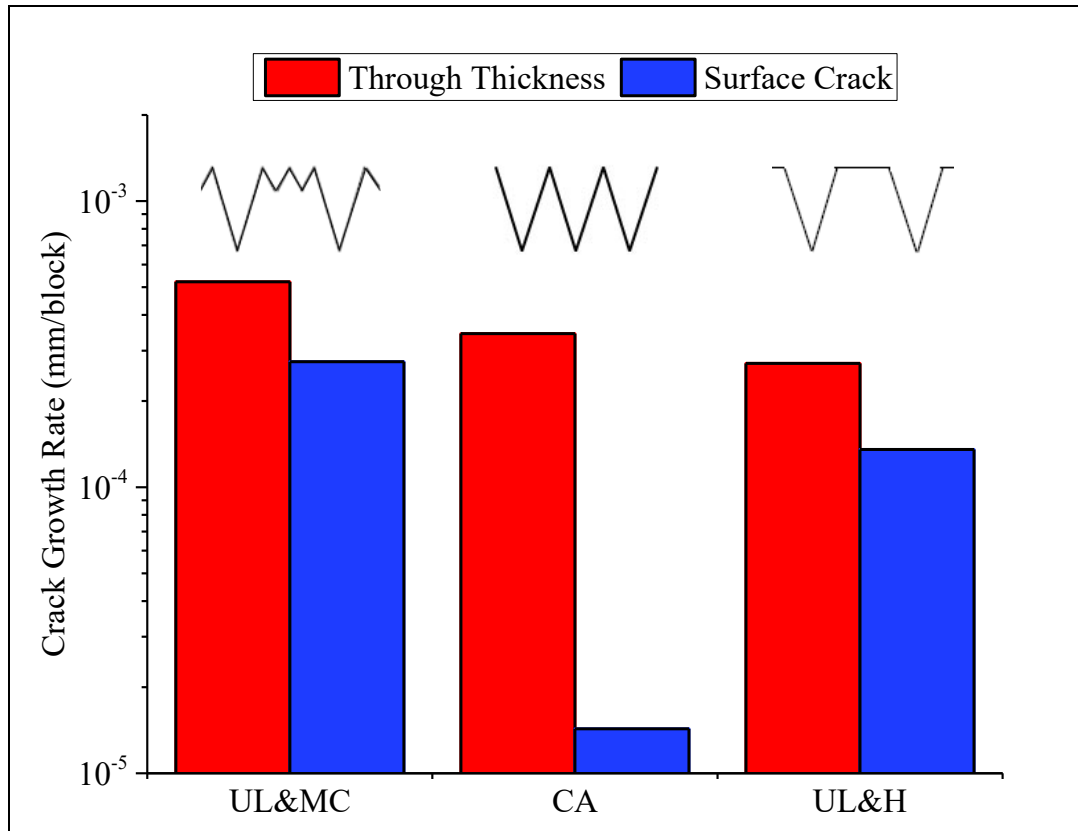


Figure 5.4 Log plot of crack growth rates for all three waveform types, where: SCT represents Test I and II OM crack's average surface data (where applicable) and CT-Yu is data taken from literature (54, 100). [Underloads/CA: $R_{UL,SCT} = 0.1$, $R_{UL,CT} = 0.1$, and $f_{UL/CA} = 10^{-3}$ Hz] [Minor Cycles: $n = 100$, $f_{MC} = 5 \times 10^{-3}$ Hz, $R_{MC} = 0.9$] [Static Hold: $K_I = K_{max}$, $t_{hold} = 350$ min]

5.2 DISBONDMENT EFFECTS ON SURFACE CRACK GROWTH BEHAVIOUR

While the previous section focused on determining a baseline for the growth behaviour of SCT cracks through comparisons with a traditional fracture mechanics specimen, the following section shifts focus towards comparing SCT cracks in different NNpH environments. First, the local environments induced by the simulated coating disbondment will be discussed. Then, the effects of the local environments on SCT crack growth behaviour will be analyzed.

5.2.1 LOCAL DISBONDMENT ENVIRONMENTS

The results and trends presented in Section 4.1.2 and Section 4.3.2 on the corrosion morphologies of the cracks provided evidence that varying levels of dissolution occurred on the specimens' bulk surface and on cracks' surface, generally decreasing from the OM to the Bottom disbondment locations. Studies on CO₂ corrosion under pipeline coating disbondments in NNpH environments

at OCP conditions have demonstrated that the decreasing corrosion rates from the OM to the Bottom locations of simulated disbondments can be attributed to time-dependent changes in the disbondment environment (22, 23, 45). Those authors concluded that measurable differences in dissolution rates and hydrogen uptake throughout a coating disbondment under OCP conditions, which is typical of NNpH field conditions (4, 8, 9), are because of two primary reasons:

1) *CO₂ Concentration Gradient*

The concept of a CO₂ concentration gradient throughout the disbondment has been used to rationalize both decreases in diffusible lattice hydrogen (45) and dissolution rates (22, 24) towards the bottom of coating disbondments. Owing to the fact that CO₂ is replenished away from disbondment's OM, in the bulk solution, CO₂ can only reach the bottom of the disbondment through diffusion from the opening at the OM resulting in a gradient in concentration. This is an appealing mechanism for the reduction in corrosion rates from the OM to the Bottom of the disbondment because the dissolution rates are directly related to the cathodic reduction of H₂CO₃ (16, 19, 24, 83).

2) *Metal Ion (Fe²⁺) Concentration Cell*

More recently, it was theorized that differences in the concentrations of Fe²⁺ within small gap size disbondments forms a differential concentration cell leading to the steel becoming anodic at locations above the OM and cathodic at locations below it (24). The formation of the concentration cell was attributed to first the rapid dissolution rates at the beginning of the test, when the CO₂ saturated solution is first added. After some time, Fe²⁺ diffusion out of the disbondment becomes suppressed because of the higher concentrations of Fe²⁺ towards the OM, which results in Fe²⁺ diffusion into the disbondment. As a result, dissolution attack below the OM, inside of the disbondment, is suppressed while dissolution above the OM is accelerated, the latter sees an enhancement over corrosion rates with infinite gap sizes. The author attributed the enhancement of corrosion rates above the OM with small disbondment gap sizes (2 mm and 5 mm) over the infinite gap size rates to the metal ion concentration cell effect (24).

Although the CO₂ concentration gradient is logical and has been validated by the results of hydrogen permeation (45) and corrosion (22, 24) tests, one author stated that the *pH* values throughout the disbondment were almost identical in spite of differences in CO₂ (45) while the

other found that pH increased towards the bottom of the disbondment (24). The former would make sense, if the concentrations of H_2CO_3 and HCO_3^- are sufficiently high to remain in equilibrium, according to the Colwell-Leis mechanism (12, 16). However, the results presented in **Table 4.6** demonstrate that nearly identical small pH gradients were present from the OM to the Bottom crack locations in both Tests I and II, opposite to that found by the second author. Since this gradient occurred for both Tests, where the pH probe and meter were calibrated prior to removing solution for each test and the extractions were performed using well developed techniques, it cannot be attributed to experimental error. In fact, differences in the pH , albeit small, indicate that there must be significant differences in the local environments because the buffering capacity of CO_2 would have otherwise been able to equilibrate the pH levels throughout the disbondment (16, 19, 73).

The different pH trends presented in **Table 4.6** from those determined in disbondment tests using coupons (24) could be an artifact of the experimental setup in that study; the small gaps between the vertically stacked coupons could lead to potential drops or interruptions in the corrosion potential across the steel surfaces while no such effect would occur for the fully intact sample used here. Potential drops could lead to changes in the pH levels by the electromigration of ionic species within the solution to accommodate the potential changes, which could have effected pH levels (116). Additionally, ultra-pure Milli-Q water was used in this study's C2 solution while distilled water was used in the preparation of the solution for the coupon tests, to the best of the current writer's knowledge, and impurities in the distilled water, such as chlorides, would rapidly diffuse towards the location of greater dissolution leading to decreases in the pH levels. The simulated disbondment, or shielding, in this study's corrosion cell did, however, have a larger total volume with distances spanning several mm on either side of the sample to the side walls of the shielding, on the same plane as the crack and corroding surface, and this could have contributed to the differences in pH trends as well.

Nevertheless, the proposal of significantly different environments at the three crack locations is supported by the elemental concentrations of species in samples of solution extracted from various locations of Test I's corrosion cell (**Table 4.7**). Of particular interest is the trends of K and Fe in **Table 4.7** which show markedly different concentrations at the OM, Middle, and Bottom crack regions. The concentration of K within the disbondment follows that of CO_2 , where the

concentration decreases from the OM to the Bottom. Thus, it can be inferred that K ions are actively migrating to achieve balance within the solution, i.e. K transport occurs through electromigration to assist the electrolyte in achieving electroneutrality with HCO_3^- , OH^- , or other anions within the disbondment's solution (116, 117). The similar concentrations Na, Mg, and Ca in the bulk and disbondment solutions indicates that they did not actively participate in the disbondment's environment(s), which is similar to the results obtained by others on pipeline disbondment corrosion (12).

While the reason for the concentration gradient of K is relatively simple, what is less obvious is the explanation for the concentrations of Fe at the various locations of the corrosion cell. From **Table 4.7**, the concentrations of Fe from greatest to least are at the Middle, Bottom, OM, and Bulk locations. The concentration of Fe within the bulk solution is a result of Fe^{2+} diffusion from the corroding surface in the OM region, i.e. a consequence of concentration gradient driven diffusion. Also, the greater concentrations of Fe within the disbondment do fall in line with the metal ion concentration cell proposed by Chevillat (24), but only to a certain extent. The author was rather vague in their description of the concentration gradient and it appears that they were attempt to state that a uniform Fe concentration occurs where the corrosion rates level off at 50 mm from the OM to the bottom of the disbondment (**Figure 2.7**). To facilitate further discussion, the rough Fe distribution profile throughout the disbondment resulting from changes in pH , CO_2 concentrations, and the dissolution of material on the Fe distribution is graphically represented in **Figure 5.5**.

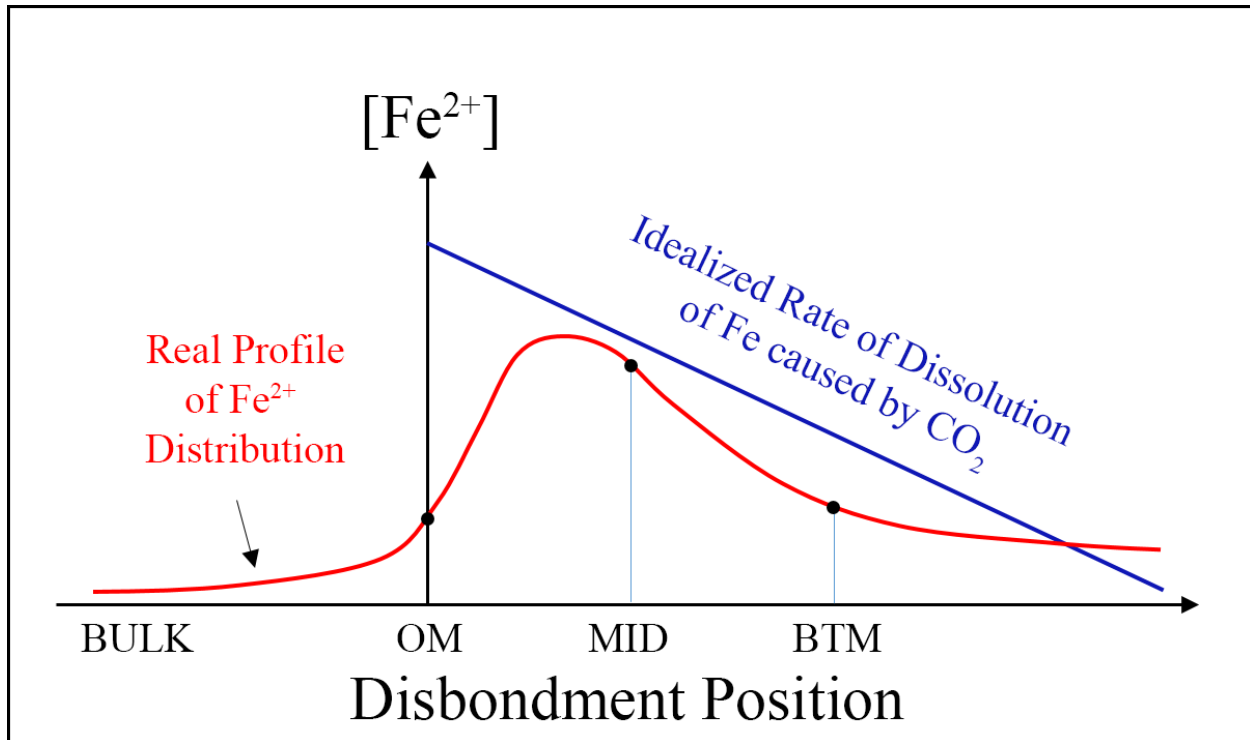
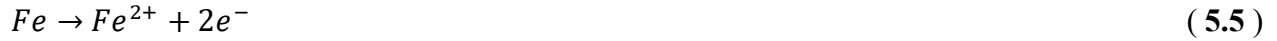


Figure 5.5 Iron distribution profile of the various key locations within the corrosion cell used in the current study.

Regardless of the discrepancies between the two systems, Fe^{2+} would be pulled towards the bottom of the disbondment by gravity as a consequence of the metal ion's weight (116). As a result, the greater concentration of Fe near the OM would inhibit diffusion of Fe out from the disbondment, and result in the greatest concentration of Fe at the bottom of the disbondment – or at least a uniform concentration at the Middle and Bottom positions. Instead, the highest concentration of Fe was measured at the Middle location and not the Bottom location. Since the corrosion rates generally decreased from the OM to the Bottom of the disbondment in both systems and electrolytic solutions tend to self-equilibrate (116), a greater concentration of Fe at the Middle location would go against the self-balancing behaviour of the solution. Therefore, another electrochemical reaction must be occurring within the disbondment at or near the Bottom location to result in the non-uniform distribution of Fe across the disbondment locations in Test I.

Based on the above discussion, it is proposed that towards the Bottom disbondment location that iron hydroxides are precipitating out through hydrolysis. It is known that in deaerated near-neutral ($4 < pH < 9$) water that iron dissolution can occur through the following hydrolysis reactions (117):



Owing to the fact that Fe^{2+} is already present in the disbondment solution, it is expected that the reactions towards bottom of the disbondment would be similar to those in **Eq. 5.3 – 5.4**, but in the reverse direction. In the presence of CO_2 , the reactions describing the hydrolysis of $FeCO_3$, rather than $FeOH_2$, would occur following (18):



The occurrence of hydrolysis through reactions within the solution or on the inner surface of the disbondment, rather than on the surface of the sample, would result in free H^+ in solution thus decreasing the pH , and result in a loss of Fe^+ from the local solution to the formation of carbonates or hydroxides – granted that the precipitates do not dissolve back into solution. This helps to provide an explanation as to why the measured pH and concentration of Fe was lower at the Bottom location of the disbondment than the Middle location. However, this likely wasn't the only reaction, and for $pH > 5$ hydrogen can be generated on the steel surfaces inside of the disbondment through the direct reduction of water, albeit kinetically slow (19), in addition to the hydrolysis and CO_2 mechanisms (19, 116, 117), the latter of which is significantly reduced by the CO_2 concentration gradient. Hydrogen reduction near the bottom of the disbondment was evident by the formation of pockets of $H_{2(g)}$ accumulating on several of the surfaces in **Figure 4.7b-c**.

As a result of the Middle location's closer proximity to the OM, it should have a greater concentration of CO_2 than the Bottom and therefore greater dissolution and hydrogen reduction rates. The surface at the OM proceeds through general CO_2 corrosion because of its ready access to CO_2 dissolved in the bulk solution, and therefore the greatest concentration of hydrogen

following the reaction in **Eq. 2.6** which produces approximately four times more hydrogen than the reduction of water alone (16). In fact, the average pH at the OM for Tests I and II, 6.38, is the value determined by the Colwell-Leis mechanism where the ratio of HCO_3^- and H_2CO_3 in solution is at unity, indicating that the corrosion rate at the OM reached steady state (12, 16). This analysis cannot confirm whether or not the metal ion concentration cell, originally proposed by Chevill (23), is responsible for the observed enhanced corrosion at the OM, but it can be deduced that the enhanced dissolution is partially driven by the flux of Fe^{2+} towards the bulk and disbondment. The accelerated corrosion observed at the surfaces near the OM in the current work are, at least in part, through hydrolysis reactions of any $FeCO_3$ at the surface of the OM, as the formation of $FeCO_3$ becomes unfavourable as Fe^+ is lost to the bulk and Bottom solutions. The effects of the local bulk environments and corrosion on crack corrosion is expanded upon in the next section.

5.2.2 LOCAL CRACK ENVIRONMENTS

The discussion in the previous section is only applicable to the local environments within the disbondment and cannot adequately describe the environments at the crack tips or inside of the cracks which are often unique from the bulk solution (56, 60, 68-73). The bulk local environments still had an influence on crack chemistry and corrosion, as demonstrated by the decreasing levels of dissolution on the cracks' fracture surfaces from the OM to the Bottom cracks in **Figure 4.16**. As data is only available on the bulk solution the corrosion and solution chemistry of the cracks can only be understood at the most fundamental level. Regardless, a brief summary of three primary conclusions on the crack corrosion and local solution inferred based on the data presented within Chapter 4 follows below.

- 1) The initial contact of solution with the sample leads to general dissolution on the surfaces, generating Fe^{2+} , HCO_3^- , and H^+ following **Eq. 2.1 – 2.6**. The flux of ions in and out of the crack by advection would be low because of the shallow crack geometry and low loading frequencies used during testing (56, 60). While light ionic species (e.g. H^+) are unaffected by the low advection and can rapidly diffuse in and out of the crack, heavy metal cations (Fe^{2+}) diffuse slowly and can accumulate to levels past their solubility limits (71). In the NNpH system, $FeCO_3$ can precipitate out from solution once the concentrations of Fe^{2+} and HCO_3^- exceed their solubility limit, i.e. Fe^{2+} becomes supersaturated (18, 19, 83) – at

25 °C the reaction is sluggish and a porous non-passivating layer will form (17-19). As a result, the corrosion products visibly compacted within the cracks shown in **Figure 4.13a-c** and along the crack walls in **Figure 4.16** are most likely a result of the saturation of Fe^{2+} inside of the cracks.

- 2) Similar to within the crack, FeCO_3 formation could become favourable through a build-up of Fe^{2+} and HCO_3^- , yet it is still sluggish, and as Fe^{2+} diffuses away from the surface any FeCO_3 is broken down through hydrolysis reactions (18, 19). Unlike the bulk surface, precipitates were retained within the cracks and enhanced dissolution occurred along the surface crevice, as shown in **Figure 4.5**, **Figure 4.6**, and **Figure 4.16**. Invoking discussion of crack geometry, fluid flow, and potential from Section 2.3.2.1, this can be considered a result of the crack itself under fatigue loading. The enhanced dissolution can then be attributed to the potential drop which emerges from the crack that balances the net cathodic current on the bulk surface (73). Therefore, the crack crevices and tips become more anodic, in comparison to the surrounding material, promoting the reduction of hydrogen in these locations and thereby the dissolution of the surrounding material (72, 73).

The build-up of Fe^{2+} from dissolution promotes the migration of anions in solution to balance the local charge or the diffusion of HCO_3^- , possibly CO_3^{2-} after HCO_3^- reduction, driven by the concentration gradient in the depth caused by the precipitation of FeCO_3 which further promote acidification at the crack tips and surface crevice through hydrolysis reactions (18, 70, 72, 73, 83). As a result, acidification lead to the enhanced dissolution of the surface crevices of the cracks, widening them significantly, while the rest of the crack in the depth direction remained compacted with corrosion products. The corrosion products are most likely FeCO_3 based on the discussion above and the EDS results presented in **Table 4.1**.

- 3) Expanding on point above, the influence of the species present in the local bulk environments should be reflected by the extent of the acidification, or dissolution and hydrolysis, at the surface crevices (**Figure 4.5**) and along the crack walls on the fracture surfaces of the cracks (**Figure 4.16**). The concentration of CO_2 and availability of anions in the local C2 solution (SO_4^{2-} and Cl^-) dictate the corrosion and chemistry at each crack tip and crevice, where greater amounts lead of either lead to greater extents of acidification. This is reflected by the greater distance of dissolution into the depth of the crack at the OM

than the Middle and Bottom cracks, with the least amount of penetration on the Bottom crack walls (**Figure 4.16**). The lack of dissolution along the crack walls within the depth direction of the Middle and Bottom cracks agrees with the corrosion trends discussed for the bulk surface in Section 5.2.1. Consequently, the crevice widths of the Middle and Bottom cracks were preferentially dissolved along the surface of the front face of the sample, i.e. dissolution was made difficult in the depth direction, because the hydrolysis of FeCO_3 on the crack walls was made difficult through a lack of participating species in solution.

The discussion and results presented here and in Section 5.2.1 may provide different evidence and conclusions for the cause of the disbondment effects, when compared to work performed by previous researchers (22, 24, 45), but the general conclusion that dissolution and hydrogen reduction decrease towards the bottom of the disbondment are in agreement with each other. Of the trends observed for the morphology of the cracks, the only trend that cannot be fully accounted for is the alternating regions of wide and thin crack crevices on the surfaces of the SCT cracks (Section 4.1.2).

Using the same material and sample type, a previous study concluded that the cause of the alternating regions crevice regions was galvanic effects induced by the presence of pearlite from the banded microstructure, exposed through the notch removal process, intersecting the surface plane with the adjacent ferrite bands (24). However, no definitive correlation between pearlite present on the surfaces and the alternating morphology of the surface crack crevices was observed. To be clear, the possibility of galvanic action between the two intersecting surface microstructural features is not being, but with no definitive evidence to make a supported conclusion other possible causes should be considered as well. Other notable possible reasons for the observed surface crack crevice morphologies may include galvanic effects caused by:

- Residual stresses induced by the milling operation to remove the pre-crack notch.
- Residual stress variations in the base material resulting from manufacturing (TMCP) and pipe fabrication.
- Stress cells induced by variations in residual compressive stresses from the fatigue pre-cracking procedure.

- Surface inclusions from surface milling and grinding operations, and within the materials thickness resulting from manufacturing operations.

5.2.3 DISBONDMENT EFFECT ON CRACK GROWTH BEHAVIOUR

5.2.3.1 Surface Growth

Thus far, any discussion on the growth behaviour of SCT specimens has been strictly focused on the comparison of growth behaviour between the SCT-OMs to that of CT specimens (Section 5.1), thereby a fundamental understanding of the SCT crack behaviour in NNpH corrosion fatigue was developed. Having done so, a baseline for comparing the growth behaviour between SCT cracks was established. Therefore, alongside the environmental information presented in the previous two subsections, the mechanisms and the differences in corrosion fatigue behaviour of the three cracks can now be understood in terms established with the OM cracks.

A trend that occurred in both tests in C2, regardless of waveform, was the decrease in crack growth rates going from the OM to the Bottom crack. A similar trend in growth rates occurred for semi-circular surface cracks in a study using notched X65 SCT samples and a 10 mm gap size disbondment, under CA loading in 5 % - CO₂ C2 solution (45). The fact that this trend occurred for two ‘different’ sample types and different disbondment geometries highlights the general impact of coating disbondments on NNpH crack propagation. The mentioned author attributed this crack growth trend under OCP conditions to the CO₂ gradient, which was expanded upon in the previous section (45), where the decreasing levels of CO₂ reduce the over-all hydrogen reduction into the disbondment and only the kinetically slow cathodic reactions of water reduction and hydrolysis generate adsorbed hydrogen towards the Bottom crack (18, 19, 83, 116, 117). Decreasing cathodic reactions, or hydrogen adsorption, on the corroding steel surfaces decreases the hydrogen available for transport to the FPZ ahead of the cracks, thereby lowering the hydrogen concentration in the FPZ and therefore the contribution of HE to crack extension (51, 53, 58, 74, 75). To reiterate, bulk hydrogen charging is the primary source of hydrogen in the NNpH system (29) and a decrease in bulk hydrogen or HE would reduce the damage by corrosion fatigue, the latter of which a highly accepted mechanism of damage in NNpH systems (7, 11, 15, 25, 28, 29, 37, 44-46, 54, 81-87, 99).

The effect of CA frequency throughout the disbondment is shown in **Figure 4.2**, where it is seen that all of the cracks demonstrate an increase in da/dN when frequency is decreased. The mechanisms for the SCT cracks' frequency response have already been discussed in detail within Section 5.1.1, and the response can be summarized as a time dependent accumulation of hydrogen. Arguably, the most important result of the differences in CA response within the disbondment is the weak responses from 10^{-2} Hz to 10^{-1} Hz of the Middle and Bottom relative to the large decreases in growth from 10^{-3} Hz to 10^{-2} Hz, in terms of both dc/dt (**Figure 4.1**) and dc/dN (**Figure 4.2**). This response indicates that a critical frequency threshold exists between 10^{-3} Hz to 10^{-2} Hz for the two cracks inside of the disbondment. Opposite to the hydrogen saturation effect found by Yu, *et al.* (54), this is a situation where the frequency is sufficiently high that hydrogen diffusion or production is too slow to provide an accelerations in growth with decreasing in frequency. As none of the cracks grew at the surface in air, hydrogen must have been able to accumulate to some degree from sources such as the crack tips and plastic zone. Similar three frequency regime responses have been found for titanium and aluminum alloys corrosion fatigue systems (52, 62). Additionally, the fact that SCT-M grew at a rate close to that of SCT-OM for $f = 10^{-3}$ Hz indicates that the loading conditions are sufficiently aggressive at 10^{-3} Hz that the environmental differences become negligible, a recognized phenomenon in the NNpH corrosion fatigue system (29, 82).

At first glance, the increasing acceleration effect of minor cycles from the OM to the Bottom in **Table 4.1** seem contradictory to the previous paragraph, given that their contribution to growth is through the time dependent accumulation of hydrogen. However, the increasing values have more to do with the low growth rates under CA loading rather than under UL&MC loading, particularly for the frequencies 10^{-1} Hz and 10^{-2} Hz where the Middle and Bottom cracks demonstrate low sensitivity to changes in frequency. This is supported by the greater differences in growth rates between the cracks under CA loading in comparison to under UL&MC loading, visually demonstrated in **Figure 4.2**.

The differences in growth between the three crack locations is related to the differences in the concentration of hydrogen in their local environments, in terms of adsorbed hydrogen on the steel surfaces or dissolved within the lattice. Mathematically, **Eq. 2.11** can be invoked to explain this effect, where the equilibrium concentration of hydrogen is proportional to the concentration of hydrogen far away from the crack tip, c_0 (54). That is to say, even under UL&MC loading, where

there's more time for hydrogen segregation, the growth rates will still decrease further into the disbondment because the equilibrium flux of hydrogen to the FPZ is dictated by the hydrogen adsorbed on the surfaces away from the crack. Even though small differences in K_{max} and ΔK existed between the three cracks the impact is not expected to be as large as the available hydrogen, based on the greater hydrogen dependency of growth due to the low mechanical driving forces of the SCT cracks, previously discussed in Section 5.1.1.

The decreasing ratios of growth between the UL&MC and UL&H waveforms of Test II, which were 1.6 and 1.4 for the Middle and Bottom cracks, respectively, infer a decreasing growth enhancement from the minor cycles further into the disbondment. As the static hold time was equivalent to the length of a minor cycle block the decrease in the minor cycles effect can be seen as a decrease in the hydrogen transported to the FPZ ahead of the crack tip by cyclic damage (29, 54, 58, 99, 100). The minor cycles enhance growth through the transport of hydrogen to the crack tip by the mobile dislocations generated over a load cycle, leading to greater growth rates over the static holds (100). It is reasonable then that if the local crack tip dissolution, or dissolution of material behind the crack tip, is decreased then the enhancement to growth by the transport of hydrogen by the dislocations generated over a cycle decreases.

5.2.3.2 Depth Growth Behaviour

In spite of the fact that the initial K_{max} and ΔK were 1.5x greater in the depth direction than at the surface, the depth growth rates presented in **Table 4.4** show that only the Bottom cracks grew faster in their depths. In fact, the crack at the OM grew faster at the surface than in the depth. This is contrary to CA testing in air, where no growth was detected on the surface cracks in either Test I or Test II, yet clear regions of growth were found and measured on the fracture surfaces – e.g., the regions indicated in **Figure 4.16**. In addition to the reasons provided in Section 5.1.1.1, growth in the depth direction but not at the surface in air makes sense from a fracture mechanics perspective, because of the small aspect ratios, as cracks tend to grow from a semi-elliptical shape towards a semi-spherical shape (118). The fact that surface growth occurred at rates either slightly above or below the depth in C2 solution defies that same logic. Therefore, several factors must be considered to explain this phenomenon:

- 1) *Crack closure*

From **Figure 4.13a-c** it is clear that corrosion products had precipitated out and compacted within the crack. Given the low R of the underloads ($R = 0.1$) the crack tip opening displacement upon unloading is quite small, and likely less than the thickness of the corrosion product inside the crack. Thus, these insoluble corrosion products can act as a mechanical wedge within the crack and retard crack growth by reducing the local ΔK through effectively increasing K_{\min} (119). This effect, otherwise known as crack closure, is known to be particularly prevalent in corrosion fatigue involving aqueous environments where corrosion debris can accumulate within the crack (59, 60, 119). Other notable closure effects in corrosion fatigue are fracture surface roughness and crack tip plasticity effects (60). The fact that the depth growth rates in air exceeded the surface growth rates in C2 for 10^{-1} Hz and 10^{-2} Hz, except for 10^{-2} Hz of the OM, is strong evidence that some form of closure occurred during testing. The comparison between in air depth and C2 surface rates is reasonable because the rates were found to be fairly comparable in C2 solution.

It is unclear, however, as to how much of an effect this will have during underloads, for the UL&MC or UL&H waveforms, because there is a potential for the crack to widen and accommodate the wedge during the minor cycles or static hold blocks. In fact, it has been shown for aluminum alloys that closure effects are reduced for low R underloads, in comparison to CA cycles, when followed by a series of high R minor cycles (97, 98). Additionally, wedging can lead to the opposite effect under monotonic loading and lead to an increase in the crack driving force, a.k.a. anti-shielding, and accelerate crack growth (119).

2) *Hydrogen availability*

The largest source of hydrogen in this corrosion fatigue system comes from the dissolution of the bulk sample surface; this is especially true in the depth, as fluid flow is very limited inside the crack, because of the corrosion products and geometry, which prevents dissolution of the crack walls and the production of hydrogen locally. This limits the transport of hydrogen to the depth crack tip to diffusion through the thickness of the sample. For example, for the deepest crack used in testing, 1.18 mm, and a hydrogen diffusivity of 2×10^{-7} cm²/s (120) it would take ~ 19.3 h ($1.18^2 / 2 \times 10^{-5}$) for hydrogen to reach the depth

crack tip by diffusion. This is an insignificant amount of time compared to the total testing time of the tests (>2000 h), but it does not indicate the time it takes to reach an equilibrium flux across the entire crack plane, which would take significantly longer. Also, as the back of the sample is coated, an equilibrium flux does not correlate to equal levels of hydrogen at the surface and depth of the crack and a gradient of hydrogen across the sample should be expected (114). Microstructural features and defects, such as pearlite bands in the banded microstructure (121) and grain boundaries (113, 114), act as effective trapping sites for hydrogen which can further inhibit hydrogen diffusion through the thickness of the material.

3) *Different stress states*

As the cracks are not through thickness, the depth of the crack should be mostly, if not entirely, in a plane strain stress state. The stress ahead of the crack in the depth direction (plane strain) should be greater than that of the surface (plane stress), following that the stress reaches a peak of σ_{YS} and $2.5\sigma_{YS}$, under plane stress and plane strain, respectively, with the latter's plastic zone $\sim 1/6$ of the size of the former which should better facilitate fracture, if they were at the same K_{max} (122). The plane strain state also has triaxial stresses, while ideally plane stress is biaxial, meaning the former has much higher stresses within the plastic zone. However, plain strain would lead to a smaller amount of hydrogen segregation in the region ahead of the crack tip, because of its smaller plastic zone, which would lead to a lower amount of material to sample for weakest links for hydrogen damage. Furthermore, the higher driving force for hydrogen diffusion because of the greater hydrostatic stress in the depth is not as significant as it would be if the surface because of the hydrogen gradient discussed in the previous point.

From the three factors listed above it is difficult to determine which has the highest impact on crack growth in the depth direction. Neither compliance nor chemical potential measurements were made during testing, so a quantitative analysis cannot be performed to help provide further insight on the magnitude of the factors or their effects. The influence of hydrogen can be confirmed, based on the greater growth in the depth of the Bottom crack yet lower at the OM which would indicate that hydrogen had a lessened effect at the Bottom, which could only result from a lower concentration of hydrogen. Additionally, it can be confirmed that hydrogen damage did indeed

occur based on the features presented in **Figure 4.20**, but these features did not increase in occurrence or density although the growth rates, some distance below the surface, increased with increasing depth. Analysis of the mechanism of hydrogen embrittlement in NNpH corrosion fatigue is beyond the scope of this study, but the micro-plasticity demonstrated within the range of the plastic zone ahead of the cracks in the depth is indicative of HELP. This agrees with the conclusions in the most comprehensive study, in recent history, on NNpH corrosion fatigue behaviour which presented evidence for the HELP mechanism over HEDE (123).

5.3 HYDROSTATIC TESTING

When comparing the depth profiles of Test I and II in **Figure 4.13**, it is clear that the hydrostatic test affected the depth crack morphologies. In spite of loading above 110 % SMYS and holding for 1 h and at 100 % SMYS for 4 h, there is no clear indication that the hydrostatic test would prevent further crack growth based on the sharp crack tips alone, as shown in **Figure 4.15d-f**. A careful eye may observe that there is plastic deformation, however, in the form of smoothed walls and void clusters ahead of the quasi-cleavage zone of damage by the hydrostatic test (**Figure 4.21**). Another consequence of the hydrostatic test was the significant widening of the crack accompanied by the loss of the wedged corrosion products inside the crack.

Similar damage along the crack walls has been observed in hydrostatic test simulations for cracks in NNpH environments, where it was found that deeper cracks exhibit less growth due to the formation of micro-cracks and plastic deformation ahead of the crack front which can reduce the driving force for crack advance (106). The damage itself can be classified as internal hydrogen assisted cracking because of the coatings applied to the surface of the sample which prevented the direct exposure of the crack to the NNpH solution during hydrogen charging and testing (74). This indicates that it is not necessary for the steel to be exposed to solution during a loading event for hydrogen damage to occur. Furthermore, the widened crack profiles in Test II in comparison to those of Test I agree with an investigation on the field crack profiles where a thick to thin transition occurred along the profile of the cracks, attributing the thick region to hydrostatic testing and the thin region to growth post-hydrostatic testing (124).

These preliminary results present a potentially dire situation for the use of hydrostatic testing of defects in the field. Even though the growth from the hydrostatic test was far from an amount that

could lead to leaks or ruptures during field testing, it is far greater in terms of da/dt than that of the fatigue waveforms used in testing. Such lines could then be approved for implementation back into service. However, these flaws, now potentially re-exposed to NNpH environments and variable amplitude loading, will now be more likely to cause a failure. This is a consequence of the pre-existing high stress intensities in the depth direction in combination with the widening of the cracks, the latter resulting in the loss of the wedged corrosion products inside of the crack. The former two factors present an increased integrity risk as they lead to increased hydrogen production or diffusion into the crack, through higher hydrostatic stresses and fluid flow. The loss of the corrosion products inside of the crack leads to the loss of the wedge induced closure effect (increased ΔK_{eff}) and an effective barrier to fluid flow inside of the crack.

The growth may initially be retarded by the plastic damage caused by the hydrostatic test, but even if the crack tips were blunted the decreased effect of closure and enhanced hydrogen generation would eventually allow the crack overcome the highly strained microstructure. Further yet, the highly deformed region ahead of the crack tip would provide an ample amount of defects for hydrogen to sample, leading to micro-crack initiation and propagation back to the main crack to re-sharpen it (29) The hydrostatic test itself can be considered effectively as an overload cycle, which can lead to reduced crack growth through crack tip blunting, compressive residual stresses surrounding the plastic zone, and residual stresses behind the crack tip resulting in plasticity-induced closure effects (48). Following a hydrostatic test, however, the line must be depressurized which can be considered as an underload event, which can reduce the effectiveness of the retardation effect of the overload (123) or, as a matter of fact, enhance crack growth based on a recent study on underload-overload variable amplitude loading (102). As such, a delayed response of the crack may occur until growth is re-initiated by an underload event, which agrees with field studies that found that crack growth has occurred in as little as four months following a hydrostatic test (125).

CHAPTER 6: CONCLUSIONS AND RECOMMENDATIONS

The objective of this investigation was to establish a fundamental understanding on the crack growth behaviour of shallow surface cracks when exposed to near-neutral pH (NNpH) environments under fluctuating internal pressure. To be more specific, it was important to simulate field conditions to the greatest extent without performing a full-scale test, while verifying the growth trends already established for traditional fracture mechanics samples. To do so, novel cracks of aspect ratios close to those found in the field were studied while simultaneously simulating the environments under coating disbondments and subjecting the cracks to fatigue waveforms designed to simulate real pressure fluctuations experienced during pipeline operations. From the results of the study, the behaviour of surface cracks at several locations under a coating disbondment and open circuit potential (OCP) conditions while subjected to various cyclic waveforms was established.

6.1 COMPARISON OF CRACK GEOMETRIES

A study comparing the crack growth behaviour of the novel surface crack tension (SCT) specimen's surface cracks to the through thickness cracks of compact tension (CT) specimens in NNpH environments was performed in Section 5.1. Only the results from the SCT crack located above the Open Mouth (OM) of the disbondment was used for the comparison, as its environment most closely represented the environment that the CT specimens were exposed to. Overall, the general behaviour of the cracks were similar, confirming that the trends observed for CT specimens were valid for the surface crack geometry. The investigation not only established a baseline behaviour for the novel specimen, but provided new information on the crack growth mechanics in NNpH environments under constant amplitude (CA) and variable amplitude (VA) loading.

6.1.1 CONSTANT AMPLITUDE LOADING

1. No growth was detected on the surfaces of SCT-OM when tested in air, but occurred when exposed to NNpH environments. The lack of growth in air was attributed to the experimental procedures used to prepare the notchless surface crack.

2. In C2 solution, the SCT-OM crack demonstrated an increase in crack growth rate (da/dN) with a decrease in loading frequency.
3. The da/dN of SCT-OM was at least one order of magnitude less than the CT specimens under CA loading, for any given frequency, because of the lower mechanical driving forces (K_{max} and ΔK) of SCT-OM.
4. The lower mechanical driving force of SCT-OM led to a more sensitive response to frequency in comparison to CT specimens under CA loading. This was a result of the slow diffusion of hydrogen to the FPZ, and a greater influence of HE damage mechanisms on SCT-OM's growth.
5. Environmentally short crack effects and enhanced hydrogen production near the SCT-OM crack tips allowed SCT-OM to grow under CA conditions far less aggressive than the Combined Factor thresholds for CT crack growth.

6.1.2 VARIABLE AMPLITUDE LOADING

1. A superficial decreased sensitivity to underload frequency was found for SCT-OM and was attributed to the lower influence of hydrogen accumulation during an underload relative to the time-dependent hydrogen accumulation during minor cycles.
2. The quasi-static loading condition (high R) and hydrogen accumulation during the minor cycles can still contribute to crack growth, even in the absence of a direct mechanical fatigue damage.
3. The enhancement in crack growth under UL&MC loading, known as the Acceleration Factor, was significantly greater for the SCT crack than the CT cracks. This reflected the low growth rates of SCT cracks under CA loading, and the relatively greater contribution of hydrogen to the damage mechanism of short surface cracks in NNpH environments.

4. The effect of minor cycles' on SCT-OM's growth relative to static holds is less pronounced than for CT cracks, linked to the minor cycles lower mechanical contribution to growth for the SCT cracks.
5. UL&H waveforms caused greater crack growth rates than CA loading, a trend opposite of the CT cracks, because of the increased hydrogen accumulation prior to an underload.

6.2 COATING DISBONDMENT EFFECTS

Section 5.2 focused on discussing the local environments located under a coating disbondment and the resulting effect on surface crack growth under variable pressure fluctuations. This was possible through the analysis and discussions in Section 5.1 which developed a baseline growth behaviour for the OM cracks, allowing for the comparison of cracks throughout the coating disbondment in Section 5.2. The three cracks on the SCT specimen were located at various locations of the 5 mm gap disbondment with the OM, Middle, and Bottom cracks located -10 mm (above), 65 mm, and 145 mm from the disbondment opening, or the open mouth of the disbondment. The initial environment at all locations was the same – C2 solution constantly purged with 5 % CO₂, under OCP conditions – and any environmental changes were caused by conditions developed during testing.

6.2.1 LOCAL ENVIRONMENT EFFECTS

1. Different local environments formed inside of the disbondment as a result of a decreasing gradient of CO₂ into the disbondment and Fe²⁺ diffusion away from the OM towards the bulk environment and into the disbondment because of gravity effects. Constant loss of Fe²⁺ in the local environment at the OM potentially lead to enhanced dissolution rates of those local surfaces.
2. Fe²⁺ could not diffuse out of the disbondment because of high local concentrations near the OM and gravity effects, leading to increased rates of hydrolysis towards the bottom of the disbondment in solution, and the precipitation of Fe corrosion products and the minor acidification of the local environments.

3. FeCO_3 precipitated and wedged inside of the cracks because of Fe^{2+} saturation, and resulted in concentration gradient driven diffusion of $\text{H}_2\text{CO}_3/\text{HCO}_3^-$ towards the crack depth. Acidification of the surface crevice and crack tips resulting from the potential drop across the crack crevice and enhanced flux of $\text{H}_2\text{CO}_3/\text{HCO}_3^-$ towards the crack depths enhanced dissolution rates along the surface crevice, increasing local production of hydrogen.
4. Decreasing concentrations of H_2CO_3 and HCO_3^- into the disbondment decreased the dissolution and hydrolysis in the thickness direction, causing preferential dissolution and widening along the surface crevices of the Middle and Bottom cracks in the other two directions.

6.2.2 EFFECT OF LOCAL ENVIRONMENTS ON CRACK GROWTH

1. The changing local environments lead to an over-all decrease in crack growth rates from the OM to the Bottom crack, because of decreased hydrogen reduction rates on the steel surfaces. All three cracks demonstrated increased da/dN with decreasing CA or underload frequency, but the magnitude of change in da/dN with changing frequency decreased from the OM to the Bottom crack.
2. A greater da/dN increase from 10^{-2} Hz to 10^{-3} Hz for the Middle and Bottom cracks, than from 10^{-1} Hz to 10^{-2} Hz, indicated that some threshold value occurs between these two frequencies and at 10^{-3} Hz the loading was aggressive enough to cause similar growth rates at the OM and Middle cracks.
3. The differences in crack responses to changing frequency reflected a decrease in corrosion fatigue behavior, or decreasing hydrogen damage. This was reflected by the decreasing ratio of growth between the UL&MC to UL&H waveforms from the OM to the Bottom crack, meaning that the cyclic nature of the minor cycles was becoming less effective at transporting hydrogen to the crack tips' FPZ. The Acceleration Factors of each frequency generally increased from the OM to the Bottom crack, owing to the greater differences in growth rates between the cracks under CA waveforms than UL&MC.

4. Growth in the depth direction of the cracks occurred in air, contrary to the lack of growth at the surface. The growth rates in C2 solution demonstrated a significantly different behaviour than in air testing, where generally only the Bottom cracks exhibiting greater depth growth rates. This was attributed largely to effects of crack closure and hydrogen gradients through the thickness of the cracks.
5. In the cleavage zone produced by fracturing the sample, evidence of micro-plasticity in the cleavage produced near micro-cracks initiated ahead the crack front, or connected to it, and other small features, namely cavity and protrusion facets, provided evidence that the atomic mechanism of HE for the SCT cracks in NNpH environments is HELP.

6.3 MINOR STUDY OF HYDROSTATIC TESTING

Hydrostatic testing was performed on the cracks of Test II, post VA waveform testing, to investigate the possible growth enhancing or retarding effects on the SCT cracks. The crack surfaces were covered during testing to prevent direct exposure to the environment, charged in C2 solution for 10 days under OCP conditions, and loaded using a simulated hydrostatic test waveform while remaining in solution.

1. Damage caused by the hydrostatic test was visibly clear by the widened crack depth profiles and by fracture surface analysis, where the hydrostatic damage, quasi-cleavage in nature, was separated from the quasi-cleavage region of corrosion fatigue by shear walls and the cleavage zone by smoothed grains and clusters of ductile dimples.
2. The application of a coating over the surfaces of the cracks prevented the direct exposure to the environment, meaning that the quasi-cleavage damage mode could only be caused by hydrogen diffusion indicating that damage was caused by either internal-hydrogen-assisted-cracking (IHAC) or hydrogen-environment-assisted cracking (HEAC).
3. Widening of the cracks and lack of crack tip blunting or wedged corrosion products in the crack depth profile meant that growth retardation of any subsequent cyclic loadings could only occur as a result of the plastic damage ahead of the crack tips. Otherwise, growth

rates could potentially be enhanced by increased fluid flow inside of the cracks and a reduced corrosion-debris-induced closure effect.

4. The overload effect of the hydrostatic damage, i.e. plastic damage, is only effective if it is not followed by an underload event, such as immediate depressurization of the pipe, otherwise the overload effects could be mitigated and the crack tip will not blunt under further loading.

6.4 RECOMMENDATIONS FOR FUTURE WORK

1. This investigation demonstrated that the growth of short surface cracks can occur at mechanical conditions well below the thresholds determined for the long, through thickness cracks of traditional fracture mechanics samples when exposed to NNpH environments. This occurred even when pre-existing overload effects or compressive stresses were present at the surface crack tips. Therefore, it is clear that the cracks experience environmentally short crack effects, that much can be said for their growth. However, in order to expand the predictive models of crack growth, e.g., the Combined Factor Model, to short crack geometries further testing using the same crack geometry is necessary under varying initial conditions of ΔK , K_{\max} , and frequency. Otherwise a full understanding of the crack growth behaviour, and thereby the accuracy of the predictive method will be flawed at best.
2. Several effects of waveforms were investigated in this study, including the effect of the frequency of low R cycles under CA and UL&MC, the acceleration effect of minor cycles versus the effect of statics holds. In actuality, pipelines experience highly variable loading spectra and this investigation can only be considered as a preliminary study. To better develop predictive methods for growth rates a larger investigation into each of the mechanical variables of the VA waveforms, such as the number of minor cycles or hold time, and their effects on SCT crack growth rates should be undertaken.
3. The current work only used a single configuration of gap size, % CO₂, and potential (OCP). Albeit that each of these factors have been studied in the past for different experimental

setups, often one or more of the experimental variables was unrealistic to field conditions, and very little has been done into investigating the effect of these environmental conditions on the growth of true surface flaws, i.e. surface cracks without a starter notch. Of particular interest would be the effect of CO₂ levels, based on the disbondment effect discussed in Section 5.2, and the effect of simulated seasonal variations of CO₂ levels and the effect on the growth behaviour of the cracks inside of the disbondment.

4. Even though the results were not reported here, the use of optical and contact step height profilometry measurement techniques were experimented with for determining the growth of the cracks. The most promising technique used was confocal microscopy, in particular confocal laser scanning microscopy. Excellent contrasts were obtained between growth bands on the fracture surface, and such images were used to aid in the differentiation of growth zones. Further investigation into the use of these characterization techniques, particularly for surface roughness measurements, could provide more reliable growth data that is less skill based if the methodology is properly developed.
5. In the discussion of Section 5.2 a point was brought up on the use of multiple coupons in disbondment corrosion studies, where interruptions of potential could be introduced by small gaps between coupons. It is recommended that in future testing, single samples of steel are used to determine corrosion rates and coating methodologies are used to preserve the segments of the original surfaces along the entire length of the sample. This can prevent transient effects of interruptions in corrosion potential, while simultaneously providing a more accurate simulation of real field conditions. Optical step height measurements could then be utilized to determine the corrosion rates, based on the initial and final step height differences between the coated and exposed steel surfaces.

BIBLIOGRAPHY

- (1) Justice J, Mackenzie J. Progress in the Control of Stress Corrosion Cracking in a 914mm O.D. Gas Transmission Pipeline. 1988; Pipeline Research Committee of the American Gas Association; 1988.
- (2) Delanty B, O'Beirne J. Major Field Study Compares Pipeline SCC with Coatings. The Oil and Gas Journal. 1992;90(24):39-44.
- (3) Authors Unknown. Stress Corrosion Cracking, Recommended Practices 2007. Calgary, Alberta, Canada: Canadian Energy Pipeline Association (CEPA); 2007.
- (4) Parkins R. A Review of Stress Corrosion Cracking of High Pressure Gas Pipelines (No. 00363). Corrosion 2000; March 26-31 2000; Houston, Texas, US: NACE International; 2000.
- (5) Authors Unknown. Report 2013-B: Pipeline Performance in Alberta, 1990-2012. Calgary, Alberta, Canada: Alberta Energy Regulator; 2013 Aug 1.
- (6) Authors Unknown. Focus on Safety and Environment - A Comparative Analysis of Pipeline Performance - 2000-2009. Calgary, Alberta, Canada: National Energy Board of Canada; 2011.
- (7) Jeglic F. Analysis of Ruptures and Trends on Major Canadian Pipeline Systems. 5th International Pipeline Conference; October 4-8, 2004; Calgary, Alberta, Canada: ASME; 2004.
- (8) Beavers J, Harle B. Mechanisms of High-pH and Near-Neutral-pH SCC of Underground Pipelines. Journal of Offshore Mechanics and Arctic Engineering. 2001;123(3):147-51.
- (9) Fang B, Atrens A, Wang J, Han E, Zhu Z, Ke W. Review of Stress Corrosion Cracking of Pipeline Steels in "Low" and "High" pH Solutions. Journal of Materials Science. 2003 Jan;38(1):127-32.
- (10) Baker M. Stress Corrosion Cracking Study. ChallengeUs.; 2005 January.
- (11) Zvirko O, Savula S, Tsependa V. Stress Corrosion Cracking of Gas Pipeline Steels of Different Strength. Procedia Structural Integrity. 2016;2:509-16.
- (12) Charles E, Parkins R. Generation of Stress Corrosion Cracking Environments at Pipeline Surfaces. Corrosion Science. 1995;51(7):518-27.
- (13) Authors Unknown. Public Inquiry Concerning Stress Corrosion Cracking on Canadian Oil and Gas Pipelines: Report of the Inquiry: MH-2-95. In: Canadian Research Index. Ann Arbor: ProQuest Micromedia; 1996.

- (14) Chen W, King F, Jack T, Wilmott M. Environmental Aspects of Near-neutral pH Stress Corrosion Cracking of Pipeline Steel. *Metall and Mat Trans A*. 2002 May;33(5):1429-36.
- (15) Parkins R, Blanchard W, Delanty BS. Transgranular Stress Corrosion Cracking of High-Pressure Pipelines in Contact with Solutions of Near Neutral pH. *Corrosion Engineering*. 1994;50(5):394-408.
- (16) Asher S, Leis B, Colwell J, Singh P. Investigating the Mechanism of Transgranular Stress Corrosion Cracking in Near-neutral pH Environments on Buried Fuel Transmission Pipelines. *Corrosion Science*. 2007;63(11):932-9.
- (17) Zhang L, Li X, Du C, Cheng Y. Corrosion and Stress Corrosion Cracking Behavior of X70 Pipeline Steel in a CO₂-Containing Solution. *J of Materi Eng and Perform*. 2009;18(3):319-23.
- (18) Hernandez J, Muñoz A, Genesca J. Formation of Iron-Carbonate Scale-layer and Corrosion Mechanism of API X70 Pipeline Steel in Carbon Dioxide-saturated 3% Sodium Chloride. *Afinidad LXIX*. 2012;69(560):251-8.
- (19) Nescic S. 19 - Carbon Dioxide Corrosion of Mild Steel. In: Revie R, Uhlig H, editors. *Uhlig's Corrosion Handbook*. 3rd ed. Danvers, MA, USA: John Wiley & Sons, Inc.; 2011. p. 229-45.
- (20) Jia Y, Wang J, Han E, Ke W. Stress Corrosion Cracking of X80 Pipeline Steel in Near-Neutral pH Environment under Constant Load Tests with and without Preload. *Journal of Materials Science and Technology*. 2011;27(11):1039-46.
- (21) Chen W, Eadie R, Sutherby R. 4. 12 - Environmental Effects on Near-Neutral pH Stress Corrosion Cracking in Pipelines. In: Shipilov S, Jones R, editors. *Environment-Induced Cracking of Materials, Volume 2 - Prediction, Industrial Developments and Evaluation*. Amsterdam, The Netherlands: Elsevier; 2008. p. 211-20.
- (22) Chevillat K, Eslami A, Chen W, Eadie R, Kania R, Worthingham R, et al. Developing Cathodic Protection Based on Disbondment Geometry (IPC2012-90675). 2012 9th International Pipeline Conference; September 24-28, 2012; Calgary, Alberta, Canada: ASME; 2012.
- (23) Chevillat K, Chen W, Van Boven G, Kania R, Been J. Correlating Corrosion Field Data with Experimental Findings for the Development of Pipeline Mitigation Strategies (IPC2014-33678). 2014 10th International Pipeline Conference; September 29-October 3, 2014; Calgary, Alberta, Canada: ASME; 2014.
- (24) Chevillat K. Investigation of Corrosion and Crack Morphology Behavior under Disbonded Coatings on Pipelines [dissertation]. University of Alberta; 2015.

- (25) Egbewande A, Chen W, Eadie R, Kania R, Van Boven G, Worthingham R, et al. Transgranular Crack Growth in the Pipeline Steels Exposed to Near-Neutral pH Soil Aqueous Solutions: Discontinuous Crack Growth Mechanism Corrosion Science. 2014;83:343-54.
- (26) Beavers J, Johnson J, Sutherby R. Materials Factors Influencing the Initiation of Near-Neutral pH SCC on Underground Pipelines (IPC2000-221). 2000 3rd International Pipeline Conference; October 1-5, 2000; Calgary, Alberta, Canada: ASME; 2000.
- (27) Elboujdaini M, Wang Y, Revie R. Initiation of Stress Corrosion Cracking on X-65 Linepipe Steels in Near-Neutral pH Environment (IPC2000-220). 2000 3rd International Pipeline Conference; October 1-5, 2000; Calgary, Alberta, Canada: ASME; 2000.
- (28) Chen W, Sutherby R. Crack Growth Behavior of Pipeline Steel in Near-Neutral pH Soil Environments. Metall and Mat Trans A. 2007 Jun;38(6):1260-8.
- (29) Chen W, Kania R, Worthingham R, Van Boven G. Transgranular Crack Growth in the Pipeline Steels Exposed to Near-neutral pH Soil Aqueous Solutions: The Role of Hydrogen. Acta Materialia. 2009;57(20):6200-14.
- (30) King F, Jack T, Chen W, Wang S, Elboujdaini M, Revie W, et al. Development of a Predictive Model for the Initiation and Early Stage Growth of Near Neutral pH SCC of Pipeline Steels (No. 01214). Corrosion 2001; March 11-16, 2001; Houston, TX, USA: NACE International; 2001.
- (31) Di Liberto S, Gabetta G. Stress Corrosion Cracking by Anodic Dissolution and Hydrogen Permeation in Pipeline Steels. Mater Sci. 1997;33(4):411-20.
- (32) Wu M, Chen X, He C, Jun X, Xiao J. Effect of CO₂ Partial Pressure on SCC Behavior of Welded X80 Pipeline in Simulated Soil Solution. Acta Metallurgica Sinica. 2011;24(1):65-74.
- (33) Zhao W, Wang YX, Zhang T, Wang Y. Study on the Mechanism of High-Cycle Corrosion Fatigue Crack Initiation in X80 Steel. Corrosion science. 2012;57:99-103.
- (34) Mustapha A, Charles E, Hardie D. Evaluation of Environment-assisted Cracking Susceptibility of a Grade X100 Pipeline Steel. Corrosion Science. 2012;54:5-9.
- (35) Van Boven G, Chen W, Rogge R. The role of residual stress in neutral pH stress corrosion cracking of pipeline steels. Part I: Pitting and cracking occurrence. Acta Materialia. 2007;55(1):29-42.
- (36) Chen W, Van Boven G, Rogge R. The Role of Residual Stress in Neutral pH Stress Corrosion Cracking of Pipeline Steels – Part II: Crack dormancy. Acta Materialia. 2007;55(1):43-53.

- (37) Asher S, Singh P. Role of Stress in Transgranular Stress Corrosion Cracking of Transmission Pipelines in Near-Neutral pH Environments. *Corrosion*. 2009;65(2):79.
- (38) Eadie R, Sutherby R. Long Seam Welds in Gas and Liquids Pipelines and Near-Neutral pH Stress Corrosion Cracking and Corrosion Fatigue (IPC2002-27118). 4th International Pipeline Conference; 2002; Calgary, Alberta, Canada: ASME; 2002.
- (39) Chen W, Wang S, Chu R, King F, Jack T, Fessler R. Effect of Precyclic Loading on Stress-corrosion-cracking Initiation in an X-65 pipeline Steel Exposed to Near-neutral pH Soil Environment. *Metall and Mat Trans A*. 2003 Nov;34(11):2601-8.
- (40) Eslami A, Chen W. Stress Corrosion Cracking Initiation Under the Disbonded Coating of Pipeline Steel in Near-Neutral pH Environment. *Corrosion science*. 2010 .;52:3750-6.
- (41) Eslami A, Chen W. Effect of CO₂ and R-Ratio on Near-Neutral pH Stress Corrosion Cracking Initiation Under a Disbonded Coating of Pipeline Steel. *Corrosion science*. 2011;53:2318-27.
- (42) Chen W, King F, Vokes E. Characteristics of Near-Neutral-pH Stress Corrosion Cracks in an X-65 Pipeline. *Corrosion*. 2002;58(3):267-75.
- (43) Chen W. An Overview of Near-Neutral pH Stress Corrosion Cracking in Pipelines and Mitigation Strategies for Its Initiation and Growth. *Corrosion*. 2016 Jul;72(7):962-77.
- (44) Chen W, Sutherby R. Environmental Effect of Crack Growth Rate of Pipeline Steel in Near-neutral pH Soil Environments (IPC2004-449). 5th International Pipeline Conference; 2004; Calgary, Alberta, Canada: ASME; 2004.
- (45) Egbewande A, Chen W, Eadie R, Kania R, Van Boven G, Worthingham R, et al. Surface Crack Growth Behavior of Pipeline Steel Under Disbonded Coating at Free Corrosion Potential in Near-Neutral pH Soil Environments. *Metall and Mat Trans A*. 2014;45(11):4946-59.
- (46) Been J, Eadie R, Sutherby R. Prediction of Environmentally Assisted Cracking on Gas and Liquid Pipelines (IPC2006-10345). 6th International Pipeline Conference; September 29-October 3, 2008; Calgary, Alberta, Canada: ASME; 2006.
- (47) Ritchie R. Mechanisms of Fatigue-crack Propagation in Ductile and Brittle Solids. *International Journal of Fracture*. 1999;100(1):55-83.
- (48) Anderson T. *Fracture Mechanics Fundamentals and Applications*. 3rd ed. Boca Raton, FL, USA: CRC Press; 2005. p. 451-491.
- (49) Sadananda K, Vasudevan A, Kang I. Effect of Superimposed Monotonic Fracture Modes on the ΔK and K_{max} Parameters of Fatigue Crack Propagation. *Acta Materialia*. 2003 Jul;51(12):3399-414.

- (50) Sadananda K, Vasudevan A. Crack Tip Driving Forces and Crack Growth Representation Under Fatigue. *International Journal of Fatigue*. 2004;26(1):39-47.
- (51) Gangloff R. Corrosion Fatigue Crack Propagation in Metals (NASA CR-4301). 1st International Conference on Environment Induced Cracking of Metals; 1988; Houston, TX, USA: NACE International; 1990. p. 4-19.
- (52) Gangloff R. Corrosion Fatigue Crack Propagation in Metals (NASA CR-4301). 1st International Conference on Environmental Induced Cracking of Metals; 1988; Houston, TX, USA: NACE International; 1990. p. 46-99.
- (53) Oriani R. Hydrogen — The Versatile Embrittler. *Corrosion*. 1987;43(7):390-7.
- (54) Yu M, Xing X, Zhang H, Zhao J, Chen W, Eadie R, et al. Corrosion Fatigue Crack Growth Behaviour of Pipeline Steel Under Underload-Type Amplitude Loading Schemes. *Acta Materialia*. 2015;96:159-69.
- (55) Gangloff R. 6.02 - Hydrogen-assisted Cracking. In: Ritchie RO, Karihaloo B, editors. *Comprehensive Structural Integrity*. Oxford, United Kingdom: Elsevier Ltd; 2003. p. 69-77.
- (56) Turnbull A, Saenz Santa de Maria M. Predicting the Kinetics of Hydrogen Generation at the Tips of Corrosion Fatigue Cracks. *Metallurgical Transactions A*. 1988;19(7):1795-806.
- (57) Zohdi T, Meletis E. Calculation of Hydrogen Buildup in the Neighborhood of Intergranular Cracks. *Journal of the Mechanical Behaviour of Materials*. 1998;9(1):100.
- (58) Oriani R. Hydrogen Embrittlement of Steels. *Annual Review of Materials Science*. 1978;8:327-57.
- (59) Gangloff R. Corrosion Fatigue Crack Propagation in Metals (NASA CR-4301). 1st International Conference on Environment Induced Cracking of Metals; 1988; Houston, TX, USA: NACE International; 1990. p. 150-4.
- (60) Turnbull A. 6.04 - Environment-assisted Fatigue in Liquid Environments. In: Ritchie RO, Karihaloo B, editors. *Comprehensive Structural Integrity*. Oxford, United Kingdom: Elsevier Ltd; 2003. p. 173-7.
- (61) Vosikovskiy O. Fatigue-Crack Growth in an X-65 Line-Pipe Steel at Low Cyclic Frequencies in Aqueous Environments. *Journal of Engineering Materials and Technology*. 1975;97(4):298-304.
- (62) Gangloff R. 26 - Environmental Cracking - Corrosion Fatigue. In: Baboian R, editor. *Corrosion Tests and Standards: Application and Interpretation*, 2nd Edition. West Conshohocken, PA, USA: ASTM International; 2005. p. 302-21.

- (63) Scott P, Thorpe T, Silvester D. Rate-determining Processes for Corrosion Fatigue Crack Growth in Ferritic Steels in Seawater. *Corrosion Science*. 1983;23(6):559-75.
- (64) Kawai S, Koibuchi K. Effect of Waveform on Corrosion Fatigue Crack Growth. *Fatigue of Engineering Materials and Structures*. 1979;1:395-407.
- (65) Pao P, Gill S, Bayles R. Effect of Ripple Loads on Stress-corrosion Cracking in Al 7075 alloys. *Scripta Metallurgica et Materiala*. 1991;25(9):2085-9.
- (66) Paulson A, Hoepfner D. Corrosion Fatigue Crack Growth Rates in Aluminum Alloys Subjected to Variable Ripple Sequences. 17th Symposium of the International Committee on Aeronautical Fatigue; June 9-11, 1993; Stockholm, Sweden; 1993.
- (67) Pao P, Bayles R, Yoder G. Effect of Ripple Load on Stress-Corrosion Cracking in Structural Steels. *Journal of Engineering Materials and Technology*. 1991;113(1):125-9.
- (68) Gangloff R. Crack Size Effects on the Chemical Driving Force for Aqueous Corrosion Fatigue. *Metallurgical Transactions A*. 1985;16A:953-69.
- (69) Turnbull A. The Environmentally Small/Short Crack Growth Effect: Current Understanding. *Corrosion Reviews*. 2012;30(1):1-17.
- (70) Turnbull A. 6.04 - Environment-assisted Fatigue in Liquid Environments. In: Ritchie RO, Karihaloo B, editors. *Comprehensive Structural Integrity*. Oxford, United Kingdom: Elsevier Ltd; 2003. p. 189-96.
- (71) Turnbull A. Theoretical Analysis of Influence of Crack Dimensions and Geometry on Mass Transport in Corrosion Fatigue Cracks. *Materials Science and Technology*. 1985;1(9):700-10.
- (72) Gangloff R. Corrosion Fatigue Crack Propagation in Metals (NASA CR-4301). 1st International Conference on Environment Induced Cracking of Metals; 1988; Houston, TX, USA: NACE International; 1990. p. 112-30.
- (73) Turnbull A, Thomas J. A Model of Crack Electrochemistry for Steels in the Active State Based on Mass Transport by Diffusion and Ion Migration. *Journal of The Electrochemical Society*. 1982;129(7):1412-22.
- (74) Gangloff R. 6.02 - Hydrogen-assisted Cracking. In: Ritchie RO, Karihaloo B, editors. *Comprehensive Structural Integrity*. Oxford, United Kingdom: Elsevier Ltd; 2003. p. 32-6.
- (75) Anderson T. *Fracture Mechanics Fundamentals and Applications*. 3rd ed. Boca Raton, FL, USA: CRC Press; 2005. p. 511-52.

- (76) Fang B, Han E, Wang J, Ke W. Stress Corrosion Cracking of X-70 Pipeline Steel in Near Neutral pH Solution Subjected to Constant Load and Cyclic Load Testing. *Corrosion Engineering, Science and Technology*. 2007;42(2):123-9.
- (77) Wang Z, Wang J, Han E, Ke W. Influence of Intermittent Loading on SCC Behavior for an X-70 Pipeline Steel in a Near Neutral pH Solution. *Materials and Corrosion*. 2007;58(8):583-7.
- (78) Gangloff R. 6.02 - Hydrogen-assisted Cracking. In: Ritchie RO, Karihaloo B, editors. *Comprehensive Structural Integrity*. Oxford, United Kingdom: Elsevier Ltd; 2003. p. 5-19.
- (79) Sutherby R, Jack T, V Boven G, Wilmott M. CEPA Study on Characterization of Pipeline Pressure Fluctuations in Terms Relevant to Stress Corrosion Cracking (IPC2000-222). 2000 3rd International Pipeline Conference; October 1-5, 2000; Calgary, Alberta, Canada: ASME; 2000.
- (80) Yu M, Xing X, Zhang H, Zhao J, Chen W. Depressurization-Induced Crack Growth Enhancement for Pipeline Steels Exposed to Near-Neutral pH Environments. 10th International Pipeline Conference; 2014; Calgary, Alberta, Canada: ASME; 2014.
- (81) Beavers J, Maier C, Jaske C, Worthingham R. Methodology for Ranking Scc Susceptibility of Pipeline Segments Based on the Pressure Cycle History (No. 07128). *Corrosion* 2007; March 11-15, 2007; Houston, TX, USA: NACE International; 2007.
- (82) Been J, King F, Sutherby R. 4.13 - Environmentally Assisted Cracking of Pipeline Steels in Near-Neutral pH Environments. In: *Environment-Induced Cracking of Materials, Volume 2 - Prediction, Industrial Developments and Evaluation*. Amsterdam, The Netherlands: Elsevier, Ltd; 2008. p. 221-30.
- (83) King F, Jack T, Chen W, Wilmott M, Fessler R, Krist K. Mechanistic Studies of Initiation and Early Stage Crack Growth for Near-Neutral pH SCC on Pipelines (No. 00361). 2000 *Corrosion*; 2000; Houston, TX, USA: NACE International; 2000.
- (84) Lambert S, Beavers J, Delanty B, Sutherby R, Plumtree A. Mechanical Factors Affecting Stress Corrosion Crack Growth Rates in Buried Pipelines (IPC2000-219). 3rd International Pipeline Conference; 2000; Calgary, Alberta, Canada: ASME; 2000.
- (85) Zhang X, Lambert S, Sutherby R, Plumtree A. Transgranular Stress Corrosion Cracking of X-60 Pipeline Steel in Simulated Ground Water. *Corrosion*. 1999;55(3):297-305.
- (86) Chen W, Kania R, Worthingham R, Kariyawasam S. Crack Growth Model of Pipeline Steels in Near-Neutral pH Soil Environments (IPC2008-64475). 7th International Pipeline Conference; 2008; Calgary, Alberta, Canada: ASME; 2008.
- (87) Eadie R, Szklarz K, Sutherby R. Corrosion Fatigue and Near-Neutral pH Stress Corrosion Cracking of Pipeline Steel and the Effect of Hydrogen Sulfide. *Corrosion*. 2005;61(2):167.

- (88) Wang S, Zhang Y, Chen W. Room Temperature Creep and Strain-rate-dependent Stress-strain Behavior of Pipeline Steels. *Journal of Materials Science*. 2001 Apr;36(8):1931-8.
- (89) Wang S, Chen W. Room Temperature Creep Deformation and its Effect on Yielding Behaviour of a Line Pipe Steel with Discontinuous Yielding. *Materials Science & Engineering A*. 2001;301(2):147-53.
- (90) Wang S, Chen W. A Study on the Pre-cyclic-load-induced Burst of Creep Deformation of a Pipeline Steel under Subsequent Static Load. *Materials Science & Engineering A*. 2002 Feb 28;325(1-2):144-51.
- (91) Van Boven G, Sutherby R, King F. Characterizing Pressure Fluctuations on Buried Pipelines in Terms Relevant to Stress Corrosion Cracking (IPC2002-27149). 4th International Pipeline Conference; Sept 29 - Oct 3, 2002; Calgary, Alberta, Canada: ASME; 2002.
- (92) Wei R, Landes J. Correlation Between Sustained-Load and Fatigue Crack Growth in High-Strength Steels. *Materials Research and Standards*. 1969;9:25-7.
- (93) Zheng W, Bidy D, Li J, Williams G, Revie W, Tyson B. Stress Corrosion Crack of Oil and Gas Pipelines: New Insights on Crack Growth Behaviour Gained from Full-Scale and Small Scale Tests. 12th International Conference on Fracture; July 12-17, 2009; Ottawa, ON, Canada: ; 2009.
- (94) Kang J, Bibby D, Blanchard R, Zheng W. Full-Scale Stress Corrosion Crack Growth Testing of an X70 Spiral-Welded pipe in Near-Neutral pH Soil Environment. 11th International Pipeline Conference; September 26-30, 2016; Calgary, Alberta, Canada: ASME; 2016.
- (95) Egbewande A, Eslami A, Chen W, Worthingham R, Kania R, Van Boven G. Growth of Surface-Type Stress Corrosion Cracks in Near-Neutral pH Environments Under Disbonded Coatings (IPC2010-31436). 8th International Pipeline Conference; 2010; Calgary, Alberta, Canada: ASME; 2010.
- (96) Zhao J, Chevillat K, Yu M, Chen W, Been J, Keane S, et al. Statistical Analysis on Underload-Type Pipeline Spectra. *Journal of Pipeline Systems Engineering and Practice*. 2016;7(4):4016007.
- (97) Zitounis V, Irving P, Cook R, Jenkins S, Matthew D. Fatigue Crack Growth Acceleration Effects under Helicopter Loading Spectra (ICF10-0434). 10th International Congress on Fracture; 2001; Amsterdam, The Netherlands: Elsevier Ltd.; 2001.
- (98) Zitounis V, Irving P. Fatigue Crack Acceleration Effects During Tensile Underloads in 7010 and 8090 Aluminum Alloys. *International Journal of Fatigue*. 2007;29:108-18.

- (99) Yu M, Chen W, Kania R, Van Boven G, Been J. Underload-induced crack growth behaviour of minor cycles of pipeline steel in near-neutral pH environment. *Fatigue & Fracture of Engineering Materials & Structures*. 2015 Jun;38(6):681-92.
- (100) Yu M, Chen W, Chevillat K, Van Boven G, Been J. Retarding Crack Growth by Static Pressure Hold for Pipeline Steel Exposed to a Near-Neutral pH Environment (IPC2016-64627). 11th International Pipeline Conference; September 26-30, 2016; Calgary, Alberta, Canada: ASME; 2016.
- (101) Zhao J, Chen W, Keane S, Been J, Van Boven G. Development and Validation of Load-Interaction Based Models for Crack Growth Prediction (IPC2014-33325). 10th International Pipeline Conference; Sept 29 - Oct 3, 2014; Calgary, Alberta, Canada: ASME; 2014.
- (102) Tehinse O, Chen W, Been J, Chevillat K, Keane S, Van Boven G. Application of Load Sequence to Control Crack Growth in Steel Pipelines Under Near-Neutral pH SCC (IPC2016-64662). 11th International Pipeline Conference; Sept 26-30, 2016; Calgary, Alberta, Canada: ASME; 2016.
- (103) ASTM Standard E647, 2013e1, "Test Method for Measurement of Fatigue Crack Growth Rates" West Conshohocken, PA, USA: ASTM International; 2013.
- (104) Baker M. Comparison of US and Canadian Transmission Pipeline Consensus Standards. US Department of Transportation; 2008 May.
- (105) Newman J, Raju L. Stress-Intensity Factor Equations for Cracks in Three-Dimensional Finite Bodies Subjected to tension and Bending Loads. Hampton, VA, USA: NASA Langley Research Center; 1984.
- (106) Kang Y, Chen W. Simulation of Crack Growth During Hydrostatic Testing of Pipeline Steel in Near-Neutral pH Environment. *Corrosion Science*. 2010;53:968-75.
- (107) Authors Unknown. Technical Notes: Cellulose Acetate Replicating Film. Redding, CA, USA: Ted Pella, Inc.; 2012.
- (108) Marder A. Replication Microscopy Techniques for NDE. In: ASM Handbook, Volume 17: Nondestructive Evaluation and Quality Control. Materials Park, OH, USA: ASM International; 1989. p. 52-6.
- (109) American Society for Testing and Materials. ASTM Standard G1, 2003 (2011), "Practice for Preparing, Cleaning, and Evaluating Corrosion Test Specimens". West Conshohocken, PA, USA: ASTM International; 2003.
- (110) Sadananda K, Vasudevan A. Review of Environmentally Assisted Cracking. *Metallurgical and Materials Transactions A*. 2011;42A(11):279-95.

- (111) Gangloff R. 6.02 - Hydrogen-assisted Cracking. In: Ritchie RO, Karihaloo B, editors. *Comprehensive Structural Integrity*. Oxford, United Kingdom: Elsevier Ltd; 2003. p. 47-64.
- (112) Thomas R, Scully J, Gangloff R. Internal Hydrogen Embrittlement of Ultrahigh-Strength AERMET 100 steel. *Metall and Mat Trans A*. 2003;34(2):327-44.
- (113) Oriani R. The Diffusion and Trapping of Hydrogen in Steels. *Acta Metallurgica*. 1970;18:147-57.
- (114) Armacanqui M, Oriani R. Plastic Deformation in B.C.C. Alloys Induced by Hydrogen Concentration Gradients. *Materials Science and Engineering*. 1987;91:143-52.
- (115) Parkins R, Beavers J. Some Effects of Strain Rate on the Transgranular Stress Corrosion Cracking of Ferritic Steels in Dilute Near-Neutral-pH Solutions. *Corrosion Science*. 2003;59(3):258-73.
- (116) Kruger J, Begum S. Corrosion of Metals: Overview. In: Reference Module in Materials Science and Engineering. Amsterdam, The Netherlands: Elsevier Ltd.; 2016. p. 1701-6.
- (117) Lyon S. 3.01 Corrosion of Carbon and Low Alloy Steels. In: Richardson T, editor. *Shreir's Corrosion*. Amsterdam, The Netherlands: Elsevier Ltd.; 2010. p. 1963-736.
- (118) Richard H, Sander M. *Fatigue Crack Growth : Detect - Assess - Avoid*. Berlin, Germany: Springer Science; 2016.
- (119) Ritchie R. Mechanisms of Fatigue Crack Propagation in Metals, Ceramics and Composites: Role of Crack Tip Shielding. *Materials Science and Engineering*. 1988;A103(1):15-28.
- (120) Hörnlund E, Fossen JKT, Hauger S, Haugen C, Havn T, Hemmingsen T. Hydrogen Diffusivities and Concentrations in 520M Carbon Steel under Cathodic Protection in 0.5M NaCl and the Effect of Added Sulphite, Dithionite, Thiosulphate, and Sulphide. *International Journal of Electrochemical Science*. 2007;2:82-92.
- (121) Vadhvana N, Chen W. Effect of Loading History on Hydrogen Content in Pipeline Steels (IPC02-27298). 4th International Pipeline Conference; Sept 29 - Oct 3, 2002; Calgary, Alberta, Canada: ASME; 2002.
- (122) Anderson T. *Fracture Mechanics Fundamentals and Applications*. Boca Raton, FL, USA: CRC Press; 2005. p. 61-80.
- (123) Yu M. *Crack Growth Behavior of Pipeline Steels under Variable Pressure Fluctuations in a Near-Neutral pH Environment [dissertation]*. University of Alberta; 2016.

- (124) Li J, Elboujdaini M, Gao M, Revie R. Investigation of plastic zones near SCC tips in a pipeline after hydrostatic testing. *Materials Science and Engineering: A*. 2008;486(1–2):496-502.
- (125) Vosikovsky O, Cooke R. An Analysis of Crack Extension by Corrosion Fatigue in a Crude Oil Pipeline. *International Journal of Pressure Vessels and Piping*. 1978;6(2):113-29.

APPENDIX A: SUPPLEMENTARY DATA – DCPD SYSTEM AND DATA

In order to monitor crack growth of multiple waveforms during a single test the sample was connected to a custom direct-current potential drop (DCPD) system. In combination with pre- and post-test crack length values this technique allowed for the determination of individual crack growth rates of each waveform ran during testing. This appendix explains in detail the setup and techniques to produce accurate data using this system.

First, stainless steel wire leads were spot welded across the back of the samples at the approximate crack tip locations, on each gauge section, in a configuration demonstrated by for Test II. Test I had leads spot welded at five, evenly spaced points along the length of the crack. The spot welded leads were all 25 mm in length and crimped to copper conductors running to individual Agilent 3458A digital multimeters (DMMs) with potential resolutions of ± 10 nV. The copper conductor shieldings were connected to a grounded faraday cage containing the DMMs, reducing noise to close to that of the DMMs internal noise and avoiding ground loops.

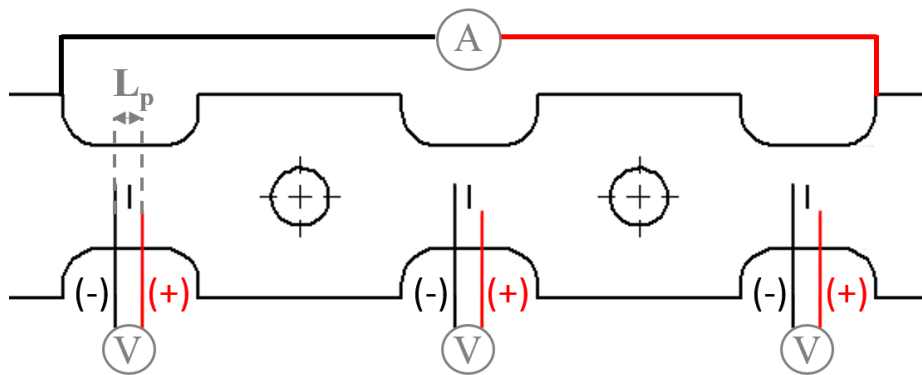


Figure A.1 Long tensile sample DCPD lead configuration for Test II.

The potential probe interspacing (L_p) was 5 mm and 2 mm for Tests I and II, respectively, which are approximately two to five times the depth of the cracks, following recommendations made by Gangloff for potential drop methods for surface cracked specimens (1-A). Additionally, the leads were welded diagonally from each other across the cracks for Test II in order to average measurements of non-uniform crack fronts.

Using a HP6672A PSU, a constant direct current of $15 \text{ A} \pm 0.07 \text{ A}$ was applied across the sample through copper leads soldered to welded steel tabs near the ends of the top and bottom gauge sections, as shown in **Figure A.1**. The power supply was programmed to apply current only during measurement periods and reverse the polarity midway through each measurement period, effectively minimizing thermoelectric effects and any possible affect on the crack tip damage processes. Also, the power supply itself was properly grounded in order to prevent any ground loops between the DCPD system, sample, and loading frame.

The entire system was controlled via LabView software measurement periods occurred automatically once every 1200 s, for 300 s. During the measurement period, sampling would occur every 20 s, averaging ten forward and reverse polarity measurements over several seconds, yielding 15 forward and reverse data points per measurement period. The max potential values of each recording period, which correlate to K_{max} , were used to determine the rates of potential change. Individual points were used to filter and remove data that was acquired during underload cycles as the force cycle is large and it was unknown whether fracture surface shorting occurred during such data measurements.

A FisherBrand temperature probe accurate to $\pm 0.1 \text{ }^\circ\text{C}$ was installed inside the corrosion cell to take measurements every 5 min to correct the potential data for changes in the local environment's temperature. Therefore, linear a relationship between temperature and potential was determined by measuring the change in potential with temperature using the same DCPD configurations, equipment, and current as the real tests on a scrap sample, and then submerging the sample within a temperature controlled water bath and measuring the potential at stablized temperatures between 25 – 30 $^\circ\text{C}$, as seen in **Figure A.2**.

The linear equation determined in **Figure A.2** was further adjusted using a simple linear scaling factor based on the starting potential for each crack, as starting resistance would vary significantly with small changes in probe placement and the temperature effect should scale accordingly. Also, since the DMMs possessed an automated internal correction for temperature and thermoelectric effects it was not necessary to monitor the temperature of the DMMs.

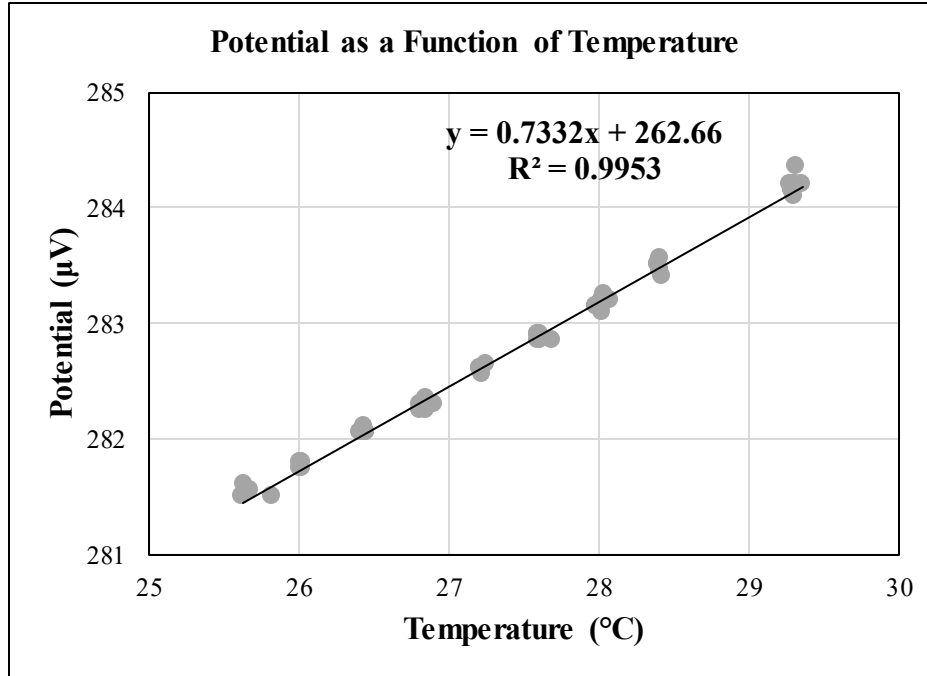


Figure A.2 Potential change of X60 steel as a function of temperature for $L_p = 2$ mm

Using the slope (m), determined in **Figure A.2**, we can determine the compensated voltage, V_c , using the measured potential (V_m), initial test temperature (T_0), and the current measured temperature (T) (2-A).

$$V_c = V_m + m(T - T_0) \quad (0.1)$$

After test completion, the potential change over time was determined using linear trendlines, assuming that crack growth was stable and approximately linear. Then, the percentage of total potential change for each waveform was determined and assumed to be equal to the change in total surface crack growth, as determined by SEM characterization. This was possible through the use of the max potential data points per recording period, obtained at K_{max} , which allowed for a direct conversion of potential change to crack extension to be used. Finally, to express the waveforms in terms of crack growth rate per block the waveforms were divided by their respective total number of underload cycles.

Using the techniques above the potential drop data for Test I were corrected, and are plotted in the Figures below.

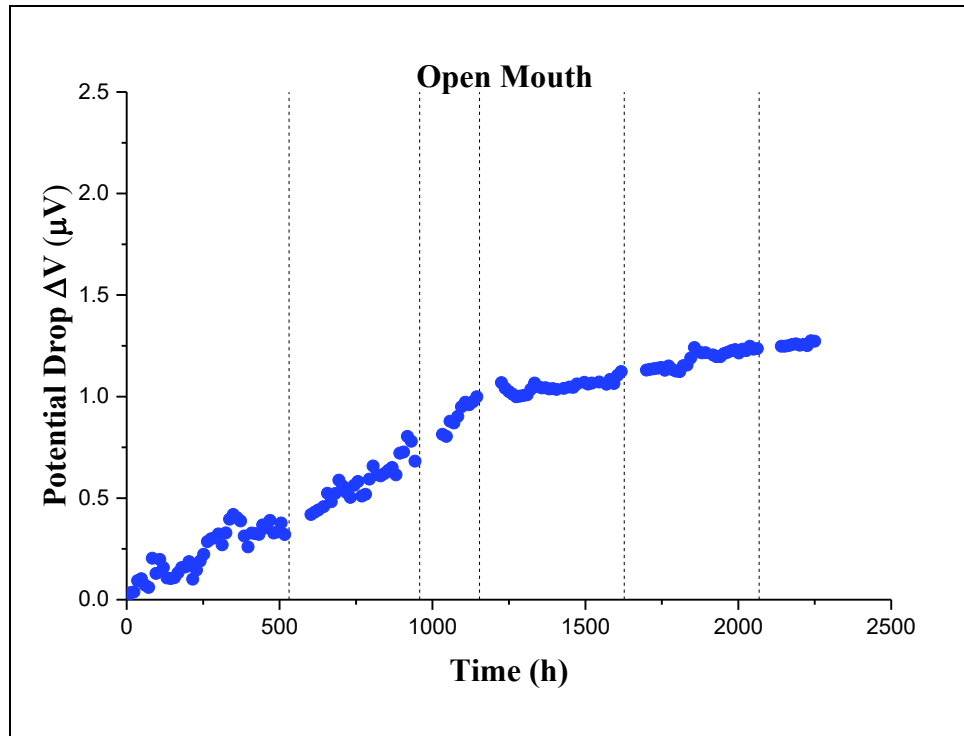


Figure A.3 Temperature-normalized DCPD potential drop plot (ΔV vs. Time) for the OM crack of Test I

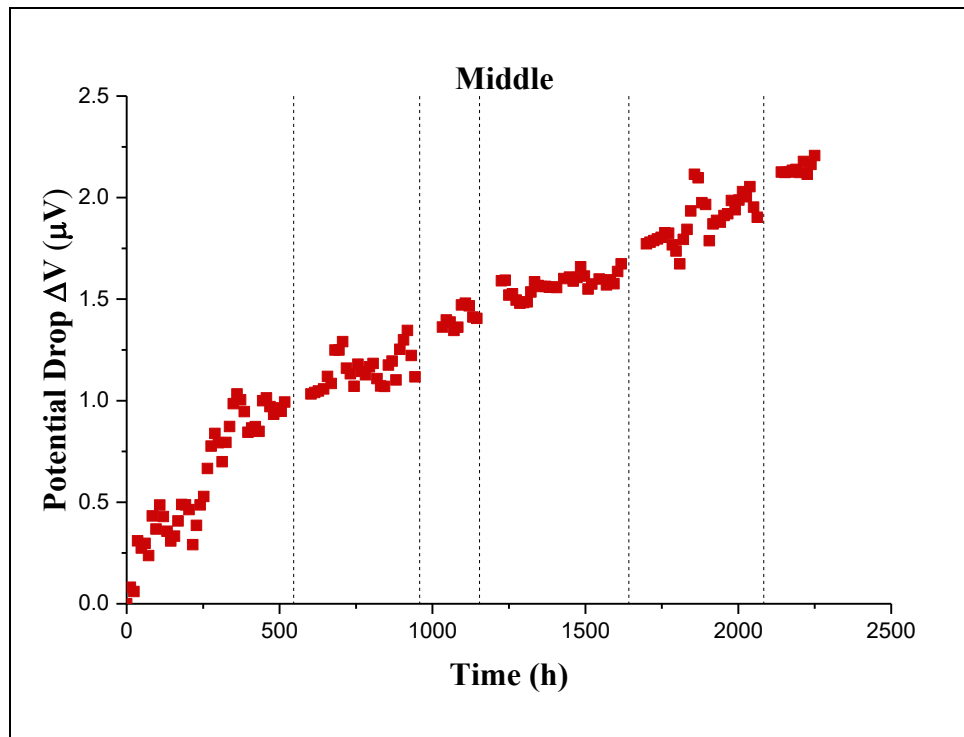


Figure A.4 Temperature-normalized DCPD potential drop plot (ΔV vs. Time) for the Middle crack of Test I

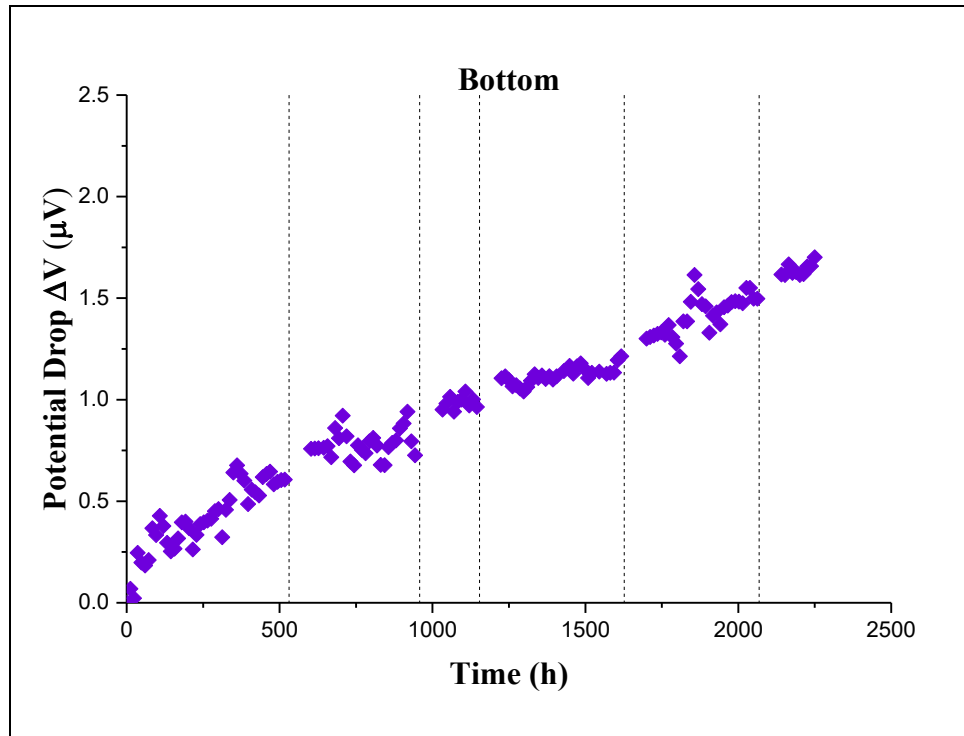


Figure A.5 Temperature-normalized DCPD potential drop plot (ΔV vs. Time) for the Bottom crack of Test I

The linear trend lines were determined for each waveform in **Figure A.3** – **Figure A.5** above. From each waveform, the slope was used to directly correlate dV/dt to dc/dN by determining the fraction of the total potential change for each waveform, and multiplying that value by the measured net crack growth as shown in **Table A.1** below. A similar methodology was used for Test II, except that the trend-line during UL&MC loading was determined over three time intervals. This was because of several large test interruptions, and in order to avoid an inaccurate determination of crack growth, the total potential change of those three time intervals were summed, rather than using a single trend-line, with the total contribution to growth determined by that summed value. The OM data in Test II is not shown here, because of the significant scatter in data it was omitted from the results and the values from the Middle crack were used to determine the OM growth rates instead.

Table A.1 Summary of DCPD data and calculations used to determine Test I's growth rates in C2 solution (dc/dN).

WF #	dV/dt	Time (h)	Blocks	Blks/h	dV/dN	dV (nV)	% dc	$\Delta 2c$ [μm]	dc/dN [$\mu\text{m}/\text{blk}$]	
1	2.37	200.92	7081	35.24	0.07	-	-	-	-	
	2.34				0.07	-	-	-	-	
	2.33				0.07	-	-	-	-	
2	0.70	530.55	1902	3.6	0.19	367	0.27	54.4	2.86×10^{-2}	
	1.91				0.53	1006	0.56	46.2	2.43×10^{-2}	
	1.00				0.28	530	0.49	17.8	9.37×10^{-3}	
3	0.90	425.21	15284	36	0.02	380	0.28	56.3	3.68×10^{-3}	
	0.37				0.01	157	0.09	7.2	4.73×10^{-4}	
	0.12				0.00	50	0.05	1.7	1.10×10^{-4}	
4	1.76	194.90	70242	360	0.00	343	0.25	50.8	7.23×10^{-4}	
	0.68				0.00	132	0.07	6.1	8.64×10^{-5}	
	0.18				0.00	34	0.03	1.2	1.66×10^{-5}	
5	0.18	472.95	85	0.18	1.00	85	0.06	12.6	1.48×10^{-1}	
	0.25				1.42	120	0.07	5.5	6.50×10^{-2}	
	0.25				1.37	116	0.11	3.9	4.59×10^{-2}	
6	0.34	439.96	72.00	0.17	2.00	144	0.11	21.3	2.96×10^{-1}	
	0.65				3.80	273	0.15	12.5	1.74×10^{-1}	
	0.63				3.70	266	0.24	8.9	1.24×10^{-1}	
7	0.20	184.29	33.00	0.18	1.14	37	0.03	5.6	1.69×10^{-1}	
	0.54				3.00	98	0.06	4.5	1.38×10^{-1}	
	0.50				2.77	91	0.08	3.1	9.29×10^{-1}	
Total (Net)		2449	94699			1358		201.0		
							1789		82.1	
							1088		36.6	

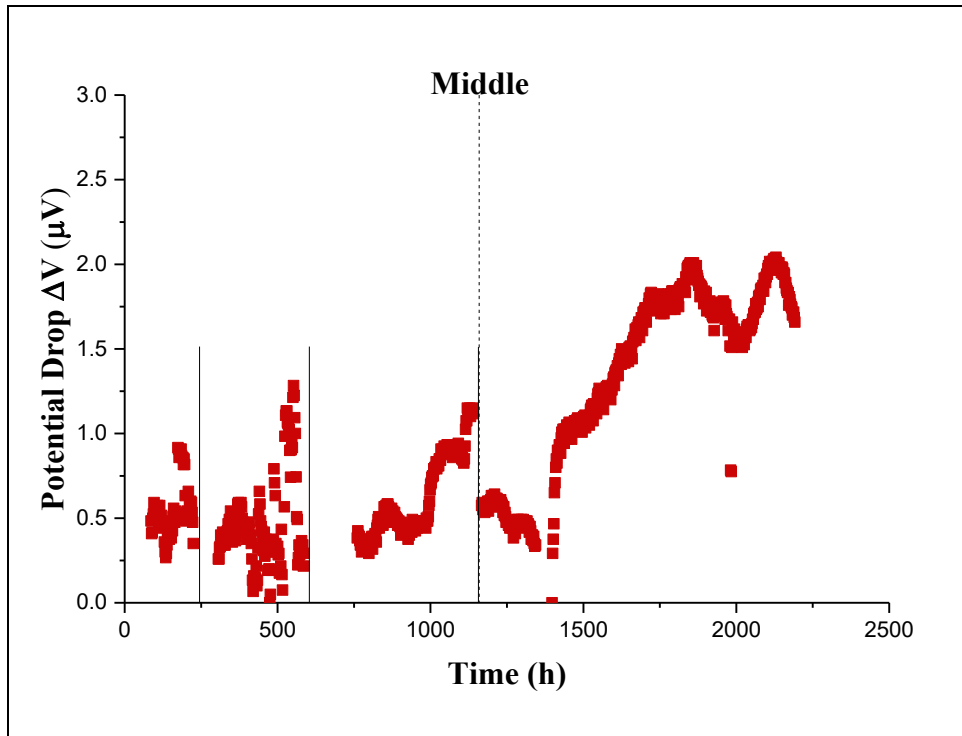


Figure A.6 Temperature-normalized DCPD potential drop plot (ΔV vs. Time) for the Middle crack of Test II

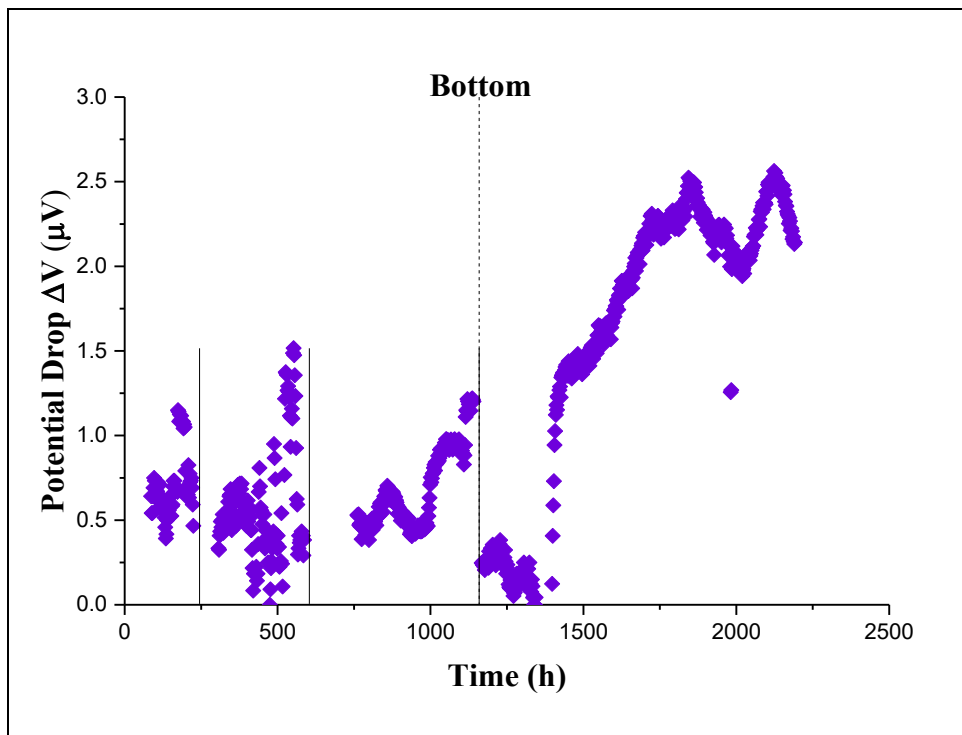


Figure A.7 Temperature-normalized DCPD potential drop plot (ΔV vs. Time) for the Bottom crack of Test II

Table A.2 Summary of DCPD data and calculations used to determine Test II's growth rates in C2 solution (dc/dN).

WF	dV/ dt	Time (h)	Blk	Blks/ h	dV/ dN	dV (nV)	% dc	Net Growth [um]	dc/dN [um/blk]
3	0.00	1106	180	0.17	6.11	-	-	84.0	2.3×10^{-1}
	0.99				6.11	1099	0.62	35.1	9.7×10^{-2}
	1.04				6.41	1153	0.57	23.9	6.6×10^{-2}
4	0.00	1024	184	0.17	3.71	-	-	52.2	1.4×10^{-1}
	0.67				3.71	683	0.38	21.8	5.9×10^{-2}
	0.84				4.65	856	0.43	17.7	4.8×10^{-2}
Total (Net)		2130				0.00		136.1	
						1782		56.8	
						2009		41.7	

REFERENCES

- (1-A). Gangloff R. Electrical Potential Monitoring of Crack Formation and Subcritical Growth from Small Defects. *Fatigue of Engineering Materials and Structures*. 1981;4(1):15-33.
- (2-A). Sposito G. Advances in Potential Drop Techniques for Non-Destructive Testing [dissertation]. Imperial College London; 2009.

APPENDIX B: SUPPLEMENTARY DATA – ADDITIONAL CRACK IMAGES

In Chapter 4, images of the cracks used in Test I and II were presented for discussion in Chapter 5. The following appendix contains supplementary crack images to Chapter 4, which support the conclusions drawn in Chapter 5, but were unnecessary to present within the main body of the text. The images obtained for the pretest replica crack tips, full post-test surface profiles, low magnification fracture surfaces, and images used to determine the growth regions on the fracture surface are provided.

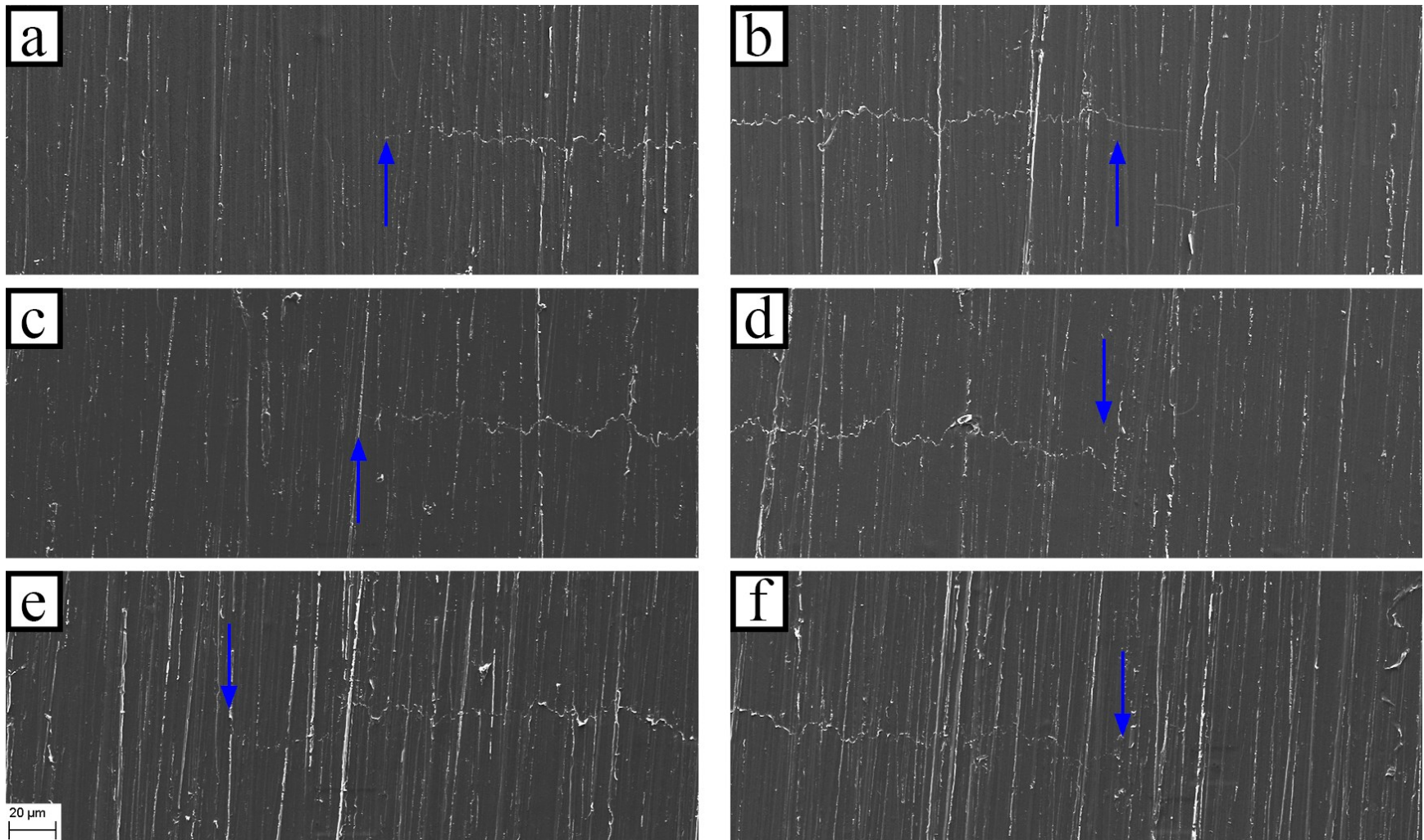


Figure B.1 SE images of Test I's pretest replicas of the (a,b) OM, (c,d) Middle, and (e,f) Bottom crack tips.

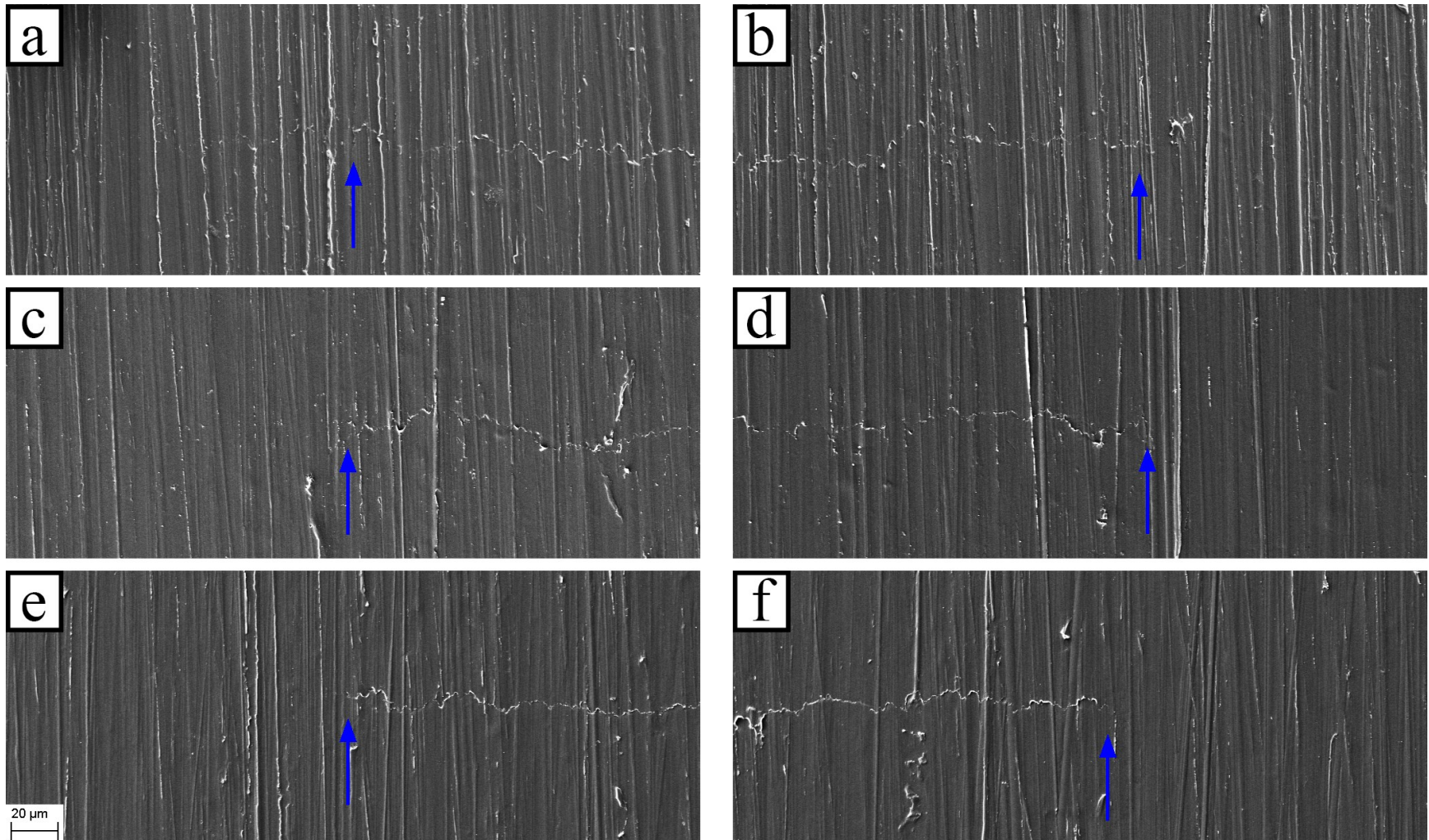


Figure B.2 SE images of Test II's pretest replicas of the (a,b) OM, (c,d) Middle, and (e,f) Bottom crack tips .

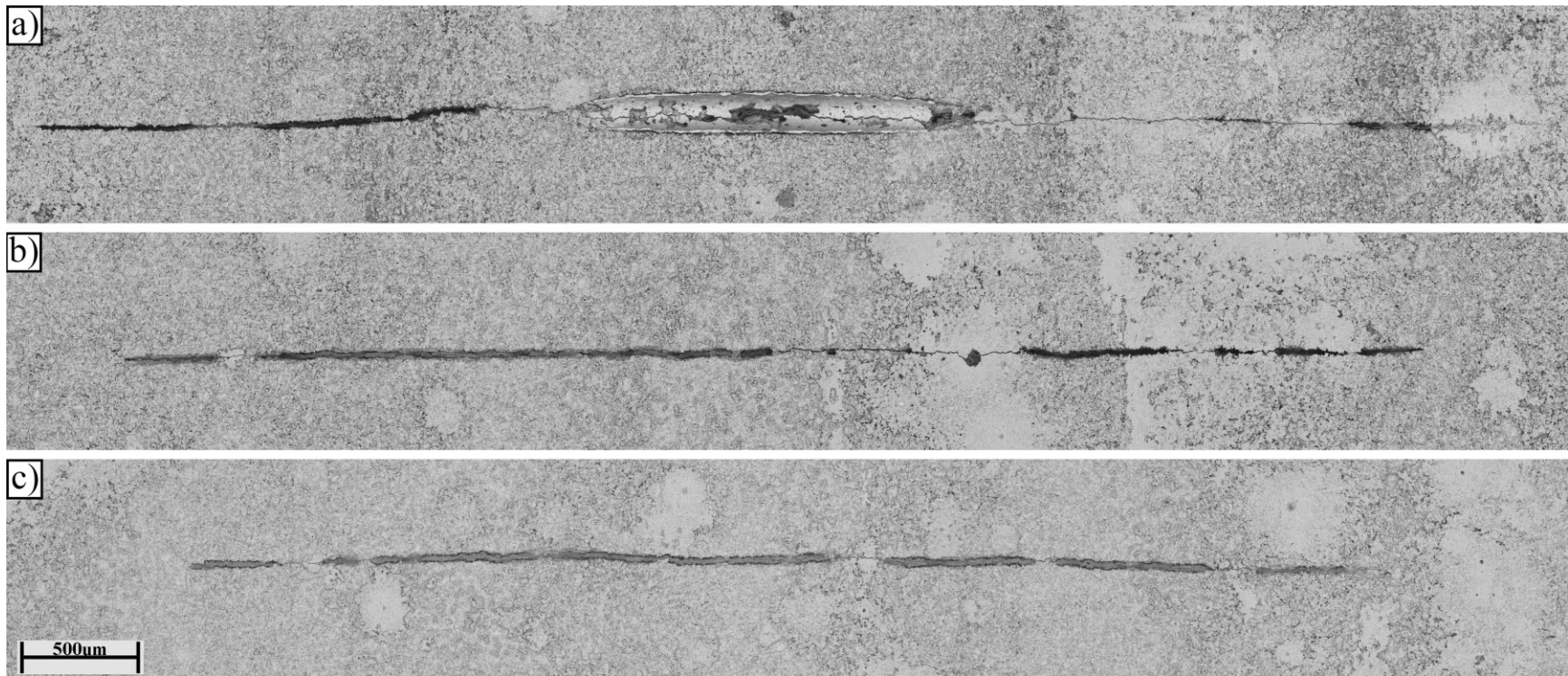


Figure B.3 BSE full surface profile post-test images of Test I's (a) OM, (b) Middle, and (f) Bottom cracks.

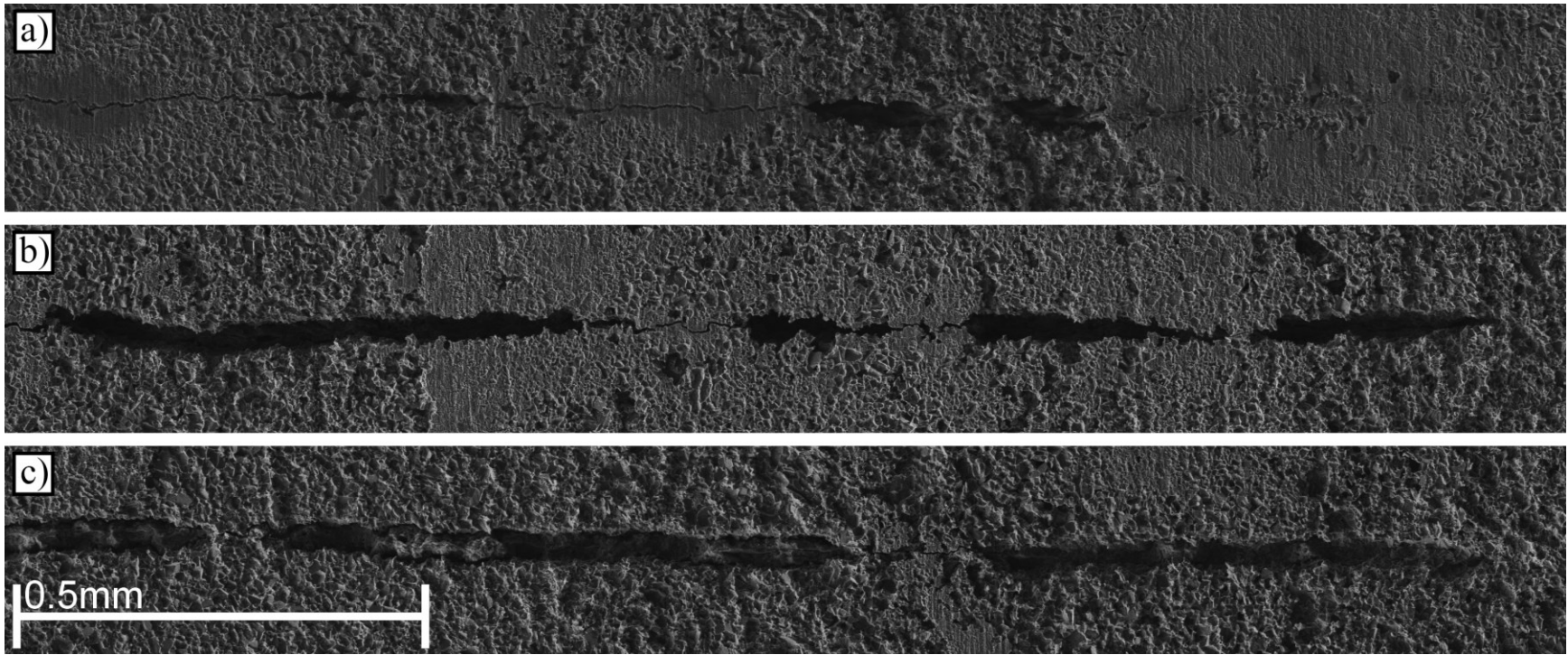


Figure B.4 SE partial surface profile post-test images of Test I's (a) OM, (b) Middle, and (f) Bottom cracks.

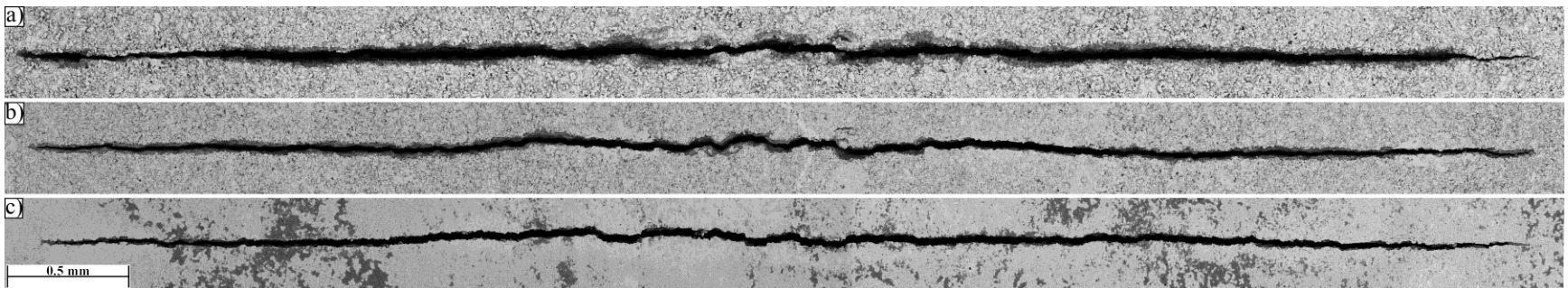


Figure B.5 BSE full surface profile post-test images of Test II's (a) OM, (b) Middle, and (f) Bottom cracks.

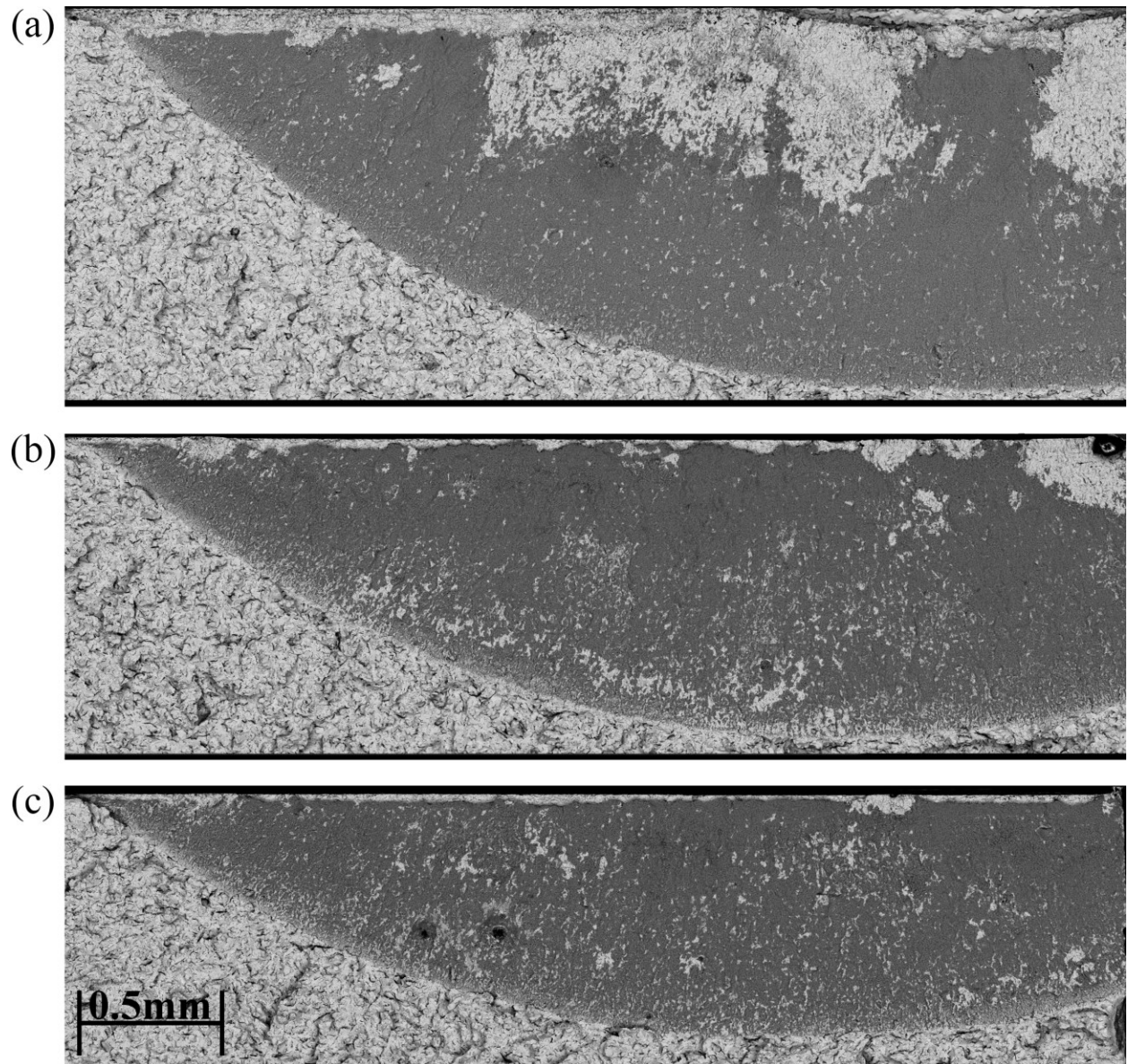


Figure B.6 Low mag BSE images of Test I's (a) OM, (b) Middle, and (c) Bottom crack fracture surfaces.

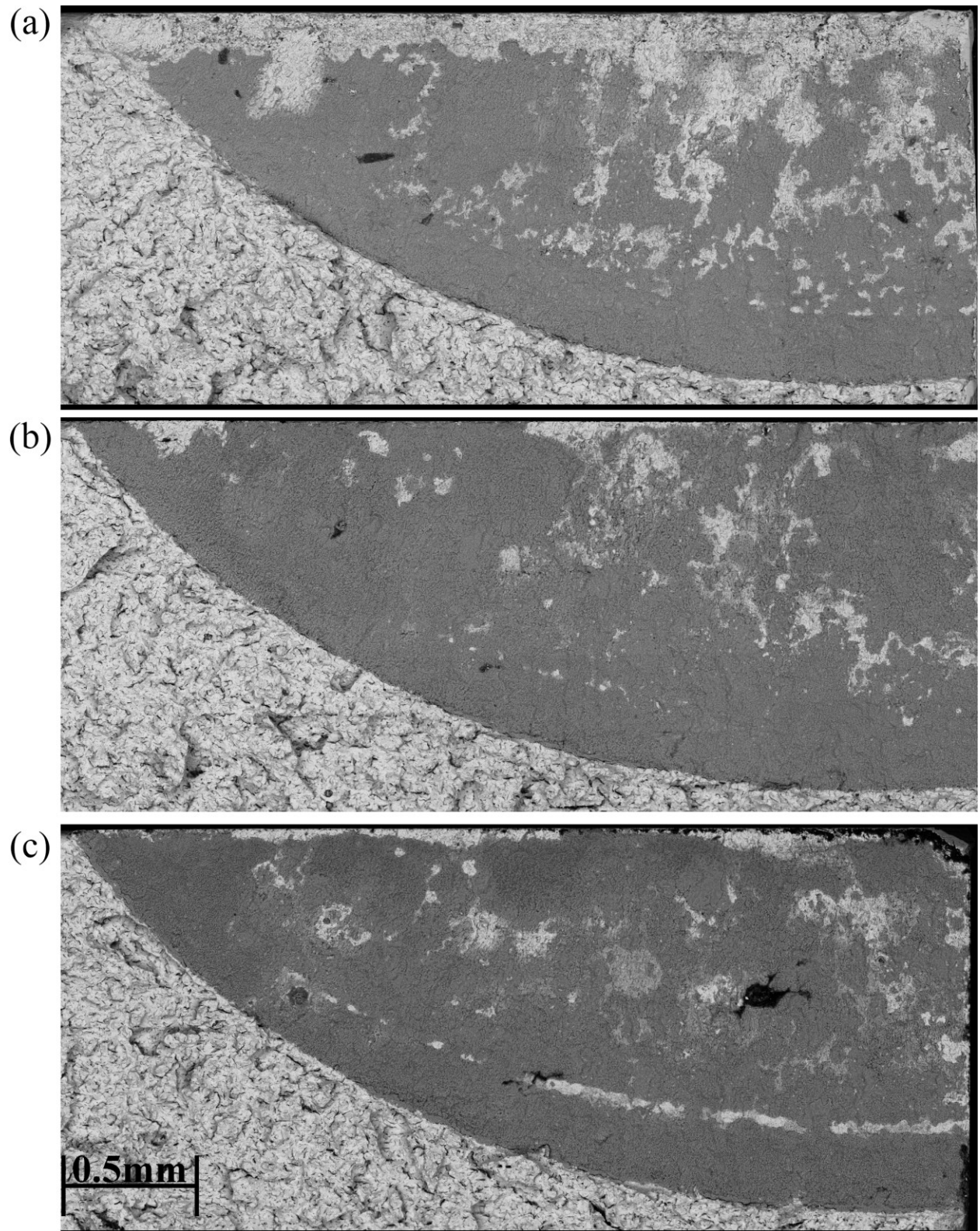


Figure B.7 Low mag BSE images of Test II's (a) OM, (b) Middle, and (c) Bottom crack fracture surfaces.

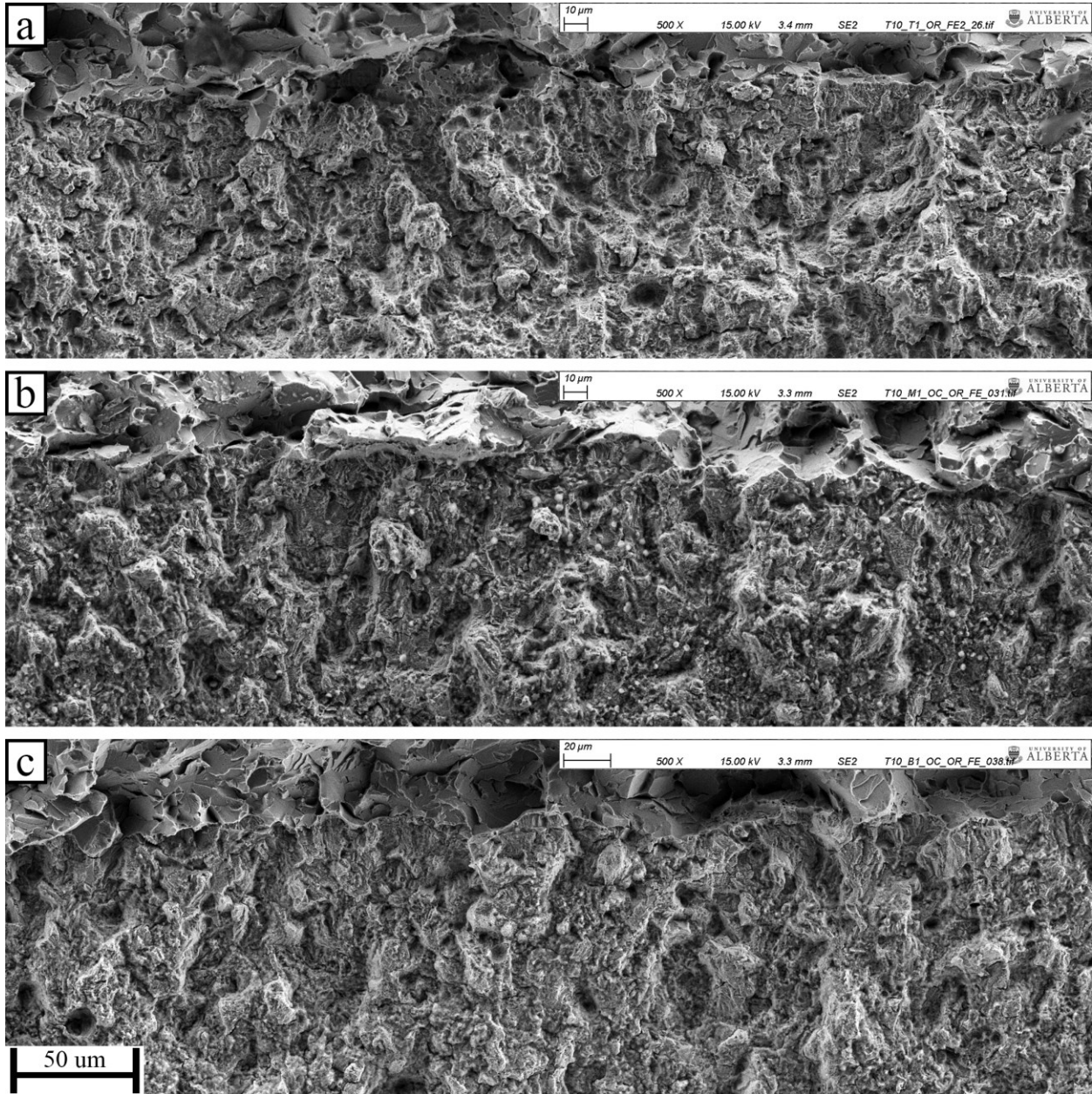


Figure B.8 SE FESEM images demonstrating growth bands in the depth on the fracture surfaces of the (a) OM, (b) Middle, and (c) Bottom cracks of Test I.

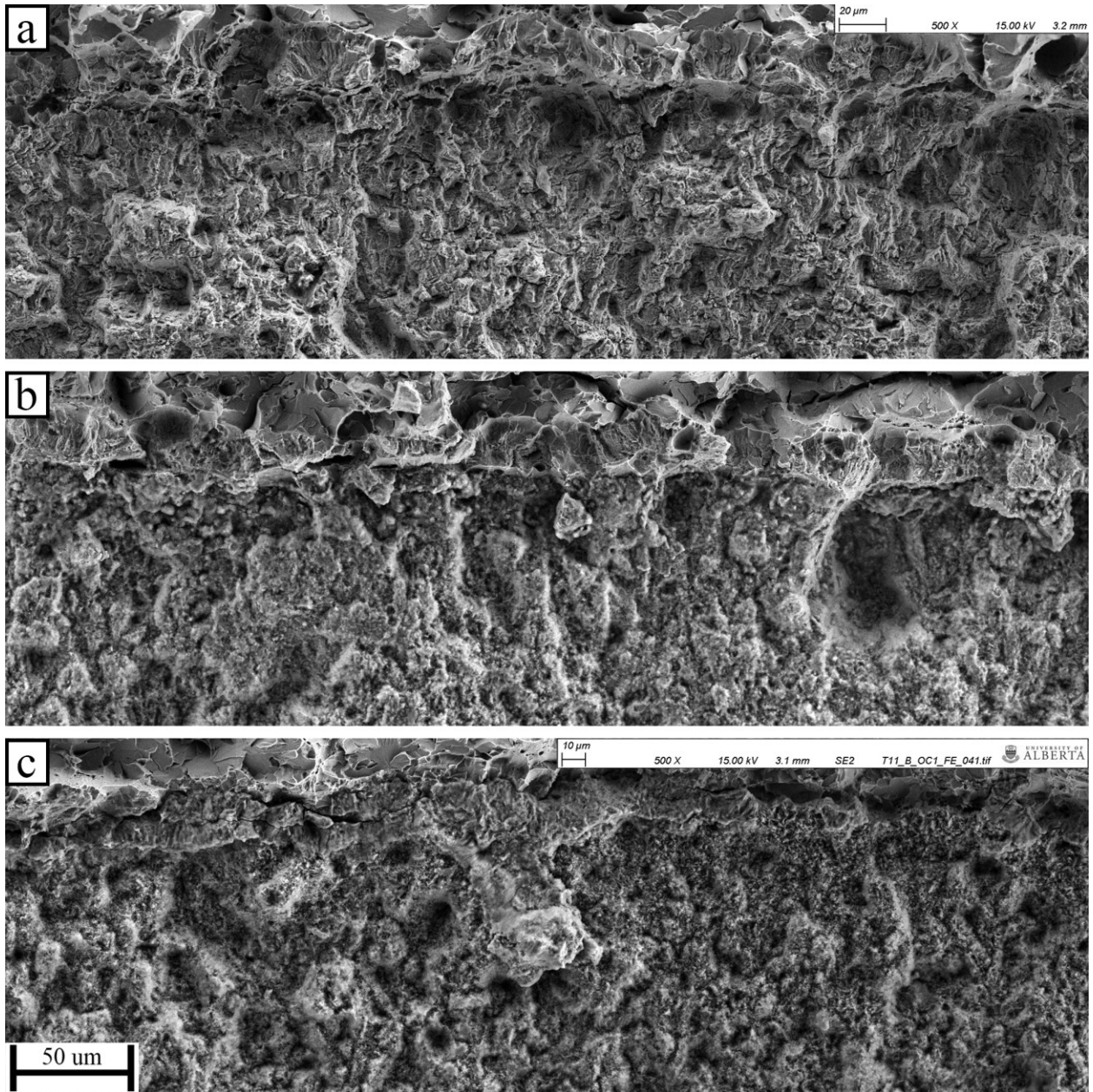


Figure B.9 SE FESEM images demonstrating growth bands in the depth on the fracture surfaces of the (a) OM, (b) Middle, and (c) Bottom cracks of Test II.

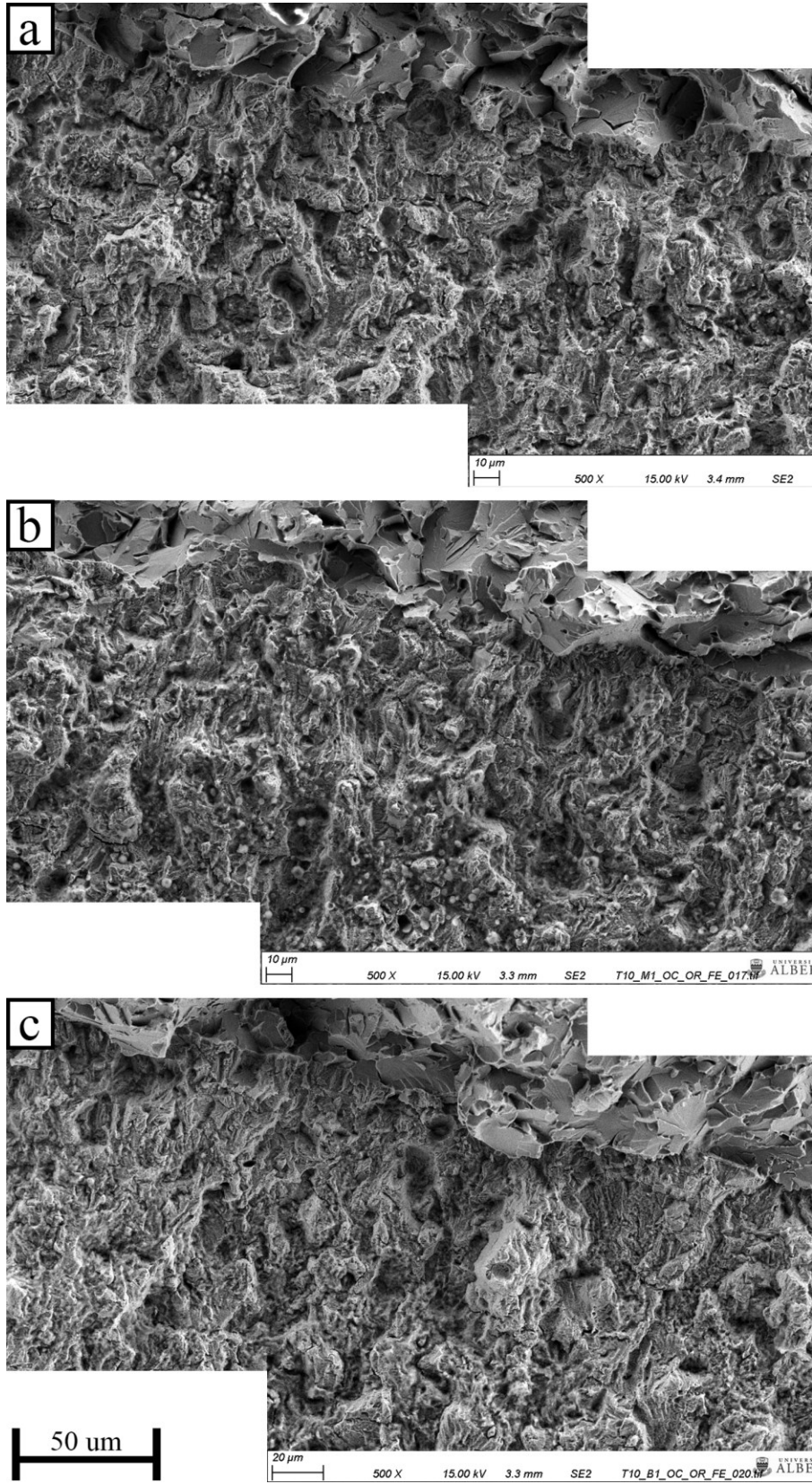


Figure B.10 SE FESEM images demonstrating growth bands at the midway point on the fracture surfaces of the (a) OM, (b) Middle, and (c) Bottom cracks of Test I.

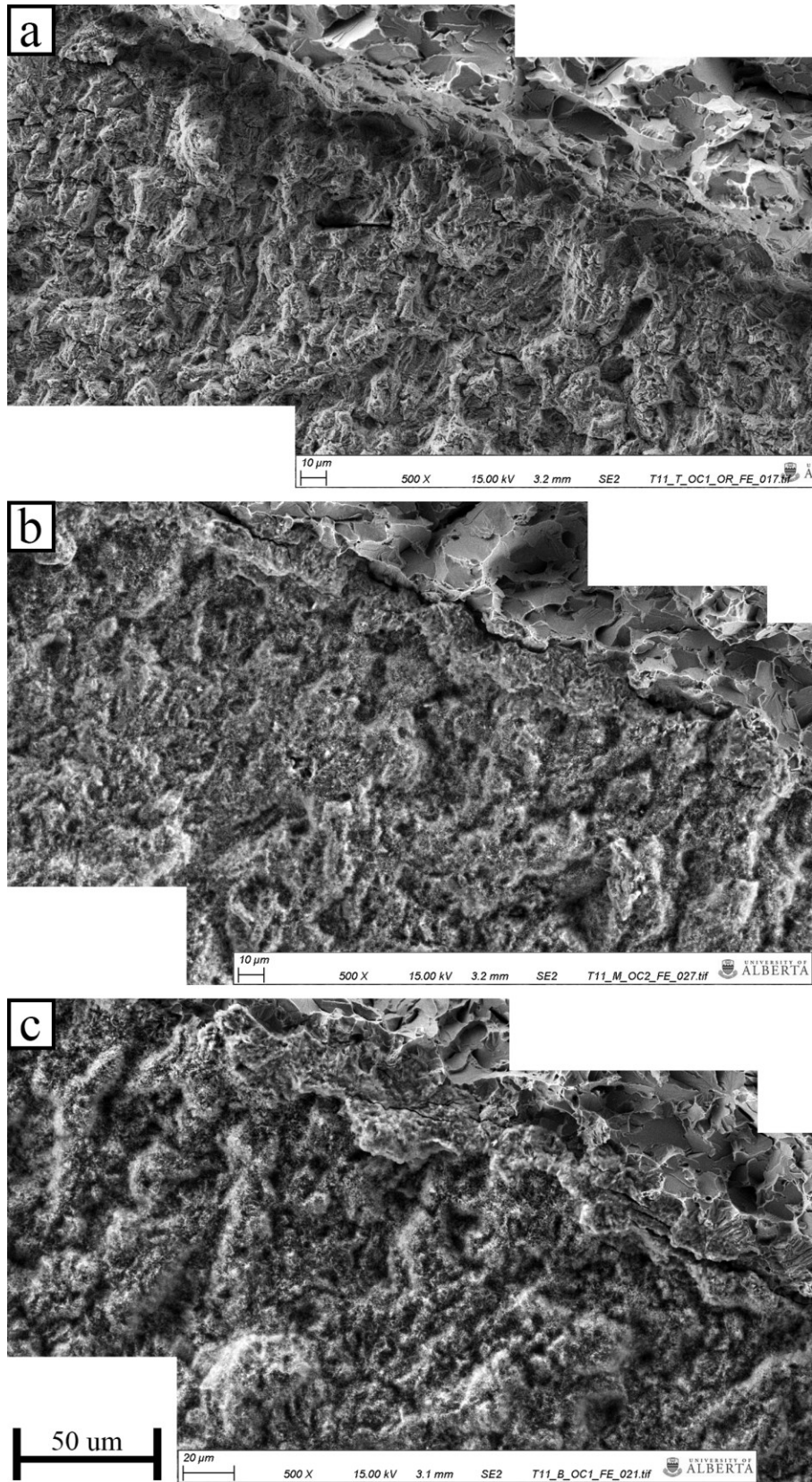


Figure B.11 SE FESEM images demonstrating growth bands at the midway point on the fracture surfaces of the (a) OM, (b) Middle, and (c) Bottom cracks of Test II.